THE EFFECT OF UNSTEADY SEA CONDITIONS ON TIDAL STREAM TURBINE LOADS AND DURABILITY

Thomas Mikael Nevalainen, M.S.A.E

A thesis submitted for the
Degree of Doctor of Philosophy

Energy Systems Research Unit
Department of Mechanical & Aerospace Engineering
University of Strathclyde

November 2016

Declaration of authenticity and author's rights

This thesis is the result of the author's original research. It has been composed by the author and has not been previously submitted for examination which has led to the award of a degree.

The copyright of this thesis belongs to the author under the terms of the United Kingdom Copyright Acts as qualified by University of Strathclyde Regulation 3.50. Due acknowledgement must always be made of the use of any material contained in, or derived from, this thesis.

Signed: ______________________________

Date: ______________________________

Dedicated to my Mum and Dad,
June and Raimo Nevalainen

Contents

List of figures

List of tables

Acknowledgements

I would like to thank my supervisor Cameron Johnstone for his support through this project and for giving me the freedom to pursuit the topics that I found interesting which is the fundamental basis of curiosity driven research. I would also like to thank Peter Davies at Lloyd's Register EMEA for his advice and encouragement during my industrial collaboration, allowing this thesis to reach a greater depth and contemporary grounding in the tidal energy field. Thank you Michael Togneri and Ian Masters for sharing the blade performance data with us. Also, thank you Andy Grant for giving me this amazing opportunity in the first place and Daniele Santomassimo at Schaeffler UK for all the advice and bearing data.

I would like to thank all my friends in the office who have helped me with my work and kept me company throughout the duration of my PhD including Katie Gracie Orr for innumerable discussions, Tom McCombes for getting me started and John Allison for all the programming/LaTeX tutorship.

I sincerely thank the funders of my research, the EPSRC through SuperGen UK-CMER, that have enabled me to work in the field of engineering that I am most interested in for the past three years.

Finally, my greatest thanks go to my family and friends at home who have had to put up with my absence over the last decade. Without your support, and just being there as always, I would never had made it to where I am now.

This thesis was typeset in LaTeX using the Texmaker 4.1.1 editor. All scripting of the methodologies presented were done in Matlab R2012b and Ansys 15 Mechanical APDL both using the academic licences at the University of Strathclyde and some airfoil data was derived using Xfoil. The figures were generated in Matlab using the 'matlab2tikz' package by Nico Schlömer and were edited in Inkscape.

Abstract

This thesis explores the effect that the unsteady hydrodynamics of the marine climate has on the load generation and subsequent durability of horizontal axis tidal stream turbines (TSTs). This is achieved through several campaigns of numerical modelling where the methodologies adopted were chosen on the principle of maximising the computational efficiency, allowing for time-domain durability calculations to be performed. The inflow was modelled by a variety of engineering wave models coupled with the underlying current profiles and the rotor loads were resolved using blade element momentum theory (BEMT). The rotor loads were then fed to a six degree of freedom drivetrain model to analyse the stresses and the fatigue damage in the system.

In order to inform on the input-output relationships of a turbine's operating conditions and the generated loads, a sensitivity analysis was performed on the BEMT model to show each input parameter's influence on the loading. The results showed that the rotor radius, blade pitch, significant wave height, inflow velocity and shear current steepness were the dominant factors in regards to the loading. Furthermore, an investigation on the internal contact stresses in the turbine's main bearing found that simplifying the turbine loading problem down to a one-dimensional phenomenon gave a significant underestimation in the internal loads.

It is concluded that to accurately model the internal loads on a TST, the full spatial range of the rotor loads including the off-axis components, must be incorporated in the structural modelling to avoid under prediction of the stresses and the related over predictions of the resulting fatigue life. The standard fatigue analysis techniques used in this work were also identified as possibly being unsuitable for the highly dynamic marine climate and suggestions on how to address this issue are provided.

Nomenclature

Commonly used symbols

x, y, z	Global coordinates
x_ℓ, y_ℓ, z_ℓ	Legrangian coordinates
u, v, w	Velocity components in respective x, y and z-direction
x'	x-coordinate in wave harmonic reference frame
z_c	Wheeler-stretched vertical coordinate
V	Relative inflow velocity vector
α	Angle of attack
$\varOmega_\mathrm{r}$	Rotor angular velocity
R	Rotor radius
U_∞	Rotor current upstream velocity
Q	Rotor torque
F	Rotor thrust, Tip-loss factor
A, A_d	Rotor area
U_∞	Rotor current upstream velocity
C_P	Turbine power coefficient
C_T	Turbine thrust coefficient
ρ	Fluid density
T	Wave period
T_app	Apparent wave period
ω	Wave angular frequency
ω_a	Observed wave angular frequency
ω_r	Relative wave angular frequency
k	Wave number
H	Wave height
a	Wave amplitude
η	Wave surface displacement
h	Water depth
L	Wave length
C	Celerity, bearing dynamic load rating
c_E	Eularian time-averaged fluid velocity
φ	Velocity potential, Inflow velocity angle of incidence
ψ	Stream function
p	Fluid pressure, load-life exponent, resolution of sampling
p_0	Fluid pressure at surface

$C(t)$	....	Intergation function
U_m	....	Eularian mean current velocity
U_s	....	Surface velocity
$\bar{U}$	....	Depth-averaged mean current
U_b	....	Bottom velocity
$\bar{u}$	....	User specified mean current
$\mathit{\Omega}_0$	....	Constant current vorticity
ϵ	....	Wave steepness
ϕ_i	....	Wave harmonic phase angle
U_{0i}	....	Current component in-line with wave
θ_i	....	Angle of incidence of wave harmonic
H_s	....	Significant wave height
T_p	....	Peak power period
T_z	....	Zero-crossing period
a	....	Axial induction factor
b	....	Angular induction factor
r	....	Rotor radial position
$\mathrm{d}r$	....	Blade element length
N	....	Number of blades
C_L	....	Blade lift coefficient
C_D	....	Blade drag coefficient
C_FA	....	Blade-local thrust coefficient
g	....	Gravitational acceleration, error function
$\phi_{\mathrm{B}i}$	....	Angle of blade azimuth
$u_{\mathrm{B}i}$	....	Blade section local axial inflow component
$v_{\mathrm{B}i}$	....	Blade section local rotational inflow component
g	....	Gravitational acceleration, error function
L_{10}	....	Bearing life in millions of revolutions
P_eq	....	Equivalent bearing load
F_r	....	Radial bearing load
F_a	....	Axial bearing load
X	....	Radial load factor
Y	....	Axial load factor
D_annual	....	Annual bearing damage
μ	....	Sea-state occurrence factor
μ^*	....	Sensitivity index
σ	....	Variable interaction index
h_hub	....	Hub operating height
θ	....	Blade pitch
ϕ	....	Blade initial azimuth
V_ecc	....	Eccentricity vector
M_{yi}	....	Blade out-of-plane bending moment in blade reference
M_y	....	Global blade out-of-plane bending moment in y-direction
M_z	....	Global blade out-of-plane bending moment in z-direction
κ	....	Shear correction factor

Acronyms

TST	....	Tidal Stream Turbine
BEMT	....	Blade Element Momentum Theory
EMEC	....	European Marine Energy Centre
AoA	....	Angle of Attack
ADCP	....	Acoustic Doppler Velocity Profiler
TSR	....	Tip Speed Ratio
FSI	....	Fluid Structure Interaction
TI	....	Turbulence Intensity
CFD	....	Computational Fluid Dynamics
URANS	....	Unsteady Reynolds Averaged Navier-Stokes
NREL	....	National Renewable Energy Laboratory
FEM	....	Finite Element Method
DoF	....	Degree of Freedom
OAT	....	One-at-time
PM	....	Pierson-Moskowitch
JONSWAP	....	Joint North Sea Wave Observation Project
YTF	....	Years to Failure
MWL	....	Mean Water Level
SD	....	Standard Deviation

Chapter 1

Introduction

1.1 Investigating the dynamic loads on tidal stream turbines operating in the unsteady marine environment

At the current stage of writing, tidal steam turbine (TST) technology has matured to the point where the first large scale commercial deployments are being undertaken. This is a crucial point in the development of the sector since the outcome of these early full-scale projects will demonstrate the feasibility of the technology and govern the future investment attitudes. Therefore, if tidal stream energy extraction is to be successful, it must prove to be a reliable and economically viable renewable energy option. This arguably puts the durability and reliability of the technology at the highest importance. The matter of durability is however a complicated subject since the loading regimes that TSTs operate in are highly varying and erratic due to the unsteadiness of the marine environment — achieving the required 10 - 25 years of operating life will thus be a considerable challenge.

It is reasonable to believe that TSTs will be highly susceptible to component failures due to the cyclic stresses brought on by the variations in inflow velocity if they are not properly engineered for. These inflow variations, caused by marine flow phenomena, fluctuate both over time such as from a passing wave train or the tidal phases, and spatially over the rotor plane where one part of the rotor can see a higher inflow velocity than another. The source of these inflow variations are most notably caused by the surface waves and velocity profiles present in the tidal flow. The presence of a constantly varying, non-uniform velocity gradient over a turbine's rotor will ultimately induce a complex thrust pattern on the blades which is likely to be translated into eccentric loads on the turbine drivetrain; such off-axis shaft loads can be highly detrimental on critical internal components such as bearings and seals.

This thesis aims to shed light on a particular area of TST loading by investigating the relationships between a turbine's operating conditions and the experienced load distributions and subsequent durability through numerical modelling. An emphasis will be placed on how the load gradients across the rotor plane give rise to additional eccentric load components and how these off-axis loads influence the internal forces that are induced in the drivetrain and bearings.

In other efforts made to quantify the hydrodynamic loads on TSTs, researchers and developers have successfully used a wide array of simulation codes and small scale experiments which have yielded insight to the dynamics of the machines. However, due to the inherent complexity of the physical problem, the simulation models tend to be highly computationally demanding making them unfit for durability calculations which require hundreds of simulation cases. On the other end of the spectrum, some commercially available numerical models tend to be highly simplified where the turbine forces are only resolved in the axial degree of freedom, assuming that the TST loading phenomenon is a one-dimensional issue, which has the result of the methods neglecting the additional directionalities of the loads translated to the drivetrain from the non-uniform rotor loads.

In the interest of carrying out a systematic study on the effects that the marine hydrodynamic forces have on the TST peak stresses and component durability, the modelling techniques used in this study were required to accurately resolve the complex hydrodynamic forces on the turbine in all degrees of freedom, while still being computationally efficient enough to allow for fatigue life calculations over large time-scales. These models, presented in the following chapters, make up the main part of the methodology used to derive the functional relationships between a turbine's operating conditions and the experienced loads and durability. In order to successfully achieve the research goals of quantifying the relationships between the unsteady sea conditions and the loads and durability of a TST, several research questions are defined below to aid in the completion of the main objective.

1.1.1 Research questions

With regards to assuring that individual TST units are designed to reach their maximum capabilities in terms of durability and reliability, several questions must be considered in greater detail to inform on how TSTs will respond to their hydrodynamic load environments and how to accurately and efficiently model the devices. When answered, the research questions listed below will aid in shedding light on the main thesis question of "how does the instationary flow in the marine climate affect the loads and life of a tidal stream turbine?”. The research questions are presented as:

1. How does the non-uniform inflow across a TST’s rotor, caused by surface waves and shear current profiles, manifest itself in terms of the load magnitudes and load directionalities on the main rotor shaft?
2. What parameters in regards to the inflow conditions, operating modes and turbine geometry are most influential when considering the generation of loads on a TST in a general manner?
3. Considering the non-uniform inflow over a turbine’s rotor in a tidal flow, will the often over-looked rotor out-of-plane bending moments induced by the load gradient over the rotor increase the internal loads on a TST when included in a drivetrain model? Is there an underprediction in the internal loads when modelling the drivetrain system as purely axial?
4. Assuming that the main bearing of a TST is the component that absorbs most of the loads from the rotor, how is its fatigue life related to variations in the inflow, operating mode and geometrical layout of the turbine?
5. How does the inclusion of the full range of the degrees of freedom of the rotor loads in the drivetrain modelling affect the fatigue life of the bearing as opposed to the traditional way of modelling the drivetrain as a one-dimensional system?

In furtherance to these identified research needs, this thesis presents a methodology to accurately and efficiently determine the loads on a TST caused by dynamic inflow conditions and resolves their translation into the turbine drivetrain. Although each of the different methodologies presented in this work are common practice in the TST sector already, it is the combination of these methods and the holistic study of the input parameters to the output loads that is the original development of this project.

Shown in the next section are the specific research objectives of the thesis, presented in a way to give an understanding of how the questions stated above were addressed and what methods were used to answer them.

1.1.2 Research objectives

As mentioned, the main aim of this thesis can be summarised as to increase the detailed understanding of how the hydrodynamic forces on TSTs, caused by the unsteady marine inflow, affect the dynamics, peak loads and durability of its components. This includes both examining the load propagation in its path through the rotor to the drivetrain and bearings in high resolution and to gain an understanding of how sensitive these loads are to changes in the input conditions. In order to achieve this, the following objectives are presented which will aid in answering the main thesis research question:

1. Develop a numerical model that can accurately and efficiently resolve the dynamic loads generated on the rotor of a TST operating in unsteady marine environments caused by surface waves and shear currents in the form of an unsteady blade element momentum theory (BEMT) routine. Along with this, the numerical model needs to include a drivetrain model that can incorporate the loads from the rotor in all degrees of freedom to determine the resulting bearing loads.

2. Identify the most important input parameters which have the largest influence on the turbine's load magnitudes and variations through a sensitivity analysis on the numerical BEMT model.

3. Map the relationships between the identified dominant parameters and the forces generated on the turbine rotor in all degrees of freedom, including the rotor out-of-plane bending moment.

4. As the main bearing fatigue life is assumed to be indicative of the durability of a TST's drivetrain, the developed hydrodynamic and structural load model will be used to investigate what effect variations in the input parameters, such as the wave height and rotor diameter, have on the main bearing fatigue life. This will inform the sensitivity of the turbine's durability to the sea-state, turbine geometry and operating conditions.

5. The effect that the inclusion of the rotor out-of-plane bending moments in the drivetrain model has on the off-axis stress distributions of the internal components will be quantified and compared to the results using the traditional purely axial approach.

6. The main focus of the study will be on the general trends and relationships of the various input-output relationships of the turbine loading, as opposed to emphasising the absolute numerical values of the results. This will make the observations and conclusions more general and applicable to a wider range of cases.

The studies presented in the following chapters were conducted in a direct numerical way, meaning that the accumulated damage and fatigue lives were determined from actual simulated time-series loads as opposed to using statistical methods such as ‘mean time to failure’ and other methods based on probability density functions. Presented in the next section is a condensed list of the main original contributions of this thesis, to give the reader a overview of what has been undertaken in the current research.

1.2 Overview of original research contributions

The following research contributions have been produced as a direct result of the work undertaken in this thesis:

- The delivery of a computationally efficient methodology that synthesizes realistic inflow conditions for TSTs and translates the generated hydrodynamic loads into the drivetrain components.
- Increased understanding of the input-output relationships between a TSTs inflow and operating conditions to the load spectrum experienced.
- The highlighting of the importance of modelling the shaft-bearing system of a TST in all degrees of freedom by quantifying the error in loading as a result of using the common one-dimensional approach.
- The identification of areas needing further research, primarily involving the impact that off-axis forces on a TSTs drivetrain has on critical components such as seals and gearboxes, and the need of producing experimental data for eccentrically loaded bearings.

It is worth mentioning at this early stage that an important aspect regarding the modelling of TST loads and durability, and indeed for any research, is the evaluation of the appropriateness of the methods used. As will be seen, the assumptions of some of the engineering methods commonly used in the TST field give rise to some questions of their applicability for tidal energy use. These possible limitations are, as for all engineering practices, a highly important topic to discuss and review in order to ensure that the correct assumptions and simplifications are being made and to identify future research needs. All the above topics and other details of the thesis are presented in an overview in the following section, giving the reader a clearer picture of the research layout.

1.3 Overview of the thesis structure

The chapters of this thesis are structured in a 'three part' manner which cover the areas of literature review, methodology and results and discussion. These are presented as:

Chapter 2 gives the reader a high level introduction to the topics covered in the later chapters and puts the presented research in context with the current state of the art of the sector. The chapter consist of a brief general overview of TST layouts and operating principles with emphasis on the drivetrains and shaft bearings. The chapter then continues to give a short literature review on the hydrodynamic modelling and hydrodynamic loads on turbine rotors and drivetrains. The state of the art in TST load modelling is then reviewed and finally the proposed new load model is summarised.

Chapter 3 is the first of three chapters comprising the theory section of the thesis, which starts off by giving a detailed account of the development of the unsteady BEMT model including all the modifications done needed for tidal energy applications. The chapter covers all aspects of the modelling from the unsteady inflow synthesis, the dynamic rotor model and finally the definition of the output rotor loads.

Chapter 4 explains the theoretical details of the sensitivity analysis method that was performed on the BEMT model, along with the verification campaign of the said model. The chapter shows the verification of the BEMT model against progressively more complex sets of data and the results of the sensitivity analysis are presented. With the dominant parameters identified, a detailed study is conducted to show the primary parameters' relationship to the generated loads on the rotor in all degrees of freedom.

Chapter 5 explains the details of the development of the turbine drivetrain model using the finite element design language ANSYS MECHANICAL APDL [1]. The first sections gives a high level introduction to the FEM method and Timoshenko beam theory and moves on to explain how the shaft bearings were represented in the drivetrain model using sets of linear springs. Finally, the modified L_{10} fatigue life method for varyingly loaded bearings and the Palmgren-Miner rule are presented.

Chapter 6 presents the investigation into the peak loading and durability of a TST as a function of the unsteady marine climate in the form of a case study on a generic horizontal axis TST. This chapter shows the application of the developed model from the previous chapters and the results focus on the loading and fatigue life of the main bearing, which served as an indicator of the turbine's drivetrain durability as a whole.

Chapter 7 finally presents the conclusions of the thesis and an in-depth discussion of the results found. The applicability and limitations of the methods used are also reviewed and the need for further research is stated as suggestions for future work. The original research contributions of this thesis are also explicitly re-stated in Section 7.2 of this chapter.

In the purpose of giving the reader a reference point on where the research and conclusions presented at the end of the thesis fits in with the wider view of TST research, the following chapter will now give the required background information needed - building up to the detailed theory of the methodologies presented in later chapters.

Chapter 2

Overview of tidal stream turbines – their operating principles, load environments and modelling techniques

> "How inappropriate to call this planet Earth when it is quite clearly ocean."
>
> — Arthur C. Clarke

The fact that all structures deployed at sea will be be subjected to a punishing and treacherous environment is undeniable, and acknowledging that the design philosophy of TSTs must be founded in ocean engineering practices is crucial in ensuring that these devices will last. Furthermore, any successful design solution of a TST must have had its economical viability weighed against the robustness of the design, meaning that it will not be feasible to simply 'over-engineer' a device to make it durable due to the related increase of cost in manufacture, weight, deployment and retrieval.

Due to this inappropriateness of managing the durability of TSTs in the marine climate through over-engineering, the focus of the literature review presented in this chapter will firstly be on the actual hydrodynamic loading climate that TSTs will encounter – which is identified as a high-probability cause of fatigue damage – and how these loads can be managed efficiently in the turbine's drivetrain. The mid part of the chapter then presents an overview of the main load-bearing components in a TSTs drivetrain, namely the shaft bearings and how their fatigue performance is predicted. Finally, the techniques commonly used to numerically model the loads and stresses on a TST are presented, which will be used later on in this thesis to investigate the functional relationships between the unsteady sea climate and the propagation of the loads into a TST's drivetrain; this knowledge will inform on how TSTs interact with their environments and will further the understanding on how to manage the troublesome marine generated load climate in an efficient way.

Before the hydrodynamics and loading of a TST can be discussed, some basic concepts and terminologies must first be covered in the next few sections, starting with the general description and operating principles of horizontal axis TSTs.

2.1 General description of TSTs and working principles

Tidal stream turbine energy extraction works by converting the kinetic energy in the oncoming tidal flow into rotational torque via a power capture device. This captured torque load is then led to an electrical generator, possibly after passing through a gearbox, and is finally sent to a grid connection after the proper electrical transformations have been done. Rotating TST designs can be divided into the three high-level classes of horizontal axis, vertical axis and venturi type machines as shown in Figure 2.1, each with their own advantages and disadvantages [2].

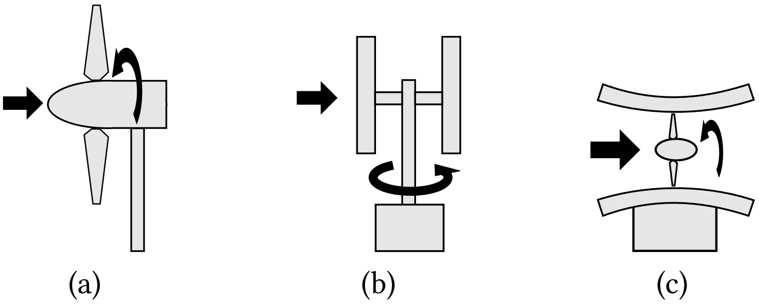

Figure 2.1: The three main classes of rotating axis TSTs showing horizontal axis designs (a), vertical axis (b) and verturi type devices (c) with the inflow coming from the left.

The vertical axis type turbines shown in Figure 2.1b are characterised by having their main axis of rotation perpendicular to the incoming flow. One notable advantage of this concept is that it can accommodate inflow from any angle and these devices do therefore not need a yawing mechanism to turn them into the flow [3]. Another advantage is that this design can be arranged to have the on-board electrical equipment above the water surface, which in turn facilitates easier maintenance and reduces costs. Vertical axis turbines do however have somewhat lower hydrodynamic efficiency than horizontal axis machines [3] and they are subjected to cyclic loading even in uniform inflow, which will complicate the mechanical design and fatigue resistance for larger machines [4].

The venturi type tidal turbine design shown in Figure 2.1c is effectively a horizontal axis TST enclosed in a flow-augmenting shroud, or duct, which decreases the kinetic pressure behind the rotor and thus increases its efficiency [5]. Due to their increased efficiency, venturi turbines are generally smaller than other types of turbines of the same power capacity. It is noted however, that most of the commercially deployed venturi turbines operate on gravity foundations close to the sea-bed, which is situated in the bottom friction boundary layer of the tidal flow. A possible reasoning for this is that the increased efficiency warrants the placement of the turbines in less energetic flows; this may result in them operating in lower flow speeds and more turbulent flow than other types of turbines.

A comparison of devices that have shown a higher technology readiness level by undertaking, or were at the time of writing about to undertake, large-scale prototype testing at the European Marine Energy Centre (EMEC) [2] showed that out of the 117 devices listed, 45 were classed as open flow horizontal axis devices. This equated to 38 % of the total number of tested devices being of horizontal axis type design and this finding was taken as an indication that there is currently a industry preference for the horizontal axis type of TST device. This preference is largely attributed to the fact that horizontal axis TSTs have a smoother and more continuous loading regime on the drivetrain since the blades do not shadow each other during operation, although as will be shown, this loading regime still shows significant fluctuations. Owing to this observation of horizontal axis preference, all the analysis and methodologies presented in this thesis will be focused on horizontal axis TSTs as this was considered to be more relevant for the current state of the sector development. From here on, the term TST will refer solely to *horizontal* axis TSTs, as shown in Figure 2.1a if not stated otherwise. Figure 2.2 shows two full scale horizontal axis TSTs ready for commercial deployment to give the reader a sense of the size of the devices.

The following sections will now give a more detailed account on the theory of operation for horizontal axis TSTs and their load environments caused by the marine inflow conditions.

2.1.1 Theory of operation for horizontal axis TSTs

The basic operating principles of TSTs are presented in this section where the generation of the thrust and torque on the rotor is briefly explored, followed by the basics of turbine station keeping from a loading perspective.

There is currently a wide variety of concepts and configurations of tidal turbines available and the designs have constantly been evolved and refined for every new device deployment [6]. The fundamental working principles of converting the velocity


(a) (b)

Figure 2.2: The commercial scale prototypes of the Andritz Hydro Hammerfest HS1000 (a) and the Atlantis Resources Ltd AR1500 ready for deployment at the full scale demonstartion site in Pentland firth with the Meygen project. Images reproduced from `http://subseaworldnews.com/`.

momentum in the inflow to rotational torque via lifting surfaces, usually in the form of rotor blades, is however a common feature for all TST designs.

The blade profiles of a TST are shaped as airfoil sections and function in the same way as an aircraft wing, generating a force perpendicular to its chord-line, called the lift force, and generating another force parallel to the chord-line known as the drag force [7] as illustrated in Figure 2.3. This diagram shows a turbine rotor with a blade pointing out of the page and the corresponding lift and drag forces on the blade cross-section are shown. The sizes of these forces are dependent on the magnitude of the relative inflow velocity vector V, the angle of attack (AoA), α, between the inflow vector and the chord-line, the Reynolds number of the fluid flow and the geometrical shape and performance of the airfoil. The relative inflow velocity is in turn composed of the horizontal inflow component, mainly caused by the tidal flow, and the apparent flow from the rotational speed of the blade at a given point along the rotor radius as seen in the vector diagram in the top left of Figure 2.3.

In order to see how the lift and drag forces affect the performance of the turbine, the forces are decomposed into their cartesian components and two resulting vectors, one being parallel and one being perpendicular to the plane of rotation, are constructed as the radial and axial force vectors respectively. The axial force vector is more commonly known as the *thrust* vector, measured in Newtons, and when multiplied by the radial distance from the rotational centre, the radial force vector is referred to as the *torque* vector, measured in Newton meters. The thrust vector on the rotor will usually constitute the largest load source on a turbine and the torque vector on the blade is what ultimately drives the turbine's generator. Both loads will be carried into the drivetrain where they must be separated and dealt with by various mechanical components discussed in Section 2.4.

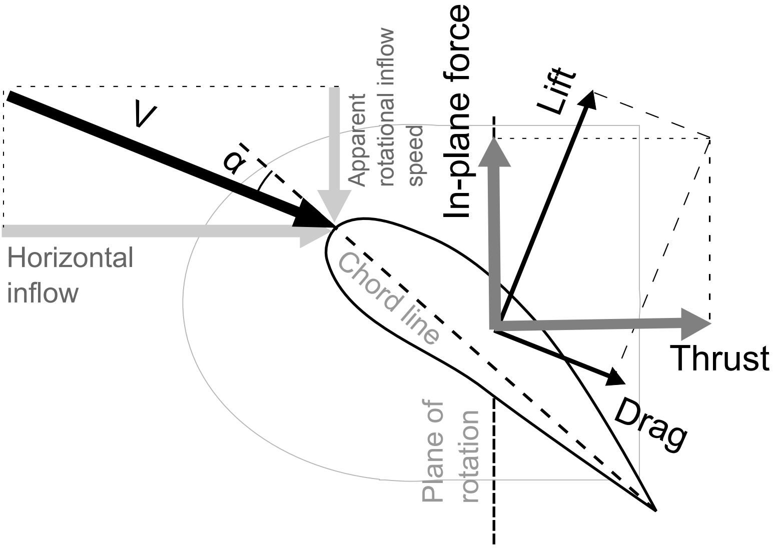

Figure 2.3: Diagram showing the inflow velocity vectors on a blade and the generated force vectors. The figure shows the inflow coming from the left and the cross-section of one blade pointing 'out' of the paper.

In addition to the apparent rotational inflow speed at a given point along the blade being dependent on the radial distance from the rotational centre of the turbine as mentioned, the presence of the turbine in the flow will in fact also modify both the horizontal and rotational inflow speeds over the blades. All these interdependencies of the design parameters, operating conditions and the loads on a turbine make for a complicated engineering problem that must be solved using appropriate analytical tools. Section 2.5 gives an overview of the numerical methods used to solve for the turbine forces used in the TST industry and research sector while Chapter 3 is dedicated to showing the details of the specific method used in this thesis.

Due to this decrease in the apparent rotational inflow velocity vector over the blades further towards the turbine hub, which is due to the tangential velocity of parts located closer to the rotational centre moving slower, the angle of attack of the inflow vector will also increase towards the blade's root; pushing the blade section into the stall region as can be deduced from Figure 2.3. To counteract this effect, the blades of horizontal axis TSTs are designed with a twist-distribution along the length of the blade that sees the geometry of the blade sections rotated towards the horizontal plane of rotation in order to maintain an optimum angle of attack over the length of the blade [8] as the AoA reduces closer to the hub. Similarly, the chord length of the blade increases the closer one gets to the turbine hub in order to maximize the lift generated from the lower inflow speeds. This also has the added benefit of increasing the blades' structural integrity since the hydrodynamic loads are resisted by a thicker blade root.

As will be seen in the next section, it is not only the design of the turbine rotor and its operating modes that determine the magnitude of loading and stresses in a turbine. Site-selection and the vertical positioning in the water column play an equally important role in the development and planning phase and must be carefully considered to assure reliable operation and longevity while maximizing the power capture.

2.1.2 Optimum positioning in the water column and station keeping

Research studying the vertical velocity distributions in tidal stream currents using Acoustic Døppler Current Profilers (ADCP) by Sutherland [9] and Colucci [10] has shown that the inflow current velocities have varying profile shapes, vary significantly over time and are site dependent. The range of vertical profile shapes observed vary from nearly uniform across the water column (plug flow), through linear to non-linear power-law distributions caused by the bottom friction. The dominant factor in the creation of the near bed boundary layer profile is the roughness of the sea-bed and the bathymetry of the site. In addition to this, surface winds may cause a velocity shearing effect originating from the sea surface that propagates down the water column [11].

The effect that the shape of the vertical velocity distribution down the water column (referred to in this thesis simply as the *current profile*) has on the loading of a TST is that it will induce a gradient of thrust force over the rotor-plane. This will in turn generate out-of-rotor plane bending moments on the rotor, which will have knock-on effects on the internal loading of a turbine's drivetrain as described in Section 2.2.7, and is one of the main aspects of TST loading studied in this thesis. As will be seen however, there are more aspects to consider when determining the optimum operating-depth of a TST.

Since maximum power capture is achieved by allowing the swept turbine area to encompass the highest flow velocities in the water column, it may seem favourable to position a turbine as shallow as possible where the flow is strongest. However, due to the presence of possibly harmful surface waves, wind current shear and naval traffic, this option is not recommended and a trade-off between optimum power capture and minimum inflow disturbances must be done. It is found that placing the turbine above the bottom shear friction layer and below the most energetic wave induced velocities, which will typically be in the upper half of the water column, has been considered a good trade-off for horizontal axis TSTs [12].

In order to fixate a turbine in the desired depth in the tidal stream, the station keeping is done by a support structure in the form of either sea-bed mounted structures or moored buoyant structures. The sea-bed mounted structures consist of rigid or flexible arrangements that are fixated to the sea-bed by either piling or by a gravity base [13]. This type of station keeping allows good support with a limit on the practical height above the sea-bed that the turbine may be held, limiting the design option to more shallow sites. From a loading perspective of the station keeping method used, Arnold et. al (2015) [14] showed using Fluid Structure Interactions (FSI) that the flexibility of the support structure of a TST had an impact on the thrust loads on the turbine hub of up to 10 % in dynamic simulations. The flexibility on the drivetrain did however not show a great impact on the hub loads in the set-up investigated.

Since the research presented here will focus primarily on the *internal* loads on the drivetrain, the drivetrain will be modelled as a flexible member, although the use a flexible support structure is out of the scope for this thesis and it will be considered fully rigid.

Another effect that the choice of station keeping can have on a TST is stanchion interactions between the blade loads and the structure. A mono-pile structure will for instance create a disturbance in the flow downstream of it, where the passing blades will experience a periodic fluctuation in the loading while passing through. This effect, although not considered in this thesis, would act to increase the rotor out-of-plane bending moments on the rotor and thereby increase the internal loads.

Before the details about the loading and efficiency of TSTs operating in unsteady flows can be given, it is useful to firstly define some characteristic parameters to aid in the interpretation of a turbine's performance, as shown in the next section.

2.1.3 Characteristic parameters

Since turbines come in many different configurations and sizes and operate in a wide range of conditions, it is convenient to define some characteristic non-dimensional parameters in order to compare the performance between different turbines in different operating conditions.

The tip-speed ratio is commonly used to describe a turbine's operating state based on the ratio of the speed of its blade-tip to the incoming flow speed, defined as

$$\mathrm{TSR} = \frac{\Omega_\mathrm{r} R}{U_\infty} \tag{2.1}$$

where Ω_r is the angular velocity of the rotor, R is the turbine radius and U_∞ is the free stream velocity.

The power coefficient C_P is another useful quantity used to determine a turbine's general power capture performance. It is the ratio of the mechanical power in the shaft captured by the turbine to the available power in the incoming flow over the swept area of the rotor. It is defined as

$$C_\mathrm{P} = \frac{\Omega_\mathrm{r} Q}{0.5 \rho U_\infty^3 A} \tag{2.2}$$

where Q is the shaft torque, ρ is the fluid density and A is the swept rotor area. As with the turbine power, the rotor thrust can be characterised by a non-dimensional thrust coefficient, which is a ratio of the force on the rotor to the dynamic force in the flow. It is defined as

$$C_\mathrm{T} = \frac{F}{0.5 \rho U_\infty^2 A} \tag{2.3}$$

where F is the thrust force on the rotor shaft.

With the most basic operating principles, terminologies and characteristic performance parameters outlined, it is now time to explore the hydrodynamic loading conditions of TSTs that are brought on by the unsteady marine climate.

2.2 Hydrodynamic loading on tidal stream turbines

The following section will give a review on the hydrodynamic loads that will be brought on the turbines from the marine environment, as described by previous researchers. The section covers the effects of the tidal current flow, wave motions and their interactions with the currents, flow turbulence and the effect of the dynamic inflow from a loading perspective; this is followed by the techniques used to model the hydrodynamics in the next section.

The fluid particle velocities beneath the sea-surface are governed by highly complicated relationships between the currents, surface waves and turbulence, each interacting with each other to create a mathematical problem so complex that the topic is still an active research field to this day. Nevertheless, it is possible to simplify this chaotic environment by treating the currents, waves and turbulence as separate phenomena and to study their individual effects on the turbine loads before attempting to resolve their interactions with each other.

First, the of the source of the static loading on a tidal turbine will be investigated, namely the inflow current loading. The later parts of this section will describe the sources of the cyclic loads caused by surface waves and ambient flow turbulence. Lastly, this section will shed light on the secondary loading affects in play generated from the fluid acceleration that causes additional loads on a submerged rotor. Finally, as was hinted on previously, the resulting off-axis loads generated by non-uniform inflow across the rotor plane which gives rise to additional internal loading complications will be reviewed.

2.2.1 Current loading

As was already mentioned, the main source of the static forces on a turbine's rotor, in the case of both the detrimental trust forces and the useful shaft torque, will be the tidal stream inflow currents. There is a large body of knowledge related to this phenomenon from experiments on both tidal and wind turbines.

The early small-scale experimental tests on TSTs were performed by Batten et al. [15] in 2007 where it was shown that tidal turbines subjected to uniform inflow produced performance curves (C_P and C_T plotted as functions of the TSR) that were similar to those of wind turbines, having peak values of C_P and C_T at 0.45 and 0.80 respectively. Both the performance parameters and the optimal TSR position were all found to be highly dependent on the blade root pitch setting. Both Batten et al. [15] and Barltrop et al. [4] successfully managed to replicate the experimental performance curves of TSTs using BEMT codes, which generally perform well close to the optimum TSR but become less accurate at the higher TSR region of high induction operation (Section 3.2.2). The performance of a TST rotor in uniform inflow is generally characterised by a steep decay in C_P and C_T in the low TSR region where the blades enter the stall regime. A similar performance-drop is also present in the high TSR region where the rotor enters the turbulent wake state [16].

Milne et al. [17] showed that for a small-scale TST in uniform inflow, the out-of-plane root bending moments on the blades were as much as 5 times higher than the in-plane bending moment. This is consistent with experimental results from Galloway et al. [18] who reported a 4 times larger out-of-plane bending moment. It is also noted that in the higher and lower bounds of the studied TSRs by Milne et al., the values of C_P and of C_T exhibit a comparatively large degree of scatter. The authors attribute this to the performance of the airfoil used in the turbine being sensitive to changes in the inflow conditions in these TSR regions due to premature boundary layer separation. This infers that small changes in the inflow state could have had a large impact on the loads on the turbine in the case investigated [19].

As mentioned previously, experimental data from real tidal sites show that the inflow current profiles are rarely uniform, but more often then not exhibit linear or exponential shear distributions [9, 10]. The effect that the sheared inflow velocity distribution has on a turbine was experimentally investigated by Tedds et al. [20] where a turbine was subjected to a 1/5th power-law inflow profile generated in a flume tank. The results of the experiment showed that, when presented non-dimensionally using the integral-average inflow velocity over the rotor area, the rotor power and thrust coefficient C_P and C_T were the same as for uniform inflow. This study did however not investigate the loading characteristics on the individual blades, which will induce a non-uniform thrust pattern over the rotor giving rise to a rotor out-of-plane bending moment, as will be seen.

2.2.2 Wave loading

Surface wave loading on structures deployed in the marine environment has been a highly active area of research since the 1970's due to the emergence of the offshore oil and gas industry. However, the influence of surface waves in the context of tidal stream generation has only recently been investigated and our current understanding of the full range of mechanisms involved is still not complete. Most of the experimental surface wave interaction studies that have been performed on TSTs are in the form of tow-tank or flume tests on scale models, which have yielded great insight to the nature of the blade and rotor load variations.

Barltrop et al. [4] showed that for a scale turbine of 350 mm diameter towed through incident waves, the variations of the blade root bending moments were as large as 50% of the mean load for the out-of-plane moment and 100% of the mean load for the in-plane moment. The experimental results showed that the main load oscillation occurred at the encountered wave frequency and that the in-plane-bending moment load signal for a single blade had a superimposed self-weight component resulting from the gravity load of the blade.

In a similar test performed by Galloway [21] the maximum loading range for the out-of-plane bending moments at the blade roots were reported as 175% of the median and the corresponding in-plane load range was 100% of the median; the out-of-plane loading was shown to be as much as 9.5 times greater than the in-plane loads. The tests were conducted for a scaled wave height of 2m and intrinsic wave period of 12.8s and the cyclic loading from the wave action was reported to be a likely source of accelerated fatigue.

While tow-tank testing provides a controlled environment to study the effects of different inflow parameters on a turbine, the towing through still water generates a turbulence free environment which is not representative of a real tidal flow-site. Furthermore, since the waves propagate over still water, no wave-current interactions are in effect using this method. On the other hand, testing small-scale devices in recirculating flumes can provide a more realistic inflow condition in terms of turbulence intensities and wave-current interactions.

One such study was performed by Gaurier et al. [22] where a three bladed turbine with 400 mm long blades, instrumented with strain gauges, was subjected to various wave and current inflow conditions. In alignment with Barltrop et al. [4], the results of the blade loading showed that the standard deviation of the blade strains increased with an order of 2 - 3 times in wave conditions compared to the pure current case. Also, it was observed that the mean value of the blade strain was the same for the wave and pure current cases, which Galloway et al. [18] attribute to the use of sinusoidal waves with an average net velocity of zero - a result that is likely to change if steeper waves with greater peak-trough asymmetry are used. It is again reported that the fatigue performance of a turbine will be dominated by the wave contribution and that this will be a significant driver of turbine durability and cost [22].

For the sake of quantifying the relative importance of the different inflow parameters on a TST, such as the mean current speed, shear profile, water depth, hub height, wave height and wave period, Milne et al. [23] conducted a numerical sensitivity analysis on the loads on a full scale turbine using the commercial BEMT model BLADED [24]. The study showed that for the parameters investigated, the wave height and period had a dominant influence on the blade loads, whilst the site depth and shear profile also showed influence. The study did however not include the influence of varying the turbine parameters and its operating state. Another finding suggested that the interplay between the rotor period and wave period can have an additive effect on the loads if synchronisation is achieved between the two, a hypothesis that is also raised by de Jesus et al. [25]. It is noted that a simplification was made in the study by neglecting the wave motion's vertical velocity component, which will be shown to have a large impact on the drivetrain dynamics later in this thesis. In another study, Milne et al. [16] also attribute the unsteady hydrodynamic blade loads on a TST subjected to planar oscillatory flow in a tow tank to boundary layer separation-effects, or dynamic stall effects, on the blades.

2.2.3 Wave-current interactions

Although the ground work for the methods of calculating wave loading on offshore structures has been established by the offshore sector and used with success, it has for a long time been a standard practice in ocean engineering disciplines to consider the current and surface wave particle velocities as separate entities [26]. As such, in most engineering cases where current and wave loads are to be determined, the velocity fields from the currents and waves are calculated individually and then added in a process called *linear superposition* [27]. Nevertheless, both experimental and numerical investigations into wave-current interactions show that there is a strong relationship between the waves' sub-surface kinematics, the wave induced surface displacement and the vertical structure of the underlying current profile [28]. An underprediction of the loads on submerged structures may be the result of ignoring these wave-current interactions, as will be discussed below.

The simplest form of wave-current interactions can be seen on waves propagating over a uniform current, which has zero vorticity distribution through the water depth. The interactions can here be treated as a simple Døppler shift of the wave frequency [29] as viewed by a stationary observer. On the other hand, waves propagating over a current with a linear shear-profile (constant vorticity), where irrotational flow is still maintained for the wave motion, effects arise in form of a modification of the dispersion relationship between the wave period and wave length (Section 3.1) [30]. Further effects of waves travelling over a linear shear-current include, as was shown by Kishida & Sobey [31], that the constant vorticity distribution of the current modifies the water-surface elevation - an effect that becomes more prominent with increasing wave steepness.

During the presence of more complex non-linear shear velocity flow distributions, the near-surface vorticity leads to an important modification of the dispersion relationship which affects the water-particle velocities throughout the water column [30] whilst also changing the surface elevation profile. This in turn causes steeper waves to have a more pronounced increase on water particle velocities and accelerations overall. As an example, Figure 2.4 shows a depiction of the velocity profile range that a TST operating in a 50m deep site may encounter due to a shear current interacting with 10.12m surface waves – this example was created using the wave-current interaction model described in Section 3.1.5.

Consequently, as wave-current interactions tend to modify the shape of the surface elevation and underlying flow-fields, they also affect the hydrodynamic forces on submerged structures. A numerical study by Wang & Li [27] showed that the inclusion of wave-current interaction effects gave as much as 40% difference in the loading on submerged structures as compared to linear superposition alone in extreme cases. The error in loading was even more prominent when the waves interacted with an opposing current. Similarly, Marcus et al. [32] presented a numerical computational fluid dynamics (CFD) study on the hydrodynamic forces on submerged structures, where the wave-current interactions were resolved using the Unsteady Reynolds Averaged Navier-Stokes (URANS) equations. The results showed that resolving the wave-current interactions gave 25 - 28% higher maximum horizontal forces on the structures when compared to the linear superposition method.

Due to the findings presented above, the hydrodynamic inflow modelling for TST loads presented in this thesis will incorporate wave-current interactions in most of

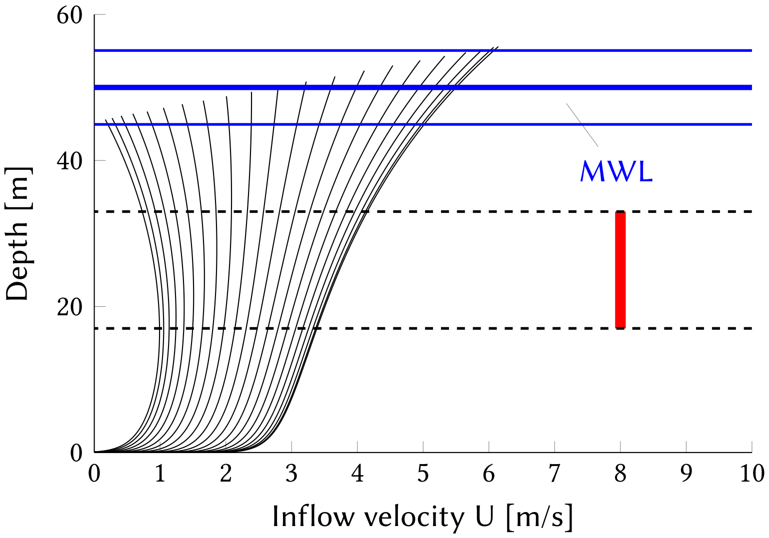

Figure 2.4: The inflow velocity profile over the swept area that a TST occupies in the water column (red) varies significantly as a result of the shear current and the surface wave orbitals. This image shows how the inflow profile is distorted over one wave period using the wave current interaction model explained in Section 3.1.5.

the cases investigated.

Finally, as most high energy tidal sites will likely be in locations where the incoming flow is channelled through narrow straights and where the incoming waves have one predominant direction, the waves and currents are assumed to be co-flowing in most cases in this thesis – this assumption is likely to have a mitigating effect on the off-axis loads generated on a TST.

2.2.4 Ambient inflow turbulence

Although characteristics of the turbulence in tidal flow sites have yet to be determined to the point where a ‘typical’ behaviour of the tidal turbulence can be assumed, there is a consensus that it contains many length scales and is highly energetic. The ambient inflow turbulence in the tidal flow affects the loads on a turbine in two major ways; through presenting velocity fluctuations on the rotor and thereby inducing cyclic loads, and by changing the performance of the airfoil sections – ambient inflow turbulence has been shown to increase the load fluctuations on a TST by a factor of 5 and modify the thrust and torque coefficients in excess of 10% [33]. It has also been shown that increased levels of inflow turbulence intensity (TI) increases the rate at which the wake recovers by dissipating the wake momentum into the free-stream [33, 34]. Furthermore, Acoustic Doppler Current Profiling (ADCP) in situ measurements have shown that that the ambient turbulence intensity in a potential tidal deployment site can reach levels of up to 10.3% [34].

McCann [35] presented a sensitivity study on the fatigue loading on a TST caused by surface wave action and inflow turbulence using a BEMT design software code. The study showed that there was a strong correlation between a turbine's blade root fatigue and the turbulence intensity of the flow, although the wave effects could be seen as dominant in the case investigated. Although Chapman [36] points out that the turbulence intensity seems to have been arbitrarily chosen, the study highlights the need for a complete exhaustive study on the inflow parameters to determine the relationships of the inflow conditions to the fatigue loading. It also recommended that other components (such as transmissions and support structures) are investigated.

It is clear that tidal stream flows have high levels of ambient turbulence intensities and a wide range of turbulent length scales; these inflow variations will ultimately increase the range of load variations on a turbine's rotor [34] and may become a driver in TST fatigue loading behaviour. However, this study will only include the effects of inflow turbulence as it effects the performance of the lift and drag characteristics of the airfoil sections on the blades, thus neglecting the additional variation brought on by the turbulence eddies. The effects of this simplification will be that the load variations over time and the load gradients across the rotor-plane will be less severe than if turbulence had been incorporated, although it is reiterated that the exact extent of the error won't be quantifiable until a typical turbulence characteristic is defined for a generic tidal site.

2.2.5 Dynamic inflow load effects

As will be discussed in the later theory chapters on how the inflow conditions are modelled in this thesis (Chapter 3), the methods used traditionally only consider the change in inflow velocity caused by the wave motion when determining the rotor loading. Essentially, these methods can be described as seeing a stationary inflow speed during every calculation, which is updated every time-step.

However, experimental data on large and small scale wind turbines has shown that any sudden change in a turbine's operation, such as a incoming wind gust or blade pitching manoeuvre, causes a temporary load enlargement on the rotor [37, 38] which over-shoots the load that the static inflow would cause on its own. This transient load overshoot has been attributed the fact that when a turbine's operating mode is changed, the pressure at the rotor plane changes with it; this change must however propagate downstream at the speed of the inflow velocity, causing the rotor and wake pressures to be in non-equilibrium for a duration of time. This in turn generates a pressure gradient across the rotor which increases the load [39, 40]. The observed phenomenon is termed 'dynamic inflow' and has been shown to be a significant factor of temporary load increase in wind turbines [41].

Øye [38] showed that a full scale wind turbine subjected to a sudden blade pitch change during operation experienced a shaft torque overshoot of 24% due to dynamic inflow effects. In the case of both wind and tidal turbines, pitch change-induced loads will only be present in pitch-controlled machines, but the results still serve as an indicator of how the turbine's loads are enlarged by dynamic effects. It is on the other hand suggested by Snel and Schepers [41] that dynamic inflow might not be a major contributor to the life-span shortening of wind turbines due to the infrequency of severe pitch manoeuvres.

However, a more immediate issue for tidal turbines would be the influence of incoming surface-waves creating time varying inflow at the rotor plane, thus causing dynamic inflow effects. Wind tunnel tests on a model wind turbine encountering a step change in inflow velocity have shown negligible increase in loads as compared to the steady-state values [41]. The reason for the insignificant load overshoot in this case was due to the time-scale of the operational change being longer than the wake recovery time, which can be approximated by D/U_∞ [41], where D is the turbine diameter; this allowed the wake to remain in near equilibrium throughout the inflow change in that experiment.

It is assumed that for TSTs, dynamic inflow effects caused by waves will be small as long as the period of the waves are larger than the turbine's wake recovery time. If the wave period is shorter than this there may be effects both from varying inflow velocity magnitudes, as well as from wave induced dynamic inflow effects. Therefore, the modelling methods used in this thesis will include the effects of the dynamic wake phenomenon.

2.2.6 Fluid acceleration effects

All submerged objects in an oscillating flow field experience drag forces due to pressure gradients and skin friction, and inertia forces due to the acceleration of the fluid. Again due to the assumptions of equilibrium of forces in the load calculation methods used in this thesis, the inertial forces on the structures from the accelerating fluid must be determined and included in the models used.

There are few low-cost engineering methodologies available which consider fluid inertia effects on rotating turbines since inertial effects do not have a great impact on wind turbines - from which most evaluation tools used for TSTs have been developed originally. Tidal turbines, as opposed to wind turbines, operate in a medium with 800 times greater density than air so it is suspected that inertial effects, also termed added mass effects, will be appreciable in the tidal environment.

The most established method of calculating wave-induced inertial forces on submerged objects is the Morison equation [42] which Buckland [43] presented a method of, as originally described by Chapman [36], where the method was employed on a blade element level for TSTs. This allowed for the force distribution caused by the added mass to be resolved along the blade and avoided empirical assumptions regarding the whole rotor.

2.2.7 Non-uniformity of loads across the rotor plane

As the literature covered in the previous sections has shown, the marine tidal flow presents a appreciably dynamic and spatially varying operating environment for TSTs. As the effects of surface waves, shear current profiles and turbulence are not evenly distributed throughout the water column, the interaction between the flow variations and the rotation of the blades will make a turbine's rotor experience a non-uniform and constantly varying load pattern across its rotor plane. This non-uniform thrust over the blades will induce an out-of-plane bending moment on the whole rotor, causing the shaft connection to be loaded in an off-axis radial direction which will increase the internal loads of the machine. This is illustrated in Figure 2.5 where a turbine is shown operating in non-uniform flow conditions and the thrust distributions along the blades are visualized, which will induce the rotor out-of-plane bending moments.

The magnitude and variational characteristics of this induced rotor out-of-plane bending moment was studied by Tatum et al. [44] who used a CFD and fluid structure interaction (FSI) approach to present rotor and blade loading time-histories. The results for a turbine operating in a sheared current flow showed a variation in the resultant rotor out-of-plane bending moment of 24 kN m, caused by the non-uniform loads over the blades. The 'pulsations' observed in the bending moment signal would be translated to the connecting flange of the drivetrain. It was also reported that the angular direction of this bending moment had a range as high as 67°, which was speculated to lead to the load being applied over a limited area of the drivetrain seals and bearings, resulting in reduced life expectancy. Although a fatigue study was also presented on the turbine's blades, no internal shaft-load analysis or fatigue calculations were conducted.

It is clear through the various studies presented on TST loading, that the loads transmitted into a TSTs drivetrain will be considerable both in terms of magnitude and in directional variation. The effects of the non-uniform loads across the rotor plane can, as the presented literature has shown, lead to premature failure of internal components such as bearings and seals. As will be shown in Section 2.5.2, the modelling techniques that are publicly available are generally too coarse in their simplifications of the input

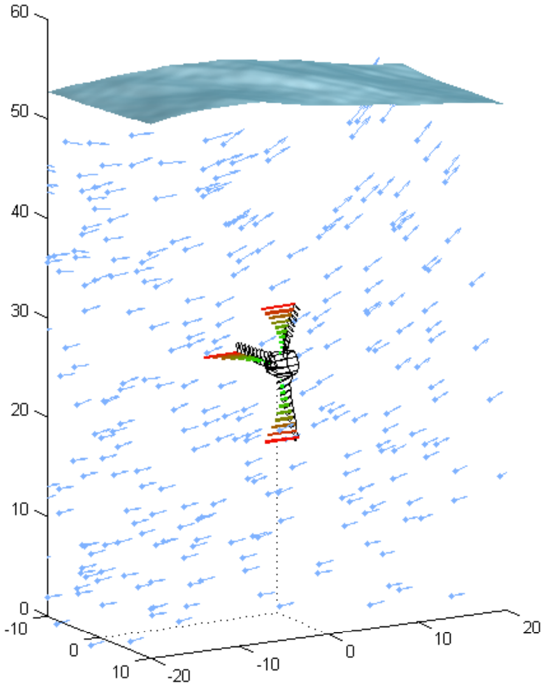

Figure 2.5: The non-uniform inflow caused by the passing wave-front over the turbine shows the generation of a thrust gradient across the rotor-plane, depicted by the red and green vectors in arbitrary scales. In this particular instance, the flow is also seen to have a significant vertical component, which will be shown has a large impact on the fluctuations of the loads.

loads or the high-end commercially available FSI packages are too computationally expensive for early design and research. This thesis, as was stated by the research questions in the introduction, aims to fill the gap left in between the very simple and the very high resolution codes by including the additional degree of freedoms of the loading caused by the rotor out-of-plane bending moment – while also showing any potential underestimations caused by neglecting the rotor out-of-plane bending moments.

The following section will elaborate on the methods for hydrodynamic inflow modelling in the marine environment, which are available at low computational cost, that will aid in developing the computationally efficient code needed to answer the research questions.

2.3 Hydrodynamic inflow modelling

With the ever increasing computational power of commercial processors, there has recently been many advancements made in the detailed modelling of the marine flow environment. Recent advancements include methods that solve the URANS equations to obtain the sub-surface velocities and pressures in combination with the volume of fluid (VoF) method to define the surface waves [45]. Even though these types of methods show an exciting potential for use in TST simulations in terms of their hydrodynamic detail and versatility, their shear computational requirements make them unsuitable for use over larger time-scales, as for time-domain durability calculations.

Fortunately, the development of marine hydrodynamic modelling has been ongoing for several decades and there exists many established theories to evaluate wave and current induced loads on structures using dedicated engineering models. One such class of methods are the ones that treat the mathematical formulation of the flow as a *potential flow* problem which offers a simpler description of the phenomena, thus requiring orders of magnitude less computing power.

The basic assumption of potential flow wave theory is that the fluid flow is irrotational with constant vorticity, thus making it appropriate to model with a velocity potential formulation along with the construction of boundary conditions on the seabed and free surface (Section 3.1). In this way, a complete mathematical formulation of the wave-current flow field throughout the water column can be generated, but, due to the non-linearity of the free surface boundary conditions, a purely analytical solution for the problem can not be found. Although there exists several numerical methods to approximate the exact analytical solution for the potential flow wave-current equations (such as by Dalrymple [46] and Swan et al. [30]), the implementation of these codes is far from trivial and has not been considered for the purpose of this research. Instead, the more widely adopted method in ocean engineering practices is to use approximate analytical solutions to the governing potential flow equations of the wave-current domain, usually composed of Fourier series expanded to the order that is required for the task [29]. Presented below is a selection of theories available in literature that have been developed using approximative analytical solutions to the potential flow equations of different orders of approximation and a range of models and their applicability to different wave steepness are shown in Figure 2.6. Theories such as these have a good potential to be implemented to computer codes due to their simplicity and low computational cost.

2.3.1 Linear wave theory

Linear wave theory, which is also called Airy wave theory or Stokes 1st order theory, is the simplest approximative analytical solution to the governing differential equations. Here, the free surface boundary conditions are linearised which allows for a analytical solution to be found by expansion around the mean water level ($z = 0$) [48]. Strictly

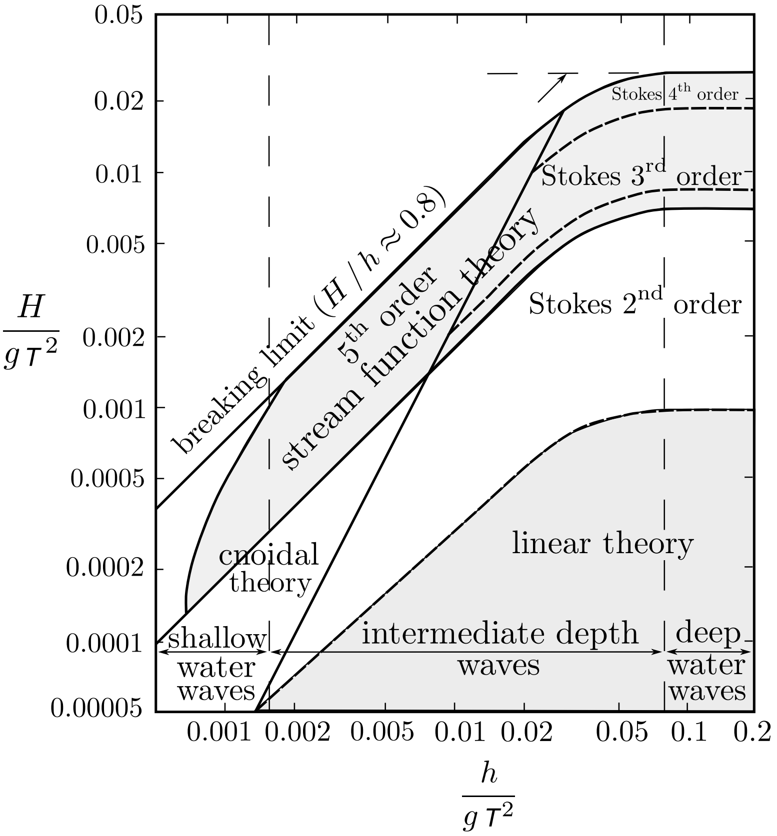

Figure 2.6: Regions of applicability for different engineering wave models based on potential theory reproduced from Le Méhauté [47]. The x-axis is the non-dimensional wave-steepness and and the y-axis is the non-dimensional depth.

speaking, the theory is only valid for waves of infinitely small wave steepness – due to the mathematical assumption that the boundary conditions are only applied to the undisturbed mean surface level – but in practice the non-dimensional wave steepnesses shown in Figure 2.6 needs only to be small. Several researchers and commercial developers have successfully integrated linear wave inflow models to BEMT schemes in order to predict the blade forces on TSTs [4, 21, 24, 49]. When verified against experimental load data, the linear wave approach shows good agreement with small waves but under-predicts the loading for steeper waves, as would be expected.

When considering the fatigue loading of marine structures, it is important to represent the inflow as caused by the *irregular* sea-states. Since all potential flow wave models assume regular waves, it is common practice to model the irregular sea by the superposition of linear waves with a distribution of wave heights and periods derived from some energy spectrum representative of the ocean climate. This method of irregular wave theory is used in the fatigue analysis of this thesis and is explained in detail in Section 3.1.7.

2.3.2 Higher order wave theories

As can be seen in Figure 2.6 and as experimental data confirms, linear wave theory is only applicable to waves of small steepness. If steeper waves are to be modelled accurately, higher order approximations of the governing potential flow equations are needed - these theories take the influence the wave has on its own characteristics into account, causing the wave shape to have higher and steeper peaks and lower, flatter troughs. Stokes [50] presented a theory on regular wave motions describing the velocity variations as a Fourier series where coefficients of the series can be written as perturbation expansions in terms of a parameter which increases with the wave height [51]. Theories based on this approach are termed Stokes wave theories.

The solution to the Stokes theory presented by Kishida & Sobey [31] expands the Fourier series to third order, making it a 3rd order Stokes theory. The theory presented couples the regular 3rd order wave train with a linear shear current of constant vorticity distribution; using the wave steepness as the expansion parameter in a reference frame moving with the waves. As the ambient flow is still irrotational in the case of constant vorticity, the potential flow assumption is still valid.

Fenton [29] presented a 5th order Stokes theory which also uses the wave steepness as an expansion parameter. The solution was shown to be accurate for waves with wavelengths 10 times shorter than the water depth [52]. As with the Kishida & Sobey theory, Fenton's approach is derived in a moving reference frame, but in contrast, it is only applicable for waves on a uniform current. The use of 5th order Stokes theories is frequent in the offshore industry and a detailed presentation of the theories mentioned above can be found in Section 3.1.

2.3.3 Wave-current interactions

It has already been mentioned in Section 2.2.3 that, in general, the interaction between surface waves and an underlying tidal current modifies both the current and the wave kinematics. This interaction plays out in a way that is hard to replicate analytically due to the rotationallity of the flow, which violates the assumption of potential flow theory. For cases like these, the analytical methods by Swan and Dalrymple provide an attractive advantage of being able to resolve the wave-current interactions for arbitrary current profiles, and the offshore engineering sector could do well with adopting these methods as standard. However, due to their complexity, these numerical methods are rarely used due to the preference of the approximate analytical methods such as Stokes theory with modified dispersion relationships [53].

Another wave-current interaction model that shows promise for TST use is the

Dalrymple ‘three-step’ model [54] which allows the wave-current interactions between any higher order wave model and current profile to be estimated. The method works by obtaining an apparent wave period that an observer following the mean current speed would see, and the wave model is evaluated using this modified parameter. The wave particle velocities are then linearly superimposed on the current velocities. This model was used in this thesis for the detailed ultimate load evaluations of TSTs and is described in Section 3.1.5.

Whenever superposition of wave and current velocities is used, as in Dalrymple’s three-step model, it must be remembered that the current velocity expression is usually only valid to the mean water level (MWL). As the wave displaces the surface above this point, the current speed becomes incorrect at the instantaneous water surface, and the current profile below the MWL is not affected by the surface displacement at all. To address this inconsistency, Wheeler [55] developed a linear extrapolation technique for the current velocities based on the instantaneous water displacement, which goes under the name Wheeler stretching. The method works by mapping the current profile to maintain a constant surface velocity regardless of the surface elevation, which results in the profile being ’stretched’ under the peaks and ’compressed’ under the troughs of a wave. This method is also described in Section 3.1.6.

The previous section has detailed some of the numerous aspects of the marine flow environment that cause load variations across a TSTs rotor over time. As these inflow fluctuations manifest themselves as varying hydrodynamic forces on the rotor, the fluctuations are transferred into the drivetrain system of a turbine where they must be accommodated to avoid damage and excessive wear on critical internal components. The following section lays out the general design strategies of TST drivetrains and how they accomplish their tasks of transferring the power to the generator while absorbing the harmful rotor-loads.

2.4 TST drivetrains and their components

It is clear from the previous section that TSTs operating in the marine climate will be subjected to an assortment of hydrodynamic forces from various aspects of the varying flow. The loads generated on the turbine’s rotor will be translated into the constantly operating drivetrain, where they must be accounted for in order to prevent serious damage on critical components and to maximise the longevity on the overall device. Since the emphasis of the research presented in this thesis will be on the loads propagation through a TST and these loads affect the drivetrain, this section will be dedicated to the general concepts of TST drivetrains and the bearings that support them. The first part outlines the common features and components that may be found in a TST drivetrain.

2.4.1 The common horizontal axis TST drivetrain layout

Although drivetrain layouts for horizontal axis TSTs vary significantly between different manufacturer's models and makes, some key elements can be expected to be found throughout. Figure 2.7 shows a diagram of a typical, wind turbine-esque (i.e three bladed horizontal axis), drivetrain layout with many of the key components and features that will be common throughout a multitude of designs [56].

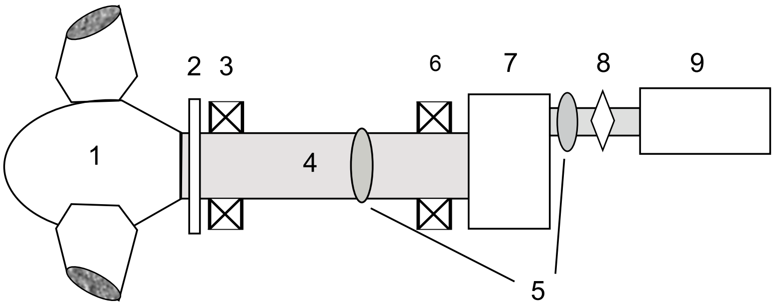

Figure 2.7: Conceptual sketch of a generic layout of a wind turbine-esque horizontal axis TST with an epicyclic gearbox. The main components that are commonly found throughout different designs are shown as the nacelle (1), main seal (2), main bearing (3), low speed shaft (4), shaft couplings (5), aft bearing (6), gearbox (7), mechanical break (8) and electrical generator (9).

The main purpose of a TST drivetrain is to transfer mechanical torque from the rotor to the generator whilst hindering the external loads that are put on the system from damaging sensitive components, such as the gearbox. Experience from the wind turbine industry suggests that the life and durability of the sensitive internal drivetrain components are one of the major reasons for the downtime of the units, with fatigue failure of the gearbox bearings being one of the main culprits [57].

There are many options available for the layout, each with its own strengths and drawbacks and Figure 2.7 shows one possible design solution. In this case, the rotor nacelle (1) is connected to the main shaft (4) with a main seal (2) preventing water ingress to the hull (not depicted). It is also possible to operate a turbine using a flooded hull without seals, although each individual component must be made capable of sea-water submerged operation. Even though there are drivetrain designs that deviate significantly from the 'wind turbine'-esque design shown in Figure 2.7, these designs – although they have many attractive advantages compared to the traditional designs – represent a minority of the contemporary designs and are therefore not considered in this research.

Presented below are brief overviews of some of the components that can be expected to be found in a conventional horizontal axis TST drivetrain design, while the description of the use of shaft bearings, the component of interest in this thesis, is elaborated upon in more detail in the next section.

Seals

Mechanical seals are critical components in dry-operation TSTs as they keep the seawater out of the hull whilst containing the lubricant fluids within. The seals typically consist of two mechanical faces allowed to slide over each other and may or may not be integrated into the main bearing. Seals are highly susceptible to mechanical failure from excessive wear, thermal stress, cracks and corrosion. Typical failure causes include shaft deflections and lubricant contamination [56] and an example image is shown in Figure 2.8a.

Gearboxes

The inclusion of a gearbox shown in Figure 2.7 (7), and as an example picture in Figure 2.8b, allows the high torque in the slow moving main shaft to be transferred into high speed rotation in the high speed shaft, which is more suitable for electrical production in most generator types. The most common gearbox type for TSTs is the epicyclic (planetary) kind, with one ore more stages, which allows for considerable size conservation. A drivetrain configuration without the use of a gearbox is called a *direct drive* system which has the main shaft directly coupled to the generator; this requires the use of a generator that can accommodate low rotational speeds but greatly decreases the mechanical complexity of the system and increases its reliability. Gearboxes are highly susceptible to damage from unwanted external loading but their use can allow for reduction in the cost and size of the generator due to the higher velocity shaft rotations achieved.

Generators

There are a number different of types of generators, Figure 2.7 (9), that can be used for tidal electricity generation and detailed descriptions of which can be found in Hase [58]. The main effect that the choice of generator has on the drivetrain loading is dependent on whether it is fixed or variable speed operated, as fixed speed operation sees an increase in torsional loads during fluctuating inflow. The type of generator used also determines the need for a gearbox since certain generator types need high rotational speeds in order to achieve synchronous speed. Induction generators are one such type that require high rotational speeds in order to achieve synchronisation with the grid frequency of roughly 1500 RPM. An example of a wind turbine synchronous generator is shown in Figure 2.8c.

Another type of generator that shows promise in the field is the permanent magnet alternators which use permanent magnets to generate the magnetic field, negating the need for an external power source. Permanent magnet alternators have high efficiency and can be grid connected to synchronise them with the grid frequency, making them fixed speed operated. They are also good candidates for use in direct drive layouts.

Shaft couplings

Finally shown in Figure 2.7 are shaft couplings (5) which link the different parts of the shaft and drivetrain together and assist during assembly. Here, the use of flange couplings (Figure 2.8d) are the most economic and simple to construct. A mechanical break (8) may also be included in the design for safety purposes and is shown here applied to the high speed shaft since it has less torque resistance. Flexible shaft couplings have also been suggested as they can reduce the loading on the shafting system.

2.4.2 Drivetrain bearings in TSTs

As can be seen in the above sections describing the different components in the TST drivetrain, there are many design options available ranging from making the drivetrain capable of preventing water ingress through the use of seals to allowing variable speed operation through the use of a gearbox. Even though most of the components outlined above are optional in the design of a turbine, the use of load carrying components, such as shaft bearings, is a necessity in order to manage the loads put on the system.

Situated directly behind the main seal in Figure 2.7 is the main bearing (3) which is a mechanical component designed to stop harmful rotor loads from propagating further down the drivetrain. There are many different choices in terms of bearing configurations and models, but the two bearing types most commonly used in marine energy are rolling element bearings and plain bearings where the former use rollers between the inner and outer raceway and the latter have the rotating and stationary surfaces in direct contact. Figure 2.7 also shows a layout using aft bearing (6) which may be used to give further support to the system and prevent shaft sag. Common naval architecture practice sees the use of two or more bearings where one is designed to resist thrust forces and the other resists radial forces.

Even though both rolling element and plain bearings show promise for the use in

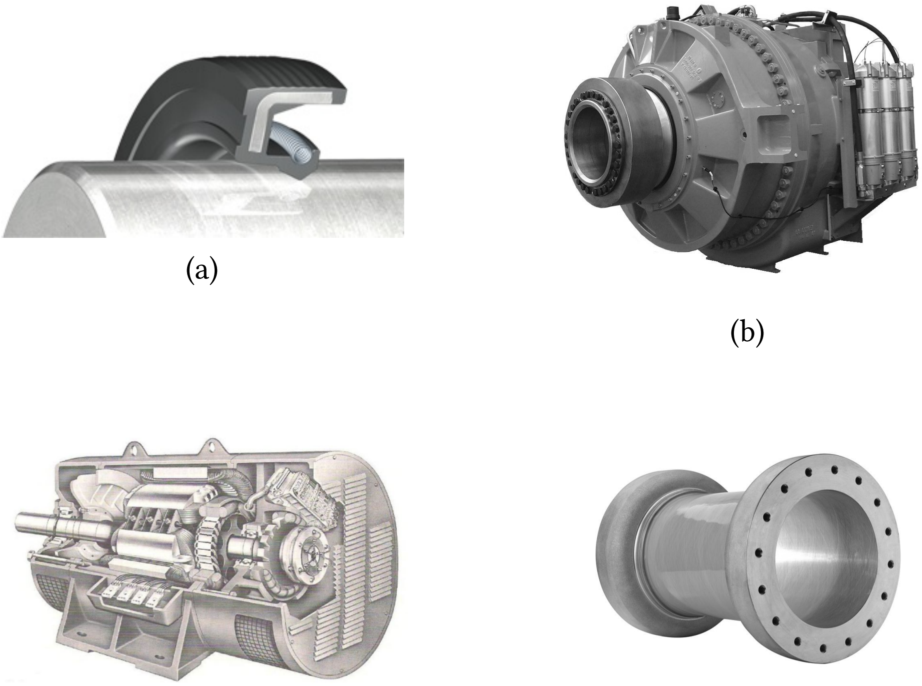

(a)

(b)

(c)

(d)

Figure 2.8: Examples of critical components that may be used in TST drivetrains showing a radial shaft face seal (a), a large-scale 500kW TST gearbox (b), cut-away of a typical wind turbine synchronous generator (c) and a wind turbine shaft coupling (d). Images reproduced from:
`www.skf.com/uk/products/seals/industrial-seals/power-transmission-seals/radial-shaft-seals/index.html`,
`http://www.wikov.com/en/mechanical-gearboxes/products/tidal-stream-planetary-gearbox-10314`,
`http://www.intechopen.com/source/html/38933/media/image7.JPG`,
`http://www.reinhausen.com/desktopdefault.aspx/tabid-967/1218_read-2965/`.

TST drivetrain applications, only the rolling element types will be investigated in this research due to limitations in scope and due to the fact that most developers seem to use the latter in contemporary designs based on the majority of the devices having been deployed at EMEC. The following sections will elaborate on the principles of rolling element bearings, and later sections will investigate the load spectrum brought on by the marine environment which may cause premature bearing failure.

Rolling element bearings

Rolling element bearings, also known as roller bearings, are load carrying mechanical components that limit a shaft's transverse and axial movements while allowing it to rotate axially under low friction [59]. This is achieved by placing balls or cylinders between a inner and outer ring, called races, which are allowed to roll freely giving a relative motion between the inner and outer race while acting as rigid supports. The rolling elements are kept at an even spacing around the races by a *cage* which also rotates freely. Figure 2.9 shows cut-away diagrams of some typical rolling element bearing types, showing the inner and outer races, rolling elements and cages.

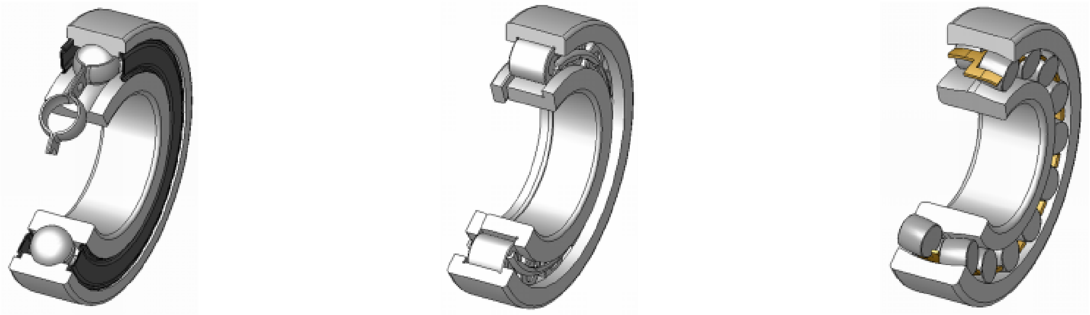

Figure 2.9: Three common types of rolling element bearings showing the outer raceway, rolling elements, cage and inner raceway. (From left) Ball bearing, cylindrical beraing and spherical roller bearing. Wind turbine components are shown due to the difficulty of finding publically available TST component images. Reproduced under licence from `https://creativecommons.org/licenses/by/2.5/deed.en`

One on the main beneficial features of rolling element bearings is their high load carrying capabilities in one or more directions. Depending on the design, it is possible to achieve high axial or radial load capacities for a bearing, or a compromise between both. A bearing designed to sustain axial loads is called a thrust bearing and a radial load carrying type is called a radial or journal bearing. The characteristics of bearing load capabilities is set by designing for maximum contact areas between the raceways and rolling elements in the direction that the main loads are transferred through the use of varying geometries.

The ball bearing to the left in Figure 2.9 shows the use of balls as rolling elements which may be designed to have four contact-points with the races, giving high axial thrust capabilities. This is in contrast to the cylindrical roller bearing in the centre of Figure 2.9 which has a higher radial load capacity due to the large contact area in that direction of the cylinders. The right image in the figure shows a double-row spherical roller bearing which has a spherically shaped raceway in the outer ring giving the rollers and inner race freedom to correct for shaft misalignment and thus reducing the loading.

In order to sustain low operational friction, expel heat, remove particulates and to minimise wear, the use of *lubricants* play a vital role in the function of a bearing. The main types of lubrications used can be classed as grease or oil lubricants and may be applied from simple approaches as having the bearing rotate in a oil-bath to advanced oil-jet injection techniques [60].

As the rolling elements move around their races, the lubricant is compressed which increases the fluid pressure. Since the lubricant is incompressible, the pressure increase results in an increase in viscosity and an oil-film is created between the contact surfaces. This means that during normal operation, the rotation of the elements creates the formation of an oil-wedge and there is no metal-to-metal contact between the rolling elements and the raceways. This goes by the name hydrodynamic lubrication. As the contact pressure between the elements and races increases, the fluid film between the bearing contact surfaces compresses the metal which elastically deforms them. This regime of lubrication is called elastohyrdodynamic lubrication which is a normal operating mode and is illustrated in Figure 2.10. A bearings maximum allowable contact pressure is defined by its *static rating*, where plastic deformations may form if the value is exceeded.

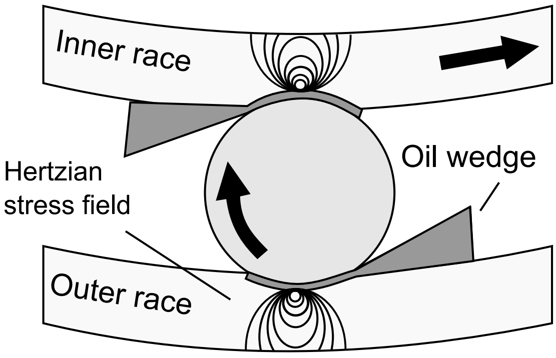

Figure 2.10: Formation of lubrication wedges during elastohydrodynamic operation of a bearing. Here, the inner race is rotating with the migrating Hertzian stress-fields shown through the raceways.

As two curved and elastically deformable solids are pressed against each other, the subsequent increase in pressure causes the solids to deform – creating a larger contact area – which in turn decreases the pressure. A local stress pattern forms in the contacting bodies, called a Hertzian stress field after Heinrich Hertz [61], which forms the basis of bearing load evaluation and fatigue life theory.

It is evident that the material in a roller bearing will be subject to constant load variations as the Hertzian stress fields travel along the raceways (and in the elements) at the points of contact. As a bearing can have a large number of elements, the metal in the races will be stressed by the number of elements each revolution causing material fatigue, which is one of the greatest failure causes in rolling element bearings as discussed in the next section.

2.4.3 Rolling element bearing failure modes

The use of roller bearings in many industrial applications can be seen as them having the role of 'sacrificial components'. In other words, these are considered cheap components that are intended to absorb fatigue damage and be replaced on regular intervals, while assuring the safe and reliable operation of other parts of a machine. This is in stark contrast to the applicability of bearings in TSTs where every action must be taken to guarantee longevity and reliability during the harsh operating conditions.

Three main challenges can be identified with the use of roller bearings as main supports for TST drivetrains. The first of which, as was already mentioned, is the higher requirement of reliability due to the cost of maintenance and lack off accessibility once a TST is installed. The second challenge comes from the dynamic, eccentric and uncertain load pattern that the bearings will encounter during marine operation; while high loads and load variations decrease the life of a bearing, unloaded situations can also cause large amounts of damage through element skidding. The last challenge identified is the environmental conditions of the marine environment itself which may pose the threat of corrosion, sea-water ingress and lubricant contamination.

When looking in detail at possible failure causes [62] of individual bearings in TSTs, one can identify the following failure modes in no order of probability or impact:

1. **Normal Fatigue Failure:** Caused by the creation of sub-surface micro-cracks in the running surfaces through cyclic loading from migrating Hertzian stress fields. As the cracks develop into advanced fissures on the races or elements, small particles are broken loose from the surfaces in a process known as spalling (Figure 2.11a). Once spalling occurs, the development is progressive since the broken loose particles initiate more surface ruptures.

2. **Excessive loading:** Usually leads to premature fatigue failure and possible

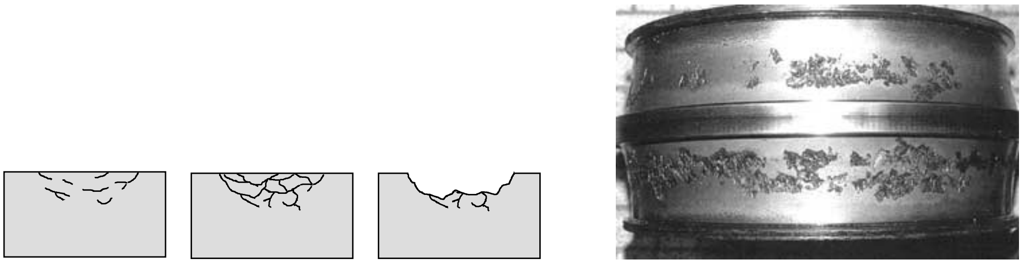
(a) (b)

Figure 2.11: (a) The presence of sub-surface micro cracks (left), caused by the cyclic loading on the raceway, leads to developed crack formation (centre) which finally causes spalling of the raceway surface (right). (b) Image of bearing with excessive spalling on the inner raceway reproduced from `http://www.machinerylubrication.com/Read/664/wear-bearings-gears`.

plastic indentations in the raceways from the rolling elements called *true brinelling* which increases vibrations and fatigue. The effect of eccentric loads also has a similar accelerating effect on the fatigue life. High loads may also cause overheating in a bearing if not accounted for, but this is deemed unlikely due to the slow rotating speed of a TST.

3. **Reverse Loading:** This failure mode traditionally refers to bearings in constant reverse loading brought on by improper installation, which causes high-stress areas and early failure. This can be avoided in TSTs, as for any other application, by applying correct pre-load and installation methods. It should be noted however that TSTs may still experience temporary reverse loads during extreme sea-state conditions during idling mode.

4. **Contamination:** Said to be one of the more common causes of bearing failure, contamination in terms of particles entering the lubricant of a bearing causes small indents in the contact surfaces which leads to abrasion and wear. As for TSTs, sea-water ingress poses a serious threat to the bearing operation as it introduces contaminates, degrades the lubricant as well as causing corrosion.

5. **Corrosion:** Caused by exposing bearings to corrosive fluid or atmosphere and results in increased vibration and wear. As an iron oxide layer forms on the contact surface of the raceways which occurs through a combination of oxygen, lubrication and heat, it is successively worn down by the lubrication wedge causing particulates to enter the lubricant. This process also increases the radial clearance between elements and races and can loosen the pre-load. Since there is an abundance of corrosive fluids in the TST working environment, reliable seals will be of utmost importance for the longevity of the turbines.

6. **Lubricant Failure:** This traditionally refers to the restriction of lubricant flow to the contact surfaces between the rolling elements and races, which in the absence of the lubricant film, causes metal-to-metal contact leading to wear and heat generation. Excessive temperatures are responsible for lubricant failures by degrading the properties of the fluids, although a possible challenge for TSTs will be too low temperatures if a lubricant with low temperature operating range is not selected.

7. **Cage Failure:** For slowly rotating bearings, cage failure is caused during low load conditions where the contact friction between the rolling elements and raceways becomes low enough for the elements to skid along the contact surfaces. This causes the soft-metal cage (usually brass or equivalent) to push against the elements, deforming it and possibly causing fragment contamination.

8. **Misalignment:** Visually characterised by the wear-path of the races not being parallel to the raceway edges. It is caused by shaft misalignment or improperly installed bearings and leads to accelerated wear through the elements moving axially over each revolution. The effect of misalignment varies with inverse proportion to the rotational speed and can be mitigated by use of spherical roller bearings or flexible shaft couplings.

9. **False Brinelling:** Visually similar to true brinelling, showing elliptical wear marks in raceways at each element position and caused by external vibrations. When a bearing is stationary, a lubricant film cannot form between the contact surfaces, leaving it vulnerable to abrasion from small vibrational movements eating away at the surface. This phenomenon may occur for a stationary TST if there are severe vortex induced vibrations coming of the structure during idling mode, causing high frequency vibrations.

As it is possible for a TST shaft bearing to undergo any of the above listed failure modes, or any amalgamation of them, it is at this stage hard to assign any level of occurrence probability or impact for most of them due to lack of historical data of failures [63]. However, there exists established methodologies to determine bearing fatigue life which can give a preliminary estimation of the durability of a TST's bearings in unsteady operation. These types of off-the-shelf fatigue evaluation methods will be used in this thesis to give a preliminary idea of the relationships between the operating parameters of a TST and its fatigue life, which are presented in Section 5.3.

2.4.4 Fatigue of metallic materials

Before going into the detailed review of the fatigue failure modes of bearings, a brief outline of the common fatigue phenomenon is firstly given here.

Fatigue failure is a process in which a piece of material or a structure ruptures without it ever being subjected to its ultimate tensile stress. It has been identified as a serious problem in many fields of engineering, where it has attracted major interest from an economical aspect as well as from a safety standpoint; material fatigue has been the cause of catastrophic instances of structural failure, where many have been fatal.

The process that causes material fatigue is the presence of cyclic stress fluctuations within the material over a long period of time, causing a surface crack initiation that eventually develops into microscopic crack formations [64]. The microscopic cracks progressively develop into macroscopic cracks, and the material reaches its fatigue life when the last stress cycle causes the crack to turn into a rupture of the material.

The two main phases in the fatigue process are identified as the crack initiation phase and the crack growth phase. The crack initiation always starts on a materials' surface since surface's material grains show a lower slip resistance, allowing slip bands to form which eventually evolve into micro cracks. The crack initiation phase is therefore dependent on the material's surface properties such as roughness, notches and corrosion pits.

Once a slip band on a material's surface has progressed into a crack initiation, the fatigue phenomena enters the crack growth phase. Here, the microscopic cracks initiated from the slip bands penetrate the material, usually perpendicularly to the stress direction. At this stage, the fatigue process becomes dependent on the material's bulk properties and the surface conditions no longer have any influence. Stress amplitudes that are below a material's *fatigue limit* are unable to initiate the crack formation phase and aggressive environments (such as corrosion from sea-water) can accelerate both the crack initiation and crack growth phase. When considering the fatigue properties of a material, the fatigue limit tends to increase for materials with higher ultimate strength. Also, the amplitude of the stress fluctuations has more influence on the fatigue life than the mean stress value [64].

The prediction of a material's or structure's fatigue life is notoriously difficult due to the complexities involving the microscopic crack development and its relationship to the applied load signal. Experimental trials have shown to be a valuable tool for fatigue prediction, notably through the creation of S-N curves (Stress-Number of cycles to failure curves) from subjecting materials to cyclic loading of different amplitudes and recording the number of cycles to failure. However, these curves only allow for comparison of materials subjected to constant amplitude loading, and if the load spectrum of a structure is more complicated, there is a need to employ additional methods to include the effect of varying amplitude loads.

A commonly used method to assess fatigue damage for structures loaded with varying amplitudes is the Palmgren-Miner rule. It is a method that estimates the fatigue damage caused by each cycle of the varying amplitude load signal and adds the cumulative life consumption for each cycle, assuming that the damage from each cycle is linearly additive; fatigue failure is then assumed to occur when the accumulated damage reaches the value of unity. The implications of the assumptions of the Palmgren-Miner rule are discussed in Section 7.3.

A shortcoming of the Palmgren-Miner rule is that the calculation of the damage of each load cycle is performed using data from S-N curves derived from constant amplitude fatigue testing, i.e. from conditions that do not include the effects of varying amplitude loading. As such, the Palmgren-Miner rule tends to be more accurate in cases where the load spectrum is more uniform, but under-predictive where there is large differences in load amplitudes. This under-prediction is partially attributed to the method's assumption that stress cycles under the material's fatigue limit do not contribute to the accumulated damage. However, it has been shown that the fatigue limit of a material is only applicable to the crack initiation process, and once a crack is formed from larger stress cycles in a load spectrum the the smaller cycles can propagate it further [64]. Experimental campaigns have indeed showed that when materials are subjected to 'block loadings', where the amplitudes are varied in large chunks which the Palmgren-Miner rule assumes, the fatigue life is longer than if they are subjected to randomly varying load patterns.

Even though the Palmgren-Miner rule for linearly accumulative fatigue damage has been shown to be inaccurate in cases where the load spectrum varies significantly, it was used as a first approximative method in this thesis as the emphasis was on the changes of the life of a turbine, rather than the absolute values.

2.4.5 Rolling element bearing fatigue in TSTs

Most turbine designs will include a number of bearings for the main shaft, gearbox, yaw mechanism and pitch mechanisms. Even though the loading regime of all these bearings will be different and complex, it can be assumed that the main shaft bearing will be subjected to the highest loads since it is usually designed to withstand the rotor thrust force. As the reliability and correct functionality of the bearings is highly important to ensure efficient and safe operation, the bearings are considered to be critical components of the TST; a failure of which can have catastrophic ramifications both structurally and economically.

For the wind turbine industry, Wood et al. [65] reported that 25 - 70% of turbine downtime is attributed to gearbox failures, of which 50 - 80% were caused by internal gearbox bearing failures. Despite that the design processes for wind gearboxes follow international standards of bearing and gearbox design, such as IEC 81400-4 [66], the desired 20 year operating life for these components has not yet been reached. Wood et al. [65] attribute this to the fact that there are no consistent and standardised methods of determining the loading conditions on the bearings despite the existence of international guidelines, and to poor communication between different sub-contractors in the gearbox design process. It is suggested that there is a need for a common methodology for calculating the external loads on the bearings for the use in standardised life prediction methods.

Zeiner-Gundersen [67] also raises the point that TST developers have not devoted enough efforts on the mechanical fatigue aspects of the devices, instead focusing on optimising them for maximum C_{P}. Further, it is recommended that the full range of load variations and non-symmetric bending forces are taken into account in the fatigue calculations on marine renewables, as the common practice of using static design safety factors is not representative of the dynamism in the tidal flow. Therefore, the TST industry must invest significant efforts in device fatigue analysis to achieve the reported 15 - 25 years of service life [65, 67].

It is clear that there is a need for increased understanding of the loading environment on TSTs and how this affects the fatigue life of the structures in general and the tribocorrosion on the bearings in particular, especially if the ambitious 25 years of service life is to be achieved. There are several standardised methods to determine the fatigue life of rolling element bearings that have risen from more 'traditional' machine engineering areas. Most notably, the theory originally published by Lundberg & Palmgren [68] which gave probabilistic survival rate of a bearing derived through the principles of Hertzian contract stress, is widely used to this day and is implemented in this thesis as described in Section 5.3. The theory relates the fatigue life of a bearing to the sub-surface originated fatigue and uses a derived *dynamic load rating* for a given bearing and the *equivalent bearing load* to determine the number of revolutions when a 10% failure probability occurs. This is also known as the L_{10} method and has been adopted by many international standards such as the ISO 76 and ISO 281 [69, 70], summaries of which can be found in Appendix D. The choice of allowing a 10% probability of failure in this thesis instead of a lower value was done in order to keep the study in-line with the recommendations and standards in the field.

The L_{10} method has also been expanded to accommodate varying bearing loads according to Palmgren-Miner's linear damage rule [59] which assumes that the damage sustained for each of a bearing's load cases can be added to give the total damage. The details of this method is also presented in Section 5.3.1 along with its possible limitations for TST applications.

2.5 State of the art load modelling approaches for TSTs

From the instationary inflow conditions to the load paths from the turbine's blades into the drivetrain, the TST hydrodynamic load issue is a complicated physical phenomenon where numerical modelling plays a vital role in its investigation. Indeed, in order to derive the loads on the TST drivetrain and bearings to be studied in this thesis, careful consideration must be given to the selection of appropriate load modelling techniques. This section gives a brief review of the methods available to determine the hydrodynamic loads on TST structures.

Currently, there only exists a handful of commercially available software packages dedicated for TST numerical modelling, such as GL Garrad Hassan's TIDAL BLADED and the National Renewable Energy Laboratory's (NREL) FAST [24, 71]. These packages are conversions of wind turbine evaluation codes, based on BEMT, with the addition of several features to simulate marine load conditions. The rationale behind this technology transfer from the wind turbine sector is that the computationally inexpensive BEMT method is applicable for certification and due-diligence studies – which require a large amount of load cases to be simulated. It seems like the majority of studies performed on TST load calculations are either performed on the aforementioned commercial packages, or in-house codes developed by researchers and developers. In addition, the use of general finite element software is widely used, such as CFD or FEM, for the study of detailed flow and load phenomena of TSTs.

The task of modelling the environmental loads on a TST in operation is here divided into three separate categories for easier presentation. These categories are the hydrodynamic inflow modelling (Section 2.3), the hydrodynamic rotor-load modelling and the structural response modelling. Depending on the level of transient detail desired, these categories can be modelled as being two-way coupled, one-way coupled, or to be fully uncoupled.

Presented below is the state of the art of hydrodynamic load modelling for TSTs, as presented in the corpus of scientific literature on the subject and from wind turbine literature. It should be noted that the hydrodynamic *load* models presented below can be used in conjunction with any of hydrodynamic *inflow* models mentioned previously in Section 2.5.1.

2.5.1 Hydrodynamic load models for TST rotors

The first task of any modelling approach will logically be to derive the loads on the turbine blades, which will later propagate into the main structure and internal components. Due to the complexity of the flow around a TST rotor in instationary sea conditions containing flow separation, turbulence, wake instabilities and added mass effects, a trade-off between the fidelity and convergence time of the simulations must always be made due to limited computing resources.

Presented below are three of the most common approaches of TST rotor-load models used to date, ranging from the simplest, most computationally efficient BEMT method to the full volumetric solution of the URANS equations using CFD packages, each offering its own advantages and disadvantages in terms of load resolution and convergence times.

Blade element momentum models

Blade element momentum theory was originally published by Glauert [72] for the performance evaluation of ship and airplane propellers. It has later been adopted as the wind energy sector's standard approach due to its simplicity and fast convergence time; making it suitable for the large amounts of load cases needed for certification exercises and fatigue analysis [5, 73, 74].

The basic principles of the BEMT method is to divide the blades into several radial elements which intersect the incoming flow at corresponding stream-tubes and enforcing momentum conservation between the blade elements and stream tubes. The forces on the blades can then be obtained by equating the lift and drag forces from the corresponding 2D airfoil sections with the fluid forces through an iterative process. This requires that the lift and drag characteristics of the airfoil are known previously and given as inputs to the model - these values are usually determined using potential flow methods or using experimental data, making the airfoil characteristics one of the major uncertainties in the BEMT method. Several other assumptions are made in BEMT in order to simplify the complex interactions between rotating machinery and the surrounding fluid. One major assumption is that the turbine operates in a non-turbulent, steady-state environment with uniform inflow [73].

Since many of the simplifications and assumptions made in BEMT make it unsuitable for use in the dynamic marine environment, it must be heavily modified from its original formulation to accommodate the additional inflow phenomena. This has successfully been done by several authors as shown in Section 2.3, showcasing that BEMT is one of the more popular load evaluation tools for TST applications when the detailed flow field around the rotor and in the wake are not needed to be resolved. The modification and corrections added to the BEMT model used in this work are presented in Chapter 3.

In this thesis, the methodology of Buckland [43] and Masters & Orme [75], originally developed by Chapman [36], will be followed when designing the BEMT model since it has repeatedly been shown to be accurate against experimental TST data.

Potential flow models

As the name suggests, potential flow models use potential flow theory to represent the flow conditions around a turbine's rotor. There are a number of different ways to model the hydrodynamics of a tidal turbine using potential theory, but all work under the assumption that the flow is inviscid, irrotational and incompressible, allowing the flow velocity expressions to be reduced to the Laplace equations of velocity potential. The flow through and around the turbine can then be modelled by different combinations of elementary flows such as sinks, sources, vortexes and dipoles [76].

The simplest form of modelling for a TST using the potential flow method is to represent each blade of the turbine by a line vortex extending from the root to the tip and placed at the quarter chord position which is the approximate location of the aerodynamic centre. The line vortex is given a varying circulation along the turbine radius to capture the effect of the lift reduction caused by tip vortexes at the blade's tip. This method is termed the 'lifting line' method and it may be expanded by assuming that the blade sections operate under 2-D flow conditions once the flow-field has been calculated, similarly to the BEMT assumption. This extension is sometimes termed 'strip theory' and the lift and 2-D airfoil characteristics may be supplied as external inputs or calculated using internal sub-routines [77].

Despite the long history of development of the potential flow models in the marine propeller and wind industry, these models are seldom used for TST applications and the role these methods will play for the tidal energy sector is unclear.

Computational fluid dynamics models

Although technically all the models presented in this section deal with fluid dynamics in a computational way, the term 'computational fluid dynamics' is reserved for methods solving the discretised versions of the Navier-Stokes equations.

CFD investigations on TSTs are commonly presented by investigators studying the detailed flow phenomena around the rotor and in the wake and the method can also be used to give high resolution pressure maps across the turbine's blades for structural analysis [78]. The main advantage of CFD models are their high resolution and versatility through the solving of the governing fluid flow equations which can natively handle all relevant phenomena such as turbulence, flow separation, stall, wave current interactions along with rotor-structure interactions - making CFD models the most detailed and general TST hydrodynamic models available.

All the flexibility and high resolution of CFD does however come with a severe penalty in computational expense. Since the Navier-Stokes equations can only be solved in their discretised form, the whole fluid domain must be discretised into computational elements with very fine resolution close to surface boundary-layers as for example the blades. The number of calculational elements in a CFD model for a TST can be up to several million and in transient simulations the convergence time can reach several weeks. Due to this, CFD models are generally considered unsuitable for certification type modelling, such as fatigue evaluations over several sea-states; instead, more simplified models such as BEMT are commonly used for such purposes.

2.5.2 Structural models for TST drivetrains

With the hydrodynamic loads on the rotor calculated using any of the methods outlined above, the next task of modelling the environmental loading on a TST is to determine how the rotor loads are propagated into the sub-components such as the support structures and drivetrain. This kind of structural modelling gives insight to the dynamic or static response of the structure which in turn allows the internal stresses and external deflections to be analysed. The identification of highly stressed areas of the material can inform on designs to withstand ultimate loading or fatigue damage, while the deflections of the structure – including the blades – can be fed back to the hydrodynamic model which will affect the fluid-structure interactions.

As is the case for the hydrodynamic models, most of the commercially available methodologies for TST structural evaluation have also been adopted from the wind turbine industry. For this reason, the following section will present an overview of the most common methods of structural modelling of turbines based on wind turbine methodologies.

Peeters [79] gives a review of the most popular codes for wind turbine simulations and identifies three main modelling approaches of the structural modelling:

1. The first approach is the multibody system (MBS) which is usually used for the simulation of large body motion. Here, each component in the turbine is represented by a discrete solid body with mass and inertia which is unable to

deform and its dynamics is modelled using Newton's equations of motion. The joints between the bodies represent the flexibility of the system and each body has a maximum of 6 DoF.

2. The second approach is the finite element method which is commonly used for the detailed, 'internal' study of individual drivetrain components. Each component is represented by a mesh of deformable nodes and elements where the deformation is linked to the elements and the mass and inertia properties are given to the nodes which may each have up to 6 DoF. The array of elements, the external forces and the kinematic constraints then form a system of matrix equations that are solved numerically.
3. The third case identified by Peeters is the flexible multibody system (FMBS) which is described as a middle ground between MBS and FEM. In this approach, each body has 6 DoF in combination with an extra set of DoFs describing the deformations of the body which are derived from a reduced FEM model via the *component mode synthesis* technique. This method is described as a compromise between the computational efficiency of the MBS model with the added detail of the components' deformation in the added DoF. It also goes by the name of the *modal* formulation.

As can be seen, there exists a large amount of developed methodologies for the mechanical models for turbine structures from the wind turbine sector that could be used for tidal applications. However, since the scope of this thesis is to investigate the *internal* loads in the turbine drivetrain, the structural modelling will be limited to the main shaft and shaft bearings. As will be seen, many of the commercially available modelling techniques used for the detailed load simulations on a turbine's drivetrain are far less refined as compared to the external structural models.

Purely torsional drivetrain models

Currently, the commercially available TST simulation packages employ the FMBS method for the larger structural calculations such as GL Garrad Hassan's Tidal Bladed and NREL's marine modification of Fast [24, 80]. However, the FMSB formulation in these codes is only used to model the larger structures of the turbine such as the tower, blades, nacelle and bed-plate. The actual description of the drivetrain is heavily simplified by modelling it as having exactly one torsional DoF along the shaft's axis of symmetry [79]. These drivetrain models are referred to as *purely torsional models* and reduce each drivetrain component as having only a torsional stiffness such as shaft stiffness, gear mesh stiffness and generator electrical torsion stiffness. The simplest form of the purely torsional model is the two-mass model consisting of only one lump mass for the rotor and one mass for the generator having a representative stiffness for the shaft and gearbox.

There are reports in literature of authors expanding the two-mass model to incorporate more individual torsional bodies along the drivetrain for wind turbine applications such as Girsang et al. [57], who modified the FAST code's two-mass model into a five-mass model. Although these approaches increase the accuracy of the torsional dynamics of the drivetrain with emphasis on the gear box, they are still purely torsional models.

Although modelling drivetrains in purely one torsional degree of freedom (DoF) can give insight into the turbine's interaction between the rotor, gearbox and generator, it gives no information about the full extent of the loading on individual components. The loads on bearings will in these models be represented as purely axial while the off-axis loads propagating into the gearbox may have a significant impact on the component life. In fact, de Vries [81] links a series of wind turbine gearbox failures to the lack of insight brought on by using models with insufficient representation of the loads.

All of the shortcomings of modelling drivetrains as purely torsional systems that have limited the design process in the wind turbine industry will be present for use in the TST field since the most popular tidal design codes use the same methodology. It is also believed that these problems may even be exacerbated due to the higher asymmetry of the hydrodynamic operational loads of TSTs due to the presence of surface waves and shear currents.

Multibody drivetrain models

Aside from the dedicated TST modelling codes using purely torsional drivetrain models, there exists specialised multibody software packages that are frequently used for drivetrain analysis in other sectors which show promise for the marine energy modelling.

One such commercial software suite is SIMPACK [82] which uses a MBS formulation for the use in the automotive, wind and manufacturing sectors to name a few. For drivetrain modelling, the shaft is modelled using rigid or flexible beams (FMBS) and the shaft bearings are represented using linear of non-linear stiffness matrices. The study on TST structural flexibility by Arnold et al. [14] mentioned in Section 2.1.2, was performed using the SIMPACK suite in combination with a CFD solver to derive the hydrodynamic loads. However, no internal stresses or deformations in the drivetrain were reported in that publication [14].

Even though these types of software packages have a good potential for TST drivetrain modelling, the proprietary nature of them and the lack of publicly available theory manuals make them unsuitable for the purpose of this research.

FEM drivetrain models

The FEM approach to TST drivetrain simulation is the most versatile and detailed method which is analogous to the CFD method for the determination of the hydrodynamic loads. With the increase in accuracy comes also a potential penalty in computational expense depending on the exact details of the models used.

The fundamental principle of the FE method is to discretise the structure under investigation into finite elements and solve the resulting matrix stiffness equation to obtain the stress and strain for each element. The FE method allows for the drivetrain to be specified in any desired DoFs and the internal stresses of every component can be analysed.

As it is the most flexible and well documented method of analysing the loads on a turbine's drivetrain, the FE method shows good potential for use in research into TST drivetrain loading. However, since the major drawback is the computing time when a large number of elements is used in a model, a balance between the fidelity and model complexity must be found. The proposed new model for TST load simulations in this thesis addresses this issue and is presented in the next section.

2.6 Proposed higher degree of freedom TST load model

The available literature on the topic of TST operational loads brought on by the marine environment shows that it is a complex field of research, requiring sophisticated modelling techniques which are generally computationally demanding. A knowledge gap can also be seen in the scientific literature on the detailed fatigue aspects on the internal components of a TSTs drivetrain, such as the response of the shaft bearings, exposed to the loading conditions expected over its lifetime.

In order to effectively investigate the loading behaviour of TSTs in the marine climate and to inform the internal drivetrain loading behaviour as stated in the research objectives in Section 1.1.2, a computationally efficient modelling tool was developed from scratch and is presented in the following chapters. The code's core solver was built upon a dynamic BEMT formulation with a library of inflow models for modelling a range of inflow conditions. The dynamic BEMT code was capable of resolving the hydrodynamic loads on the rotor in four DoFs, namely thrust, torque and the vertical and horizontal rotor out-of-plane bending moments, which were fed to a simplified FEM drivetrain model to derive the bearing loads; the remaining two DoFs of the forces in the axially perpendicular horizontal direction and vertical direction were neglected since the projected area of the turbine is minuscule in these directions and the self-weight of the hub is assumed to be balanced by its buoyancy. This modelling technique increased the fidelity of the input load pattern compared to the traditional purely torsional models by the inclusion of the out-of-plane rotor bending moments while still retaining the high computational efficiency inherent in the BEMT method.

Utilising the fast convergence time of the new BEMT-FEM model, the fatigue loading on the drivetrain bearings could be studied over a realistic number of differing load states. The fatigue life for the dynamically loaded TST drivetrain bearings was determined in post-processing using the well established L_{10} method. In addition, the maximum internal contact stresses were determined using the static load ratings as defined by the international standard IEC 61400-4 [66].

It should be mentioned that although the methodology of using BEMT to derive the rotor loads on a TST has been presented by several researchers previously, it is the continuation of investigating how the loads propagate through the drivetrain using a high resolution FEM scheme that constitutes the novelty of the method presented. Finally, the knowledge of the sensitivity of the bearing life to the operational parameters of the model produced one of the major contributions of this thesis.

2.7 Sensitivity analysis

The final topic to be discussed in this literature review is the concept of a sensitivity analysis on a numerical model which was performed on the unsteady BEMT model in Chapter 4.

Simply put, sensitivity analysis is the study of the relationships between the inputs and outputs of a computational model [83], or put more precisely, it is the study of the propagation of variability through the model from the input to the output. Sensitivity analysis can provide insight to a model's behaviour and performance in extreme cases in addition to determining the model's sensitivity toward its input parameters. The use of a sensitivity analysis on a computational model becomes necessary when the code is complicated enough to make classical mathematical analysis impossible, and the model needs to be investigated using empirical analysis through *computational experiments* [84].

The motivation to perform a sensitivity analysis on the unsteady BEMT model was the expectation that it would yield insight into which parameters were most influential in regards to turbine loading and turbine load variations, which was specified as a research objective. When the parameters to which the loads were most sensitive toward had been identified, a detailed parameter study could be conducted on these primary variables; the sensitivity analysis could therefore be considered as a screening process for the parameter study.

There exists many different types of sensitivity analysis methods, each having their own advantages and weaknesses for different applications to different types of models. The main categories of sensitivity analysis methods that are commonly found in literature are *one-at-a-time* (OAT), *local*, and *regression* methods [85]. OAT methods derive a model's sensitivity towards its input by setting all parameters to a base value, change one by a given amount and recording the output variation. The parameter is then re-set to its base value and the next parameter is changed, and so on. This allows information of what parameters has what effect on the output to be retained, but the method does not account for parameter interactions [85].

Local methods are defined as a method of taking the partial derivative of the output change for each input variation. This is one of the simplest methods to implement, but has the drawback that it only uses a fixed point in the input space to calculate the derivatives, thus limiting the applicability of the method to a small value range of the inputs.

The third method identified, the regression method, involves fitting a linear regression to the model outputs and using the regression coefficients as sensitivity measures. The advantage of these type of method is that they explore the full range of the input space for each parameter while taking into account the interactions with other parameters. Because of the exploration of the full input ranges and interactions, these types of models are referred to as *global*, to distinguish them from local and OAT methods [85]. A disadvantage of regression methods is that they perform poorly for non-linear models and no information is retained on what parameter causes what output change.

The lack of insight into how varying the different inflow and operational parameters affects TST loading in a *global* sense highlights the need for an exhaustive sensitivity analysis to be performed on all parameters affecting the loads on a TST in a quantitative manner. Therefore, the method of sensitivity analysis selected for this thesis has been that of Morris [84] which is an OAT method, allowing the information of the effect of each individual parameter on the output to be retained, while it also considers the interaction between parameters. The Morris method also evaluates the input parameters over the whole range of their defined input space, which makes it more of a global approach than local. The details of the Morris method are given in Chapter 4.

2.8 Conclusions

It is clear that tidal stream energy technology has the potential to provide a large contribution to the renewable energy mix sought after by many political institutions today. The high level of engagement can be seen in the ever increasing interest from the research community and from the large commercial investments currently being undertaken. However, even though it is rarely reported, several early deployments of TSTs have resulted in premature failures where many cases were related to fatigue or ultimate load issues [86], implying that there is a long way to go before the 15 - 25 years of operating life of the devices is achieved, and a stable industry can be created.

The literature study presented in this chapter has shown that there is a need for an over-arching study on how the loading and durability of TSTs varies as a function of the unsteady marine inflow climate. This would aid in the understanding on what parameters drive the durability and design economies of TSTs, as well as acting to 'link' together previous studies by informing on how important each of the studied loading phenomena are in relation to each other. Furthermore, emphasis will be put on identifying what parameters in the marine inflow, turbine operating states and turbine geometry have the largest effect on the loading and load variations. Also, the detailed load propagation from a TSTs rotor into the drivetrain must be investigated and the potential error present when using the common purely torsional drivetrain methods, which neglect the full DoF spectrum of the loads from the rotor, must be quantified.

The theory used to derive the turbine loads will be the BEMT method due to its identified simplicity, modifiability and fast convergence time. The use of this method, along with a simplified yet high fidelity FEM drivetrain model will aid in answering the research questions presented in the first chapter through meta-studies on the model itself, in the form of sensitivity studies and parameter investigations, and finally through a case study on a 'generic' turbine in real sea-conditions.

Relating to the durability of tidal stream technology, the main shaft bearings have been identified here as components in the TST drivetrain that have not been investigated sufficiently in regards their loading spectra and fatigue response. As is listed in Section 2.4.3, there are many possible failure modes for shaft bearings subjected to irregular load patterns, and many of these failure modes are hard to predict numerically. However, it was shown that there are simplistic methods available for determining the sub-surface raceway fatigue and maximum contact stresses. These bearing life methods will be used in combination with the developed load model to serve as an first indicator of the fatigue damage and maximum stresses that will be present in a TST during realistic operating conditions.

The next chapter gives the detailed description of the hydrodynamic BEMT model used to simulate the rotor loads on TSTs operating in unsteady seas, which will later be used to determine the relationships between the inflow and operating conditions to the loads – as presented in Chapter 4.

Chapter 3

Development of an unsteady blade element momentum theory for TST load calculations

> "I predict that within 100 years computers will be twice as powerful, ten thousand times larger, and so expensive that only the five richest kings of Europe will own them."
>
> — Johnathan N. Frink

According to the international design standard for marine energy converters [11], when wave driven load events on the structures are to be analysed, a period of no less than 3 hours should be simulated for each sea-state to ensure that the load output derived is statistically stationary. It is easy to see that, with the required time-step size to resolve small-scale events, this requirement puts a large emphasis on the convergence speed of the models used for load investigations of TSTs.

This chapter details the theory behind the hydrodynamic rotor-load model used in this thesis and the alterations made to it to enable the capture of the marine loading phenomena. The model was based on an unsteady BEMT formulation due to its superior computational efficiency and was implemented in the Matlab R2012b [87] computing environment, where it could easily be run on a home laptop. The BEMT model will in later chapters be coupled with a minimalist FEM drivetrain model which lets the hydrodynamic rotor loads be translated into the internal components for the bearing fatigue analysis.

Since the inflow conditions in a tidal stream are anything but static and uniform, the model must be able to incorporate a diverse range of inflow phenomena. As such, the BEMT model comes equipped with a library of engineering hydrodynamic inflow models, shown in the first part of this chapter, that can determine the sub-surface velocity distributions in a computationally efficient manner for a variety of flow conditions.

Further, this chapter goes on to describe the steady-state formulation of the BEMT equations and the standard corrections added to compensate for three-dimensional effects such as tip-losses and highly loaded turbines. The inclusion of the unsteady inflow effects are then detailed along with the method of mapping the non-uniform inflow patterns onto the rotor-plane and the solving scheme for the governing equations towards the mid part of the chapter. Finally, the definition of the resultant rotor out-of-plane bending moment vector is given, which will be the main original expansion of this BEMT model when used in combination with the 6 DoF drivetrain model.

3.1 Hydrodynamic inflow synthesis

The hydrodynamic inflow models used for the purpose of TST load and fatigue evaluations must fulfil the following requirements as identified:

1. Ability to resolve both the horizontal *and* the vertical velocity distributions of the inflow current.
2. Inclusion of surface wave induced velocity components.
3. Ability to account for wave-current interactions.
4. Representation of irregular sea-state spectral density distributions from real tidal energy sites.

It should be noted that the ambient flow turbulence is left out of the above criteria due to scope limitations and since this is not believed to be a major contributor to internal fatigue loading when compared to the larger amplitude variations from the waves and shear-current effects. However, it is restated that the presence of ambient turbulence would extenuate the dynamic loading effects on the drivetrain of a TST. The effect of ambient inflow turbulence is however included as a factor on the airfoil performance characteristics, which are derived from the external linear-vorticity panel method package XFOIL by Drela [88] or provided as experimental airfoil performance data.

Due to the limitations of the potential flow wave-theories used, no single model can incorporate all the requirements listed above. However, this does not present a major issue as the high resolution of inflow distribution across the rotor plane, given by the first three requirements, is not crucial when considering the detailed temporal distribution of inflow given by the last requirement. In other words, the irregular sea-state modelling can be conducted using a more crude representation of the velocity distributions down the water column, although this layout is not ideal as discussed in the limitations section of this thesis.

The first inflow model to be explained will be the linear wave theory as presented by Dean [48]. Even though this model is only applicable in the calmest of seas, which is not of great use for the purpose of TST wave loading, the theory will be used to define the mathematical problem of potential flow wave models which forms the basis for the higher order theories. The irregular sea-state model presented in Section 3.1.7 is also based on the equations derived from linear theory.

3.1.1 Governing potential flow equations

The following section sets up the mathematical problem for surface wave motions expressed as a potential flow problem, including its boundary conditions. Since the free surface boundary conditions will be shown to be non-linear and the instantaneous free surface deformation, η in Figure 3.1 is unknown, an analytical solution to the problem is impossible.

Figure 3.1 also shows the definition of the flow domain in all wave models used herein, where the origin is at the mean water level (MWL), as well as the definition of the wave celerity (wave speed), C, wave height, H, wave amplitude, a, wave length L and water depth h. The amplitude of the wave differs from the instantaneous water level such that the former is a fixed scalar value and the latter is a variable.

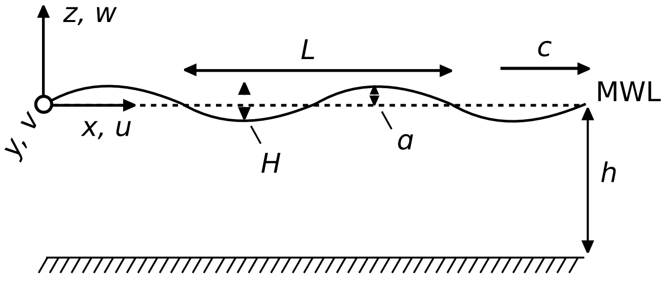

Figure 3.1: Diagram showing the definition of the flow domain as used by the wave models with the origin at the mean water level including parameters used to define a regular wave-train.

Governing equations and boundary conditions

Due to the fact that in all potential flow wave models the fluid flow is considered two dimensional, irrotational and incompressible, a potential flow field may be assumed throughout the domain and thus the Laplace equation [89] shown below must be satisfied along the horizontal and vertical coordinates, x and z, as

$$\frac{\partial^2 \varphi}{\partial x^2} + \frac{\partial^2 \varphi}{\partial z^2} = 0. \tag{3.1}$$

Here, φ is the velocity potential and from potential flow theory the horizontal and vertical velocity components, u and w, are given by the relationships

$$u = \frac{\partial \varphi}{\partial x}, \quad w = \frac{\partial \varphi}{\partial z}. \tag{3.2}$$

The equations of motion for a fluid parcel in the flow are then represented by the Navier-Stokes equations, which relate the parcel's mass and acceleration to the forces acting upon it according to Newton's second law. In the case of inviscid an fluid, this relationship reduces to the Euler equation [48] as the viscous forces can be neglected and it is written as

$$\rho \frac{\partial \overline{v}}{\partial t} = -\nabla p + \rho \overline{g} \tag{3.3}$$

where ρ is the fluid density, $\overline{v}$ is the fluid velocity vector, ∇p is the pressure gradient over the fluid parcel and $\overline{g}$ is the gravitational acceleration. As the flow has been assumed to be irrotational, the Euler equation can be integrated over a streamline and is then transformed to the generalised Bernoulli equation as

$$gz + \frac{p}{\rho} + \frac{1}{2}\left(\left(\frac{\partial \varphi}{\partial x}\right)^2 + \left(\frac{\partial \varphi}{\partial z}\right)^2\right) + \frac{\partial \varphi}{\partial t} = C(t) \tag{3.4}$$

where the velocity field is independent of the integration function $C(t)$, but the reference pressure will depend on it.

The boundary conditions for the problem can de divided into the free surface boundary conditions, bottom boundary conditions and the periodicity boundary conditions. At the bottom, the boundary condition is simply set to zero vertical velocity since there can be no flow going through the seabed. This can be written as

$$w = 0 \rightarrow \frac{\partial \varphi}{\partial z} = 0 \quad \text{for} \quad z = -h. \tag{3.5}$$

The fluid is however allowed to slip along the seabed, meaning that there is no constraint for the horizontal velocity component. The two conditions that are set at the surface are the kinematic boundary condition and the dynamic free surface condition. The kinematic boundary condition relates the surface water-particles' vertical velocity component to the surface vertical velocity component expressed as

$$\frac{\partial\varphi}{\partial z} = \frac{\partial\eta}{\partial t} + \frac{\partial\eta}{\partial x}\frac{\partial\varphi}{\partial x} \quad \text{for} \quad z = \eta. \tag{3.6}$$

where η is the free surface displacement around the mean water level. The dynamic free surface boundary condition specifies that the pressure at the surface must be equal to the atmospheric pressure which is assumed as a constant p_0. Using Equation (3.4) one can express the pressure at the free surface as

$$gz + \frac{p}{\rho} + \frac{1}{2}\left(u^2 + w^2\right) + \frac{\partial\varphi}{\partial t} = \frac{p_0}{\rho} \tag{3.7}$$

which, when setting $z = \eta$ as the surface displacement and $p = p_0$ at the surface, may be expressed as

$$g\eta + \frac{1}{2}\left(\left(\frac{\partial\varphi}{\partial x}\right)^2 + \left(\frac{\partial\varphi}{\partial z}\right)^2\right) + \frac{\partial\varphi}{\partial t} = 0 \quad \text{for} \quad z = \eta. \tag{3.8}$$

The final boundary condition states that the periodicity of the waves must be upheld, which is expressed as

$$\eta(x,t) = \eta(x + nL, t) = \eta(x, t + nT). \tag{3.9}$$

As is shown, the free-surface kinematic boundary condition expressed in Equation (3.6) and dynamic boundary condition in Equation (3.8) are both non-linear; this in combination with the governing Equation (3.1) not containing the free surface deformation η, makes an analytical solution impossible for this mathematical problem. Suitable approximations are needed to the governing equations which will allow for the creation of useful wave models.

3.1.2 Linear wave theory model

The linear approach to solving the governing equations of motion according to Dean & Dalrymple [48] involves assuming that the wave-steepness, H/L, is so small that the unknown surface elevation, η, can be eliminated from the governing equations. This corresponds to the surface boundary conditions being evaluated at $z = 0$ instead of $z = \eta$.

The kinematic surface condition is first linearised, for waves propagating over stationary waters, by investigating the influence of the non-linear term in Equation (3.6). It can be shown that, assuming that $H/L << 1$, neglecting the non-linear term only generates a small error [48]. Through the use of Taylor expansions, which are omitted here for brevity, the final form of the linearised kinematic free-surface boundary condition evaluated around $z = 0$ becomes

$$\frac{\partial \varphi}{\partial z} = \frac{\partial \eta}{\partial t} \quad \text{for} \quad z = 0. \tag{3.10}$$

The dynamic boundary condition is then linearised in the same manner as for the kinematic condition, and the resulting equation becomes

$$g\eta + \frac{\partial \varphi}{\partial t} = 0 \quad \text{for} \quad z = 0. \tag{3.11}$$

Equations (3.10) and (3.11) can be combined to form a single free-surface boundary condition as

$$\frac{\partial \varphi}{\partial z} + \frac{1}{g}\frac{\partial^2 \varphi}{\partial t^2} = 0 \quad \text{for} \quad z = 0. \tag{3.12}$$

The exact solution of the Laplace equation can now be found by using the linearised free-surface boundary condition in Equation (3.12), the periodicity condition expressed in terms of the Laplace equation, and, the bottom boundary condition in Equation (3.5) through the method of separation of variables. The final expression of the linear velocity potential then becomes

$$\varphi = -\frac{ag}{\omega}\frac{\cosh k(z+h)}{\cosh kh}\sin(\omega t - kx). \tag{3.13}$$

where ω is the wave angular frequency defined as $\omega = 2\pi/T$ and k is the wave number defined as $k = 2\pi/L$.

Dispersion relationship

A two-dimensional, regular water wave can be fully defined by its amplitude, a, angular frequency, ω, wave number, k, and by the underlying water depth h. These parameters have however been found to be dependent on each other in such a way that waves with longer periods travel faster than waves with shorter periods. The period of a wave is also dependent on the water depth, so that the wave length increases with wave period for a given water depth. This relationship is called the *dispersion relationship* since the differing celerities of waves of different wave lengths makes them dispersive. The equation for the linear dispersion relation is defined as

$$\omega^2 = gk\tanh(kh) \tag{3.14}$$

and is solved for k in the present model using an iterative Newton-Raphson method.

Waves on a uniform current U_∞

As the linear velocity potential expressed in Equation (3.13) was derived for waves propagating over waters without the presence of currents, the linear wave model would not satisfy the third requirement needed for the inflow models for this thesis in Section 3.1. To fulfil this wave-current interaction requirement, the wave induced velocity equations used in the model are instead taken from a velocity potential derived from waves propagating on a uniform current.

Indeed, the simplest form of wave current interactions can be found when observing waves propagating on a current which is uniform with depth and flow direction. In this case, if one defines a moving coordinate system travelling with the current speed U_∞, the waves can be described using the same equations as for waves travelling over stationary water. From a fixed reference frame, the uniform current does not alter the waves in any other way than changing the wave frequency through Döppler shifting so that

$$\omega_a = \omega_r + kU_\infty \tag{3.15}$$

where ω_a is the observed frequency and ω_r is the relative wave frequency in the moving reference frame. Using the methodology and notations as described by Dean & Dalrymple [48] one can assume a velocity potential of the form

$$\varphi = U_\infty x + \frac{ga}{\omega(1 - U_\infty k/\omega)\cosh kh} \cosh k(h+z) \cos(kx - \omega t) \tag{3.16}$$

which according to Dean & Dalrymple's definition of velocity potential gives the following final particle velocity components that are used as an inflow model for the BEMT code. The analytical expressions for the horizontal and vertical particle velocities are found as

$$u = U_\infty + \frac{gak}{\omega(1 - U_\infty k/\omega)\cosh kh} \cosh k(h+z) \sin(kx - \omega t) \tag{3.17}$$

$$w = -\frac{gak}{\omega(1 - U_\infty k/\omega)\cosh kh} \sinh k(h+z) \cos(kx - \omega t) \tag{3.18}$$

and the dispersion relationship becomes

$$\omega^2 = \frac{gk\tanh(kh)}{1 - U_\infty k/\omega^2}. \tag{3.19}$$

Figure 2.6 in the previous chapter showed that linear wave theory is only applicable for waves with the smallest steepness, and the previous derivation showed that it can only incorporate wave-current interactions as a Döppler shift for waves on a uniform current. Due to these limitations of linear wave theory, higher order models are needed if the inflow conditions seen at tidal stream sites are to be replicated realistically.

3.1.3 Coupled third order Stokes wave-current model

Stokes wave theory refers to a method of solving the governing potential flow equations with *non-linear* boundary conditions using a perturbation method. The order of the theory refers to how many terms are kept in the perturbation expansion of the variables, which are then inserted into the governing equations and solved for.

A third order Stokes theory coupled with a linear shear current profile is used in this thesis as originally described by Kishida & Sobey [31]. The wave dynamics can still be considered irrotational due to the constant vorticity of the linear shear flow and the model can incorporate wave-current interactions between the shear current and 3rd order waves. This allows for the adoption of an inviscid analysis with a Lagrangian reference frame moving with Stokes first definition of wave speed with its origin on the seabed.

The current flow field is specified by a surface velocity, U_s, and a bottom velocity, U_b, from which the mean Eularian current U_m and constant current vorticity Ω_0 are calculated by

$$U_\mathrm{m} = U_\mathrm{s} - \frac{(U_\mathrm{s} - U_\mathrm{b})}{2} \tag{3.20a}$$

$$\Omega_0 = \frac{(U_\mathrm{s} - U_\mathrm{b})}{h} \tag{3.20b}$$

The linear current profile is assumed to be an adequate representation of a tidal flow for most cases, although it will be highly site-dependant. It is also noted that using a linear shear profile to mimic a more commonly used 1/7th power-law profile generates an error towards the bottom of the rotor-plane, which can be seen in Figure 3.2.

With the current and wave parameters specified, the first definition of Stokes wave speed is used as a dispersion relationship to define the celerity, C, which is used as the velocity of the moving reference frame [31]. The dispersion relationship for the model is then defined by the equations

$$C = C_0(a_{11} - \epsilon^2 a_{20}) + U_m + \frac{1}{2}\omega_0 h \tag{3.21}$$

$$C_0 = [gk \tanh(kh)]^{1/2} \tag{3.22}$$

$$\omega_0 = \Omega_0 / kC_0 \tag{3.23}$$

where the lengthy perturbation constants a_{11} and a_{20} are as given in Kishida & Sobey [31]. Equations (3.21) - (3.23) are again solved using the Newton-Raphson method.

The governing equations of the particle velocities are derived by introducing a stream function, ψ, where the velocity components are found as $u = \partial\psi/\partial z$ and $w = -\partial\psi/\partial x$. Through a perturbation expansion and use of the Euler equation, the third order solution of the stream function was found by Kishida & Sobey [31] to be

$$\psi = \frac{C_0}{k}\left[a_{00}kz_\ell + a_{01}(kz_\ell)^2 + \epsilon a_{11}\frac{\sinh kz_\ell}{\sinh kh}\cos kx_\ell + \epsilon^2\left(a_{20}kz_\ell + a_{22}\frac{\sinh 2kz_\ell}{\sinh 2kh}\cos 2kx_\ell\right)\right.$$
$$\left.+\epsilon^3\left(a_{31}\frac{\sinh kz_\ell}{\sinh kh}\cos kx_\ell + a_{33}\frac{\sinh 3kz_\ell}{\sinh 3kh}\cos 3kx_\ell\right)\right] \tag{3.24}$$

where the x_ℓ and z_ℓ coordinates are in the Lagrangian frame of reference which are related to the global reference frame by $x_\ell = x - Ct$ and $z_\ell = z$. In this equation, $\epsilon_{\text{K.S}} = kH/2$ is the wave steepness and as before, the perturbation constants are left out for brevity and can be found in Kishida & Sobey [31].

3.1.4 Fifth order Stokes model

To model waves that are close to the breaking limit, an even higher order solution to the governing potential equations is needed. Presented here is a fifth order Stokes theory as described by Fenton [29] which is used when modelling waves with dimensionless steepness defined by Fenton, $\epsilon_\text{F} = H/gT$, above 0.02.

The theory uses the wave steepness itself, this time defined as kh, as an expansion parameter for the perturbation expansion of the Fourier series. The expansion yields an elaborate set of expansion parameters which must be used in the expressions for the particle velocities and the details of these can be found in the above reference.

As the governing equations of this theory are also solved in a Lagrangian reference frame moving with the waves, the celerity of the waves is calculated using the definition of the mean uniform current. The Eularian time-averaged fluid velocity, c_E, is at any point given by

$$c_{\mathrm{E}} = C - \overline{u} \tag{3.25}$$

where $\overline{u}$ is the user-specified mean current speed and the dispersion relation relating k, h and H is presented [29] as

$$\left(\frac{k}{g}\right)^{1/2} c_{\mathrm{E}} - \frac{2\pi}{T(gk)^{1/2}} + C_0 + \left(\frac{kH}{2}\right)^2 C_2 + \left(\frac{kH}{2}\right)^4 C_4 = 0 \tag{3.26}$$

where C_0, C_2 and C_4 are coefficients which have functional dependence on kh. Equation (3.26) is highly non-linear and is again solved by iteration using the Newton-Raphson method.

With the celerity and wave number solved for using equations (3.25) and (3.26), and the wave steepness calculated by $\epsilon = kH/2$, the velocity potential in the Eularian reference frame is given as

$$\varphi = (c - \overline{u})x + C_0 \left(\frac{g}{k^3}\right)^{1/2} \sum_{i=1}^{5} \epsilon^i \sum_{j=1}^{i} A_{ij} \cosh jkz \sin jk(x - ct) \tag{3.27}$$

where the fluid velocities are obtained in the same way as for the linear theory by $u = \partial\varphi/\partial x$ and $w = \partial\varphi/\partial z$. The constants of A_{ij} are given in the referenced paper by Fenton [29].

3.1.5 Approximative three step wave-current interaction model

Since the fifth order Stokes model presented above is only applicable for waves on a uniform current, the fifth order wave modelling used in combination with the BEMT code had to incorporate a ‘three step’ approximate wave-current interaction model as developed by Dalrymple [54]; this allowed the regular fifth order model to account for wave-current interactions. This ‘three step’ model modifies the wave particle kinematics of any chosen higher order wave theory, based on an underlying arbitrary current profile.

The method works by obtaining the apparent period, T_{app}, which is the wave period an observer moving with the depth-averaged mean current velocity would see. T_{app} is then used as the input for an appropriate wave model (fifth order Stokes as used in this thesis), where after the wave kinematics are calculated and the current velocities are finally linearly superimposed to the wave induced velocities.

To calculate T_{app}, the Döppler shift equation is defined as follows

$$\frac{L}{T} = \frac{L}{T_{\text{app}}} + \bar{U} \tag{3.28}$$

where $\bar{U}$ is the depth-averaged mean current. The wave length and period are related by the first-order dispersion relationship

$$T_{\text{app}}^2 = \frac{2\pi L}{g \tanh(2\pi h/L)} \tag{3.29}$$

and the depth-mean current is approximated via linear wave theory by

$$\bar{U} = \frac{(4\pi L)}{\sinh(4\pi h/L)} \int_0^h U(z) \cosh\left(4\pi \frac{(z+h)}{L}\right) \mathrm{d}z. \tag{3.30}$$

where $U(z)$ is the arbitrary vertical current velocity profile. Equations (3.28) - (3.30) have three unknowns and are solved iteratively for T_{app} and L. With these variables known, $\bar{U}$ can then be found.

Before the current profile velocities are superimposed to the wave kinematics, the profile function is evaluated with a vertical coordinate *stretched* to the instantaneous surface in a process called Wheeler stretching. This method is detailed in the following section.

3.1.6 Inflow current profile modelling

Three types of distinct vertical inflow profiles are used in this thesis to represent the tidal flow environment. These are, ranging from simplest to most complex, uniform inflow, linear shear profile and 1/7th power-law profile.

The uniform inflow profile was, as mentioned, only used in conjunction with the irregular sea-state model due to its inability of resolving the wave-current interactions for more complex flows. The linear shear profile used in the coupled third order Stokes model is defined by the surface and bottom velocities U_{s} and U_{b} as depicted in Figure 3.2. The linear shear profile can be set to approximate the power law profile over the swept turbine area by giving it a non-zero value at the bottom, as it is nearly linear in this region, except towards the bottom where the power law profile has a lower velocity and therefore higher thrust gradient, as shown in the figure. The positioning of the turbine in the water column will also affect the inflow gradient over its area when using the power-law profile, although in this thesis' investigations the turbines are normally located at the mid-depth.

The 1/7th power-law profile is in turn generated by the standard equation [26] from the wind turbine industry

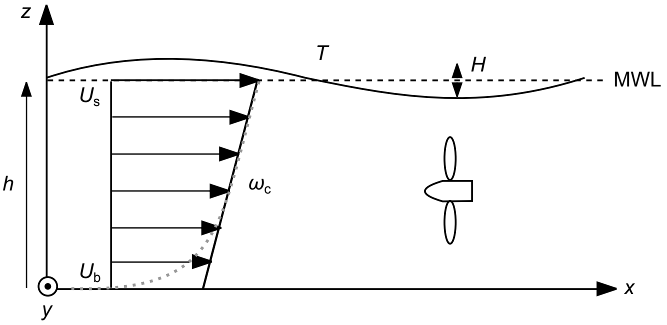

Figure 3.2: Diagram depicting inflow parameters which were given as input variables to the Kishida & Sobey wave-current theory showing the regular wave train and the coupled linear shear profile. The mimicing of the 1/7th power law over the turbine area is shown as a comparison to the dashed grey line.

$$U(z) = U_\mathrm{s} \left(\frac{z}{h}\right)^{1/7}. \tag{3.31}$$

Equation (3.31) only defines the inflow velocity correctly to the mean water level ($z = 0$), above which it is over predictive compared to observations of wave particle velocities [26]. To account for this phenomenon, a correction known as Wheeler stretching must be applied as described below.

Wheeler stretching

As the free surface is distorted by the passing wave train, the current profile must be modified in order to maintain a constant surface velocity. Wheeler stretching [55] is a method of mapping a current profile defined from the seabed to the mean water level into a profile from the seabed to the instantaneous water level. Before the current profile velocities are added to the wave kinematics, the function is evaluated with a coordinate stretched to the instantaneous water level defined as

$$z_\mathrm{c} = \frac{h(z-\eta)}{h+\eta}. \tag{3.32}$$

The method of Wheeler stretching is in this thesis used in the approximative three-step model described in Section 3.1.5.

3.1.7 Irregular sea-state wave model

Linear wave theory is used to represent the stochastic developing sea-state by superimposing a large number linear wave harmonics with a random distribution of wave parameters [90].

Using this method, the wave elevation in one dimension can be written as the sum of the displacement contributions from N number of waves, and is in this thesis defined as

$$\eta(x,t) = \sum_{i=1}^{N} a_i \cos(k_i x - \omega_i t + \varphi_i) \tag{3.33}$$

where the parameters are the amplitude a_i, wave number k_i, angular frequency, $\omega_i = 2\pi/T_i$, and random phase angle, φ_i between 0-2π for the i-th wave component. The wave number and angular frequency are again related by the dispersion relationship in Equation (3.19) and the wave amplitudes are derived using the JONSWAP [91] power spectral function, as described further down.

Similarly to the surface displacement, the linear equations for particle velocities for waves on a uniform current by Dean & Dalrymple [48] (Equations (3.17) and (3.18)) are here re-written in harmonic form as

$$u_i(x,z,t) = \frac{g a_i k_i}{\omega_i (1 - U_{0i} k_i/\omega_i) \cosh k_i h} \cosh k_i(h+z) \sin(k_i x - \omega_i t + \varphi_i) \tag{3.34}$$

$$w_i(x,z,t) = -\frac{g a_i k_i}{\omega_i (1 - U_{0i} k_i/\omega_i) \cosh k_i h} \sinh k_i(h+z) \cos(k_i x - \omega_i t + \varphi_i) \tag{3.35}$$

where the term for the current velocity U_∞ has been omitted for now, as it will be added to the equations in a later stage, and U_{0i} is the current velocity component aligned with individual wave harmonic's direction of propagation. The wave harmonic components are given a random distribution of directional spread which is described below.

Random wave directional distribution

When looking out at a developed irregular sea, it can be seen that the wave-components are not unidirectional, instead they display a large range of directional spread in two dimensions. To capture this observation of real random seas, each harmonic component is given a normally distributed random incidence angle, θ_i, between the wave orthogonal and the current flowing in the x-direction; by doing so, the wave motion is made three-dimensional. The range given to the directionality of the waves is between $\pm\pi/2$ from coflowing. A coordinate system rotated to the angle of incidence is then defined for each wave-component and equations (3.33) - (3.35) are evaluated using the x_i'-coordinate from this reference frame, which is transformed from the global reference frame by

$$x_i' = \cos(\theta_i)x + \sin(\theta_i)y \tag{3.36}$$

as is illustrated in Figure 3.3.

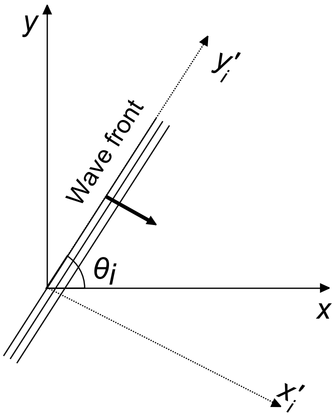

Figure 3.3: Wave-centred coordinate system transformation for each harmonic component. The vector perpendicular to the wave-front is the wave orthoganol and θ_i is the angle of wave incidence. The kinematica of the wave component velocities are evaluated using the local coordinate x_i'.

The wave induced velocities for the added wave harmonics are finally expressed in three space-dimensions and time in the global coordinate system, where the current velocity in the x-direction is now added, as

$$u(x, y, z, t) = U_\infty + \sum_{i=1}^{N} \cos(\theta_i)u_i(x_i', t) \tag{3.37}$$

$$v(x, y, z, t) = \sum_{i=1}^{N} \sin(\theta_i)u_i(x_i', t) \tag{3.38}$$

$$w(x, y, z, t) = \sum_{i=1}^{N} w_i(x_i', t) \tag{3.39}$$

The JONSWAP power density spectrum

It is not possible to assign arbitrary values of a_i and ω_i to the wave components in Equations (3.33) - (3.35), as this would allow for the creation of waves with unrealistic energy, or steepness distributions. However, a relationship between the distribution of wave heights and frequencies can be found if the instantaneous sea-surface described by the elevation in Equation (3.33) is considered as a *signal.* Since the surface elevation is composed of a superposition of sine waves, it can be represented by a Fourier series composed of sine and cosine waves with constant harmonic parameters. This assumption also holds true for real sea-states observed in the field, which can be used to determine the distribution of wave heights among the wave components based on real sea-state data.

Pierson & Moskowitch [92] performed field tests where the irregular ocean surface elevation was recorded and the discrete Fourier transfer was taken on the collected signal in order to derive the power spectral density for a natural sea-state. A function was then fitted to the spectra in the frequency domain which is known as the Pierson-Moskowitch (PM) spectrum, $S_{\mathrm{PM}}(\omega)$, where the power density in the waves is a function the wave component frequency.

The PM spectrum provides an accurate fit for sea-state power density curves created by the wind blowing over a long period of time, allowing the sea to become *fully developed*. Owing to this, Hasselmann et al. [91] modified the PM spectrum to fit data from the Joint North Sea Wave Observation Project (JONSWAP) project which was collected from the North Sea for *developing* sea-states. This allows seas that are not yet in equilibrium with the wind to be analysed. The PM spectrum is firstly defined by the standard DNV-RP-C205 [26] as

$$S_{\mathrm{PM}}(\omega) = \frac{5}{16} H_{\mathrm{s}}^2 \omega_{\mathrm{p}}^4 \omega^{-5} \exp\left(-\frac{5}{4}\left(\frac{\omega}{\omega_{\mathrm{p}}}\right)^{-4}\right) \tag{3.40}$$

where H_{s} is the significant wave height of the sea, defined as the mean of the third largest recorded wave heights and $\omega_{\mathrm{p}} = 2\pi/T_{\mathrm{p}}$ is the spectral peak angular frequency – the frequency of the highest wave energy. The JONSWAP spectrum, S_{J}, is then defined as

$$S_{\mathrm{J}}(\omega) = A_{\gamma} S_{\mathrm{PM}}(\omega) \gamma^{\exp\left(-0.5\left(\frac{\omega-\omega_{\mathrm{p}}}{\sigma\omega_{\mathrm{p}}}\right)^2\right)} \tag{3.41a}$$

$$A_{\gamma} = (1 - 0.287 \ln(\gamma)) \tag{3.41b}$$

$$\sigma = \begin{cases} 0.07, & \omega \leq \omega_p \\ 0.09, & \omega > \omega_p \end{cases} \tag{3.41c}$$

where γ is a non-dimensional peak shape parameter and σ is a spectral width parameter. It is noted that for $\gamma = 1$, the JONSWAP spectrum collapses into the PM spectrum, and in this thesis a γ value of 3.3 is adopted as recommended in DNV-RP-C205 [26]. The shape of several JONSWAP spectra can be seen in Figure 3.4 for different wind speeds.

With the JONSWAP spectrum for the irregular sea-states defined, the relationship between the wave component amplitudes and angular frequencies in Equations (3.33) - (3.35) can be found as in Faltinsen [90], expressed as

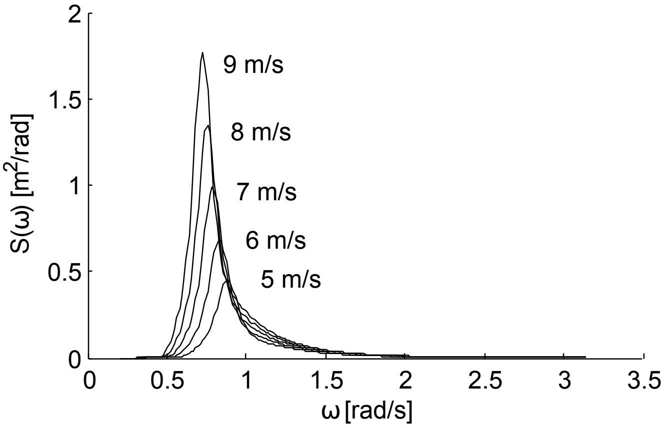

Figure 3.4: An example of 5 different power density spectra for different sea-states generated from different wind speeds. The figure illustrates the change in peak frequency, ω_p, as the wind-speed increases.

$$\frac{1}{2}a_i^2 = S_\text{J}(\omega_i)\Delta\omega. \tag{3.42}$$

Here, $\Delta\omega$ is the constant bandwidth between the N sampled frequencies from the power density spectrum used to construct the irregular sea-state.

The defining parameters H_s and ω_p used to generate the JONSWAP spectrum are in this thesis supplied through experimental wave-rider buoy from the UK Offshore Operators Association, provided by the British Oceanographic Data Centre and funded by the Institute of Oceanographic Sciences [93], in the form of time histories of the significant wave height, H_s, and average zero-crossing period, T_z. The zero-crossing period can for the JONSWAP spectrum be empirically fitted to the peak period [26] by

$$T_\text{p} = T_\text{z}/(0.6673 + 0.05037\gamma - 0.006230\gamma^2 + 0.0003341\gamma^3) \tag{3.43}$$

which is finally used as an characteristic input parameter to the irregular wave model.

3.2 Steady-state blade element momentum theory

With the inflow synthesis defined as in the previous section, it is now time to define the rotor-load BEMT model which can incorporate the given inflow variations generated by the presented flow kinematics models.

As was already mentioned, a successful numerical model for TST load evaluations must be able to incorporate the variations in inflow both spatially across the rotor-plane and temporally over several different time-scales. In addition, the time-step size of a time domain simulation must be small enough to resolve the smallest variations caused by the interference between the inflow velocities and the turbine's operation. These requirements make BEMT modelling a good candidate for early stage development and makes it an appropriate tool to inform on fundamental relationships between inflow conditions and the experienced turbine loads.

This section describes the fundamental governing equations of the BEMT method as well as the commonly adopted correction factors used to increase its accuracy for turbine applications. Later in the section the modifications done to the model to make it capable of resolving the dynamic effects caused by the varying inflow are detailed, as well as a description of the solving scheme used.

3.2.1 Governing equations of the BEMT model

To understand the derivation of, and the rationale behind, the governing BEMT equations, it is informative to look at the origins of the theory as a combination of two distinct sets of equations. These equations are the momentum theory equations for an actuator disc and the blade element equations, which are combined within the BEMT method in order to close the mathematical problem and solve for the forces. First, the derivation of the momentum equations as presented by Burton [74] will be looked at.

One dimensional momentum theory

A turbine generates power by extracting energy from the working fluid passing through the rotor area, thus slowing the fluid down. If it is assumed that the fluid affected by the rotor disc does not interact with the ambient fluid, a control volume can be defined in the form of a *stream tube* enclosing the rotor and the passing flow as in Figure 3.5. At this stage, the only interaction the turbine has with the incoming flow is to extract kinetic energy without giving any detail on how this is achieved. Therefore, the turbine's rotor can be assumed to be an *actuator disc*, which acts as a momentum sink in the control volume and, at this stage, imparts no rotational momentum to the flow.

It can be seen in Figure 3.5 that the presence of the actuator disc changes the shape of the stream tube from smaller than the rotor area, to larger than it downstream. This is because the mass flow-rate through the stream tube must be conserved, and as the flow is slowed down behind the actuator disc, the area is increased [74].

Owing to the mass conservation across the stream tube, a relationship can be set up between the areas, velocities and fluid density in the upstream, downstream and at the actuator disc region [74] as

$$\dot{m} = U_\infty A_\infty \rho = U_\mathrm{d} A_\mathrm{d} \rho = U_\mathrm{w} A_\mathrm{w} \rho \tag{3.44}$$

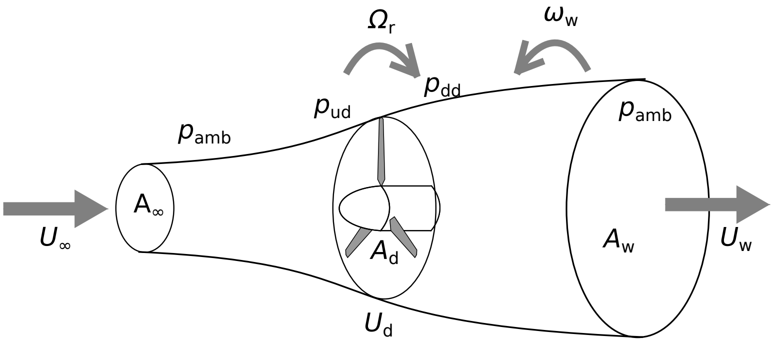

Figure 3.5: Definition of the annular stream tube control volume over the turbine and flow domain. Also shown are the various physical quantities at the different flow locations upstream, downstream and at the turbine. Note that the wake rotation is opposite to the turbine's rotation since it imparts a reactive rotational momentum to the flow.

where $\dot{m}$ is the mass flow rate, U is the fluid speed, A is the area and the corresponding subscripts stand for conditions in the far upstream (∞), at the actuator disc (d) and in the wake (w) as illustrated in Figure 3.5 and ρ is the fluid density.

It is common to define the flow velocity at the actuator disc as a function of the free-stream velocity by

$$U_\mathrm{d} = U_\infty(1 - a) \tag{3.45}$$

where the axial induction factor, a, is the fractional reduction in flow speed between the free stream and the actuator disc.

Since both the mass flow rate and fluid density across the stream tube is constant, the rate of change of fluid momentum that is imparted by the actuator disc must be caused by the total velocity change, $U_\infty - U_\mathrm{w}$. The rate of change in fluid momentum is thus given as the product of the velocity change and the mass flow rate as

$$\text{Rate of change of momentum} = (U_\infty - U_\mathrm{w})\rho A_\mathrm{d} U_\mathrm{d}. \tag{3.46}$$

Also, as any change in momentum must be caused by a force, it can be seen that the the term on the Left Hand Side (LHS) in Equation (3.46) can be substituted by the force on the disc caused by the pressure differential across it as

$$A_\mathrm{d}(p_\mathrm{ud} - p_\mathrm{dd})A_\mathrm{d} = (U_\infty - U_\mathrm{w})\rho A_\mathrm{d} U_\infty(1 - a) \tag{3.47}$$

where the velocity at the disc, U_d, has been substituted by Equation (3.45). The pressure differential can be found by applying the Bernoulli equation along the stream tube, in the upstream and downstream region separately - the equation is valid since the total energy is constant along the stream tube in the different regions upstream and downstream of the disc. The Bernoulli equation for the upstream and downstream regions, assuming that the flow is incompressible (ρ is constant) and horizontal, reduces to the equations

$$\frac{1}{2}\rho U_\infty^2 + p_{\mathrm{amb}} = \frac{1}{2}\rho U_{\mathrm{d}}^2 + p_{\mathrm{ud}} \tag{3.48a}$$

$$\frac{1}{2}\rho U_{\mathrm{d}}^2 + p_{\mathrm{dd}} = \frac{1}{2}\rho U_{\mathrm{w}}^2 + p_{\mathrm{amb}} \tag{3.48b}$$

and it is assumed that the pressures far up and down stream from the rotor are ambient, p_{amb}. The pressure gradient is given by subtracting the above equations as

$$A_{\mathrm{d}}(p_{\mathrm{ud}} - p_{\mathrm{dd}}) = \frac{1}{2}\rho(U_\infty^2 - U_{\mathrm{w}}^2) \tag{3.49}$$

and insertion into Equation (3.47) gives

$$\frac{1}{2}\rho(U_\infty^2 - U_{\mathrm{w}}^2)A_{\mathrm{d}} = (U_\infty - U_{\mathrm{w}})\rho A_{\mathrm{d}} U_\infty (1-a) \tag{3.50}$$

and from this equation it is shown that

$$U_{\mathrm{w}} = (1-2a)U_\infty \tag{3.51}$$

and the force on the fluid from Equation (3.47) in combination with Equation (3.51) becomes

$$F = (p_{\mathrm{ud}} - p_{\mathrm{dd}})A_{\mathrm{d}} = 2\rho A_{\mathrm{d}} U_\infty^2 a(1-a). \tag{3.52}$$

Inclusion of rotational momentum

In order to derive an expression for the turbine torque, the previous analysis can be extended to the case where the rotor imparts angular momentum to the flow as presented by Masters & Orme [75].

Since the torque exerted on the rotor by the fluid is dependent on the local turbine radius, r, the analysis is performed by dividing up the stream tube into several annular sections with thickness $\mathrm{d}r$, each having a cross sectional area of $2\pi r \mathrm{d}r$ as illustrated in Figure 3.6.

If it is assumed that the angular velocity ω_{w} imparted on the flow is small compared to the turbine angular velocity, Ω_{r}, it can be assumed that the pressure in the far wake is the same as the pressure in the free stream [94].

The inclusion of the wake rotation involves the analysis of an annular control volume rotating with the turbine's angular velocity Ω_{r}. This allows the Bernoulli

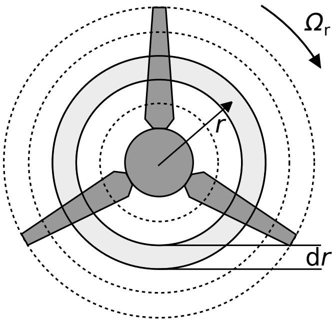

Figure 3.6: The control stream tube of Figure 3.5 is divided into annular sections with thickness dr. The annular sections are assumed to be fully independent of each other, with no flow going between them in the radial direction.

energy equation to be used in the sections before and after the actuator disc, giving the pressure difference across it while assuming the axial flow across the disc is constant [72] as

$$p_{\mathrm{ud}} - p_{\mathrm{dd}} = \rho\left(\Omega_{\mathrm{r}} + \frac{1}{2}\omega_{\mathrm{w}}\right) r^2\omega_{\mathrm{w}}. \tag{3.53}$$

The resulting thrust across an annular element is then the pressure difference multiplied by the annular area as

$$\mathrm{d}F_{\mathrm{A1}} = \left(\rho\left(\Omega_{\mathrm{r}} + \frac{1}{2}\omega_{\mathrm{w}}\right) r^2\omega_{\mathrm{w}}\right) 2\pi r \mathrm{d}r \tag{3.54}$$

and the angular induction factor, b, is then defined as

$$b = \frac{\omega_{\mathrm{w}}}{2\Omega_{\mathrm{r}}}. \tag{3.55}$$

The annular thrust of Equation (3.54) can now be rewritten in terms of b to give

$$\mathrm{d}F_{\mathrm{A1}} = (4b(1-b)\frac{1}{2}\rho\Omega_{\mathrm{r}}^2 r^2)2\pi r \mathrm{d}r. \tag{3.56}$$

Since the wake rotation has now been included in the analysis, an expression for the torque on an annular stream tube section, dT – which equals the change in angular momentum in the wake – can be written as

$$\mathrm{d}T = \mathrm{d}\dot{m}(\omega_{\mathrm{w}} r)r = \rho U_{\mathrm{d}} 2\pi r \mathrm{d}r(\omega_{\mathrm{w}} r)r \tag{3.57}$$

Finally, using Equation (3.57) in combination with Equations (3.45) and (3.55) gives an expression for annular torque expressed in terms of the free stream flow as

$$\mathrm{d}T_1 = 4\pi\rho b(1-a)U_\infty\Omega_{\mathrm{r}} r^2 r \mathrm{d}r. \tag{3.58}$$

Furthermore, since the rotation of the turbine imparts an angular velocity component to the flow, the kinetic energy in the wake is increased [74]; this increase in wake energy is balanced by a loss of static pressure in the wake equal to $\Delta p = 0.5\rho(2\Omega_{\mathrm{r}}br)^2$ which is the dynamic pressure just downstream of the actuator disc where the tangential velocity is assumed to be twice as large as at the rotor. When this pressure drop is multiplied by the annular area of $2\pi r\mathrm{d}r$ to yield the induced force, and added to the thrust in Equation (3.52). The expression for the thrust in Equation (3.52) is now expressed as the thrust on an annular ring as Equation (3.59) by multiplication of $2\pi r$ and inclusion of the pressure differential. the final expression for the thrust on the fluid is given as

$$\mathrm{d}F_{\mathrm{A1}} = 4\pi\rho\left(U_\infty^2 a(1-a) + (b\Omega_{\mathrm{r}}r)^2\right) r\mathrm{d}r. \tag{3.59}$$

Although momentum theory gives the expressions for the thrust and torque on the fluid imparted from a turbine, an issue remains that the axial and angular induction factors, a and b, in Equations (3.58) and (3.59) are not known a priori but vary depending on the turbine's design and operation. Thus, momentum theory must be combined with blade element theory in order to close the set of equations and allow the forces to be calculated.

Blade element theory

Blade element theory works on a principle of dividing the rotor's blades into several equally sized *elements* that intersect with the stream tubes defined in Figure 3.6. The lift and drag forces on the blade elements are then solved for, treating the elements as two-dimensional airfoil sections that are independent from each other. The calculations are performed via the use of external look-up tables of 2-D airfoil data and the geometric turbine parameters such as local twist and chord distributions at the blade radius for each section.

Figure 3.7a shows the relative inflow velocity vectors on a blade section as they were defined by the momentum theory. The resultant flow vector, V, is the resultant vector composed of the induced axial inflow velocity $U_\infty(1-a)$ and the induced angular inflow velocity $\Omega_{\mathrm{r}}r(1+b)$. The angle between V and the chord line of the blade element is the angle of attack, α, which is determined by the resultant velocity's angle of incidence, φ, the blade root pitch, θ_{pitch} and the local blade twist at that particular blade section, $\theta_{\mathrm{sect.}}$. The angles are all measured from the plane of rotation and the angle of attack becomes

$$\alpha = \varphi - (\theta_{\mathrm{sect.}} + \theta_{\mathrm{pitch}}) \tag{3.60}$$

which influences the performance of the 2-D airfoil section, thus determining the magnitude of the lift and drag forces.

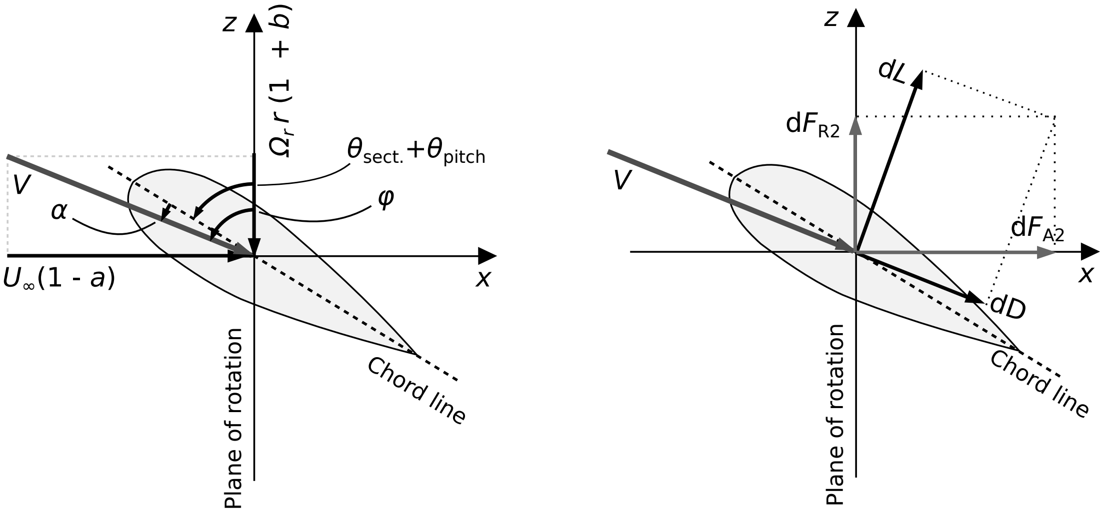

(a) (b)

Figure 3.7: Diagrams of inflow velocity vectors (a) and induced blade-forces (b) on a blade section as viewed from the blade tip towards the hub. The inflow U_∞ is originating from the left and the rotational plane is perpendicular to the paper.

From the elemental lift and drag forces, dL and dD, shown in Figure 3.7b it is possible to determine the elemental loads on the rotor by creating the resultant forces that are in plane, and perpendicular to, the plane of rotation. Since the drag force is always parallel to the resultant inflow vector V, and the lift force is always perpendicular to it, the elemental axial force (thrust) and the elemental radial force (which becomes torque by multiplication with r) can be calculated using φ through

$$\mathrm{d}F_{\mathrm{A2}} = \mathrm{d}L\cos\varphi + \mathrm{d}D\sin\varphi \tag{3.61a}$$

$$\mathrm{d}F_{\mathrm{R2}} = \mathrm{d}L\sin\varphi - \mathrm{d}D\cos\varphi \tag{3.61b}$$

where φ is determined through the Pythagorean theorem from Figure 3.7a as

$$\varphi = \tan^{-1}\left(\frac{U_\infty(1 - a)}{\Omega_{\mathrm{r}} r(1 + b)}\right) \tag{3.62}$$

and the resultant flow vector, V, becomes

$$V = \sqrt{(U_\infty(1 - a))^2 + (\Omega_{\mathrm{r}} r(1 + b))^2} \tag{3.63}$$

Now, the elemental thrust and torque contributions to the rotor loads, dF_{A2} and

$\mathrm{d}T_2$, can be defined through the use of Equations (3.61a) and (3.61b) as

$$\mathrm{d}F_{\mathrm{A2}} = N\frac{1}{2}\rho V^2 c(C_{\mathrm{L}}\cos\varphi + C_{\mathrm{D}}\sin\varphi)\mathrm{d}r \tag{3.64a}$$

$$\mathrm{d}T_2 = N\frac{1}{2}\rho V^2 c(C_{\mathrm{L}}\sin\varphi - C_{\mathrm{D}}\cos\varphi)r\mathrm{d}r \tag{3.64b}$$

where C_{L} and C_{D} are the lift and drag coefficients for the airfoil sections for the specific α at the blade section, N is the number of blades of the turbine and c is the blade section chord length.

The traditional approach to solve the set of equations derived from momentum theory and blade element theory is to set the two thrust expressions, Equation (3.59) and Equation (3.64a) equal as well as equating the elemental torque expressions, Equation (3.58) and Equation (3.64b); the solution is then found through iteration of a and b until a convergence criterion is met. The elemental forces for each blade are then added to give the total thrust and torque acting on the rotor.

However, the model presented in this thesis goes about solving the set of force equations in an alternative way, by the use of error minimisation through an optimisation routine as presented by Masters & Orme [75] and Chapman [36] in an effort to increase its robustness and modifiability. This solution method is expanded upon in Section 3.3.4.

3.2.2 Correction factors for steady-state BEMT

Several assumptions are made in BEMT in order to simplify the complex interactions between rotating machinery and the working fluid. A major assumption is that the turbine operates in a non-turbulent, steady-state environment in order to allow the force equations of the blade and the fluid to be equated [73]. As was seen in the previous section, the blade sections are assumed to be independent of each other, meaning that it is assumed that there is no flow interactions between the elements, or equally, that there is no radial flow over the blades.

As the strength of BEMT is it's simplicity and low computational cost, it inevitably has its theoretical limits of operation. One of these limitations are that at high TSRs, the axial induction factor a can exceed its upper theoretical limit of 0.5, implying that the flow downstream of the rotor is reversed. In reality, the downstream flow is at these TSR regions slowed down and fluid is drawn from outside of the stream tube, causing the flow to become turbulent which is known as the turbulent wake state [5].

Presented below are the commonly used correction factors that address the errors and inconsistencies in the BEMT equations derived in the previous sections.

Prandtl tip-loss correction factor

The assumption that there is no radial flow over the blades of the turbine is violated close to the blade tips due to the fact that the pressure difference between the pressure and suction side of the blades creates a radial flow over the blade tips. This in turn gives rise to tip vortices which decrease the performance close to the blade tips and corrections must be added to account for the turbine's efficiency loss in BEMT.

The Prandtl tip loss correction factor is a function that tends to zero at the blade tips and to one the closer one gets to the root [95]. The factor is defined as

$$F_{\text{tip}} = \frac{2}{\pi} \cos^{-1} \left(\exp \left[-\frac{N}{2} \frac{(1 - (r/R))}{(r/R) \sin \varphi} \right] \right) \tag{3.65}$$

where R is the rotor radius. A hub loss correction factor may also be added in a similar manner as suggested by Moriarty [71] as

$$F_{\text{hub}} = \frac{2}{\pi} \cos^{-1} \left(\exp \left[-\frac{N}{2} \frac{(r - R_{\text{hub}})}{r \sin \varphi} \right] \right). \tag{3.66}$$

where R_{hub} is the radius of the turbine hub. The total loss factor is then defined as the product of Equations (3.65) and (3.66)

$$F = F_{\text{tip}} F_{\text{hub}} \tag{3.67}$$

which is included in the momentum equations for thrust and torque, Equation (3.58) and Equation (3.59), to give

$$\mathrm{d}T_1 = 4\pi\rho F b(1 - a) U_\infty \Omega_{\mathrm{r}} r^2 r \mathrm{d}r \tag{3.68a}$$

$$\mathrm{d}F_{\mathrm{A1}} = 4\pi\rho F \left(U_\infty^2 a(1 - a) + (b\Omega_{\mathrm{r}} r)^2 \right) r \mathrm{d}r. \tag{3.68b}$$

Spera high induction correction factor

As the turbine enters its turbulent wake state during high axial induction factors, usually experienced at high TSRs, the original BEMT theory will underpredict the thrust on the rotor. This can be corrected for by letting the code switch to an empirical formulation of the axial induction factor at large a-values that is derived from experimental turbine data.

A frequently used method to correct for the thrust under-prediction in the turbulent wake state is the Spera high induction correction as discussed in Shen et al. [95], where the critical induction factor a_{c} is tuned between 0.2 and 0.3 to give the best results. The local thrust coefficient of the blade element, C_{FA}, is defined based on a criterion of the element's axial induction factor

$$C_{\mathrm{FA}} = \begin{cases} 4a(1-a)F, & \text{if } a \leq a_{\mathrm{c}}; \\ 4(a_{\mathrm{c}}^2 + (1-2a_{\mathrm{c}})a)F, & \text{if } a > a_{\mathrm{c}}; \end{cases} \tag{3.69}$$

and if the axial induction factor exceeds the limit, an empirical value is given to it defined as

$$a = \frac{1}{2}\left[2 + K(1-2a_{\mathrm{c}}) - \sqrt{(K(1-2a_{\mathrm{c}})+2)^2 + 4Ka_{\mathrm{c}}^2 - 1}\right] \tag{3.70}$$

where K is expressed in Equation (3.71) using the local blade solidity, $\sigma = Nc/2\pi r$, as

$$K = \frac{4F\sin^2\varphi}{\sigma C_{\mathrm{L}}\cos\varphi + C_{\mathrm{D}}\sin\varphi}. \tag{3.71}$$

Glauert high induction factor correction

Another widely used empirical method of high induction correction that has been included as an option for the presented BEMT model is the high induction correction factor by Glauert [73], expressed as

$$a = \frac{1}{F}[0.143 + \sqrt{0.0203 - 0.6427(0.889 - C_{\mathrm{FA}})}] \tag{3.72}$$

where the local thrust coefficient C_{FA} is this time around defined as

$$C_{\mathrm{FA}} = \frac{Nc}{2\pi r\sin^2\varphi}(1-a)^2(C_{\mathrm{L}}\cos\varphi + C_{\mathrm{D}}\sin\varphi). \tag{3.73}$$

The Glauert correction is employed for cases when a >0.4 or equivalently for C_{FA} >0.96.

Buhl high induction factor correction

When the two high induction corrections described above are used in combination with the Prandtl tip and hub loss factors, a numerical inconsistency arises as illustrated in Figure 3.8. The figure shows the thrust coefficient, C_{FA}, for a single blade element plotted against the axial induction factor, a. It can be seen that a discontinuity arises at the critical a-value of 0.4 for the empirical Glauert high induction formulation when an arbitrary Prandtl loss factor of 0.7 is present. It can also be seen that the Spera formulation under predicts the thrust coefficient in the turbulent state ($a > 0.4$).

Buhl [97] addressed the issue that the Spera and Glauert high induction corrections do not incorporate the Prandtl loss factor by fitting a parabolic curve to the highly

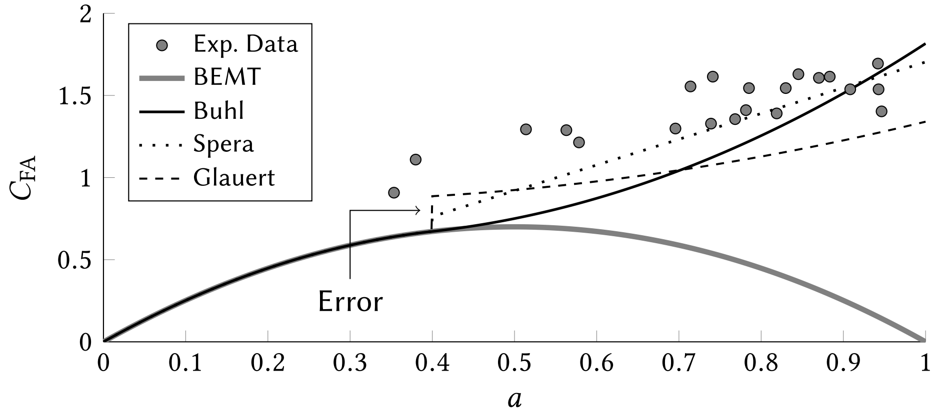

Figure 3.8: Local element thrust coefficient, C_{FA}, for various empirical models plotted against axial induction factor with Prandtl tip-loss factor $F = 0.7$. The discrepancy between the Glauert and Spera models to the standard BEMT thrust coefficient shown with the 'error' marker compared with the experimental high induction turbine thrust data from Glauert [96].

loaded experimental turbine data shown in Figure 3.8. This curve is constrained to be tangent with the BEMT C_{FA}-curve regardless of the value of the Prandtl loss factor. The value that the function reaches at $a = 1$ can be specified through the variable C_{FA1} and is set to 1.816 in this model as suggested by Burton [74]. When using the Buhl correction, the thrust coefficient for a blade element with an a value greater than 0.4 is given by the equation

$$C_{\text{FA}} = \frac{4C_{\text{FA1}}}{9} + \left(4F - \frac{20C_{\text{FA1}}}{9}\right)a + \left(\frac{25C_{\text{FA1}}}{9} - 4F\right)a^2. \tag{3.74}$$

and it is this formulation of the high induction correction that is used as the default method of modelling the turbulent wake state of turbines in this thesis.

Viterna-Corrigan post stall modelling of lift and drag coefficients

Fixed-pitch rotors will have their blades operating in the full range of boundary layer regimes for the airfoils which are classified as the 'attached', the 'high lift' and the 'stall' regions of the lift and drag curves. It is therefore important to know the details of the lift and drag behaviour of the airfoils in the high lift and stall regime to allow the loads on turbines operating in these conditions to be replicated; these types of post-stall loading behaviours may otherwise not be captured when using 2-D blade section data in the BEMT model.

An empirical model has been developed by Viterna & Corrigan, and discussed in Spera [98], that modifies experimental or numerical 2-D airfoil lift and drag data in the high lift/post-stall boundary layer regimes to more accurately capture the airfoil behaviour observed for stalling turbines. The model is based on the main assumptions that in the attached regime, 2-D lift and drag airfoil data will adequately represent the behaviour of the turbine's blades and that in the stall-development regime, the torque on the blade element does not decrease with increasing AoA. When the blade element enters the fully stalled regime, the model assumes that the blade acts as a three dimensional flat plate with the dominant parameter being the maximum drag coefficient, $C_{\mathrm{D,max}}$, which will occur at 90° AoA. The maximum drag coefficient is in turn dependent on the aspect ratio of the blade, defined as μ = (Blade length)^2/Blade area.

The equations for the Viterna-Corrigan post stall model for a blade element with an angle of attack greater than its pre-defined stall angle, α_{s}, are given as

$$C_{\mathrm{L}} = \frac{C_{\mathrm{D,max}}}{2} \sin 2\alpha + K_{\mathrm{L}} \frac{\cos^2 \alpha}{\sin \alpha} \tag{3.75a}$$

$$C_{\mathrm{D}} = C_{\mathrm{D,max}} \sin^2 \alpha + K_{\mathrm{D}} \cos \alpha \tag{3.75b}$$

$$K_{\mathrm{L}} = (C_{\mathrm{L,S}} - C_{\mathrm{D,max}} \sin \alpha_{\mathrm{s}} \cos \alpha_{\mathrm{s}}) \frac{\sin \alpha_{\mathrm{s}}}{\cos^2 \alpha_{\mathrm{s}}} \tag{3.75c}$$

$$K_{\mathrm{D}} = \frac{C_{\mathrm{D,S}} - C_{\mathrm{D,max}} \sin^2 \alpha_{\mathrm{s}}}{\cos^2 \alpha_{\mathrm{s}}} \tag{3.75d}$$

$$C_{\mathrm{D,max}} = \begin{cases} 1.11 + 0.018\mu, & \text{if } \mu \leq 50; \\ 2.01, & \text{if } \mu > 50; \end{cases} \tag{3.75e}$$

where $C_{\mathrm{L,S}}$ and $C_{\mathrm{D,S}}$ are the lift and drag coefficients at the stall angle. The Viterna-Corrigan model allows for turbines operating in the low TSR region to be accurately modelled, where the blade-roots tend to stall due to the low contribution of the induced rotational vector, as seen in Figure 3.7a, resulting in high α values in those blade sections.

3.3 Unsteady blade element momentum theory

The standard BEMT formulation described in the previous section is limited to turbines in steady-state operation with uniform inflow conditions. This is due to the numerous assumptions and simplifications made on the complex interactions between the rotor and working fluid, one of which being the assumption that the momentum exchange for a blade section is averaged over a whole stream tube. This is equivalent of the turbine having an infinite number of infinitely thin blades. As such, the original BEMT formulation is unfit for use in dynamic TST load calculations and it must be modified to be unsteady as will be detailed in this section.

Firstly, this section details the measures taken to enable the BEMT method to incorporate a *finite* number of rotating blades in a turbine that were allowed to rotate through the water column. This requires the stream tubes across the rotor-plane to be discretised into smaller stream lines which can resolve the inflow velocity distribution and subsequently the thrust gradient over the rotor. The unsteady model thus builds upon the architecture of the steady model with the addition of a time-stepping scheme.

Further, as the inflow does not only vary across the rotor spatially but also over time, the effect of the dynamic wake must be modelled to take into account the force enlargements it generates on a turbine. Also, as the inflow is now allowed to accelerate due to the wave motions, the effect of the added inertial forces on the blades must be incorporated in the unsteady BEMT model and the method is shown. Finally, this section details the alternative solving-scheme used for both the steady-state and unsteady BEMT models as presented by Masters & Orme and Chapman [36, 75].

Here follows the detailed descriptions of the modifications of the steady state BEMT model made, starting with the incorporation of the finite number of rotating blades.

3.3.1 Three dimensional inflow mapping

Figure 3.9 shows the definition of the three-dimensional spatial locations of the 2-D blade sections for a turbine, which are used here to illustrate the effect of blade rotation in the BEMT model. As previously mentioned, the unsteady BEMT model represents each blade section by a single-point blade element with coordinates (x, y, z) in the global coordinate system, C1, which are rotated for each time-step. These global elemental coordinates are used as the space coordinate inputs for the selected inflow model and the global inflow velocities are thus calculated at each blade element position.

Since the blade elements are now given an instantaneous angle relative to the incoming vertical component of the inflow, in the form of the blade's azimuth angle $\phi_{\mathrm{B}i}$, the relative inflow velocity components over the blade section that are along the radial direction, $w_{\mathrm{B}i}$, and rotational direction, $v_{\mathrm{B}i}$, of the blade must be defined respectively as only the former will affect the inflow vector V. For example, a blade with zero azimuth, aligned vertically, will have the global vertical wave-induced velocity component aligned with its radial direction, $z_{\mathrm{B}i}$, meaning that this vertical velocity component will not affect the flow over the two dimensional blade sections as defined by the BEMT formulation. This implementation of the vertical inflow velocity as a function of the blade azimuth is an original contribution of this thesis and is expanded below.

To capture this effect of angular dependency of the blades in the unsteady BEMT model, the inflow velocities over the blade elements are evaluated in the blade-fixed coordinate systems for each blade, named CBi, where $i = 1, 2, 3 \ldots N$ designate the

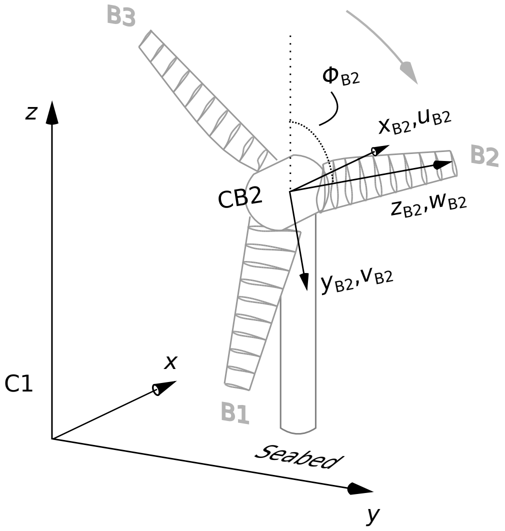

Figure 3.9: Definition of the global stationary, bottom fixed coordinate system, C1, and an example of the local rotating blade coordinate system (CB2) for blade number 2 (B2). The blade coordinate systems are defined to be oriented to the global coordinate system when ϕ_{Bi} is zero.

number of blades on the turbine. These rotating coordinate systems have their x-axes aligned with the global x-axis while the z-axes are aligned with each blade's radial direction and the y-axes are defined in the direction of rotation for clockwise motion. Shown in Figure 3.9 is the local coordinate system for blade number two, B2, of a turbine given a blade azimuth angle of ϕ_{B2} which is defined as positive in the clock-wise direction viewed from upstream.

The transformation of the global inflow velocities, (u, v, w), to the rotated blade velocities, $(u_{\mathrm{B}i}, v_{\mathrm{B}i}, w_{\mathrm{B}i})$, is done through a Eularian rotation around the global x-axis using the matrix

$$R_x(\phi_{\mathrm{B}i}) = \begin{bmatrix} 1 & 0 & 0 \\ 0 & \cos\phi_{\mathrm{B}i} & -\sin\phi_{\mathrm{B}i} \\ 0 & \sin\phi_{\mathrm{B}i} & \cos\phi_{\mathrm{B}i} \end{bmatrix} \tag{3.76}$$

where the blade's azimuth angles, $\phi_{\mathrm{B}i}$, are input with a negative value as the velocities need to be rotated counter-clockwise to align with the blade-sections in Figure 3.9.

With the velocities over the blade elements defined in the local blade coordinates, the $u_{\mathrm{B}i}$ and $v_{\mathrm{B}i}$ values are used to define the modified relative inflow vectors in the local blade coordinate systems, while $w_{\mathrm{B}i}$ is discarded as it does not affect the 2-D flow over the blade sections.

Modification of governing equations

The governing equations for the unsteady BEMT model are presented as modified versions of the inflow angle (Equation (3.62)) and the resultant inflow vector (Equation (3.63)) using the blade-local inflow velocities [99] to account for the blade azimuth orientation as

$$\varphi = \tan^{-1}\left(\frac{u_{\mathrm{B}i}(1-a)}{\Omega_{\mathrm{r}} r(1+b) - v_{\mathrm{B}i}}\right) \tag{3.77}$$

$$V = \sqrt{(u_{\mathrm{B}i}(1-a))^2 + (\Omega r(1+b) - v_{\mathrm{B}i})^2} \tag{3.78}$$

where $v_{\mathrm{B}i}$ is subtracted as to be consistent with the definition of the blade-local $y_{\mathrm{B}i}$-axis in the opposite direction of of the wake rotation; a vertical wave-induced velocity aligned with the direction of the wake rotation is thus defined as a contribution to the total relative velocity.

The above equations are used to find the modified inflow velocity vector and its angle which are then used in Equations (3.68a) - (3.68b) and Equations (3.64a) - (3.64b), which are each divided by the number of blades, N, to solve for the blade forces as shown in Section 3.3.4.

3.3.2 Dynamic wake model

The methodology adopted to include dynamic inflow effects in the BEMT model was employed on a blade element level and was originally developed by Pitt & Peters and presented in Schepers & Snel [39] and GL Garrad Hassan [24, 100].

To capture the time-lag of the wake recovery due to inflow variations, the time derivative of the axial induction factor, $\dot{a}$, was calculated at each time-step using a backward difference scheme, and the momentum thrust Equation (3.68a) was given a functional dependence on $\dot{a}$. Here follows a brief derivation of the method:

The elemental thrust, $\mathrm{d}F_{\mathrm{A2}}$, on a blade element bounded by radii R_1 and R_2 in uniform axial inflow U_∞ can be re-written as

$$\mathrm{d}F_{\mathrm{A2}} = 2U_\infty a\dot{m} + U_\infty m_{\mathrm{A}}\dot{a} \tag{3.79}$$

where $\dot{m}$ is the mass flow through the intersecting fluid annulus and m_A is the apparent mass of the blade section, which describes the inertia added to the system due to the accelerating fluid surrounding the blade.

The mass flow through the annular element can be written as

$$\dot{m} = \rho U_\infty (1 - a)\mathrm{d}A \tag{3.80}$$

where $\mathrm{d}A = \pi(R_2^2 - R_1^2)$, or in the notation as used in Equation (3.64a), $\mathrm{d}A = 2\pi r \mathrm{d}r$.

For a turbine of radius R, Tuckerman [101] suggests that the apparent mass which acts on the rotor can be approximated by an enclosing fluid ellipsoid, which through the use of potential flow theory is expressed as

$$m_\mathrm{A} = 8/3\rho R^3. \tag{3.81}$$

Substituting Equations (3.80) and (3.81) into Equation (3.79) gives

$$\mathrm{d}F_\mathrm{A2} = 2a(1-a)\rho U_\infty^2 \mathrm{d}A = 2U_\infty^2 \rho a(1-a)\mathrm{d}A + \frac{8U_\infty \rho R^3}{3\rho U_\infty^2 \mathrm{d}A}\dot{a} \tag{3.82}$$

and it is recalled that the thrust on a blade element is equal to that on the stream tube so that $\mathrm{d}F_\mathrm{A2} = C_\mathrm{FA}\rho A U_\infty$ which if each term is divided by π, ρ, U_∞^2, $\mathrm{d}A$ and multiplied by 2 the new expression form of the *unsteady* thrust coefficient for an annulus can be written as

$$C_\mathrm{FA} = 4a(1-a) + \frac{16}{3\pi U_\infty}\frac{(R_2^3 - R_1^3)}{(R_2^2 - R_1^2)}\dot{a} \tag{3.83}$$

where the volume of the apparent mass was taken as that of the annular segment of the turbine.

Equation (3.83) was used to substitute the steady-state thrust coefficient in Equation (3.68b) making it into a differential equation; the solving of this equation then altered the blade forces and related them to the variation of the a and b values. The added thrust load from the dynamic wake equation was finally divided by the number of blades effectively giving each turbine blade an equal area of fluid influence in the same manner as done by Hansen [5].

It is noted that the dynamic used as outlined above does not incorporate the effect of the accelerated dissipation of the wake for flows of higher turbulence levels. In a real tidal site, the high levels of turbulence are likely to dissipate some of the pressure differences between the wake and the rotor-plane, hence decreasing the associated transient loads.

The addition of the dynamic wake equation also alters the equations in the solving scheme, where the additional force from the dynamic wake effects are added as terms in the error function used, as shown in Section 3.3.4.

3.3.3 Fluid acceleration effects

The effect of fluid acceleration forces caused by surface waves was taken into account by use of the Morison equation as presented by Buckland [43] and Chapman [36], which is expressed as the sum of the drag, F_{dr}, and inertial forces, F_{in},, on a submerged object in oscillatory flow as

$$F_{\mathrm{tot}} = F_{\mathrm{dr}} + F_{\mathrm{in}}. \tag{3.84}$$

As the drag term in Equation (3.84) is given by the BEMT solution, the inertia term from the Morison equation can simply be added to the obtained lift and drag forces to get the total load on the blade element.

The inertial force per unit length, $\mathrm{d}l$, in the wave propagation direction on a submerged body can be written as Equation (3.85), where the inertia coefficient, C_{m}, is given a dependence on the added mass coefficient, C_{A}, in Equation (3.86) for an arbitrary geometry

$$\mathrm{d}F_{\mathrm{in}} = \rho C_{\mathrm{m}} A \frac{\partial U}{\partial t} \mathrm{d}l \tag{3.85}$$

$$C_{\mathrm{m}} = 1 + C_{\mathrm{A}} = 1 + \frac{M_A}{\rho A \mathrm{d}l} \tag{3.86}$$

where A is the cross sectional area parallel to the flow and M_A is the added mass [43].

The added mass terms for a blade element in axial and tangential directions are approximated with that of a fixed pitched plate as from Theodorsen's theory [42] defined as

$$M_{\mathrm{A,axial}} = \rho\pi \left(\frac{c\sin(\theta)}{2}\right)^2 \mathrm{d}l \tag{3.87}$$

$$M_{\mathrm{A,tan}} = \rho\pi \left(\frac{c\cos(\theta)}{2}\right)^2 \mathrm{d}l \tag{3.88}$$

which are the masses of enclosing fluid cylinders with radii of half the vertical and horizontal chord components of the respective blade sections with section angle θ. Substituting Equations (3.86), (3.87) and (3.88) into Equation (3.85) gives the expressions for the inertia forces for a blade element in the axial and tangential directions as

$$\mathrm{d}F_{\mathrm{in,axial}} = \rho \left(1 + \frac{\pi((c\sin\theta)/2)^2}{A_\alpha}\right) A_\alpha \frac{\partial U_x}{\partial t} \mathrm{d}r \tag{3.89}$$

$$\mathrm{d}F_{\mathrm{in,tan}} = \rho \left(1 + \frac{\pi((c\cos\theta)/2)^2}{A_\alpha}\right) A_\alpha \frac{\partial U_y}{\partial t}\mathrm{d}r \tag{3.90}$$

where A_α is the cross sectional area of the airfoil at the blade section and the unit length $\mathrm{d}l$ is expressed as the blade element length $\mathrm{d}r$.

3.3.4 Solving scheme

The derivation of the BEMT method has yielded two expressions for torque and two expressions for thrust, each pair consisting of one equation for the force on the fluid and one for the force on the blade. The standard solution method for these equations involve equating the two expressions for thrust and torque respectively, and re-arranging them to solve for the axial and angular induction factors a and b. However, since no analytical solution exists for these non-linear quadratic equations, a numerical approach is often employed to find convergence for the unknown variables, such as a fixed-point iteration scheme [102].

A reported issue with the iterative solution methods is that they tend to struggle to find convergence in certain regions of the turbine design-space, such as for blade elements having high AoA [75]. Another issue is that the implementation of certain corrections and additions, such as the dynamic wake effect in Section 3.3.2, can prove cumbersome when the expressions for the induction factors need to be derived.

In order to increase the robustness and modularity of the presented BEMT model, an alternative solution scheme is adopted as presented by Masters & Orme [75] and Chapman [36]. This approach is based on the creation of an *error function*, g, which defines the squared cumulative error between the forces on the blades and the fluid. The values of a and b are then found by viewing the equations as a two-dimensional optimisation problem where g is minimised through an optimisation routine, using a and b as optimisation variables.

The square of the total error between the fluid forces and blade forces for one blade section can, using the standard BEMT equations (3.68a), (3.68b), (3.64a) and (3.64b) divided by the number of blades N, be written as

$$g = (dF_{\mathrm{A1}} - dF_{\mathrm{A2}})^2 + (dT_1 - dT_2)^2 \tag{3.91a}$$

$$\begin{aligned} g = {} & \left(4\pi\rho F \left(U_\infty^2 a(1-a) + (b\Omega_{\mathrm{r}} r)^2\right)\frac{1}{N} r\mathrm{d}r - N\frac{1}{2}\rho V^2 c(C_{\mathrm{L}}\cos\varphi + C_{\mathrm{D}}\sin\varphi)\frac{1}{N}\mathrm{d}r\right)^2 \\ & + \left(4\pi\rho F b(1-a)U_\infty\Omega_{\mathrm{r}} r^2\frac{1}{N} r\mathrm{d}r - N\frac{1}{2}\rho V^2 c(C_{\mathrm{L}}\sin\varphi - C_{\mathrm{D}}\cos\varphi)\frac{1}{N} r\mathrm{d}r\right)^2 \end{aligned} \tag{3.91b}$$

where a and b define the search-space of the error function g.

The minimisation of g was performed using MATLAB R2012b's built in *fmincon* function [103] which is an optimisation routine using the sequential quadratic programming method to find convergence of a and b within a pre-defined search-space. This search space is typically set to $\{-2 < a < 1.5\}$ and $\{-1 < b < 1\}$ to allow rapid convergence while still allowing for solutions where the blade elements are acting as propellers, having negative induction factors. With the induction factors known, the relative inflow vector and its angle of incidence can be found which are used in the thrust and torque equations.

To decrease the possibility that the optimisation routine converges on a local minima of the error function, the function is evaluated for several random starting conditions throughout the search-space for the first element each new time-step. The solution from this element is then passed down to the next as the starting conditions, which also aids faster convergence. This multiple function evaluation with random starting conditions is performed with MATLAB's built-in *globalsearch* routine. It is clear that the use of high-level optimisation packages does come with a computational penalty in terms of convergence speed (average 10 minutes real-time per every 2 min simulated), but this is made up for with the increased robustness and generality of the BEMT model.

Modified error function for dynamic wake formulation

To include the various additions and corrections done to the standard BEMT equations, the error function must be modified accordingly. The addition of the different high induction models that replace the standard momentum theory thrust coefficient equation, $C_\mathrm{T} = 4a(1-a)$, is done by substituting this factor in Equation (3.91b) with any of the models presented in Section 3.2.2 re-arranged as C_T factors.

As for the inclusion of the dynamic wake effect, the thrust contribution from dynamic wake effects on one blade element is calculated using the dynamic wake formulation as

$$dF_\mathrm{dyn} = \left(\frac{16}{3\pi U_\infty} \frac{(R_2^3 - R_1^3)}{(R_2^2 - R_1^2)} \dot{a} \right) U_\infty^2 \rho \pi r \mathrm{d}r \tag{3.92}$$

which is added to the standard expressions of the fluid and blade thrust in Equation (3.91b) to create the modified error function as

$$g = ((dF_\mathrm{A1} + dF_\mathrm{dyn}) - (dF_\mathrm{A2} + dF_\mathrm{dyn}))^2 + (dT_1 - dT_2)^2. \tag{3.93}$$

When the dynamic formulation is turned off in the BEMT model the term dF_dyn is simply set to zero. Again, Equation (3.93) is used to derive the values for a and b which are used with the standard of high-induction formulations of the thrust and torque equations to derive the forces.

3.4 Calculation of rotor out-of-plane bending moment

As has already been discussed, the non-uniform inflow velocities over a TST's rotor plane will produce thrust forces on the blades with differing magnitudes that will induce an out-of-plane bending moment on the rotor as a whole which is illustrated in Figure 3.10. As this is suspected to put additional stresses on the internal drivetrain components of a TST, the bending moment must be extracted from the unsteady BEMT results to be included in the drivetrain FEM model.

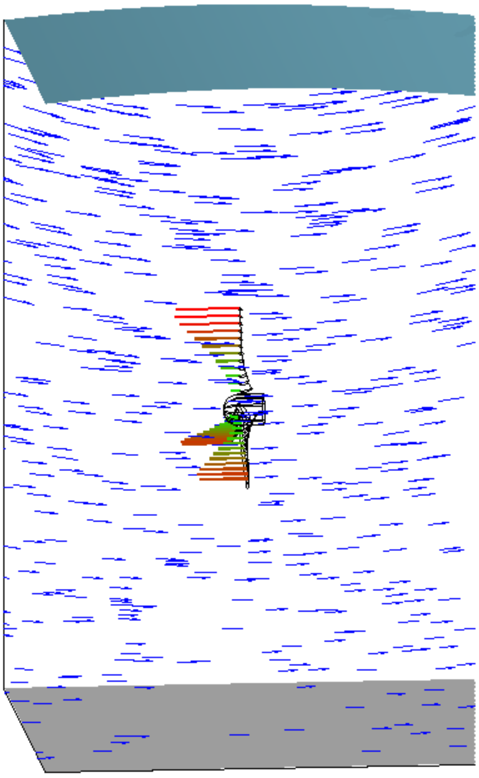

Figure 3.10: A turbine encountering the non-uniform velocity distribution from a passing wave crest experiences higher loads on the blade elements on the upper blade than on the blades in the lower positions. This ultimately leads to the generation of the rotor out-of-plane bending moment.

The method of calculating the rotor out-of-plane bending moment, M_r is to synthesize the load signal by vectorial addition of each blade's individual out-of-plane bending moment signal in the global coordinate system, M_{yi}, where the 'i' subscript again denotes the blade's number. In creating the rotor bending moment signal, the blade's bending moments are broken down to their components and re-constructed to make up the components of the rotor bending moment. An analogue to this process is shown in Section 4.3.3 where the visual representation of the rotor out-of-plane bending moment vector, the 'eccentricity vector', is derived. This vector is simply the rotor out-of-plane bending moment vector rotated 90° in the rotational-plane to show the 'direction-of-action' of the load.

3.5 Conclusions

This chapter has presented the development of a BEMT-based load model modified to be applicable for the dynamic simulations of TSTs operating in unsteady sea-conditions. The modifications done to the standard BEMT formulation include a library of unsteady inflow models, capable of resolving wave-current interactions and the incorporation of site-specific conditions, as well as the mapping of the non-uniform inflow to the rotor-plane. As the simulations are performed in the time-domain, the effects of the dynamic wake phenomenon are also included in the model.

The methodology presented here is arguably the simplest form of representing the complicated interactions between the instationary marine environment and the rotating turbine blades, while still retaining the capability to resolve the most dominant hydrodynamic loading effects. This approach conforms with the first research objective in Section 1.1.2, where the inflow and loading is resolved in high detail while still allowing fast convergence-time of 10 minutes per load case, which is needed for the fatigue calculations presented in later chapters. The inclusion of the extra degree of freedom, namely the rotor out-of-plane bending moment, in the model output will also serve to increase the fidelity in the modelling of the load propagation from the rotor to the drivetrain.

In the next chapter, the unsteady BEMT model will be used to inform the relationships between a turbine's inflow, operating and geometrical parameters to the generated loads on the rotor. This investigation can be done since the model's computational efficiency allows for the large amount of simulations to be run within a realistic time-frame. With the input-output relationships of the model known, it is possible to identify which parameters are most influential in generating the hydrodynamic load magnitudes and variations. This information will not only be of great importance to the understanding of the TST loading regime, but will also serve as guidance as to which parameters should be studied in the later chapters.

Chapter 4

Investigation of the relationships between the rotor loads and input parameters including BEMT model verification

> “ Models can also be used for sensitivity analysis — for exploring ”what if” questions — thereby illuminating which aspects of the system are most in need of further study, and where more empirical data are most needed. Thus, the primary value of models is heuristic: Models are representations, useful for guiding further study but not susceptible to proof.”
>
> — Naomi Oreskes et al., 1994

In their paper entitled ‘Verification, Validation and Confirmation of Numerical Models in the Earth Sciences’ [104] quoted above, Oreskes el al. argue that the ability of a numerical model to accurately predict a physical system, commonly referred to as verification, cannot be described with a binary ‘yes or no’ condition. Instead, it is advocated that a more continuous scale is adopted that represents the model’s probability to accurately replicate a physical system over a wide range of cases. It is only when comparing the accuracy of a model over a wide set of experimental data, while ruling out the possibilities of data-errors or other case-specific anomalies, that one can place the model’s ‘empirical adequacy’ of a scale from *good* to *bad*. For this reason, several investigations must be performed on the unsteady BEMT model presented in the previous chapter in order to assure that it has a high probability of being empirically adequate for the diverse conditions presented by the marine climate.

Despite the theoretical simplicity of the unsteady BEMT model, it is still a complex piece of software composed of several sub-routines with various input parameters and outputs. In order to determine the empirical adequacy of the model as a whole, it is good practice to verify each sub-routine individually, to as great extent as possible, to make sure each sub-routine (such as the dynamic wake model) replicates the physical data correctly. Also, in a complex model such as the BEMT code it can be hard to determine how the various input parameters are related to the output loads and how the parameters interact with each other. To address these issues, this chapter sets out to increase the confidence of the BEMT model's accuracy and to inform on the input-output relationships, as specified in the research questions, through a number of meta-studies.

As a first study presented in this chapter, the BEMT code was compared against empirical turbine load-data to ensure the accuracy of its various sub-components by verifying its steady-state, quasi-static and dynamic formulations separately in Section 4.1. The verifications were performed against empirical data on tidal and wind turbines found in literature over a wide range of inflow sources, scales and turbine set-ups to ensure that the idealisations of the BEMT model and its scalability were valid.

Secondly, this chapter presents a sensitivity analysis on the unsteady BEMT model which gave insight into the relationships between a tidal stream turbine's input parameters and the generated loads on the rotor. The parameters investigated covered variables from the separate inflow, geometric design and operational domains, as well as determining their global importance. The main role of the sensitivity analysis was to explore how a turbine's loading, and ultimately its durability, was affected by the conditions in which it operated in and how the loads propagated into the drivetrain, as was also specified in the research questions of Section 1.1.1. The secondary role of the sensitivity study was however to aid in the model's verification process as it informed on the input-output relationships of the software and identified which input parameters needed to be defined with high levels of certainty.

Later, with the dominant parameters in regards to the load generation identified through the sensitivity analysis, this chapter presents a detailed investigation on how these parameters influenced the eccentric out-of-plane bending moment loads on the rotor. As the eccentric rotor bending moments were suspected to play a major role in the contribution of load transfer into the drivetrain components, the detailed study of the parameters relation to these loads gave insight into how the they influenced the dynamics of the rotor loading, shaft loading and ultimately the turbine durability which was later studied in detail in Chapter 6.

At last, an investigation is presented on how the kinematics of the wave motions and the rotation of a turbine's blades interact to create the highly varying load patterns that were observed in the detailed parameter investigation.

However, before any of the more detailed studies can be presented with confidence, the following section will show the verification of the BEMT model to increase the validity of the results presented in later chapters.

4.1 BEMT Model verification

The experimental data used for the verification of the BEMT model was taken from a variety of peer-reviewed sources found in literature ranging from small scale tow and flume tests for TSTs to full scale wind turbine load data. The verification campaign is presented using data-sets with increasingly complex physical phenomena present, starting with steady-state operation and uniform inflow for small-scale TSTs, continuing with transient operation of a large scale wind turbine with uniform inflow, and finally showing the results for small scale TSTs operating in unsteady wave conditions generating non-uniform inflow. All data-sets used were shown to have displayed a high levels of statistical accuracy in the results, thus increasing the confidence in the numerical model.

The steady-state BEMT verification was performed by replicating several C_P and C_T-curves plotted against the TSR for small scale TSTs in flume and tow-tank tests. The main difference between experimental data derived from flume and tow-tank tests is that the latter generates zero ambient turbulence. This phenomenon was represented in the modelling through the derivation of the lift and drag characteristics for the various airfoils using XFOIL. The set-ups and turbine characteristics for all tests presented are shown in Table 4.1 and all cases were simulated using Buhl high induction correction, Prandtl tip and hub losses and Viterna-Corrigan post stall modelling.

The verification of the unsteady formulation of the BEMT code was performed by investigating the performance of the dynamic wake formulation and the wave-current inflow sub-routines separately. In both cases, empirical time-series data of the turbine loads, both on the shaft and individual blades, were replicated with the appropriate sub-routines activated and inactivated for comparison.

4.1.1 Steady-state results

The verification of the steady state BEMT formulation was performed against tow-tank experimental data from scale-model TST tests presented by Doman et al. [105] and Galloway [21] and cavitation tunnel tests by Batten et al. [15]. Flume test data

Table 4.1: Experimental parameters for the cases used in the BEMT model verification campaign divided into steady and unsteady operation. The blade pitch settings, θ, were in some cases estimated from vague descriptions in the presented literature and the values giving the most consistent results were selected.

Steady Data	Rotor Ø[m]	Blade profile	Blade θ [°]	U_∞ [m/s]	Ω_r [rad/s]
Doman et al. [105]	0.762	NRELs814	1.75	0.8	5.2-14.6
Batten et al. [15]	0.8	NACA638-xx	5	1.54	6.1-37.3
Pinon et al. [106]	0.7	NACA63418	2	0.8	0.02-22.3
Gaurier et al. [22]	0.9	NACA63418	-3	0.6	0.01-11.6
Galloway [21]	0.8	NACA48xx	0	0.9	6.7-18
Unsteady Data					
Øye [37]	61	NACA4418	0.07-3.72	8.7	2.29
Snel & Schepers [41]	1.2	NACA0012	2	4.9-5.7	75.39
Gaurier et al. [22]	0.9	NACA63418	-3	0.67	5.34
Barltrop et al. [99]	0.35	NRELs814	5	0.3-1	20.94

presented by Pinon et al. [106] and Gaurier [22] were also used in the verification and the comparisons of all the experimental data to the numerical results are presented in Figure 4.1. Here it can be seen that the code adequately predicts the thrust and torque on a TST operating in steady-state conditions and that the C_P is generally replicated better than the C_T. A possible reason for this is that the lift forces on the blades, contributing to the torque and thus the C_P, are better predicted in the external Xfoil package, which is discussed in Section 7.3.

For the majority of the verification runs presented below, Xfoil predictions were used to derive the lift and drag characteristics of the airfoils used. The only exception to this is in the Doman et al. verification case where experimental flume data collected by Togneri & Masters [107] was used instead, as it gave favourable results for this low Reynolds number case.

The blade pitch settings reported in the literature for the experiments were sometimes vague, with descriptions such as ‘close to optimum’ or ‘approximately zero’ being common. For this reason, the blade pitch settings have been estimated to reasonable values in the numerical set-up that gave favourable results over the widest range of data for each case as presented in Table 4.1.

As can be seen in Figure 4.1, the code reproduces the results well overall for most cases especially in the peak power region of the turbines. It is also observed that the C_P-curves are reproduced more accurately than the C_T-curves. One explanation to this is related to the blade-section performance data supplied being produced by potential flow models or small scale experiments. Since the viscous effects that account for some of the drag forces are harder to replicate than the lift forces, inaccuracies may be transmitted to the thrust force on the turbine since this force is primarily composed of the drag of the blades.

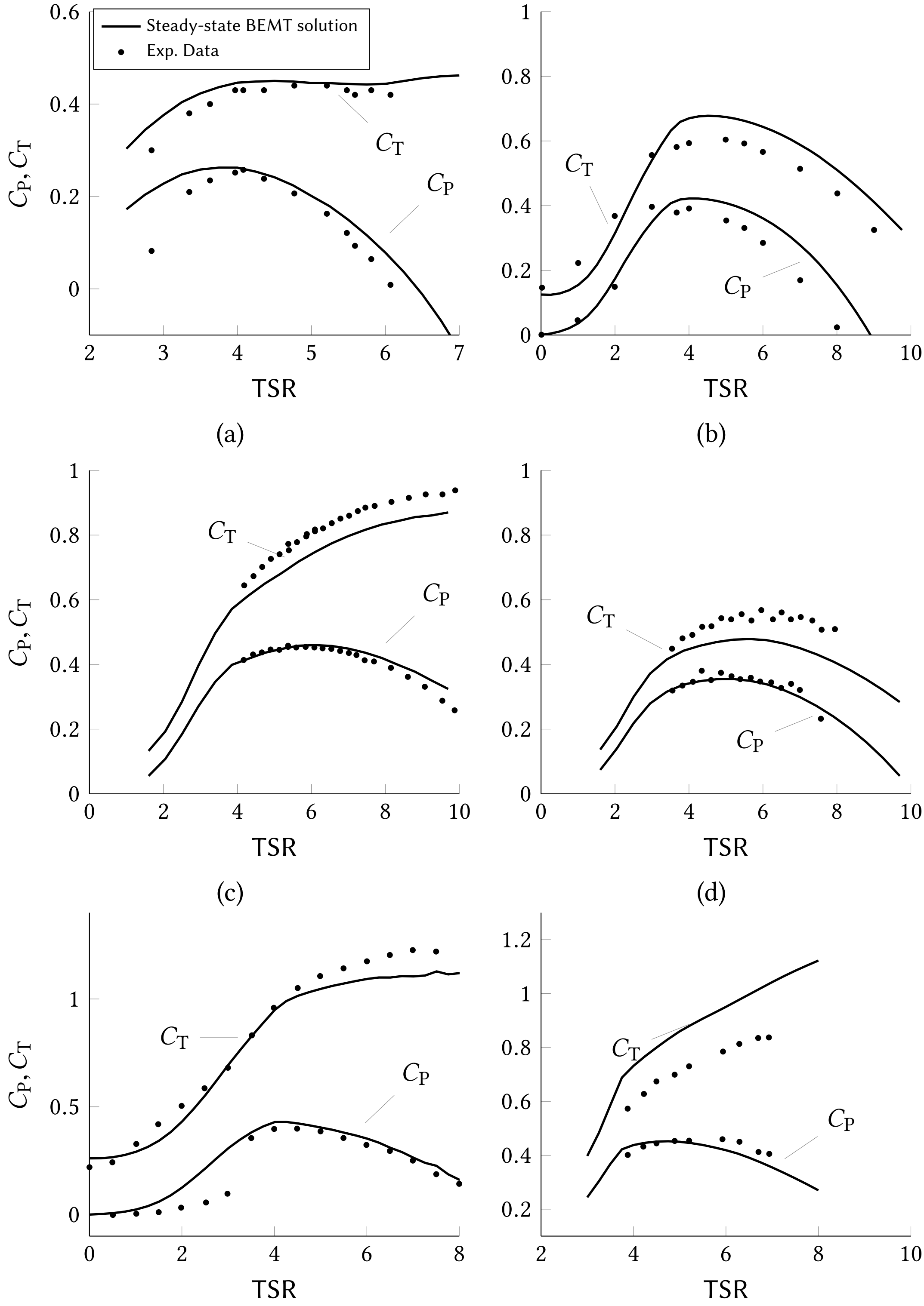

(a) (b)

(c) (d)

(e) (f)

Figure 4.1: Numerical replication of the steady-state C_P and C_T data from the small scale TST experiments. The plots shown are from the Doman et al.[105] case (a), Pinon et al. [106] case (b), Batten et al. [15] case with $\theta = 0°$ (c), Batten et al. [15] case with $\theta = 5°$ (d), the Gaurier et al. et al. [22] case (e) and the Galloway [21] case (f).

4.1.2 Unsteady results

The verification of the dynamic wake model was conducted against two sets of transient wind turbine data. The first set was the pitching-manoeuvre load-response case for the Tjæreborg wind turbine presented in Øye [38] where the blades were pitched from 0.1 to 3.7° and back again during operation in 8.7m/s winds with a recovery time for the wake to settle in between pitching events. The second data set was from a small scale wind turbine operating in a wind tunnel where it was subjected to a step-change in its inflow velocity presented by Snel et al. The experimental data of the dynamic wake phenomenon and numerical replication results for these cases are shown in Figures 4.2a - 4.2b for the Øye [37] case and Figures 4.2c - 4.2d for the Snel et al. [41] case. The figures show the numerical results with the dynamic wake formulation activated along with the results from the equilibrium wake formulation shown in the same plots for comparison.

As shown, the dynamic wake model greatly increases the ability of the code to replicate the full-scale transient load-enlargement phenomena in Figures 4.2a and Figure 4.2b, although this is less prevalent for the small-scale results in Figures 4.2c and Figures 4.2c.

The third data set used for the verification of the unsteady BEMT model was from the Gaurier [22] tidal turbine flume tank test. Here, all the modifications done to the BEMT scheme to include the effects of non-uniform inflow and unsteadiness are included as presented in Chapter 3. The dynamic wake model and steady-state BEMT's performances were again compared in Figure 4.3 by plotting both solutions on the same graphs. The Gaurier model turbine was subjected to a inflow of 0.67m/s and incident regular waves, where the wave height and frequencies were varied between the different cases as described in Figure 4.3. As can be seen in the figures, the dynamic wake formulation creates a better fit on the amplitude of the load signal for most cases by 'holding' the load at a higher level in the local minima, which is a result of the pressure gradients between the rotor and the wake.

Finally, the fourth set of data the unsteady BEMT model was verified against was from the Barltrop (2007) experiment as presented in Figure 4.4. As with the Gaurier experiment, the 0.35m diameter Barltrop turbine was subject to regular waves with differing height and wave periods between the cases shown in the plots. The pitch angle was assumed to be 7° and the numerical results have been shifted by $-0.1140\,\mathrm{N\,m}$ for the M_y data and $-0.4525\,\mathrm{N\,m}$ for the M_x data to compensate for a reported 'calibration datum'. Once again, the results from BEMT model are shown with and without the inclusion of the dynamic wake formulation in the plots for comparison.

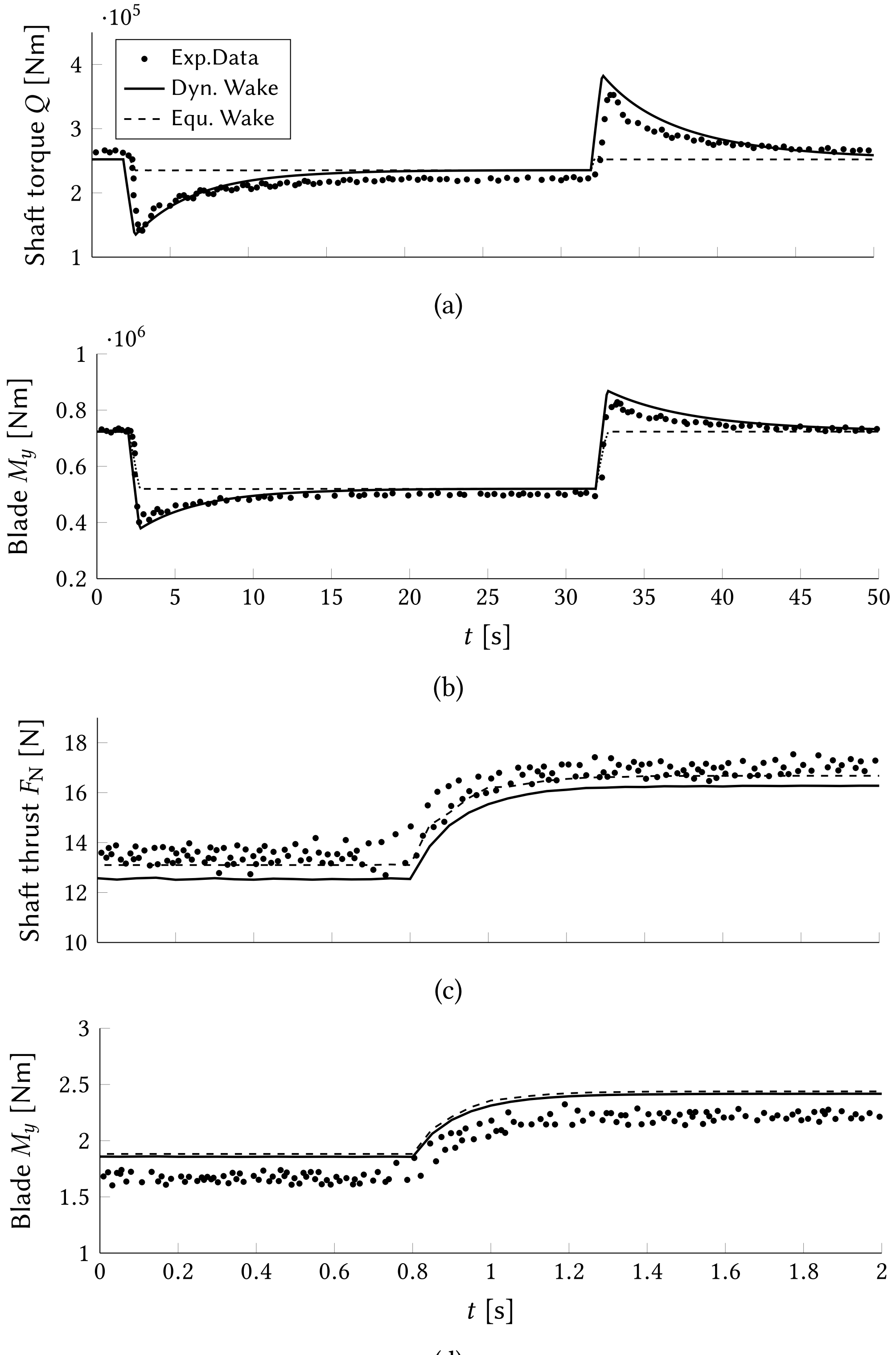

(a)

(b)

(c)

(d)

Figure 4.2: The verification of the accuracy of the dynamic wake formulation in the BEMT model. The figures show the performance of the dynamic wake model (Dyn. Wake) compared to the standard equilibrium wake solutions (Eq. Wake). The plots shown are from the 60m Øye [37] wind turbine torque signal (a) and blade out-of-plane bending moment (b), and the Snel & Schepers [41] small scale wind turbine thrust (c) and out-of-plane bending moment (d) on each respective time-axis. The pitching manouvres can clearly be seen in the reaction loads at 2 and 32s for the Øye case, and the inflow step-change is also visible at 0.8s for the Snel & Schepers experiment.

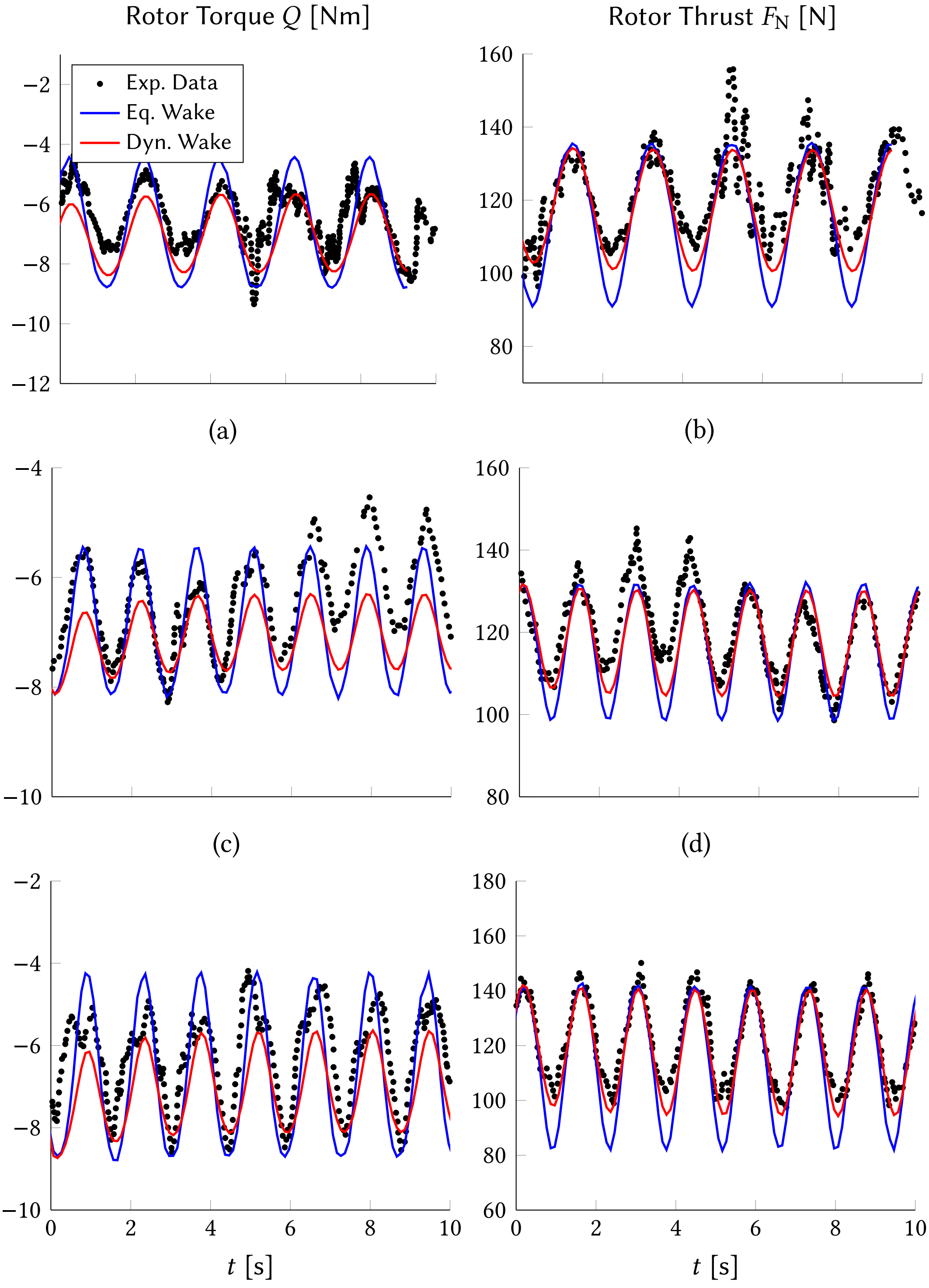

(e) (f)

Figure 4.3: Numerical replication of the Gaurier experiment on a model TST in a flume tank. The figures on the left show the rotor torque and the figures on the right show the rotor thrust for the steady state BEMT formulation (Eq. Wake) and the dynamic wake formulation (Dyn. Wake) where all plots are on the same time-axis. The latter model uses has all the modifications presented in this thesis and the negative sign of the torque is a result of the mounting of the transducer in the experiment. The wave parameters for the cases are; $T = 2$s, $H = 0.16$m (a), (b); $T = 1.42$s, $H = 0.16$m (c), (d); $T = 1.42$s, $H = 0.28$m (a), (b).

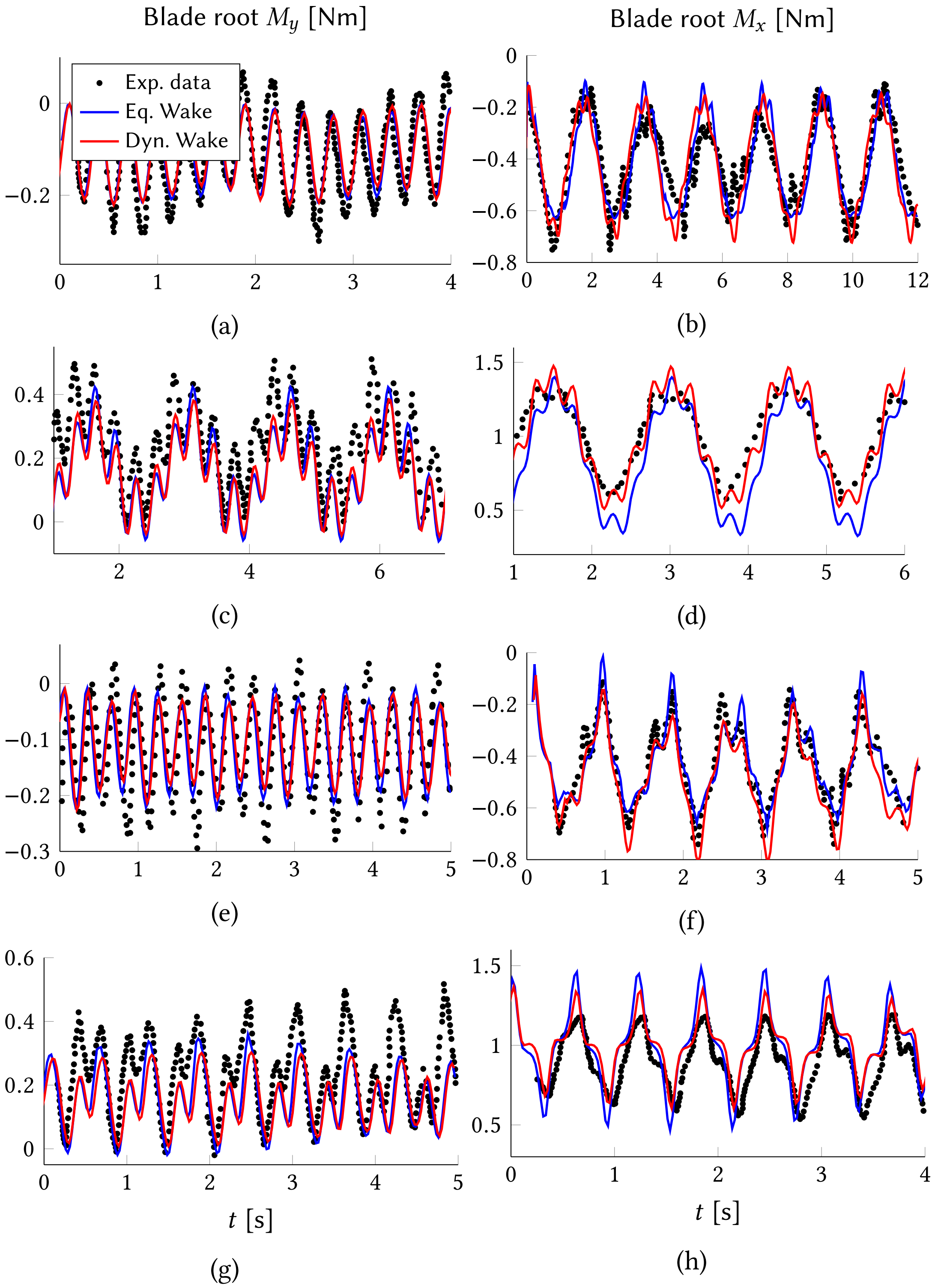

Figure 4.4: Numerical replication of the Barltrop et al. [99] experimental cases showing out-of-plane root bending moments, M_y, in the left column and in-plane bending moments, M_x, in the right. Both BEMT solutions including and excluding the dynamic wake formulation are shown for comparison against the experimental load data. The wave and inflow conditions for the different cases are $U = 0.3\text{m/s}$, $T = 2\text{s}$, $H = 0.15\text{m}$ (a), (b); $U = 1\text{m/s}$, $T = 2\text{s}$, $H = 0.15\text{m}$ (c), (d); $U = 0.3\text{m/s}$, $T = 1\text{s}$, $H = 0.15\text{m}$ (e), (f); $U = 1\text{m/s}$, $T = 1\text{s}$, $H = 0.15\text{m}$ (g), (h).

4.2 The theory of Morris method sensitivity analysis

As the previous section showed, the unsteady BEMT model can adequately predict the loading behaviour of both small scale TSTs operating in unsteady conditions and for full scale wind turbines during transient operation. In order to further the confidence in the model and to investigate its complex input-output relationships, a sensitivity analysis was performed with the intent of identifying the dominant input parameters in regards to the rotor load generation.

Sensitivity analysis is an established method in the wind turbine industry where it is used for load and cost investigations of turbines [108, 109] and there are several different classes of approaches available, each having their own advantages and weaknesses for different applications. One major distinction that can be made regarding the classification of sensitivity analysis methods is dividing them into either *local* or *global* [85] approaches, where the former focuses on small perturbations of the input parameters and the latter explores the parameters' full input space.

The method of sensitivity analysis selected for the study presented here has been that of Morris which is a one-at-a-time method, meaning that each input parameter was varied separately over its whole assumed input range while the others were kept at a base value. One significant advantage that the one-at-a-time method has over other methods where all parameters are varied simultaneously is that the causality of which parameter impacts what output metric is retained and can be studied in detail. The next section shows the derivation of the Morris method sensitivity analysis as originally presented in [110]

4.2.1 The Morris method sensitivity analysis algorithm

In essence, the Morris sensitivity analysis method is based on the assumption that when varying all the parameters of a computational model simultaneously and with the same relative amount, the parameter causing the largest output change is considered as the most important. The parameters are subsequently ranked according to their relative importance to each other in a qualitative way.

The method of determining the sensitivity of a model's output to changes in its input parameters was achieved through the calculation of the so called *elementary effect* of each parameter change. The elementary effect, EE, was the standardised, non-dimensional, rate of change of the model's output that was caused by a variation of the i-th input parameter. The variations of the input parameters was set to a uniform size of positive or negative Δ, known as the magnitude of step. The definition of the elementary effect caused by a change in the i-th parameter was defined by Morris [84] as

$$EE_i(\mathbf{x}) = \frac{y(x_1, x_2, \ldots, x_{i-1}, x_i + \Delta, x_{i+1}, \ldots, x_k) - y(\mathbf{x})}{\Delta} \tag{4.1}$$

where $\mathbf{x}$ was an array containing all the model's k input parameters at a base value and y was the model to be evaluated.

To calculate one elementary effect caused by one parameter change, two model evaluations are needed to determine the output values prior to and after the input change which were supplied to Equation (4.1). Traditional one-at-a-time sensitivity algorithms therefore need $2k$ number of model evaluations to obtain one elementary effect for each of a model's input parameters. In contrast, the Morris method reduced the number of evaluation points needed to calculate one elementary effect for each of a model's parameters by the creation of a randomised trajectory through the variable space as shown in Figure 4.5. Since the evaluation points used to calculate the elementary effects were shared within a trajectory, the Morris method only required $k + 1$ model evaluations which made the algorithm considerably more efficient than standard methods.

Figure 4.5 shows an example of a $k = 3$ parameter model where the input space has been discretised with a so called resolution of sampling (the number of value each parameter can assume), p, equal to four. The Morris method's model evaluation-states through the input space is shown in blue where each parameter was varied once along the trajectory by the magnitude of step, Δ, calculated as a multiple of $1/(p - 1)$.

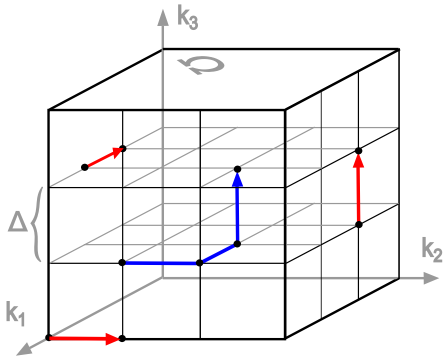

Figure 4.5: Illustration of Morris method input space, also called region of experimentation (Ω), for a $k = 3$ variable model with a resolution of $p = 4$ levels. The red trajectories show traditional one-at-a-time sensitivity analysis needing 6 model evaluation points; the blue trajectory is the Morris method requiring only 4 points.

The model's evaluation trajectory through the input space was created via a set of matrices that enabled each parameter to be varied once throughout the simulation and allowing the calculation of the elementary effects.

In a complex computational model such as the unsteady BEMT code, there are likely to be interactions between the different input parameters giving rise to non-linear effects on the output. To ensure that statistically significant results are achieved and to account for the parameter interactions, the Morris method generates an r number of trajectories which gives an r number of elementary effects for *each* input parameter. The elementary effects were then stored as finite distributions for each input parameter, denoted F_i for the i-th parameter, and the output-changes were studied in a statistical manner by the calculation of the absolute mean value, μ^*, and standard deviations, σ of these finite distributions. These values are known as the *sensitivity indices* and were used to rank the output's sensitivity to the individual input parameters as explained later in Section 4.2.1.

The detailed mathematical method used to generate the trajectories and sensitivity indices are now presented below.

Trajectory Construction

The matrix used to define the r number of trajectories through the input space Ω is called the commute matrix, and in order to implement it, Ω was divided into p equally spaced levels as in Figure 4.5.

If the vector $\mathbf{x} = \{0, 1/(p-1), 2/(p-1), \ldots, 1\}$ is defined as a set in Ω, the values for the input parameters could be sampled from it where each sample step is a multiple of $1/(p-1)$. A vector $\mathbf{x}^*$ was then created which consisted of base values randomly selected from $\mathbf{x}$ in the range $(0, 1-\Delta)$, giving a set of parameter values all within the bounds of Ω. The values of $\mathbf{x}^*$ and Δ were scaled with the respective real-world variable ranges before being given as inputs to the model. This allowed for comparisons to be made between the changes in each variable independently of their ranges and dimensional units.

Morris [84] defines the matrix for a single evaluation trajectory through the input space as

$$\mathbf{B}^* = (\mathbf{J}_{m,1}\mathbf{x}^* + \Delta\mathbf{B}')\mathbf{P}^* \tag{4.2}$$

where $m = k + 1$ and $\mathbf{J}_{m,1}$ is a $(m \times 1)$ unit matrix. Equation (4.2) was used to construct several trajectories in the final commute matrix, $\mathbf{X}$, as

$$\mathbf{X} = \begin{bmatrix} \mathbf{B}^*_1 \\ \mathbf{B}^*_2 \\ \vdots \\ \mathbf{B}^*_\mathrm{r} \end{bmatrix}. \tag{4.3}$$

The first step of constructing the trajectory matrix is to define the modified sampling matrix, $\mathbf{B}'$, as

$$\mathbf{B}' = \frac{1}{2}\left[(2\mathbf{B} - \mathbf{J}_{m,k})\mathbf{D}^* + \mathbf{J}_{m,k}\right] \tag{4.4}$$

where $\mathbf{J}_{m,k}$ was a $(m \times k)$ unit matrix and $\mathbf{B}$ was a matrix of the same dimensions containing elements of 0s and 1s having the property that for each column ($i = 1, 2, 3, \ldots, k$) there were two rows that differed only in their i-th entries. A convenient choice of $\mathbf{B}$ was to let it be a lower left triangle unit matrix with its diagonal shifted down one row defined as

$$\mathbf{B} = \begin{bmatrix} 0 & 0 & 0 & \cdots & 0 \\ 1 & 0 & 0 & \cdots & 0 \\ 1 & 1 & 0 & \cdots & 0 \\ \vdots & \vdots & \vdots & \ddots & \vdots \\ 1 & 1 & 1 & \cdots & 1 \end{bmatrix} \tag{4.5}$$

and $\mathbf{D}^*$ was a k-dimensional matrix with its diagonal having elements taking random values of 1 or -1 as

$$\mathbf{D}^* = \begin{bmatrix} 1 & 0 & 0 & \cdots & 0 \\ 0 & 1 & 0 & \cdots & 0 \\ 0 & 0 & -1 & \cdots & 0 \\ \vdots & \vdots & \vdots & \ddots & \vdots \\ 0 & 0 & 0 & \cdots & 1 \end{bmatrix} \tag{4.6}$$

thus allowing for the occurrence of both positive and negative Δ-changes. The final component, $\mathbf{P}^*$, of Equation (4.2) was a k-dimensional permutation matrix where each row and column contained a randomly placed 1 and all other elements were set to 0, thereby increasing the number of possible trajectories.

The trajectory matrix $\mathbf{B}^*$ was finally assembled by the substitution of Equations (4.4) - (4.6) into Equation (4.2) and a random example of a trajectory matrix with $k = 5$, $p = 4$ and $\Delta = 1/3$ is given as

$$\mathbf{B}^* = \begin{bmatrix} 1/3 & 2/3 & 1 & 2/3 & 1/3 \\ 1/3 & 2/3 & 2/3 & 2/3 & 1/3 \\ 1/3 & 2/3 & 2/3 & 2/3 & 0 \\ 1/3 & 2/3 & 2/3 & 1 & 0 \\ 1/3 & 1 & 2/3 & 1 & 0 \\ 0 & 1 & 2/3 & 1 & 0 \end{bmatrix}. \tag{4.7}$$

It is noted that Equation (4.7) shows only one parameter change (one change per column) between two adjacent rows (model runs) in the matrix which allowed every parameter to be varied once in a given trajectory. The final set of trajectories was then created by substituting an r number of $\mathbf{B}^*$ matrices into the design matrix Equation (4.5) for evaluation of the model.

Morris Method Indices

Finally, with the appropriate number of trajectories created through the model's input space, and a statistically significant number of elementary effects collected in each of its input parameters' finite distributions F_i, the parameters' sensitivity indices can now be calculated.

Each F_i contained r independent calculated elementary effects where the absolute mean value, μ^*, and standard deviation, σ, of the distributions were determined and used as sensitivity indices. A parameter yielding a distribution with a high μ^* index value indicated that the elementary effects in the distribution had large magnitudes, meaning that there was a large change in the model's output from the changing of that parameter; implying that the model output is sensitive to it. In a similar way, a parameter giving a distribution with a high σ index value indicated that there was a large fluctuation within the parameter's elementary effects, which according to Morris means that it had a non-linear relationship to the output or that there existed interactions between it and other inputs.

4.3 Sensitivity analysis set-up and results

Based on the identified lack of knowledge on the parameter influence on hydrodynamic loads on TSTs in a global sense as mentioned in Chapter 2, the main aim of the sensitivity analysis was to present a method to rank the importance of the parameters from the three input domains of inflow, operational and geometrical parameters and to inform on the relationships between the parameters and the output loads. Special attention is given to the parameters' influence on the *variance* of the loads on a turbine's components, as this was considered to be a major driver for the durability and fatigue life of a device, which was also mentioned in Section 2.2.2. Furthermore, since the studies on TST loading found in literature unanimously show that the rotor thrust is the dominant load on the structure, the focus of the sensitivity study presented was solely on the parameters' influence on the thrust loads. Finally, since the non-uniformity of the thrust loads across the rotor plane was found to be an often over-looked aspect of TST loading in Chapter 2, the influence of the identified dominant parameter's effect on the eccentric shaft bending moments was studied in greater detail.

Presented in the next section is the set-up of the three sensitivity analysis cases for the three input domains and the definition of the investigated parameters and output metrics, followed by the results of the study.

4.3.1 Sensitivity analysis input variables and case set-up

The sensitivity analysis was performed using three separate cases in an attempt to isolate the dominant parameters in the sea-state and operational domains, the geometry design and operational domain and one case concerning *all* variables to identify the primary parameters in the global domain. Using this approach, further insight was given into the hierarchy of the parameters in each sub-group of variables relating to the different aspects of the turbine's operations. To exemplify, the dominant parameters in the sea-state and operational domain gave an indication of which *uncontrollable* environmental parameters need to be known in high detail and which can be neglected. In contrast, the identification of the dominant parameters in the turbine geometry and operational domain exposed which parameters of a turbine's geometrical design were most influential on the loading and durability. The three sensitivity cases are summarised as:

Case 1: **Sea-state and operational parameters** were varied to investigate their influence on the thrust loads and their interconnectivity, while all other parameters were kept constant. A uniform current profile was assumed in order to isolate the effect of the wave-rotor interactions. The output studied here was the thrust load signal for a single blade.

Case 2: **Turbine geometry and operational parameters** were varied in this case while the sea-state parameters were kept constant. A uniform current profile was also assumed here and the output studied was again the thrust load signal for a single blade.

Case 3: **Sea-state, turbine geometry and operational parameters** were varied to show the influence of the parameters globally. In this case, a linear shear velocity profile was assumed to include the effects of the non-uniform inflow across the rotor. The output studied in this case was the *eccentricity vector* of the rotor (Section 4.3.3) which served as a visual representation of the rotor out-of-plane bending moment.

Figure 4.6 illustrates the three studied domains of the sea-state, turbine geometry and operational parameters. The sea-state parameters included in the study were the wave height H, wave period T, uniform inflow velocity U, surface velocity U_s, bottom velocity U_b, and current constant vorticity ω_c which are shown in blue in the figure. The bottom velocity was kept at a non-zero value in order to create the desired shear current gradient over the rotor plane to be as close to a 1/7-th power-law profile. The operational parameters studied were the rotor angular velocity Ω_r, blade root pitch θ, blade initial azimuth position ϕ and hub height h_hub as shown in red. Finally, the turbine geometry parameters studied were the turbine radius R, the blade chord distribution defined by the root chord ('Root chord'), and a scalar factor modifying the blade's twist distribution ('Twist dist.'), all shown in green in Figure 4.6. The ranges of the variables and units for each case are shown in Table 4.2 and the parameters that were kept constant through all cases were the water depth, h, and all of the fluid parameters such as water density, ρ, dynamic viscosity, and the Reynolds number using the average blade chord as characteristic length.

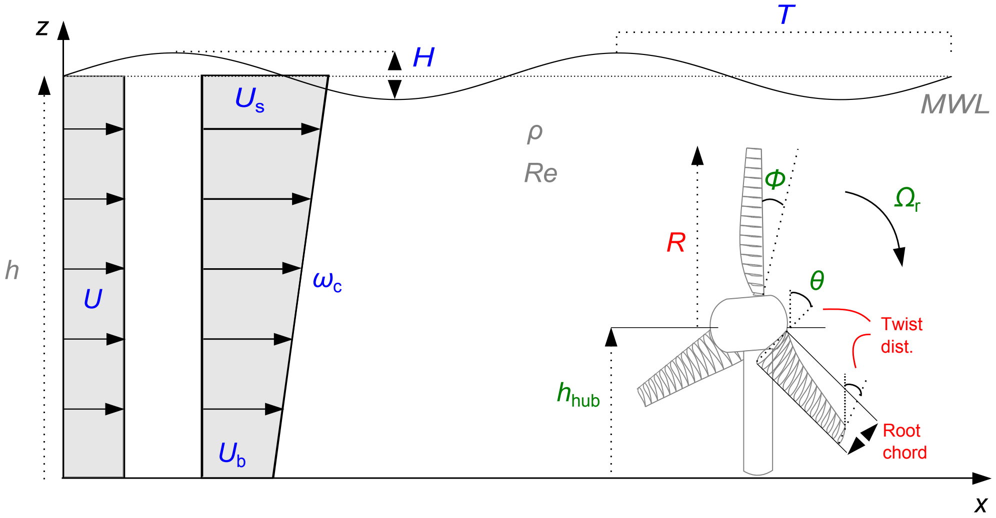

Figure 4.6: The three domains of the parameters investigated in the sensitivity analysis were the sea-state parameter domain (blue), the turbine operational parameter domain (green) and the turbine geometrical parameter domain (red). The grey parameters were kept constant through all cases. Also shown is the two different inflow current profiles used throughout the cases, which are used in combination with the Kishida and Sobey inflow model.

The relationships between the rotor radius, inflow speed and rotor angular velocity were kept as independent variables in the sensitivity analysis in order to determine each individual parameter's influence. As a consequence, the tip-speed ratio of the turbine varied with changing parameters putting it in a non-optimal C_P region in many cases. This is however considered consistent with fixed speed operation and similar effects may occur in turbines where the inertia of the rotor is too great to respond to inflow fluctuations instantaneously, hence exposing them to greater load variations.

The time-step size of the BEMT simulations was kept at 0.1s in order to resolve any possible synchronisation effects between the rotation of the blades and the wave period. It was believed that at certain phase differences between the two parameters, there would be a significant increase in the variations of the loads which was why the blade initial azimuth angle was included in the study. All fluid properties were also kept constant, such as the density and viscosity, and the Reynolds number was also given as a constant input to the model. This latter assumption is obviously non-physical since the actual Reynolds number will change with varying inflow speeds and chord length, but was deemed negligible as the real Reynolds number will be in the same order of magnitude as the input one.

Table 4.2: Variable ranges investigated in each of the three sensitivity analysis cases. Each group of the table shows which parameters were set to vary and which were kept as constant.

Case 1: Varying sea-state and operational parameters							
Var.	H[m]	T[s]	h_{hub}[m]	U [m/s]	θ [°]	Ω_r [rad/s]	ϕ [rad]
	1 - 6	6 - 10	30 - 40	2.5 - 4	−5 - 5	0.8 - 1.6	0 - 2ß
Const.	ρ[kg/m^3]	Blade sect.	Root chord [m]	Twist dist. [-]	Re nr [-]	R [m]	h [m]
	1027	NRELs814	3.14	1	1.5×10^4	12.5	70
Case 2: Varying turbine geometry and operational parameters							
Var.	R[m]	θ[°]	Ω_r [rad/s]	Root chord [m]	Twist dist.	ϕ [rad]	h_{hub}[m]
	10 - 15	−5 - 5	1.2 - 1.5	2.5 - 3.5	0.7 - 1.3	0 - 2ß	30 - 40
Const.	ρ[kg/m^3]	Blade sect.	H [m]	T [s]	Re nr [-]	U [m/s]	h [m]
	1027	NRELs814	3.5	8	1.5×10^4	3.25	70
Case 3: Varying sea-state, turbine geometry and operational parameters							
Var.	R[m]	θ[°]	Ω_r [rad/s]	Root chord [m]	Twist dist. [-]	ϕ [rad]	H[m]
	10 - 15	−5 - 5	1.2 - 1.5	2.5 - 3.5	0.7 - 1.3	0 - 2ß	1 - 6
	T[s]	h_{hub} [m]	U_s [m/s]	ω_c [m/s]			
	6 - 10	30 - 40	2.5 - 4	0 - 0.0286			
Const.	ρ[kg/m^3]	Blade sect.	Re nr [-]				
	1027	NRELs814	1.5×10^4				

4.3.2 Sensitivity analysis output metrics

For Case 1 and Case 2 of the sensitivity analysis, the model outputs that were studied were the time-histories of the root thrust for a single blade over the time-span of two wave periods. Since this model output was a load *signal* composed of a multitude of harmonics of varying frequencies and amplitudes, it was necessary to derive several statistics from the signal in order to describe the variation and magnitude of the blade loads.

Figure 4.7a shows the four statistical metrics derived from the thrust load signals that were studied in Case 1 and Case 2. These metrics were defined as the load signal's mean value (blue line), its standard deviation (green lines), the absolute amplitude of the signal (red range) and the fraction of time outside the standard deviation bands. The motivation for the choice of these metrics was that the mean value would be representative of the total thrust magnitude on the turbines blades while the standard deviation and absolute amplitude would reflect the variations of the signal, which was related to the fatigue loading of the turbine. Finally, the fraction of time outside the standard deviation bands informed on the 'steepness' of the smaller signal harmonics, which was also believed to have an effect on the fatigue life due to the abruptness of the load spectrum, as was mentioned in Section 2.4.4.

Conversely, the output signal studied for Case 3 was the eccentricity vector defined in Section 4.3.3, which can essentially be described as the rotor out-of-plane bending moment vector rotated 90° to aid in the visual representation of the direction-of-action of this load. The eccentricity vector was of course also caused by the non-uniform blade loads and ultimately acted as an off-axis load on the shaft connecting flange. Figure 4.7b shows an example of the studied DoFs from the BEMT model in the form of a polar plot, in-plane with the swept rotor area, with the eccentricity vectors plotted for several time-steps. The area and shape of the pattern created by the eccentricity vectors was a visual indicator of the magnitude and directional spread of the out-of-plane bending loads on the rotor. The output metrics defined to be studied in the sensitivity analysis for this case were the maximum value of the eccentricity magnitude, the arc angle enclosing the load vectors, the standard deviation of the eccentricity vector angles to the vertical, and the number of peaks in the signal's magnitude, all shown in Figure 4.7b.

By using two different sets of output metrics for the three sensitivity analysis cases, it was possible to obtain information about the parameter's influence on the loads in two degrees of freedom.

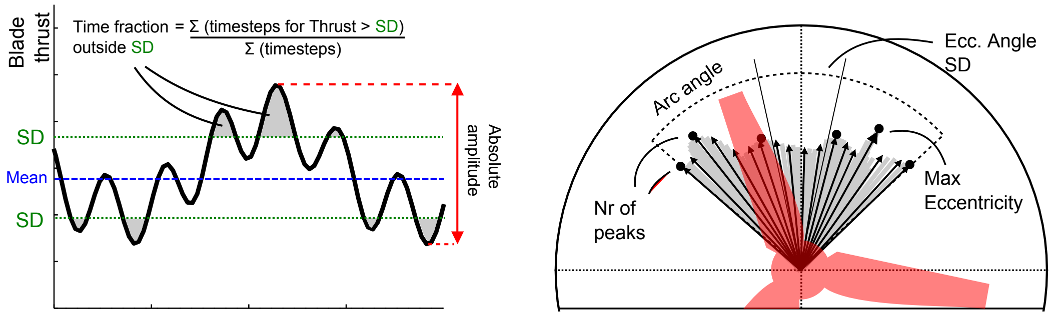

(a)

(b)

Figure 4.7: Definition of the output metrics for the different cases of the sensitivity analysis. For Case 1 and Case 2 the metrics in the (a) part of the figure were used. Here, the blade root thrust signal was analysed by the four characteristic metrics of signal mean value, standard deviation (SD), time fraction outside SD and absolute amplitude. For Case 3 the metrics in the (b) part of the figure were used. Here, the eccentricity vector pattern was analysed by the characteristic metrics of maximum eccentricity magnitude, enclosing arc angle of the load pattern, number of peaks in the signal and the SD of the vector angles to the vertical.

4.3.3 Calculation of thrust load eccentricity vector

When considering the effect that the out-of-plane bending moment of the rotor has on the drivetrain, it is convenient to define an imagined *eccentricity vector* which works as a visual indicator of the direction-of-action of the loading at any given time. This eccentricity vector was used as a metric for the BEMT sensitivity analysis described above and was originally presented in Nevalainen et al. [111] and is in essence a vector of the same magnitude as the rotor out-of-plane bending moment with the difference of being aligned to 'point' in the direction that the rotor is being forced. The eccentricity vector thus described the direction and magnitude in which the rotor was forced due to the out-of-plane bending moment caused by the non-uniform loading across the turbine's blades.

The eccentricity vector was constructed by first allowing the individual blade's out-of-plane bending moment vectors, $M_{y,1}, M_{y,2}, M_{y,3}$, to be decomposed to their components and summed to create the rotor out-of-plane bending moment M_y as shown in Figure 4.8 in a coordinate system centred in the rotational centre of the turbine. The eccentricity vector, V_{ecc}, was then simply defined as a vector rotated 90° clockwise to the rotor out-of-plane bending moment which aligned it with the direction-of-action of the non-uniform hydrodynamics loads on the turbine.

With the eccentricity vector defined, it could be used in the sensitivity analysis and parameter study presented in this chapter where it provided greater visualisation of the off-axis component of the thrust loading of a TST operating in unsteady flow. This also aided in the qualitative interpretation of the analysis of the primary parameters presented in Section 4.4.

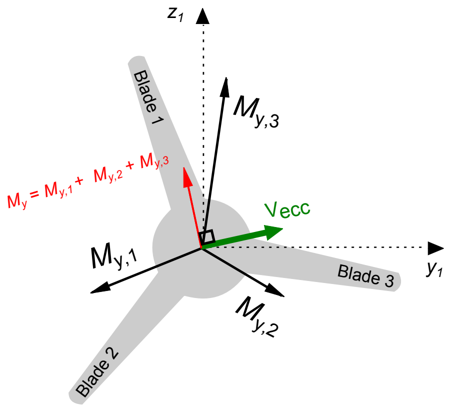

Figure 4.8: The vectors V_1, V_2 and V_3, which represented the direction-of-action of the thrust-induced out-of-plane bending moments for each blade, were de-constructed to their components in a shaft-centred coordinate system. Each blade's bending moment-components were then added to create the components y_{ecc} and z_{ecc} of the eccentricity vector V_{ecc}.

4.3.4 Morris method sensitivity analysis results and discussion

Shown in Figures 4.9 - 4.11 are the results of the three sensitivity analysis cases respectively. The data are displayed so that each of the defined output metrics correspond to one scatter plot in each figure, resulting in a total of four plots per case. The sensitivity of an output metric towards changes in the input parameters is shown by the relative score of the sensitivity indices of each parameter, where the μ^* index is plotted as a function of the σ index. As an example, Figure 4.9a shows that the sensitivity of the mean value of the blade thrust signal was most sensitive to the uniform inflow velocity, U, indicated by the parameter's high μ^*-score. It is recalled that since the sensitivity indices μ^* and σ denote the parameter's influence and inter-parameter interactions respectively, the rotor angular velocity, Ω_{r}, therefore shows the highest level of interaction with other parameters in Figure 4.9a. In short summary, parameters that are plotted to the upper right corners of the plots show higher dominance in regards to the respective metric, and parameters plotted towards the lower left are less important.

In general, the results in Figures 4.9 - 4.11 showed that the six most influential parameters on the loads out of the 12 investigated were the inflow velocity, wave height, wave period, rotor angular velocity, rotor radius and blade pitch angle. These results were not surprising since these parameters governed the local inflow velocities over the blades, the angles of attack over the blades and power capture area of the turbine, which are all highly influential in regards to the loading. However, further

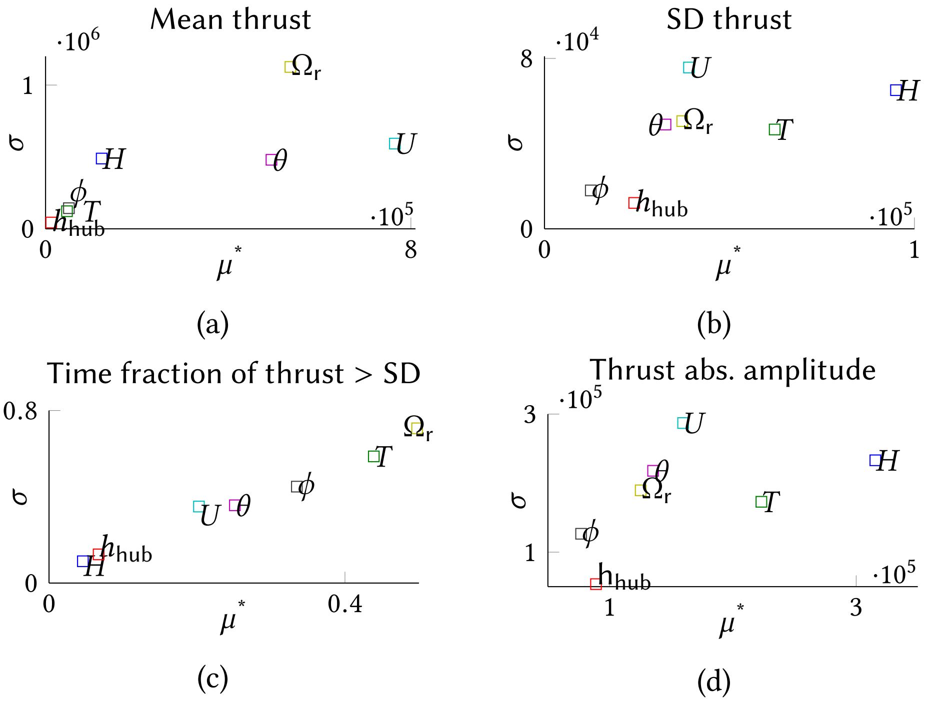

(a) (b) (c) (d)

Figure 4.9: The results from Case 1 of the sensitivity analysis on the BEMT code showing four scatter plots for the output metrics mean thrust (a), standard deviation (SD) of thrust (b), fraction of time of thrust outside the standard deviation bands (c) and the amplitude of the thrust signal (d).

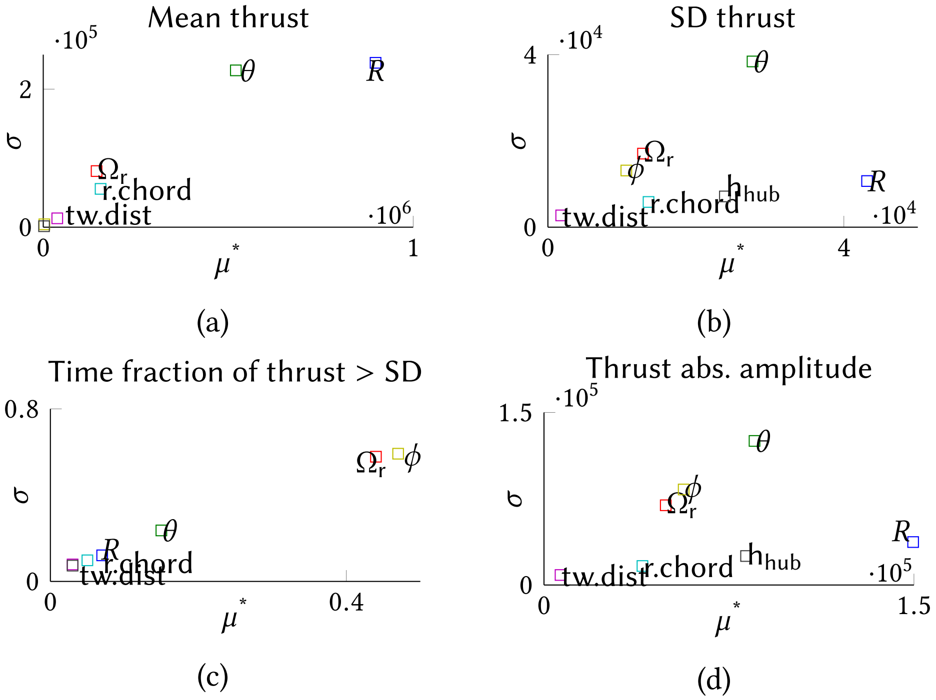

(a) (b) (c) (d)

Figure 4.10: The results from Case 2 of the sensitivity analysis on the BEMT code showing four scatter plots for the same metrics as in Figure 4.9.

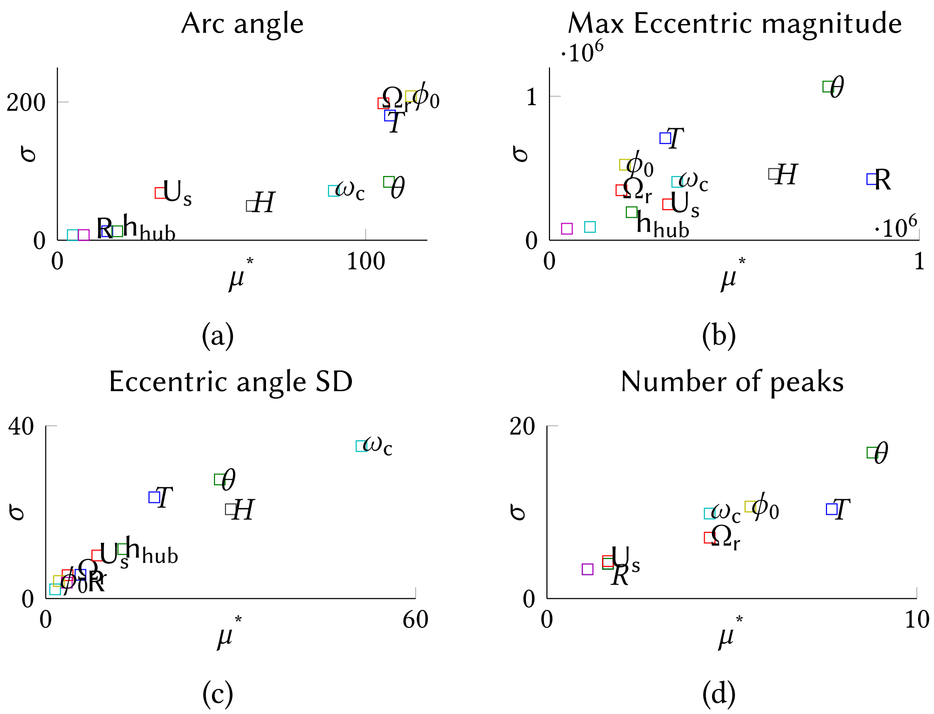

(a) (b) (c) (d)

Figure 4.11: The results from Case 3 of the sensitivity analysis on the BEMT code showing four scatter plots for the output metrics defined for the eccentricity vector, derived from the out-of-plane bending loads on the rotor. The metrics studied were the load pattern's arc angle (a), max eccentric magnitude (b), eccentricity angle standard deviation (SD) (c) and the number of peaks in the load signal (d). Figure 4.7b is referenced for the metric definitions.

details of the input-output relationships can be revealed when examining the results of each sensitivity analysis case in greater detail.

It can be seen in Figure 4.9a that the current velocity, rotor angular velocity and blade pitch were the dominant parameters concerning the mean thrust load in Case 1, which explored the sea-state domain. This was likely caused by these parameters' influence on the local inflow angle over the blade in Equation (3.77), which has been identified as a having a strong impact on the blade thrust.

Since the rotor angular velocity and blade pitch of a TST can be varied during operation depending on what power control-scheme is adopted, this finding suggests that the mean blade loads could theoretically be managed by optimising the trade-off between the turbine's power capture and blade-loading. In contrast, Figures 4.9b - 4.9d show that the wave height, wave period and inflow velocity were the dominant factors on the *varience* of the loads. Since these parameters were influential in regards to the load fluctuation it was believed that they would be design drivers for the fatigue loading. Also, since these parameters cannot be controlled in the same manner as the rotational velocity and the blade pitch, site selection and characterisation will be of great importance to ensure TST device longevity.

The results for Case 2 of the sensitivity analysis is shown in Figure 4.10 revealed that the rotor radius R and blade pitch θ were the primary parameters on both the generation of the mean loads and load variance in the geometry parameter domain. A possible explanation for the rotor radius influence on the variance is that the longer blades in a larger turbine swept a larger section of the water column, thus exposing them to a greater range of inflow velocities.

The results for Case 3 is shown in Figure 4.11 indicate the same parameters having the largest influence on the eccentric loading as in the previous cases, with the exception of the blade's initial azimuth position, ϕ, having a greater sensitivity score. The arc angle of the swept eccentricity vector in Figure 4.11a shows greatest sensitivity to the blade initial azimuth, ϕ, the rotor angular velocity, Ω_r, and the wave period, T – parameters which were all related to the relative phasing between rotor and incident waves. This result indicates that the synchronisation between the rotating blades and the passing waves may have had a large influence on the eccentric load variance and load directionality as will be elaborated in Section 4.5. Worth mentioning is that the wave direction is assumed to be in-line with the current in the previous investigation. This simplification is assumed to be valid for TST loading since most tidal sites are in sheltered tidal runs where the waves may be directed towards the predominant flow direction. The blade pitch also showed high importance on the arc angle which was unexpected, and a further analysis of this result is shown in Section 4.4.

When considering the maximum magnitude of the thrust eccentricity in Figure 4.11b, the rotor radius, blade pitch and wave height were identified as the primary parameters. Again, the sensitivity towards the turbine radius is explained by the greater velocity gradient over the rotor plane, which gives rise to a larger eccentricity vector, and a similar reason is given for the influence of the wave height. The pitch angle's large influence on the eccentricity magnitude is hypothesised to be caused by the parameter changing how close to or far away from the optimum angle of attack the blades operate; having the blades operating in a range close to the stall region for example will induce a greater and more unpredictable load range, and thus higher eccentricity. This last statement is however unconfirmed and would a need more detailed analysis of the angle of attack over the blades during operation to be proven.

4.4 Detailed analysis of identified primary variables

Based on the results from the sensitivity analysis in the previous section, 8 of the most influential parameters out of the 12 investigated were selected for a detailed analysis of their influence on the rotor out-of-plane bending loads. This study aided in answering the second and third research questions in Section1.1.1 regarding the influence of the parameters and the internal loading contribution of the rotor out-of-plane bending moment. The parameters selected for further analysis were the current vorticity distribution, the rotor angular velocity, the blade root pitch, the rotor radius, the blade initial azimuth position, the surface velocity, the wave period and the wave height.

To reiterate, the purpose of this analysis was to show the effect that the variation of a single input parameter had on the magnitude and directionality of the rotor out-of-plane bending moment load-pattern caused by the non-uniform blade loading, as visualised by the eccentricity vector; this would ultimately inform on which parameters had the largest impact on the internal drivetrain loading of a TST in terms of producing additional stresses from the off-axis shaft forces. Section 4.5 later provides explanations for some of the rotor-loading phenomena uncovered by this study.

The detailed analysis of the primary parameter was performed by first defining a base-case turbine load environment where each parameter assumed the mean values of the ranges presented for Case 3 of the sensitivity analysis (as shown in Table 4.2). The base-case thus consisted of a 12.5m radius turbine operating in a constant gradient velocity profile with a 3.25m/s surface velocity, a rotational velocity of 1.35rad/s and so on.

Each of the investigated parameters was then varied over the ranges defined in

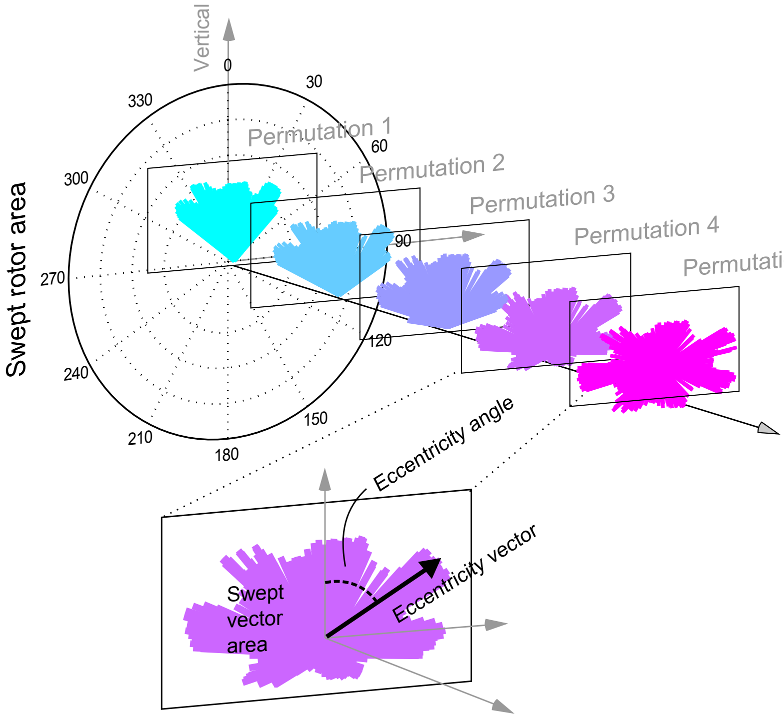

Figure 4.12: Illustration of the method of presentation of the results of the detailed analysis of the primary parameters. The figure shows the superposition of the five permutations of one single variable, while the others variables are kept constant. This presentation allows the effect of the parameter variation on the eccentricity pattern to be seen in a comparative and qualitative way. The definition of the eccentricity vector is shown in Section 4.3.3.

Table 4.2 in five uniform increments making five permutations for each variable, keeping all other parameters constant. The results of each permutation were presented as the polar plot of the eccentricity vectors graphed over two wave periods and having the five permutations superimposed for visual comparison as illustrated in Figure 4.12. This allowed both the variations in eccentricity magnitude and angular distribution to be visually compared for each parameter change. Shown below the polar plots are the corresponding out-of-plane bending moment signals, M_y, for one single blade, that related change in the off-axis loading from the eccentricity vector to the change in the single blade load for each variable permutation.

4.4.1 Primary variable analysis results and discussion

The results of the detailed analysis of the primary parameters' impact on the rotor's eccentricity vector are shown in Figures 4.13 - 4.14. It can be seen that the eccentricity vector, and thereby the rotor out-of-plane bending moment loads, transmitted to the shaft were significant and could reach values as high as approximately 8.75×10^5N m as shown in Figure 4.13d. This bending load is equivalent to a point load of approximately

6.9 tonnes acting on the turbine blade tip of 12.5m radius.

Figure 4.13a shows the variation of the eccentricity vector induced by the changing of the current shear steepness. It can be seen that as the current shear steepness was increased, the eccentricity pattern increased in magnitude towards the vertical upward direction due to the lower inflow velocity distribution towards the bottom of the rotor. However, as can be seen in the lower graph of Figure 4.13a, the loading on the individual blades *decreased* for increasing current shear as it was generated by reducing the bottom inflow velocity. This implied that a site having strong current shear steepness would generate lower loads when *averaged* over the entire rotor area while increasing the eccentricity magnitude due to the velocity gradient.

The load pattern in Figure 4.13a was also the only case where a ‘downward’ directionality of the eccentric loads can be observed in the permutation where the current shear is zero, i.e uniform inflow. This phenomenon will occur whenever the trough of a large enough wave passes over a turbine operating in a uniform current since the top of the rotor is then exposed to the largest velocity reversal from the wave, creating an inverted load gradient over the rotor-plane with the largest thrust seen on the bottom part.

As mentioned in Section 4.3.4, the blade root pitch setting showed a large influence on the eccentricity magnitude which can be seen in greater detail in Figure 4.13c. Here, the eccentricity magnitude increases while the load directionality decreases with higher values of blade pitch. Similarly to the current shear results, the eccentricity magnitude was in this case also increased at the same time as the loads on the individual blades decreased, as can be seen in the bending moment plot of Figure 4.13c. This latter finding is interesting from a condition monitoring aspect of a turbine since, if the load signal from a single blade is used to monitor the turbine’s loads, one might unintentionally generate higher loads on the drivetrain by reducing the time-averaged load on the blade which causes a larger rotor out-of-plane bending moment.

The results of the loads generated during the rotor radius variations in Figure 4.13d show a quite predictable load-change where the eccentricity pattern was ‘scaled’ geometrically with increasing radius. This parameter variation also showed the largest change in the individual blade loads and also produced a significant increase in the load signal variance as predicted by the sensitivity analysis. The results from the surface velocity variations showed a similar geometrical shape-change in the load pattern although it was less severe in magnitude, as shown in Figure 4.14b.

As mentioned in the previous section, the wave period was one of the parameters that had a strong impact on the arc angle of the eccentricity. This is visualised in Figure 4.14c where the longer periods showed a larger angular range and a larger eccentricity magnitude towards the extreme angles. The case where the wave period was 10s was where the rotor, having a rotational period close to 5s, may have synchronised with the incoming wave train giving rise to the largest eccentricity magnitudes. This interaction phenomenon between the rotating blades and the orbital velocities of the waves, creating fluctuations in the load signals of a turbine's blades, is investigated in the next section.

4.5 Hydrodynamic mechanisms of the rotor out-of-plane bending moment

The previous section showed how the out-of-plane bending moment of a turbine's rotor varied as a function of various input parameters in a high-level, empirical manner. It was noted that many of the load-patterns created by the rotor out-of-plane bending moment component (Figures 4.13 - 4.14) had several peaks, or local maxima, at various points in time and in different angular directions. In order to explain the origin of these peaks and the variations in the rotor out-of-plane bending moment load histories, it is useful to examine the *relative* inflow over the individual blades and how it relates to their instantaneous positions in the water-column. This section aims to investigate the cause of these load peaks by decomposing the rotor out-of-plane bending moment signal as the thrust components from the individual blades and how their thrust forces relate to the wave kinematics.

Recalling that the eccentricity vector was defined in Section 4.3.3 as the rotor out-of-plane bending moment vector rotated to align with the direction-of-action of the moment, Figure 4.15a shows the time-history of the eccentricity vector magnitude for the base-case load conditions defined in Section 4.4, albeit with a uniform current profile of 3.25m/s to accentuate the effect of the surface wave kinematics. Here, the local maxima and minima in the load signal created by a passing wave peak can clearly be seen over one 8s wave period. A global maximum in the rotor bending moment is seen to occur at 2s and is marked with a red line throughout the figures; this maximum will serve as a focus-point in this analysis to show the origin of the eccentricity variations.

Figure 4.15b shows the individual thrusts on the turbine's three blades, plotted on the same time-axis as the rotor bending moment, where it can be seen that the largest difference in thrust forces occurs at the point in time of the eccentricity maximum. This was to be expected as the thrust gradient across the turbine's rotor is what gives rise to the rotor out-of-plane bending moment in the first place. At the instance of largest blade thrust variation, 'blade 2' (denoted by the green curve), is shown to have

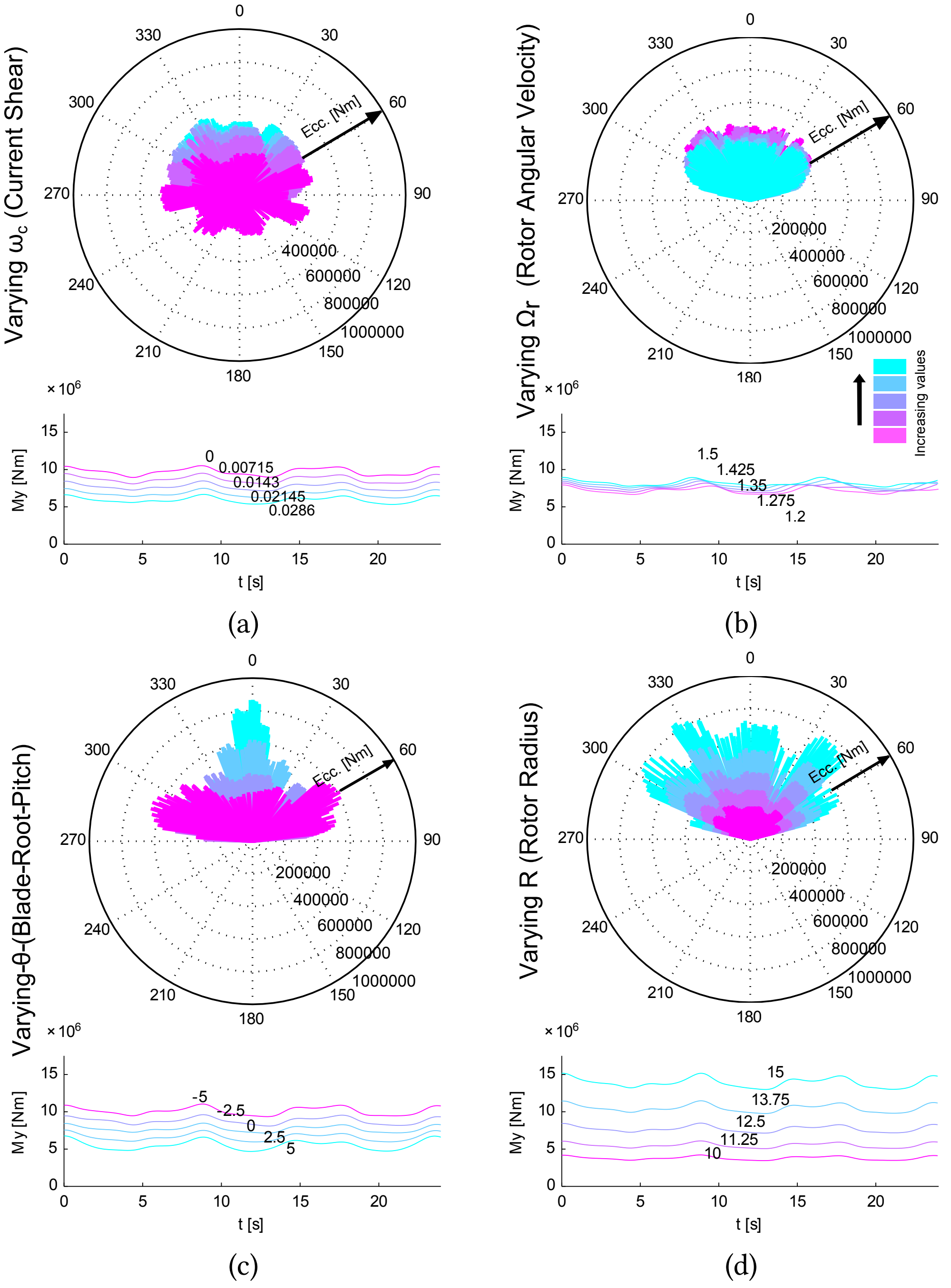

(a)

(b)

(c)

(d)

Figure 4.13: Results from primary the variable analysis showing polar plots of the eccentric load patterns and single blade bending moments (M_y) for different single variable permutations. The parameters varied are: varying shear current (a), varying rotor angular velocity (b), varying blade root pitch (c), varying rotor radius (d).

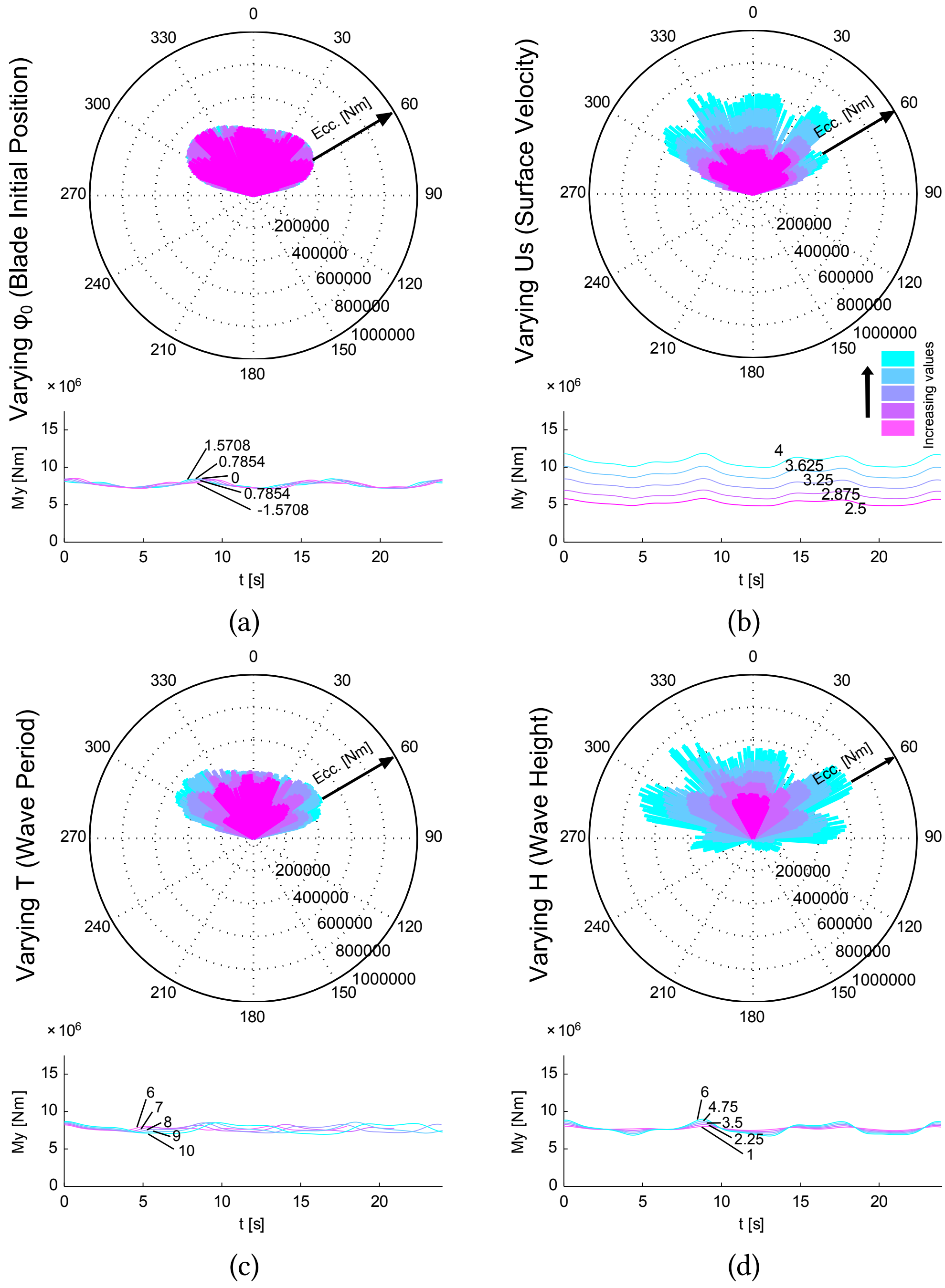

(a) (b) (c) (d)

Figure 4.14: Results from the primary variable analysis showing polar plots of the eccentric load patterns and single blade bending moments (M_y) for different single variable permutations. The parameters varied are: varying blade initial azimuth position (a), varying surface velocity (b), varying wave period (c), varying wave height (d).

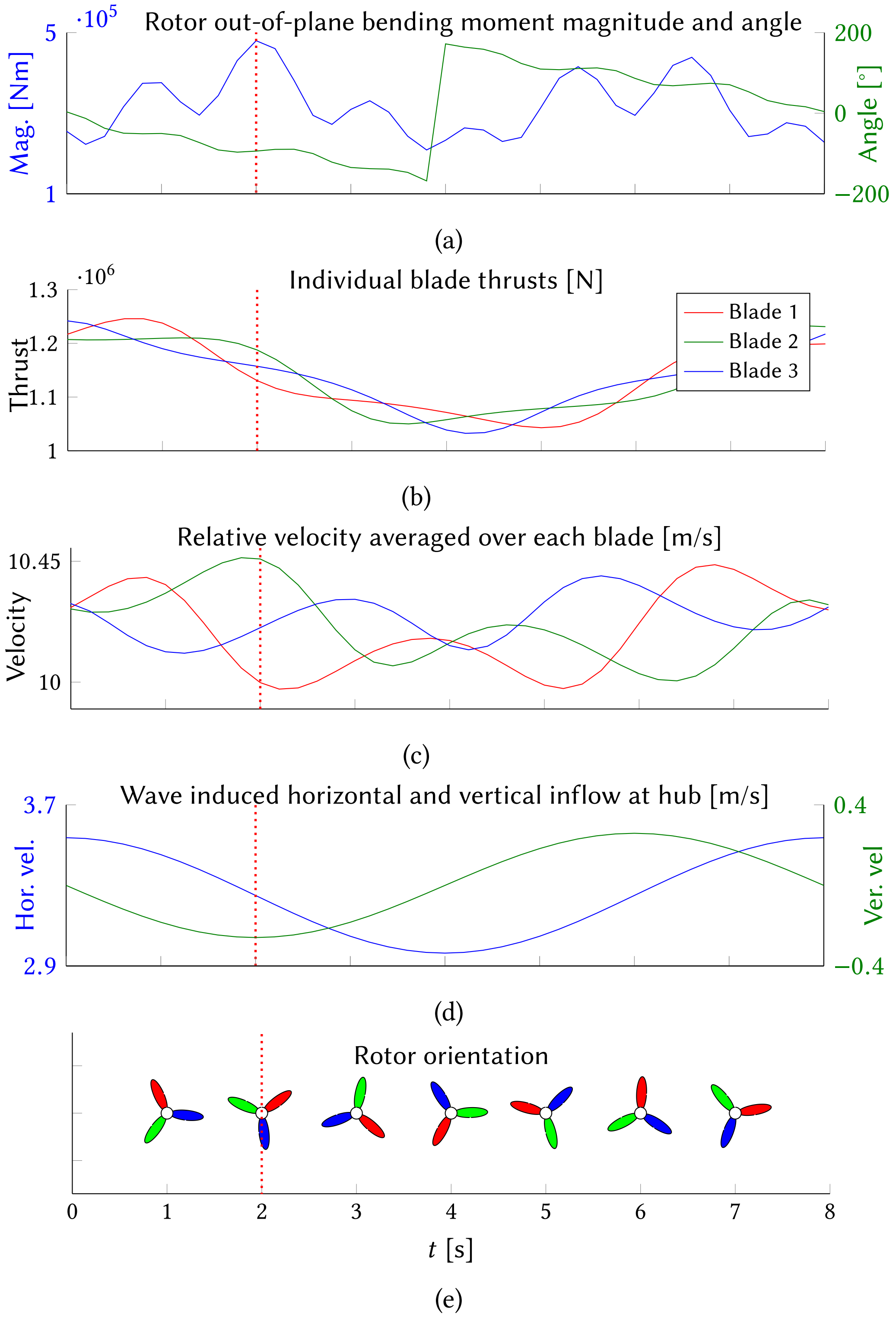

Figure 4.15: Breakdown of the rotor out-of-plane bending moment (analagous to the eccentricity vector) load history over one wave passing for the base case defined in Section 4.4. The figure shows the magnitude and angular direction of the rotor out-of-plane bending moment (a) and its corresponding blade thrusts (b), the relative inflow velocities averaged over the blades (c), the wave induced horizotal and vertical velocity (d) and the rotor orientation (e).

the largest thrust force out of the three blades. This is directly correlated to the blade having the largest relative velocity (Equation (3.78)) averaged over its length, as is represented by the green curve in Figure 4.15c.

Up to this point, the cause of the highlighted eccentricity maximum has been as straight forward as being caused by a thrust enlargement on blade 2 which had seen the largest relative flow velocity of the blades. However, an interesting observation is made when the graph of the wave induced horizontal and vertical velocity components is consulted in Figure 4.15d. Here it can be seen that the horizontal wave velocity is actually *decreasing* at the point of maximum eccentricity, and that the wave phase is approximately one quarter after the peak height. To explain the large average velocity difference between blade 2 and blade 1 in Figure 4.15c, the *vertical* component of the wave velocity must be considered which is shown to be at its largest negative value in Figure 4.15d at the marked time (green curve).

The interaction of blade 2 moving up through the water column, as shown in Figure 4.15e, at the point in time when the wave train generated its largest downward pointing vertical velocity, in combination with blade 1 moving downwards at this point, is what caused velocity difference between the two blades and ultimately allowing the eccentricity maxima to occur at 2s.

Hence, it was found that the vertical velocity component of the wave kinematics in combination with the rotation of the blades was responsible for the pattern of smaller amplitude local maxima and minima in the eccentricity patterns of Figures 4.13 - 4.14. The maximum of the eccentricity is likely to occur whenever the of the vertical wave component superimposes with blade's vertical velocity to increase the relative inflow over the blade. This a phenomenon is repeated in Figure 4.15 at 6.6s when blade 1 moved down through the positive vertical wave velocity component,generating a higher perceived velocity over the blade.

4.6 Conclusions

This chapter has demonstrated the unsteady BEMT model's high probability to adequately replicate the loading on turbines operating in a wide variety of conditions. Each of the model's sub-systems was verified to be empirically adequate by replicating increasingly complex flow situations, ranging from steady-state, dynamic, to dynamic with non-uniform inflow. The model has shown adequacy over a range of rotor diameters and Reynolds numbers and was shown to replicate results down to the details of individual blade root loads. The accuracy of the model is highly dependent on high quality and well defined input data, such as blade-pitch setting and low Reyolds number airfoil lift and drag data for small scale turbines. The latter of these has been identified as the largest uncertainty when dealing with small-scale devices, as this data is hard to reproduce using the external XFOIL package, and may be the reason why the model tends be more successful in predicting loads on large-scale machines. This is discussed in greater depth in Section 7.3. The successful verification of the unsteady BEMT model strengthens the confidence in the results presented throughout this thesis and is aligned with the first research objective in Section 1.1.2. The Morris method sensitivity analysis presented in this chapter will also serve to further increase the confidence in the modelling undertaken since it will illuminate any areas where the input parameters must be known with high certainty.

Based on the results from both the sensitivity analysis and the detailed analysis of the primary parameters, it is shown that the current shear, blade root pitch, rotor radius, surface velocity and wave height will be the most influential parameters in terms of the loading on a tidal stream turbine in no order of significance. It is clear that these parameters have a large impact on the magnitudes of the loads and their angular distributions, or degrees of freedom, as shown in Figures 4.13 - 4.14. The sensitivity analysis on the turbine loads also revealed that some parameters, such as the wave height, had a large impact on the *variance* of the loads but did not have a significant impact on the mean value loading magnitude. These parameters will be important to consider when investigating the fatigue life of a device in the following chapters. It is acknowledged that the immersed operating depth showed very little impact on the loads on a TST in the presented analysis, which may be due to the conservative depth range that was investigated due to the limitations of the unsteady BEMT code close to the free-surface. Another reason for this insensitivity may be that the linear shear current used in the model gave a constant current gradient over the rotor-plane regardless of the operating depth, which would not be the case if a 1/7th power law profile had been used.

The results for the analysis of the primary parameters' effect on the rotor eccentricity showed that the rotor out-of-plane bending moments transmitted to a TST's shaft were appreciable and varied drastically depending on the turbine's inflow conditions, geometrical design and operating modes. It is believed that when transmitted to a turbine's drive train, these non-axial loads will have a detrimental effect on internal components such as bearings, seals and gearboxes which are usually not designed to withstand large variations in load-magnitude and directionality. The results show that there is a clear need to investigate the role of the thrust eccentricity on the turbine's internal structural components when considering ultimate and fatigue load calculations.

Furthermore, this chapter has investigated the cause behind the shape of the rotor out-of-plane bending moment's load-pattern where it was found that the wave's vertical velocity component in combination with the rotation of the blades caused the many local maxima observed in the load signal. This result has implications in terms of understanding possible fatigue damage drivers caused by the variations in the load pattern, but more immediately it shows that the waves' vertical velocity component cannot be neglected in TST load modelling.

The knowledge gained from the studies presented in this chapter will aid in focusing the investigation of the relationship between a tidal turbine's operating environment and its durability presented in Chapter 6. The dominant parameters, identified in this chapter as causing the largest load variance and eccentricity of the shaft loads will be investigated in further detail by showing their functional relationships to the TST drivetrain durability using the higher degree of freedom TST drivetrain model.

The next chapter will give the details of this refined drivetrain model, and how the various loads derived from the unsteady BEMT model feed in to it, and with its completion, the effect that the dominant input parameters have on the bearing life will be investigated.

Chapter 5

Development of a higher degree of freedom TST drive train model

> "The economical factor in design under the present conditions of competition is becoming of growing importance. The construction must be sufficiently strong and reliable, and yet it must be designed with the greatest possible saving in material. Under such conditions, the problem of a designer becomes extremely difficult. Reduction in weight involves an increase in working stresses, which can be allowed only on a basis of careful analysis of stress distribution in the structure …"
>
> — Stephen P. Timoshenko, 1940

The load environments in which TSTs are designed to operate in generate a complex, nearly permanently present, internal force fluctuation on the shaft, producing unknown tribological effects on other mechanical components such as the shaft bearings. It is also reasonable to believe, that if the outer components such as the blades and support structure of a TST are made stiff (or fully rigid as is assumed in the unsteady BEMT model), the fatigue loading hot-spots will simply be transferred from the blades to the next flexible member in the load-path − namely the drivetrain. In order to assure safe and reliable operation, it is imperative that TST developers strike a balance between the devices' fatigue resistance and the related capital costs through the detailed understanding of the internal tribological effects.

Currently, developers typically employ the use of design load safety factors in determining the structural capabilities of the devices [67]. This method does not reflect the material properties of the components and the time-dependency of the stress cycles that will be induced by the marine loading. As has been covered in Section 2.5.2, there also exists dedicated software design packages for TST drivetrain load calculations, although they tend to simplify the problem down to one dimension which will not capture the full extent of the loading of the bearings or resolve the coupling between the degrees of freedom of forces in the shaft. This poses a considerable limitation on the simulation of TST drivetrain loads and may lead to an underestimation of loading on critical components, which has been linked to failures in the wind turbine sector [65].

Presented in this chapter is a higher fidelity six DoF drivetrain model for TSTs that aims to increase the degrees of freedom that are incorporated from the input hydrodynamic loading as compared to traditional methods while still remaining simple enough for time-domain durability calculations. The drivetrain model adopts conventions that are widely used in the naval architecture discipline of ship drivetrain analysis, where simple multi-beam models of shafts are solved using FEM methods [112]. The method presented, where the shaft is composed of one-dimensional Timoshenko pipe elements with three-dimensional displacements, allows the coupling between the torsional and axial forces in the shaft to be resolved [112]. This force-coupling phenomenon is particularly noticeable in short shafts.

The shaft bearings are represented using a matrix of linear springs as shown in Section 5.2.1 which is a commonly used method in various drivetrain modelling applications [113] as it allows the shaft system to deflect and for the bearing axial and radial reaction loads to be calculated. This approach will give a higher level of confidence in the input loads for the bearing durability calculations, which is based on the L_{10} method presented in Section 5.3, as the full six DoFs of the loads can be included in the calculations.

The scope of this thesis has focused on the sub-surface raceway fatigue failure mode of the drivetrain bearings to be investigated using the model presented, even though it has been shown that seals and gearboxes are also components that are prone to failure. However, since the main bearing is the most loaded component in the drivetrain system, it served as an indicator of the total loads and fatigue damage experienced by the system. The drivetrain model presented consists only of the main shaft and the main supporting bearings, while the sole influence of the gearbox is to give a constant reactive torque at the far end of the shaft. However, since all software presented in this thesis is built in a modular form, a gearbox model could be added in future research.

The model presented in the following sections will aid in the achievement of the research objectives presented in Section 1.1.2 covering the need to investigate how a turbine's inflow conditions, geometrical design and operating parameters relate to the durability of the device. Presented in this chapter are the details of the FE methods used, the bearing representation and stiffness estimations, and finally a description of the L_{10} method for the bearing life calculations.

5.1 The finite element method

The finite element method is a numerical procedure of solving problems that do not have a analytical solution. It is a widely used technique in science and engineering disciplines with a range of applications from solving partial differential equations in mathematics to studying the non-linear plastic behaviour of solids [114].

For the use in structural engineering, the FE principle can be summarised by dividing the procedure into six steps. The first step is to discretise the analysed domain, which may be too complicated to solve analytically, into smaller and geometrically simpler elements connected by *nodes* [115]. The equations describing the physical properties of these elements (sub-domains) can then be assumed to be simpler forms of the governing elasticity equations over each element, called shape functions. These equations in turn produce matrices of algebraic equations for each element in the case of steady-state problems.

The third step is to assemble the individual element matrices into a global stiffness matrix by using inter-element relationships, this effectively 'places' the elements in the correct section of the global domain and links them together through their nodal connections. With the global stiffness matrix constructed, the global boundary conditions can be applied which may be a node having zero displacement at a point attached to a rigid surface for example.

The fifth step of the FE method is to solve the global stiffness equation to obtain the nodal values of the displacements, which can then be used to calculate the elemental stresses and strains. The solving of the equations is usually done by some numerical method such as Gaussian elimination for linear systems or the Runge-Kutta method for transient problems. Finally, the sought after quantities are extracted from the nodal and elemental solution using a post-processing package where further data-analysis and presentation can be performed.

The modelling of the TST drivetrain is, in this thesis, was performed by sub-dividing the length of the main shaft into smaller beam elements with nodal connections in the areas of interest, such as the bearing locations. Since the main shaft of a TST is short in comparison to its diameter, Timoshenko beam elements are used as they can better accommodate the shear deformations present in short beams than the equivalent Euler-Bernoulli beam elements that assume slender beams. The next sections take a closer look at the detailed theory of the Timoshenko beam formulation and the definitions of the shaft bearing representation, before the full assembly of the TST drivetrain model is shown in Section 5.2.

5.1.1 Theoretical details of FEM beam theory

This section gives the reader a deeper understanding of the beam theories used in the structural model through their derivation, the definition of key concepts and the details of how beam theory is implemented as a FEM scheme are given in Appendix C. First, the derivation of the basic Euler-Bernoulli beam theory is given as in Carrera et al. [116] to introduce the basic mechanical concepts of beams, stresses, strains etc. and secondly the derivation of the Timoshenko beam is given to highlight the contrast of the two formulations. All the derivations presented here are for brevity kept two-dimensional and neglecting beam axial deflection. Lastly, a simplified 2-D case of a FE implementation of Timoshenko beam theory is given as a explanatory example which shows the concepts used by the Ansys 15 APDL software environment explained in Section 5.2.2.

Euler-Bernoulli beam theory

As has already been said, the derivation of the beam theories are presented as having only two DoFs, namely transverse displacement and in-plane rotation for the purpose of simplicity. The complete formulation used in the Ansys 15 APDL code expands these concepts to three dimensions and allows six DoFs on each element node.

The basic kinematic assumptions in the Euler-Bernoulli beam theory are given as follows:

1. The cross-section of the beam is rigid on its plane and does not deform under the application of transverse or axial loads.
2. During deformation, the cross-section rotates around the neutral plane of the beam and remains planar as shown in Figure 5.1.
3. The beam cross-section remains perpendicular to the neutral plane during deformation.

According to the first kinematic assumption, the in-plane displacements u_y and u_z depend only on the axial beam-coordinate x. Using this assumption and the definition of the *strain* in the beam being $\epsilon = \Delta L/L$, where L is the length of the beam and δL is the deformation, the strain relationships

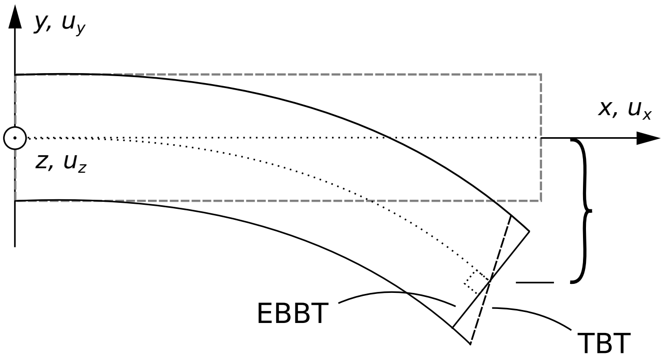

Figure 5.1: The vertical deformation of a cantilever beam showing the initial and displaced positions. The difference between the kinematic assumptions of the Euler-Bernoulli beam theory (EBBT) and Timoshenko beam theory (TBT) are shown as the former does not include the transverse shear deformation of the beam, while the latter does.

$$\begin{cases} \epsilon_{yy} = \dfrac{\partial u_y}{\partial y} = 0 \\[2ex] \epsilon_{zz} = \dfrac{\partial u_z}{\partial z} = 0 \\[2ex] \gamma_{yz} = \dfrac{\partial u_y}{\partial z} + \dfrac{\partial u_z}{\partial y} = 0 \end{cases} \tag{5.1}$$

are given where the double subscript yy refers to the strain in the y-direction (denoted by the first variable) on the plane normal to the y-direction (denoted by the second variable). Similarly, the *shear* strain γ is denoted as the strain in the first subscript direction (y) acting on the plane normal to the second subscript (z). This leads to the transverse displacement formulas to be written as

$$\begin{cases} u_y(x, y, z) = u_{y1}(x) \\ u_z(x, y, z) = u_{z1}(x) \end{cases} \tag{5.2}$$

where the subscripts $y1$ and $z1$ denote pure rigid body translations in the respective directions.

According to the second Euler-Bernoulli kinematic assumption, where the cross-section remains plane after the beam deformation, the axial displacement field consists of a rigid body translation and two rigid body rotations as

$$u_x(x, y, z) = u_{x1}(x) + \phi_y(x)z + \phi_z(x)y \tag{5.3}$$

where the two rotational terms are approximations for the sine of small angles and ϕ_y and ϕ_z are the rotation angles along the y and z-axes. The third kinematic assumption then allows the shear deformations γ_{xz} and γ_{yx} to be set to zero. The rotation angles of the cross section can now be defined as derivatives of the in-plane displacements by the definition of shear strain and Equations (5.2) - (5.3) as

$$\begin{cases} \gamma_{yx} = \dfrac{\partial u_x}{\partial y} + \dfrac{\partial u_y}{\partial x} = \phi_z + \dfrac{\partial u_{y1}}{\partial x} = 0 \\ \gamma_{xz} = \dfrac{\partial u_x}{\partial z} + \dfrac{\partial u_z}{\partial x} = \phi_y + \dfrac{\partial u_{z1}}{\partial x} = 0 \end{cases} \Rightarrow \begin{cases} \phi_z = -\dfrac{\partial u_{y1}}{\partial x} \\ \phi_y = -\dfrac{\partial u_{z1}}{\partial x} \end{cases} \tag{5.4}$$

keeping in mind that the in-plane shear definition is set to zero by the third assumption. The displacement field can then be written as

$$u_y = u_{y1} \tag{5.5}$$

$$u_x = u_{x1} - \frac{\partial u_{y1}}{\partial x} y - \frac{\partial u_{z1}}{\partial x} z \tag{5.6}$$

$$u_z = u_{z1} \tag{5.7}$$

which consists of the three unknown rigid deformation variables. Since the Euler-Bernoulli beam theory assumes the beam to be long and slender, it only accounts for axial strain as the derivative of Equation (5.6) as

$$\epsilon_{xx} = \frac{\partial u_x}{\partial x} = \underbrace{\frac{\partial u_{x1}}{\partial x}}_{k_x^x} - \underbrace{\frac{\partial^2 u_{y1}}{\partial x^2}}_{k_{xx}^y} y - \underbrace{\frac{\partial^2 u_{z1}}{\partial x^2}}_{k_{xx}^z} z = k_x^x + k_{xx}^y y + k_{xx}^z z \tag{5.8}$$

where the terms k_x^x, k_{xx}^y and k_{xx}^z have the physical meaning of the membrane deformation and curvature about the axes respectively.

The *stress* in the beam, σ, is defined as the strain multiplied by the Young's modulus, E, which for the axial beam stress becomes

$$\sigma_{xx} = E\epsilon_{xx} = E\left(k_x^x + k_{xx}^y y + k_{xx}^z z\right) \tag{5.9}$$

and the beam's *stress resultants* are defined as the integral of the membrane stresses over the cross-section area as axial force

$$
\begin{aligned}
N(x) &= \int\limits_{\Omega} \sigma_{xx}\,\mathrm{d}\Omega = \int\limits_{\Omega} E\left(k_x^x + k_{xx}^y y + k_{xx}^z z\right)\,\mathrm{d}\Omega \\
&= E\left[k_x^x \underbrace{\int\limits_{\Omega} \mathrm{d}\Omega}_{A} + k_{xx}^y \underbrace{\int\limits_{\Omega} y\,\mathrm{d}\Omega}_{S_y} + k_{xx}^z \underbrace{\int\limits_{\Omega} z\,\mathrm{d}\Omega}_{S_z} \right],
\end{aligned}
\tag{5.10}
$$

the bending moment around the z-axis as

$$
\begin{aligned}
M_z(x) &= \int\limits_{\Omega} \sigma_{xx} y\,\mathrm{d}\Omega = \int\limits_{\Omega} E\left(k_x^x + k_{xx}^y y + k_{xx}^z z\right) y\,\mathrm{d}\Omega \\
&= E\left[k_x^x \underbrace{\int\limits_{\Omega} y\,\mathrm{d}\Omega}_{S_y} + k_{xx}^y \underbrace{\int\limits_{\Omega} y^2\,\mathrm{d}\Omega}_{I_{zz}} + k_{xx}^z \underbrace{\int\limits_{\Omega} yz\,\mathrm{d}\Omega}_{I_{yz}} \right],
\end{aligned}
\tag{5.11}
$$

and the bending moment around the y-axis as

$$
\begin{aligned}
M_y(x) &= -\int\limits_{\Omega} \sigma_{xx} z\,\mathrm{d}\Omega = -\int\limits_{\Omega} E\left(k_x^x + k_{xx}^y y + k_{xx}^z z\right) z\,\mathrm{d}\Omega \\
&= -E\left[k_x^x \underbrace{\int\limits_{\Omega} z\,\mathrm{d}\Omega}_{S_z} + k_{xx}^y \underbrace{\int\limits_{\Omega} yz\,\mathrm{d}\Omega}_{I_{yz}} + k_{xx}^z \underbrace{\int\limits_{\Omega} z^2\,\mathrm{d}\Omega}_{I_{yy}} \right].
\end{aligned}
\tag{5.12}
$$

Equations (5.10) - (5.12) can be written in matrix form as

$$
\begin{Bmatrix} N \\ M_z \\ -M_y \end{Bmatrix} = E \begin{bmatrix} A & S_y & S_z \\ S_y & I_{zz} & I_{yz} \\ S_z & I_{yz} & I_{yy} \end{bmatrix} \begin{Bmatrix} k_x^x \\ k_{xx}^y \\ k_{xx}^z \end{Bmatrix}
\tag{5.13}
$$

where the middle matrix containing the cross-section area A, first moment of area $S_{xx,yy,zz}$, and the second moment of area, $I_{xx,yy...}$, is called the fourth tensor of inertia.

The fourth tensor of inertia can be simplified if a *centroidal* reference system is adopted, which makes first order of area and the product moments of area terms equal to zero. The centroidal reference system is centred on the beam's *barycentre* which is where the cross sectional area, Ω, of the beam has its midpoint. The diagonal fourth tensor of inertia then becomes

$$\begin{Bmatrix} N_c \\ M_{zc} \\ -M_{yc} \end{Bmatrix} = E \begin{bmatrix} A & 0 & 0 \\ 0 & I_{zczc} & 0 \\ 0 & 0 & I_{ycyc} \end{bmatrix} \begin{Bmatrix} k_{xc}^{xc} \\ k_{xcxc}^{yc} \\ k_{xcxc}^{zc} \end{Bmatrix} \tag{5.14}$$

where the subscripts c denote that the properties are defined in the centroidal coordinate system, which for a symmetrical beam means in the geometrical centre of the cross-section.

The matrix system of equations in (5.14) can now be inverted to give the expressions for the membrane deformations and curvature in the central reference frame in terms of the stress resultants

$$k_{xc}^{xc} = \frac{N_c}{EA}, \quad k_{xcxc}^{yc} = \frac{M_{zc}}{EI_{zczc}}, \quad k_{xcxc}^{zc} = \frac{-M_{yc}}{EI_{ycyc}} \tag{5.15}$$

and the insertion of the above equations into Equation (5.9) gives the axial stress in terms of the stress resultants in the centroidal reference frame as

$$\sigma_{xcxc} = \frac{N_c}{A} + \frac{M_{zc}}{I_{zczc}} y - \frac{M_{yc}}{I_{ycyc}} z. \tag{5.16}$$

Finally, the equations in (5.15) are combined with the expressions for the membrane deformations in Equation (5.8) to give the relations between the vertical displacement and cross-section rotation, called the *elastica*, as

$$\begin{cases} \dfrac{\partial^2 u_{yc1}}{\partial x_c^2} = \dfrac{M_{zc}}{EI_{zczc}} \\ \dfrac{\partial^2 u_{zc1}}{\partial x_c^2} = \dfrac{-M_{yc}}{EI_{ycyc}} \\ \phi_{zc} = -\dfrac{\partial u_{yc1}}{\partial x_c} \\ \phi_{yc} = -\dfrac{\partial u_{zc1}}{\partial x_c} \end{cases} \tag{5.17}$$

Timoshenko beam theory

In the Timoshenko beam theory, the transverse shear deformations of the beam are taken into account, allowing the cross section to deform around the neutral plane as shown in Figure 5.1. In other words, the Timoshenko beam theory is built on the Euler-Bernoulli beam theory but with a relaxation of the third kinematic assumption [116].

According to the previously stated assumptions in the Euler-Bernoulli beam theory, the displacement field can be written as

$$u_y(x, y, z) = u_{y1}(x) \tag{5.18}$$

$$u_x(x, y, z) = u_{x1}(x) + \phi_y(x)z + \phi_z(x)y \tag{5.19}$$

$$u_z(x, y, z) = u_{z1}(y) \tag{5.20}$$

and the strain components can then be obtained by substituting Equation (5.18) - (5.20) into the geometrical relations as

$$\begin{cases} \epsilon_{xx} = \dfrac{\partial u_x}{\partial x} = \dfrac{\partial u_{x1}}{\partial x} + \dfrac{\partial \phi_z}{\partial x} y + \dfrac{\partial \phi_y}{\partial x} z \\ \gamma_{yx} = \dfrac{\partial u_x}{\partial y} + \dfrac{\partial u_y}{\partial x} = \phi_z + \dfrac{\partial u_{y1}}{\partial x} \\ \gamma_{xz} = \dfrac{\partial u_x}{\partial z} + \dfrac{\partial u_z}{\partial x} = \phi_y + \dfrac{\partial u_{z1}}{\partial x}. \end{cases} \tag{5.21}$$

The constitutive equations are then used to obtain the axial and shear stress components in the beam as

$$\sigma_{xx} = E\epsilon_{xx} = E\left(\frac{\partial u_{x1}}{\partial x} + \frac{\partial \phi_z}{\partial x} y + \frac{\partial \phi_y}{\partial x} z\right) \tag{5.22}$$

$$\sigma_{yx} = \kappa G\left(\phi_z + \frac{\partial u_{y1}}{\partial x}\right) \tag{5.23}$$

$$\sigma_{xz} = \kappa G\left(\phi_y + \frac{\partial u_{z1}}{\partial x}\right) \tag{5.24}$$

where G is the shear modulus defined as

$$G = \frac{E}{2(1+\nu)} \tag{5.25}$$

where ν is the Poisson ratio and κ is a shear correction factor which is related to the beam cross-sectional geometry [117] which is defined as

$$\kappa = \frac{10(1+\nu)}{12+11\nu} \tag{5.26}$$

for a rectangular cross-section and

$$\kappa = \frac{6(1-\nu)}{7+6\nu} \tag{5.27}$$

for a circular one.

The stress resultants are again obtained through integration of the axial stress and shear stresses over the cross-section area to give the axial force

$$N(x) = \int\limits_{\Omega} \sigma_{xx} \, \mathrm{d}\Omega = E \int\limits_{\Omega} \left(\frac{\partial u_{x1}}{\partial x} + \frac{\partial \phi_z}{\partial x} y + \frac{\partial \phi_y}{\partial x} z \right) \mathrm{d}\Omega, \tag{5.28}$$

bending moment around the z-axis

$$M_z(x) = \int\limits_{\Omega} \sigma_{xx} z \, \mathrm{d}\Omega = E \int\limits_{\Omega} \left(\frac{\partial u_{x1}}{\partial x} z + \frac{\partial \phi_z}{\partial x} yz + \frac{\partial \phi_y}{\partial x} z^2 \right) \mathrm{d}\Omega, \tag{5.29}$$

bending moment around the y-axis

$$M_y(x) = \int\limits_{\Omega} \sigma_{xx} y \, \mathrm{d}\Omega = E \int\limits_{\Omega} \left(\frac{\partial u_{x1}}{\partial x} y + \frac{\partial \phi_z}{\partial x} y^2 + \frac{\partial \phi_y}{\partial x} yz \right) \mathrm{d}\Omega, \tag{5.30}$$

shear force along the y-axis

$$V_y(x) = \int\limits_{\Omega} \sigma_{yx} \, \mathrm{d}\Omega = \int\limits_{\Omega} \kappa G \left(\phi_z + \frac{\partial u_{y1}}{\partial x} \right) \mathrm{d}\Omega = \kappa G \left(\phi_z + \frac{\partial u_{y1}}{\partial x} \right) A, \tag{5.31}$$

and shear force along the z-axis

$$V_z(x) = \int\limits_{\Omega} \sigma_{xz} \, \mathrm{d}\Omega = \int\limits_{\Omega} \kappa G \left(\phi_y + \frac{\partial u_{z1}}{\partial x} \right) \mathrm{d}\Omega = \kappa G \left(\phi_y + \frac{\partial u_{z1}}{\partial x} \right) A. \tag{5.32}$$

As with the EBBM, the above equations are expressed in a centroidal reference system which reduces the axial force and bending moments to

$$N_c = \int\limits_{\Omega} E \frac{\partial u_{xc1}}{\partial x_c} \, \mathrm{d}\Omega = EAk_x^x, \tag{5.33}$$

$$M_{zc} = EI_{ycyc} \frac{\partial \phi_{yc}}{\partial x_c}, \tag{5.34}$$

$$M_{yc} = -EI_{zczc} \frac{\partial \phi_{zc}}{\partial x_c}. \tag{5.35}$$

The elastica for the Timoshenko beam theory then becomes

$$
\begin{cases}
\dfrac{\partial \phi_{zc}}{\partial x_c} = \dfrac{M_{yc}}{EI_{ycyc}} \\[2ex]
\dfrac{\partial \phi_{yc}}{\partial x_c} = \dfrac{-M_{zc}}{EI_{zczc}} \\[2ex]
\dfrac{\partial u_{yc1}}{\partial x_c} = \dfrac{V_{yc}}{\kappa GA} - \phi_{zc} \\[2ex]
\dfrac{\partial u_{zc1}}{\partial x_c} = \dfrac{V_{zc}}{\kappa GA} - \phi_{yc}.
\end{cases}
\tag{5.36}
$$

With the basic concepts of the Timoshenko beam theory and finite element method described above and in Appendix C, the implementation of the higher fidelity TST shaft model can now be described in the next section. The model used is built on the Timoshenko finite element beam theory described above expanded to three dimensions with three displacement and three rotational degrees of freedom on each node.

5.2 Construction of the TST shaft model using the FE method

The TST drivetrain model presented in this thesis was constructed by letting the main shaft of the turbine be represented by several Timoshenko beam elements with circular cross-sections. The elements were aligned with the shaft centre-axis as shown in Figure 5.2 making the geometry of the model one-dimensional while still allowing deformation and rotation in all three space dimensions.

The geometric attributes of the shaft were specified by the location of the element's nodes and the elemental cross-sectional diameters. The nodes were placed at points of interest, such as at the axial locations of diameter changes of the shaft, where the cross-sectional diameter of each element influenced the shaft's bending resistance expressed in the stiffness matrix in Equation (C.35), its shear deformation in Equation (C.33) and its second moment of area. The nodal positions were also placed at the bearing support points of the shaft, in order to obtain the external forces they were subjected to through representing the bearings as sets of linear springs as described in Section 5.2.1.

Figure 5.2 shows an illustration of the FEM representation of an example TST shaft consisting of 10 nodes and 9 elements, with two of the nodes representing bearing locations as seen by the linear spring constraints. The figure shows that the input loads derived from the BEMT model are applied to the node in the origin in the four degrees

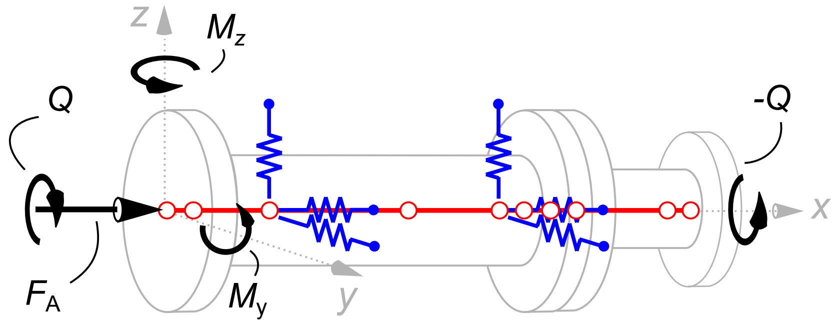

Figure 5.2: A tidal stream turbine main shaft as represented by the multi-beam FEM model. Here, the beam elements are shown in red with the nodes being shown as white dots. The input loads derived from the unsteady BEMT model are given in four degrees of freedom as the axial rotor thrust, F_A, the axial torque, Q, and the two rotor out-of-plane bending moment components, M_y, and M_z. The shaft bearing flexibilities are represented by linear springs (blue), where the torsional springs are not shown.

of freedom of shaft thrust, F_A, shaft torque, Q, rotor out-of-plane bending moment z-component, M_z and y-component M_y. The end node is constrained in the rotation around the x-axis, subjecting it to a reactive torque of $-Q$, under the assumption that a spur-geared gearbox is used which does not impart a thrust component. In addition, the self-weight load component of the shaft is applied to all nodes to account for the deformations and bearing loads brought on by it.

In order to keep the TST drivetrain model as computationally efficient as possible, a quasi-static formulation was adopted meaning that each time-step was simulated using the steady-state formulations presented in the previous section. Furthermore, since the shaft is symmetrical around its axis, the rotation of it is ignored as the load propagation to the bearings will be equivalent for a non-rotating shaft. The implication of this approach is that no inertial effects are taken into account on the shaft loading, although this is believed to be of negligible consequence for TST applications as the rotational period of the devices are in the slower range.

5.2.1 Shaft bearing representation

The shaft bearings are the most loaded components in a TSTs drivetrain, and as such, they must be engineered to withstand the large thrust forces generated from the rotor as well as the radial and torsional operating loads. The variations of the load magnitude and directionality is also likely to be a major influence in the expected life of the bearings. As a consequence, the accurate prediction of the response of the bearings operating under conditions with high load magnitudes, variations and directionality becomes a complex modelling problem.

The most commonly used types of bearings in TST at the point of writing are rolling element types as shown in Figure 2.9. These types of bearings are surprisingly difficult components to model using the FE method since they contain moving parts and several contact surfaces. This requires the geometry of the bearing to be highly discretised in order to resolve the moving contact points and deformations [79]. This direct simulation approach is however usually only taken to investigate the detailed stresses inside a bearings raceways and rollers, and since it was too computationally demanding for the purposes of this investigation, the bearings were represented as simplified spring elements in the TST drivetrain model.

The linear spring bearing modelling was performed as by Peeters [79] and Vinayak et al. [118] where the bearing translations were restricted isotropically by three longitudinal springs in the x, y and z-directions and the rotations were restricted by torsional springs in the same manner as shown in Figure 5.3. The bearing model thus requires three stiffness values for the bearing in the translational degrees of freedom, $k_{\text{long},x}$, $k_{\text{long},y}$ and $k_{\text{long},z}$, as well as three torsional stiffness values, $k_{\text{tors},x}$, $k_{\text{tors},y}$ and $k_{\text{tors},z}$. The torsional stiffness constant around the x-axis was set to zero as the shaft was unrestricted in the axial rotation degree of freedom. The bearing stiffness effects were then included in the FEM model as linear spring relations where the nodal deformation was related to the force by $d = F/k$ and substituted into the global displacement vector in Equation (C).

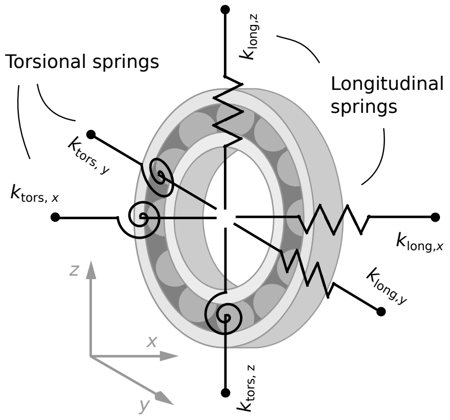

Figure 5.3: The shaft bearing flexibility was modelled using six linear springs for each bearing, three lateral and three torsional. The lateral spring constants could be estimated using the method described in Section 5.2.1, but the torsional stiffness constants had to be supplied by the bearing manufacturer. To allow unconstrained movement around the axis, the $k_{\text{tors},x}$ value was set to zero.

The method of representing the bearing flexibility in the drivetrain model by linear springs allowed the deformations, reaction forces in radial and axial directions and bending moments for the bearings as a whole to be efficiently obtained. The inclusion of the bearing flexibility was also vital to the replication of the dynamics of the drivetrain

[119], as the bearings could move and rotate as the shaft deformed under the loads.

However, the linear spring model has limited validity in cases where the load variations are extremely large. This is related to the fact that the stiffness of a bearing is inherently non-linear due to the Hertzian deformations of the rolling elements and raceways. As the load on the bearing increases the roller is pressed into the raceway, increasing the contact area and the number of rollers that are loaded, which changes the stiffness constant. This problem was overcome in this thesis by assuming linear bearing stiffness over the expected load range, which minimised the error caused.

Conversely, if a modal analysis had been performed on the shaft, the correct non-linear bearing stiffnesses had to be used as the modes and transient vibrations are sensitive to these inputs. The investigation of quantifying the actual sensitivity of the shaft model loads to the linear versus non-linear bearing stiffnesses are stated as recommendations for future work in Section 7.4.

Estimation of bearing stiffness constants

Since bearings deflect when loaded, their kinematic behaviour is similar to that of mechanical springs [119]. The stiffness is however a complex function of the bearing housing, raceways, preload, the rolling elements and their position, which makes the flexibility highly dependent on the bearing design and load conditions.

As was explained in the previous section, the method chosen to represent the bearing flexibility required six values of stiffness constants, three for the translational flexibility and three for the rotational flexibility. Since the determination of these constants can be a difficult and time-consuming task, values supplied by the bearing manufacturer can be used to assure that the right stiffness is given to the bearings used.

It is nevertheless worth mentioning that there exists a method to approximate the radial and axial stiffness constants of a bearing using its geometrical properties as presented by Gargiulo [120]. Using the notation presented in this thesis, the method gives the two off-axis stiffness constants $k_{\text{long},y}$ and $k_{\text{long},z}$ as well as the axial stiffness constant $k_{\text{long},x}$. For reasons of completeness, the equations for this approximative method are given in Table 5.1.

5.2.2 The ANSYS Parametric Design Language (APDL)

The drivetrain model presented in the previous sections can be executed using any general FEM solver. For the work done in this thesis, the model was solved using the commercial simulation environment ANSYS Parametric Design Language (APDL) [1],

Table 5.1: Estimation of the linear stiffness constants for rolling element bearings as reproduced from Garguilo [120].

Bearing type	Radial bearing stiffness k_r [lb/in.]	Axial bearing stiffness k_r [lb/in.]
Deep-groove or angular-contact radial ball	$0.0325 \cdot 10^6 \sqrt[3]{DF_r Z^2 \cos^5 \alpha}$	$0.0949 \cdot 10^6 \sqrt[3]{DF_a Z^2 \sin^2 \alpha}$
Self-aligning ball	$0.0203 \cdot 10^6 \sqrt[3]{DF_r Z^2 \cos^5 \alpha}$	$0.0593 \cdot 10^6 \sqrt[3]{DF_a Z^2 \sin^5 \alpha}$
Thrust ball	-	$0.0789 \cdot 10^6 \sqrt[3]{DF_a Z^2 \sin^5 \alpha}$
Spherical roller	$0.0921 \cdot 10^6 \sqrt[4]{F_r \ell^2 Z^3 \cos^7 \alpha}$	$0.308 \cdot 10^6 \sqrt[4]{F_a \ell^2 Z^3 \sin^7 \alpha}$
Cylindrical or tapered roller	$0.300 \cdot 10^6 F_r^{0.1} Z^{0.9} \ell^{0.8} \cos^{1.9} \alpha$	$1.28 \cdot 10^6 F_a^{0.1} Z^{0.9} \ell^{0.8} \sin^{1.9} \alpha$

D = rolling element diameter [in.]
F_r = external radial force [lb]
F_a = external axial force [lb]
ℓ = effective roller length [in.]
Z = number of rolling elements
α = contact angle [rad]

due to its high level of modifiability and generality. APDL is a general purpose FEM solver for stress, thermal, modal and fatigue simulations which has the ability to be run in batch-mode which was well suited for the time-stepping simulations performed in Chapter 6.

The definition of the TST drivetrain model's geometrical mechanical properties was performed in APDL using so called *direct generation* where the location of each node and element as well as the element properties are specified by the user [121]. This is in contrast to the more common *solid modelling* technique where the geometry is automatically discretised, or *meshed*, and the nodes and elements are located by the software's algorithms. In a simple geometry as for the drivetrain shaft and bearings, the direct generation method has the advantage of being simpler, providing greater control and being more cost effective. This kept the drivetrain model general and capable of simulating many different shaft and bearing configurations.

The execution of the model in the APDL environment was performed using the built-in *scripting* function where the geometry, material properties and load conditions were input as a simple text file. This allowed the model to be run in batch mode, where one load-state file was generated from the instantaneous BEMT loads for each time-step and the program ran each file as a steady-state problem to reduce computing time and finally compiled the load histories once converged.

The construction of the main shaft of the model was performed using the pre-defined cylindrical Timoshenko beam elements 'PIPE288' and the bearing's stiffness properties were modelled using the linear spring elements 'COMBIN14'. The details of these elements and their settings are given below.

ANSYS Timoshenko pipe element (PIPE288)

The PIPE288 element, available in the APDL library of elements, is a three-dimensional, two-node element based on Timoshenko beam theory which includes shear-deformation effects [122]. The element comes pre-defined with a circular pipe cross-section defined by an inner and outer diameter. Each node has six degrees of freedom where three are translational in the x, y, and z-direction respectively and three are rotational around each axis. The PIPE288 element can be used for moderately thick pipes and it is recommended that a defined 'slenderness ratio' of $(GAL^2)/EI$, based on the shear deformation factor in Equation (C.33), should be kept above 30 (29.27 for the shaft used in the later study) to assure that the its use is appropriate. The parameters in the previous equation are the shear modulus G, cross-sectional area A, member length L, Young's modulus E and second moment of area I, and the turbine shaft gave an appropriate value.

Table 5.2: Input options for the Pipe288 beam element used in the APDL code and their meanings.

Element options	Value	Description
KEYOPT(3)	2	Quadratic shape functions
KEYOPT(4)	2	'Thick pipe' theory used
KEYOPT(7)	3	Output sectional values extrapolated to nodes
KEYOPT(9)	2	Output max stress/strain at each integration point and section node
KEYOPT(11)	3	Additional values of extrapolated quantities output to section nodes

The shape functions used along the length of the Pipe288 element were set to quadratic, meaning that the element had an internal node for the interpolation of the nodal values across the element. Using this option, two points of integration were used for the element solution quantities resulting in linear variations of the calculated values along the element length. The wall thickness of the elements were also set to half of the corresponding shaft diameters which gave it a solid cross-section.

Presented in Table 5.2 is a summary of the options used for the Pipe288 element in the APDL batch-script.

Ansys linear spring-damper element (Combin14)

The linear spring-damper element Combin14, available in the APDL library, is a flexible element capable of representing longitudinal or torsional flexibility in one, two or three-dimensional applications. For the purpose of modelling the bearing stiffness in the TST drivetrain system, each of the six degrees of freedom of bearing flexibility was represented by *one* Combin14 element capable of deforming in the corresponding degree of freedom. The damping capability of the elements was disabled for the purpose of this thesis.

The Combin14 only needs a stiffness constant as its input along with the specification of its allowed one-dimensional direction of action. For the longitudinal springs representing the bearings axial and radial stiffnesses, the stiffness constant is given with units of Force/Length and the torsional springs, representing the bearings torsional stiffness, the constant has the units Force·Length/Radian. Once the allowed one-dimensional degree of freedom of the spring element has been defined in the nodal coordinate system (global), the orientation and length of the element has no importance and it can be defined as having zero length.

The shape-functions applied to the element are linear and the stiffness-displacement

Table 5.3: Input options for the Combin14 linear spring element used in the APDL code and their meanings.

Element options	Value	Description
KEYOPT(1)	0	Linear solution
KEYOPT(2)	1	1-D longitudinal spring (UX Degree of freedom)
KEYOPT(2)	2	1-D longitudinal spring (UY Degree of freedom)
KEYOPT(2)	3	1-D longitudinal spring (UZ Degree of freedom)
KEYOPT(2)	4	1-D torsional spring (ROTX Degree of freedom)
KEYOPT(2)	5	1-D torsional spring (ROTY Degree of freedom)
KEYOPT(2)	6	1-D torsional spring (ROTZ Degree of freedom)

relation is represented in Equation (C) where the element's degree of freedom components in the $\overline{u}$-vector are related to the stiffness constant by Hooke's law.

The settings for the Combin14 spring-damper elements used in the drivetrain model are given in Table 5.3.

5.3 Bearing life calculations using the L_{10} method

As was mentioned in the 4th research objective in Section 1.1.2, the fatigue life of the main bearing was in this thesis considered to be an indicator of the amount of fatigue damage that a TST drivetrain has sustained in general. The main bearing will in most drivetrain layouts be the single most loaded component in the whole turbine shaft system, which will be even more prominent when the blades of the turbine are assumed rigid. This means that the rotor loads are fully translated into the turbine's shaft, which is the case for the presented BEMT method.

Section 2.4.3 of the literature review identified three main challenges when using rolling element bearings in marine energy applications. These challenges can be summarised as high reliability requirements, unpredictable and highly varying loads and contamination and corrosion from the sea-water. Even though several possible failure modes were identified to be present for the TST bearings, the method of estimating the bearing life presented in this section only accounts for the mechanical raceway fatigue. This allow the effect of the varying inflow from the marine environment to be related to the bearing's, and ultimately the whole turbine's, fatigue life.

The technique used to calculate the preliminary bearing fatigue life was the commonly used L_{10} method, originally published by Lundberg & Palmgren [68]. This method forms the basis of the international standard ISO 281 [70] on the dynamic rating life on roller bearings, and has over the years been modified with adjustment factors to include the effects of desired reliability, lubrication, contamination and more, although these additions are not utilised here. The method is also widely cited in the wind turbine industry where it has been incorporated in several technical design standards [11, 26, 66]. Due to its establishment within the industry for bearing fatigue evaluations and its frequent occurrence in the design standards, it was selected as the preliminary method of bearing evaluations in this thesis.

The main issue that the L_{10} method addresses is that if a large set of identical bearings are run under the same load conditions, there will be large variation in their time to failure from raceway fatigue failure [123]. Therefore, fatigue failure is defined as occurring when there is a 10 percent chance that a bearing experiences the first onsets of raceway or rolling element spalling from sub-surface originated fatigue. The length of time for this failure to occur is defined as L_{10} millions of revolutions as

$$\mathrm{L}_{10} = \left(\frac{C}{P_{\mathrm{eq}}}\right)^{p} \tag{5.37}$$

where C is the dynamic load rating of the bearing defined as the constant load which gives the bearing a life of one million revolutions, P_{eq} is the equivalent load on the bearing and p is the load-life exponent assuming the value of 3 for ball bearings and 10/3 for roller bearings [70]. Alternatively, if the rotational speed of the bearing is constant, the L_{10} life can be expressed in operating hours as

$$\mathrm{L}_{10\mathrm{h}} = \frac{10^{6}}{60n}\left(\frac{C}{P_{\mathrm{eq}}}\right)^{p} \tag{5.38}$$

where n is the rotational speed in RPM.

For bearings experiencing both axial and radial loading simultaneously, the equivalent load, P_{eq}, is defined as the hypothetical constant load acting in one direction on the bearing, radially for radial bearings and axially for thrust bearings, that would have the same effect on the bearing life as the actual loads. The equivalent load in Equations (5.37) and (5.38) were defined as

$$P_{\mathrm{eq}} = XF_{\mathrm{r}} + YF_{\mathrm{a}} \tag{5.39}$$

where F_{r} and F_{a} are the radial and axial external bearing loads and X and Y are its radial and axial load factors. The values of X and Y vary depending on the bearing design and arrangement and an extensive list of values can be found in the ISO 281 standard [70] or are supplied by the bearing manufacturer.

5.3.1 Palmgren-Miner's rule for linear damage

The L_{10} method in its original form, shown in Equations (5.37) and (5.38), is derived from empirical data of bearings operating under constant loading conditions. As such, the theory must be modified to accommodate varying loads.

The Palmgren-Miner rule or the 'linear damage rule' assumes that, for a bearing operating under varying load conditions, the load can be discretised into several *duty cycles* of constant loading as shown in Figure 5.4 and the damage caused in each cycle can be linearly added. For each duty cycle with constant load $P_{\text{eq}1}, P_{\text{eq}2}$ and so on, the bearing will have a corresponding L_{10} life related to that load level. It is then assumed that in each duty cycle, a portion of the bearing's life is consumed which equals the number of revolutions in the duty cycle divided by the corresponding revolutions in its L_{10} life. As such, a bearing that is subjected to a certain duty cycle load for M_1 million revolutions where it has a life of $L_{10,1}$ million revolutions consumes $M_1/L_{10,1}$ of its life as defined in Zaretsky [124].

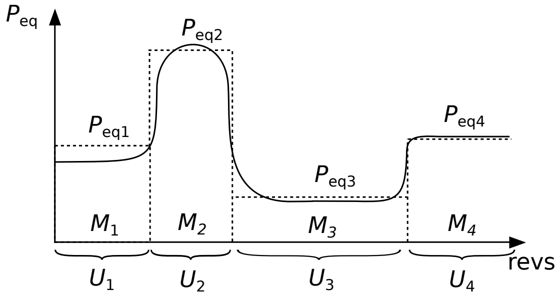

Figure 5.4: The varying equivalent bearing load discretised into four duty cycles (bloc loading in this case) using the Palmgren-Miner rule. Each duty cycle sees a constant bearing load of $P_{\text{eq}1}, P_{\text{eq}2}$ etc. during the corresponding number of revolutions M_1, M_1 etc. The cycle fraction of each duty cycle are calculated as $U_1 = M_1/M_{\text{tot}}, U_2 = M_2/M_{\text{tot}}$ and so on where M_{tot} is the total number of bearing revolutions in the time-series.

Summation of the damage from all duty cycles in the bearings operational life gives the damage D as

$$D = \frac{M_1}{L_{10,1}} + \frac{M_2}{L_{10,2}} + \frac{M_3}{L_{10,3}} \dots \tag{5.40}$$

where failure is assumed to occur when the damage reaches the value of unity. By defining the life *cycle-fractions* for each duty cycle, U_1, U_2 and so on, as the number of revolutions in the cycle divided by the total number of revolutions in the bearing's lifetime, the L_{10} life for a bearing operating in varying load conditions can be expressed as

$$\mathrm{L}_{10} = \frac{1}{\frac{U_1}{\mathrm{L}_{10,1}} + \frac{U_2}{\mathrm{L}_{10,2}} + \frac{U_3}{\mathrm{L}_{10,3}} \dots}. \tag{5.41}$$

5.3.2 The L-N curve

As was discussed in the literature review, fatigue failure is caused when a structure is repetitively loaded and unloaded which causes microscopic crack formations in the material that grow until the structure suddenly fractures; the number of cycles until the failure occurs is defined as the fatigue life [125]. The fatigue life of a structure is a function of several parameters including the amplitude of the applied load fluctuations, their frequency, the geometry of the structure and material properties including micro and macroscopic imperfections.

Since fatigue life is such a complicated and stochastic mechanism, experimental data is often used to characterise the performance of a material by subjecting it to repetitive stress reversals and measuring the number of cycles before failure. The data of such experiments are commonly presented as the amplitude of the applied stress cycles on the material (S) as a function of the number of cycles to failure (N) on a logarithmic scale also known as a S-N curve [126]. These types of plots allow designers to estimate the expected life of a structure based on the amplitude of the monochromatic stress variations.

When considering the fatigue life of a uniformly loaded bearing, a stress reversal is assumed to occur in the outer raceway on every revolution, as is the basis of the L_{10} method. As an analogy to the S-N curve, a plot of the expected L_{10} bearing life (in millions of revolutions) can be created as a function of the applied load for a uniformly loaded bearing. Figure 5.5 shows the 'L-N curve' of a bearing with a specific dynamic load rating where Equation (5.37) is plotted against the revolutions to failure on a logarithmic axis.

As can be seen in Figure 5.5, the life of the bearing decreases with increasing applied loads in a logarithmic fashion, as is expected from the exponent in Equation (5.37), and it is this curve that is used as a look-up for the calculation of the cumulative damage in the Palmgren-Miner's rule in Equation (5.41).

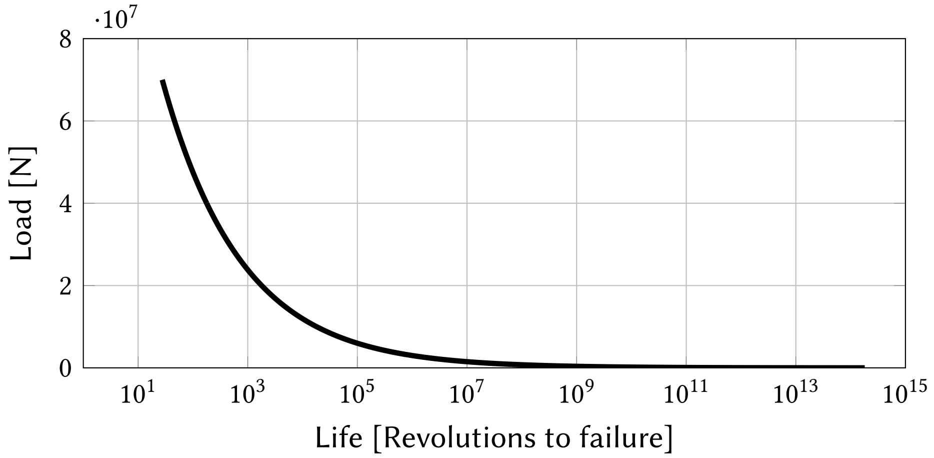

Figure 5.5: Graph showing the relationship between the operating load on a bearing of a specific rating and its L_{10} fatigue life, analogous to a S-N curve for a specific material. The graph shows a exponential decline in bearing life as the load increases.

5.3.3 Extrapolation of calculated bearing damage

Throughout this thesis, the selection of the methodologies and the design of the software used have been done in favour of computational efficiency and theoretical simplicity. Even so, the relatively fast convergence times of the unsteady BEMT and drivetrain FEM model are not sufficient to evaluate the fatigue damage of a TST over its whole operating life. It is therefore necessary to extrapolate the results obtained from shorter simulation runs of a turbine over several years of operation to obtain the total lifetime fatigue damage.

In the case of obtaining the fatigue damage on a turbine caused by its inflow conditions, oceanographic data detailing the wave and tidal occurrences for a specific site must be used in order to accurately define the inflow conditions and extrapolate the results. In this thesis, the oceanographic data were supplied by the British Oceanographic Data Centre in the form of time-series wave data consisting of significant wave height and zero-crossing period measurements over a three year collection period. It is suggested in the certification standard IEC 62 600 - Part 2 [11] that a minimum of 50 years worth of site met-ocean occurrences are used to assure that all the expected load-states are included in the study, but three years of data was deemed sufficient at this stage. Other types of wave-data may be used for this purpose as long as the necessary modifications are done to it according to the methodology of this thesis.

A two-dimensional histogram was then constructed, using the available wave-data, that showed the statistical distribution of the wave climate at the selected site by plotting the significant wave height against the wave period for each data point. The 2-D histogram was then discretised into a desired number of equally sized 'bins', where each bin represented a sea-state, and the total collection of sea-states which made up 90% of the data were included as environmental conditions in the study. This 2-D histogram is also known as an occurrence matrix which is frequently used in fatigue analysis the wind turbine industry.

Once each sea-state in the occurrence matrix had been simulated using the unsteady BEMT model, the bearing reaction loads obtained through the FEM drivetrain model and the bearing damage calculated using Equation (5.40), the time-to-failure of the bearing was calculated using extrapolation in a similar way as in Hayman [127]. This was performed by replicating the bearing loads for a period of time long enough to capture the full variational range for each sea-state and dividing the calculated damage of the time-series by the number of revolutions of the turbine in the time-series, assuming that the rotational speed was constant. This yielded the average damage per revolution for each time-series, which could then be multiplied by the number of revolutions per year, assuming that the distribution of sea-states was equal for every year, to give the annual damage contribution for each sea-state. Finally, the annual damage generated by each sea-state was multiplied by the 'occurrence factor' of each sea-state, derived by dividing the number of occurrences in each bin by the total number of data-points in the occurrence matrix. The equation for the annual damage of the bearing, D_{annual}, is given as

$$D_{\mathrm{annual}} = \sum_{\mathrm{sea-state}=1}^{i} \frac{D_i}{N_i} N_{\mathrm{annual}} \quad \mu_i \tag{5.42}$$

where D_i is the damage in the time-series of the i-th sea-state, N_i is the number of revolutions of the turbine in the time-series, N_{annual} is the number of revolutions in a year and μ_i is the occurrence factor of the sea-state.

The number of years to failure is then given as the inverse of Equation (5.42) as

$$\mathrm{YTF} = \frac{1}{D_{\mathrm{annual}}}. \tag{5.43}$$

The method of bearing damage extrapolation presented here does not take into account the variation of the tides in the determination of the annual damage due to limitations of scope. Instead, the tidal inflow is assumed as the greatest value that may occur at the given site, giving a worst-case scenario for the bearing damage. The tidal distributions could be included in further studies by adding an extra dimension to the occurrence matrix, where the tidal variations over the years is given.

5.3.4 Limitations of the L_{10} method

The main reason for selecting the L_{10} method to determine the bearing life of a TST in this thesis was that it was the most widely cited method and the most computationally efficient to implement. For the early stage investigations and comparative studies on turbine durability presented in the next chapter, the L_{10} method is deemed as a sufficient evaluation tool, albeit an approximate one. There are however a number of phenomena present in the dynamic loading situation of a TST operating in unsteady inflow that the L_{10} method does not incorporate, which are worth mentioning at this stage.

Since it was originally developed for the evaluation of bearings under constant load conditions, the L_{10} method has a limited capability of accounting for the highly varying load conditions present during TST operation. Even though methods exist to incorporate the different magnitudes of the loads at different times in the calculation of the bearing L_{10} life, such as the Palmgren-Miner method shown in Section 5.3.1, the actual *rate of change* in the material stresses will be ignored due to the assumption of constant loading within a duty cycle. The consequence of not including the rate of change in the loading of the bearings are unknown at the time of writing since there is, to the knowledge of the author, no experimental data available comparing the life of a bearing under truly varying load conditions to that of a bearing loaded ‘quasi-statically’.

Furthermore, the definition of a stress reversal in the L_{10} method becomes unclear when dealing with varyingly loaded bearings. This is because the fatigue characteristics of the raceway material of a bearing is determined through empirical studies of constantly loaded bearings, where a stress reversal is formed on every rotation by the moving rolling elements. This is in contrast to the stress reversals present in the external loading of a bearing operating in unsteady seas, where several stress reversals brought on by the operating load can be present for one revolution of the bearing. This creates a complicated pattern of the internal loading on the bearing, with several load signals superimposed on the raceway material, which is unaccounted for in the L_{10} method.

Finally, the L_{10} method is also limited in how it assumes that the radial loads on the bearing are in a constant direction; it will be shown in the next chapter that the radial loads have a large directional spread in most cases. The effects of this simplification can only be speculated upon at this point, and a thorough investigation into it is out of the scope of the work presented here. The effects of this latter assumption, and the others outlined above, are treated in greater depth in the discussion of the thesis in Section 7.3.

5.3.5 Maximum internal bearing contact stress post-processing algorithm

The maximum Hertzian contact stresses between the bearing's raceway and rolling elements are used in the next chapter to inform on the ultimate load case on a turbine in unsteady sea-conditions. This is performed as a post-processing exercise on the calculated external bearing loads using a method presented in the international standard IEC 61400-4 [66] and the algorithm is presented in Appendix B for reference.

5.4 Conclusions

This chapter has presented the details of a quasi-static drivetrain model with six degrees of freedom at each computational node which is a significant increase in fidelity compared to the purely torsional models commonly used in the industry. The model was based on a multi-beam FEM formulation which is a commonly used practice in naval architecture disciplines and is computationally efficient while still being able to incorporate the full range of expected loading on the drivetrain. Special attention was given to accurately represent the shaft-bearing flexibility and bearing reaction loads by modelling the bearing stiffnesses as linear springs. The efficiency and accurate representation of the load propagation made the presented drivetrain model suitable for investigating both the internal ultimate load distributions and for the fatigue analysis of a turbine. The chapter also introduced key concepts of structural mechanics used in later chapters of the thesis.

In order to make possible the investigation of the relationships between a turbine's expected lifetime and the given hydrodynamic load environment, as specified in the research objectives, a post-processing routine of the derived bearing reaction loads was presented in the form of the L_{10} method. This method was used to inform the bearing raceway sub-surface initiated fatigue life under the varying load conditions present in TST operation, which was to be used as an indicator of the turbine durability as a whole in the upcoming chapter. In addition to this, another post-processing method of the bearing loads was referenced which will be used to derive the maximum internal bearing contact stresses for ultimate load analysis.

With the drivetrain model specified, the entire load-path through a TST can now be modelled from the varying inflow from the wave-current models, to the hydrodynamic loads on the rotor, to the internal load distribution in the drivetrain, to the reaction loads in the shaft bearings and ultimately the internal stresses in the bearing's contact surfaces. The next chapter will make use of the presented set of models by investigating the internal dynamics on the drivetrain, along with the bearing fatigue life, as a function of the dominant input parameters specified in Chapter 4. This will be achieved by the means of a case study on a generic turbine, based on horizontal axis tidal turbines currently in prototype testing, that will give insight on how contemporary turbine designs are affected by the marine hydrodynamic load environment. Increased understanding of the relationships between a turbine's load environment and its durability will also help to inform designers on how to tackle the issue of component fatigue by identifying possible means of load mitigation.

Chapter 6

Case study on a generic horizontal axis TST exploring the drivetrain loads and fatigue life

> "The sea, once it casts its spell, holds one in its net of wonder forever."
>
> — Jacques Cousteau

The complexity regarding the hydrodynamic loading on tidal stream turbines has been stated repeatedly throughout this thesis. It has been shown in the sensitivity analysis that many of the variables involved in the physical loading process are interdependent and the path of causality is not always easily traced through the models. Indeed, the theoretical chapters of this thesis have shown that even the simplest representations of the processes involved require a reasonably complicated mathematical model. Due to these inherent complexities of the engineering problem of hydrodynamic loads on TSTs during unsteady operation, it is hard to generalise the outcome of the loading for a specific turbine design or operating climate. In other words, it is hard to make predictions in the likes of 'a rotor of x metre diameter will induce a thrust load of y kilonewtons', since the outcome will be dependent on the interaction of a multitude of design and environmental parameters.

For the sake of gaining valuable insight into the behaviour of TST loading and durability, it is the belief of the author that studying how the loads and durability change as *functions* of the input parameters will yield greater insight into the loading behaviour than studying the absolute values alone. For this reason, a case study on a generic TST operating in realistic sea conditions is presented in this chapter to conclude the thesis and to investigate the eponymous functional effects of the unsteady sea conditions on tidal turbine loads and durability. In keeping with the mantra that the input-output relationships of the phenomena will yield most insights into the loading behaviour, the conclusions drawn from the results will also be relevant over a wide range of turbine designs and inflow conditions.

The objectives of the case study can be listed as:

1. To investigate relationships between the identified primary input parameters and the loads on a tidal turbine and to show how the fatigue life of the main bearing varies as a function of these parameters.

2. To show that the rotor out-of-plane bending moment load component must be included as an input in the drivetrain model in order to accurately capture the full range of eccentric loads present within the shaft system.

3. To perform the study on a generic turbine design based on contemporary industry solutions that have shown higher levels of technology readiness (TRL) operating in realistic sea-conditions. This will keep the results relevant for the designs that the tidal stream sector is currently employing and highlight any possible obstacles and detrimental impacts from the marine inflow.

4. To demonstrate the applicability and the process of the methodologies outlined in previous chapters.

Presented in the following sections are the set-ups and executions of the theories presented in the methodology chapters including the inflow wave-models, unsteady BEMT model, drivetrain model as well as the L_{10} bearing life and ultimate bearing contact stress post-processes. The set-up of the inflow model involved the acquisition of sea-state data representative of a tidal location and creation of the occurrence matrix to determine the expected load states. The turbine geometric inputs were then determined from estimated average values of devices deployed in full scale at EMEC [2].

Finally, the results presented in this chapter constitute the main part of the original contribution of this thesis, along with the results from the sensitivity analysis. The analyses presented here were performed using two different load scenarios; one ultimate load case and one fatigue load case with a realistic distribution of sea-states. The results from the ultimate load case showed that there was an underprediction of the internal bearing stresses if the rotor out-of-plane bending moment was neglected in the drivetrain model and the bearing fatigue results showed a high dependency on the rotor size and inflow speed, and a discussion is presented to shed light on the processes behind the observed trends.

The following sections outline the set-up of the case study with the definition of the generic turbine layout and representative sea climate.

6.1 Definition of a generic horizontal axis TST

As was pointed out in Section 2.1, the current state of the tidal energy sector seems to have a favour towards three bladed, horizontal axis turbines based on the devices listed as having undergone pre-commercial testing at EMEC. It should be mentioned that it is not the intention of this thesis to regard these design choices as more suitable than any other; the selection of the ‘wind turbine’-esque design for the case study was merely aimed to reflect the majority of higher TRL devices currently seen in the industry.

Table 6.1 shows the four devices in which the generic turbine used in the case study was based on. These devices were the Atlantis MCT SeaGen turbine, the Andritz Hydro Hammerfest HS1000 turbine, the Alstom Oceade turbine and the Atlantis Resources AR-1000 turbine. Most values of the devices were found in publicly available literature although the drivetrain main shaft lengths, Shaft L, and the shaft diameters, Shaft Ø, had to be estimated from published images of the devices. The bottom entry of the table shows the average values of the parameters which were used to inform the geometry of the generic turbine for the study.

Table 6.1: The generic turbine design used in the case study was defined using the average values of the devices presented below. Each of the turbines listed in the table have seen large-scale prototype testing at the European Marine Energy Centre [2].

Device Name	Rotor Ø[m]	P_{Rated} [MW]	Rot. Speed [RPM]	U_∞ (Rated) [m/s]	Shaft L [m]	Shaft Ø[m]	Gearbox	Generator
SeaGen	16	0.7	12	2.4	~ 1.52	~ 0.31	Planetary	Induction
HS1000	21	1	10	-	~ 2.01	~ 0.489	Planetary	Induction
Oceade	18	1	14	2.7	~ 3.67	~ 0.723	Planetary	-
AR-1000	18	1	12.6	1.65	~ 2	~ 0.387	Planetary	Perm. Sync.
Average	18.25	1	12.15 RPM	2.25	~ 2.3	~ 0.478	Planetary	Induction

6.1.1 Ratings and rotor geometry of the generic turbine

The generic horizontal axis tidal turbine was defined as a three bladed rotor with a diameter of 16m rated at 2.5m/s inflow velocity. The hub of the turbine was specified as 2.4m diameter, which is the scaled version of the experimental Barltrop [99] turbine, giving blades of length 6.8m.

The rotational speed of the turbine was set to a constant value of 1.35rad/s (12.89 RPM) which would be consistent of a device using a constant speed control scheme and permanent magnet type generator. This put the turbine as having a TSR of 4.32, which was slightly higher than the optimum power capture TSR as can be seen in Figure 6.1a, although this did not affect the conclusions of the study which were based on relative comparisons and trends of the loads.

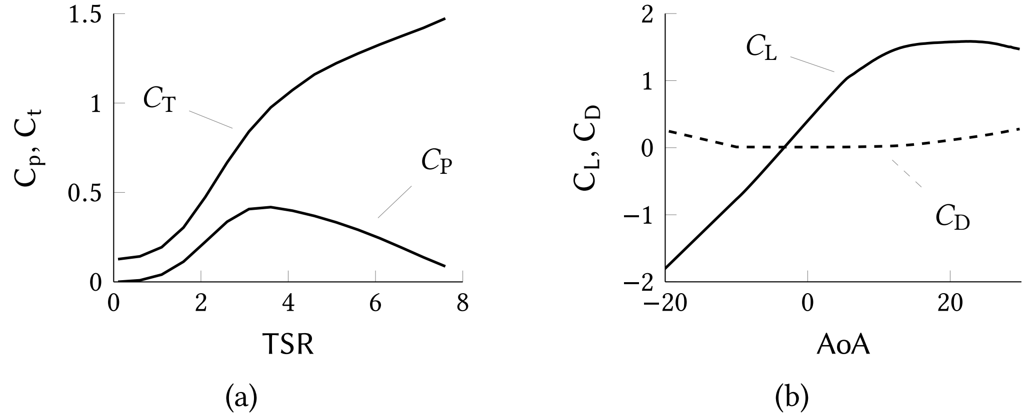

Figure 6.1: Power and thrust curves for the generic turbine plotted against the tip-speed ratio (a). These values were derived using the steady-state BEMT model and the airfoil performance data for the NRELs814 blade section (b) using Xfoil.

The blade section geometry selected for the turbine was the NRELs814 profile which is often quoted in TST research literature [17, 99, 107]. The blade-average Reynolds number calculated using the resultant velocity and chord distributions averaged over the blades for a flow speed of 2.5m/s was used to derive the performance curves for the blade sections using Xfoil. These results are shown in Figure 6.1b.

At last, the radial geometry distributions of the blades are shown in Figure 6.2 depicting the chord and twist distributions along the length of the generic turbine's blades. This data was the geometrically scaled-up version of the turbine presented in Barltrop et al. [99].

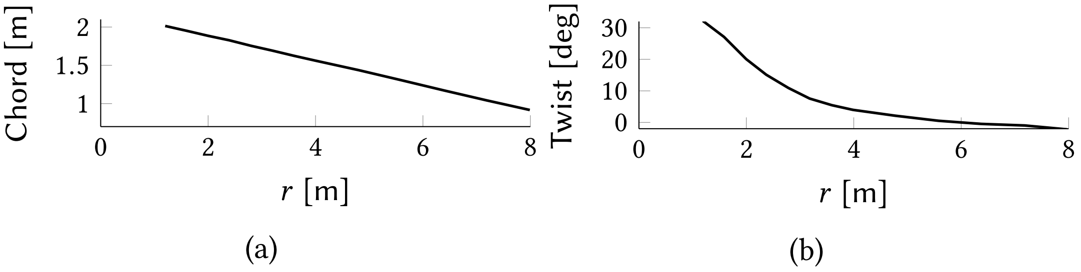

Figure 6.2: Chord (a) and twist (b) distributions for the blades of the generic turbine. The geometries are a geometrically scaled verion of the small-scale TST presented in Barltrop [99] as it represents the most fundamental form of a TST design.

6.1.2 Generic drive train layout based on contemporary industry solutions

Most tidal turbine developers regard the layout of their turbines to be proprietary information, meaning that it is hard to come across detailed plans about their internal designs. However, through studying publicly available images showing 'cut aways' of turbines listed in Table 6.1, it was possible to get a picture the design choices made in the drivetrain layouts.

The drivetrain of the generic TST was given a main shaft of solid cross-section connected to the rotor with bolted flange connections. The main shaft consisted of two sections where the aft part, which connected to the gearbox, had a smaller diameter and all connections were bolted to the end flanges (solid connection between flanges in the FE model). The shaft operated at constant RPM and the gearbox was assumed to only input a reactive torque to the shaft.

Rolling element bearings were chosen as shaft supports. A three-bearing arrangement using a spherical roller bearing as the main bearing and radial cylindrical bearings as the mid bearing and and aft bearings was selected. The main bearing was a semi-locating axial spherical roller bearing capable of withstanding both axial and radial loads while accommodating shaft deflections by permitting the inner raceway to swivel around its central axis by a few degrees. The mid bearing was chosen as a non-locating cylindrical journal bearing which acted as a radial support for the main shaft and prevented sag. The aft bearing was a semi-locating cylindrical journal bearing, mounted in reverse to constrain the shaft in the negative x-direction, which acted to further support the shaft in the radial direction and to protect the drivetrain from load reversals on the rotor.

The sizing of the bearings and the selection of the specific serial makes based on the L_{10} lives derived from the expected steady-state forces are also shown in this Section.

Sizing of the main shaft

The length of the main shaft was specified as 2828mm based on an estimate from the turbines presented in Table 6.1. However, the diameter of the shaft was determined using the Lloyd's Register certification standard for ship shaft design [128] with the steady-state operating loads on the turbine as input. This gave a minimum diameter of 540mm which was consistent with the estimated values in Table 6.1 and was therefore used as the diameter of the first section of the generic shaft. The second section was given a diameter of 420mm as suggested by the equations in the standard [128]. The

Table 6.2: Material properties defined for the main shaft as given as inputs to the FE drivetrain model. The values are based on typical characteristics of naval steel.

Property	Young's modulus (E)	Poisson's ratio (ν)	Density (ρ)	Yield strength
Value	200 [GPa]	0.265 [-]	7850 [kg/m^3]	0.38 [GPa]

two flange connections on the first section of the shaft were given a diameter of 880mm while the connecting flange to the gearbox had a 800mm diameter to assure that adequate space was available for boltin. All flanges had a thickness of 60mm and the dimensions of the main shaft are shown in Figure 6.3.

Main shaft layout dimensions and material properties

The Figures 6.3 and 6.4 show the dimensions of the shaft and bearing locations as well as a 3-D drawing of the main shaft for easier size comparison. Here it can be seen that the main bearing (B1) is inset 400mm to accommodate any possible seals that would be used in a dry hull system. Also, from a construction perspective, the flanges would have to be welded on after the bearings were fitted.

It is emphasised that the design of the shafting system for the generic TST has not in any way been optimised for its use, nor has any consideration gone into the economical aspect of this design. The presented layout is only intended as a *plausible* design choice and is meant to reflect an average of the present state-of-the-art designs with the use of commonly available off-the-shelf components.

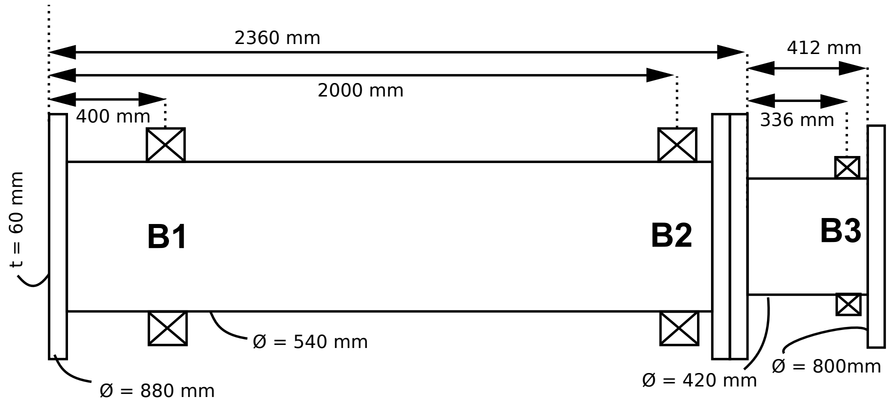

Figure 6.3: Dimensions of the main shaft of the generic TST along with the locations of the three shaft bearings. The flange connections are assumed to be bolted with non-deformable bolts with the same diameter as the flange thickness.

A material was defined for the shaft having engineering properties typical of stainless steel used for naval purposes. These material properties are shown in Table 6.2 and the structural properties related to the geometry of the beam elements, as

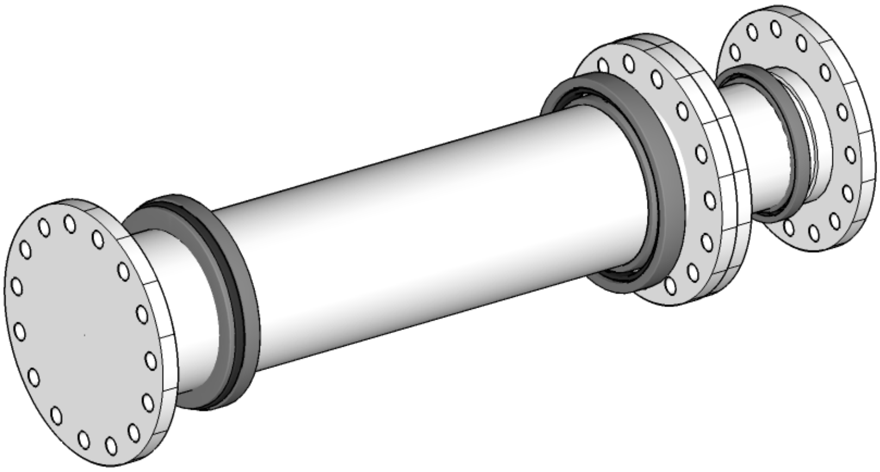

Figure 6.4: 3-D CAD sketch of the generic turbine's main shaft showing the three bearings for size comparison. The aft bearing of the shaft can technically be considered to be a part of the gearbox as it resides within the planet carrier, as seen in Figure 6.9.

shown in Chapter 5, were calculated automatically by the ANSYS APDL solver.

Sizing of the shaft bearings

The selection of the shaft bearings was done using the on-line bearing sizing tool MEDIAS ONLINE [129] which is based on the standard L_{10} method and gave access to a wide range of off-the-shelf bearing designs by the manufacturer Schaeffler UK [130]. The load cases that were given as inputs to the sizing tool were derived from a steady-state simulation of the turbine operating in 2.5m/s inflow with the various maximum wave velocities added to the inflow speed. Advice was also taken from the design engineers at the bearing manufacturer on how to define the shaft-bearing arrangement to meet the expected load conditions.

The shaft bearings selected for the case study are shown in Table 6.3. It can be seen that the inner diameters are not fully the same as the shaft diameters, but the bearing properties will nevertheless be close to bearings of the exact size. The reason that the shaft diameter was used to size the bearings and not vice-versa was that the shaft was designed to withstand loads just above the expected average load range to give non-conservative results in the study. The stiffness values of the main bearing selected were considered proprietary information by the bearing manufacturer, and could therefore not be published in this thesis. However, a check using the approximative method presented in Section 5.2.1 gave good agreement with the values supplied by the manufacturer, allowing for the approximative values to be used in replications of this study.

Table 6.3: Properties of the three shaft bearings used in the generic turbine's drivetrain layout that together form a fully locating configuration. The dynamic rating of the main bearing was used in the calculation of its fatigue file in combination with the dynamic load factors given in Table 6.4.

Bearing series	292/530-E1-MB	NU19/560-M1	SL181884-E
Designation	B1	B2	B3
Bearing type	Spherical roller	Radial cylindrical	Radial cylindrical
Restriction	Semi-locating	Non-locating	Semi-locating
Inner Ø	530mm	560mm	420mm
Dynamic rating, C_a, C_r,	3×10^6N	1.46×10^6N	6.8×10^5N
Static rating, C_{0a}, C_{0r},	1.54×10^7N	2.95×10^6N	1.42×10^6N

Main bearing technical specifications

The geometrical and operational details of the main spherical roller bearing, used in the calculations of the maximum internal contact stress, are presented in Table 6.4. It should be noted that the *static* axial and radial load factors, X_0 and Y_0, are used in the internal stress calculations, as they have been derived for bearings that were not subjected to dynamic loading effects on the rollers as recommended in the design standard IEC 61400-4 [66].

Table 6.4: The values for the main 292/530-E1-MB bearing parameters used in the calculation of the maximum internal bering stress were provided by the bearing mainufactorer Schaeffler UK and descriptions of the parameters are found in Appendix B. Note the use of static load factors for the stress calculations.

Main bearing parameters	Type	Ø	X_0	Y_0	α_0	Z	e	L_{we}	D_w	D_{pw}
Value	Spherical roller	710mm	1	2.7	47°	42	0.55	57.5mm	43.2mm	656.15mm

6.2 Definition of representative sea-states from experimental data

With regards to subjecting the generic TST to load cases that are expected to be present in real tidal sites, experimental wave-data collected from the North Sea using an accelerometer-wave rider buoy was used to synthesise the sea-states. The wave data was collected by the UK Offshore Operators Association, provided by the British Oceanographic Data Centre [93] and funded by the Institute of Oceanographic Sciences and included significant wave height and average zero-crossing periods over a three year span (1977 - 1979).

The hypothetical site chosen for the generic turbine was at the northern part of the 'Pentland Firth Tidal Area of Interest' as shown on the map in Figure 6.5. By consulting the on-line Atlas of UK Marine Renewable Energy [131], the chosen site was found to have a mean depth of 45m and a mean spring peak flow of 2.19m/s as well as being fully exposed to the part of the North Sea between the Orkneys and Shetland.

Taking the environmental site-conditions from the northern Orkney site as a basis, the surface inflow speed for the case study was set as 2.5m/s for every load case investigated. Therefore, this study did not take into account the occurrence of the lower tidal flow speeds, making the absolute values of the results presented later pessimistic, although it will not have an effect on the general trends shown.

The site-depth was set to 50m with the turbine operating mid-way up the water column at 25m depth.

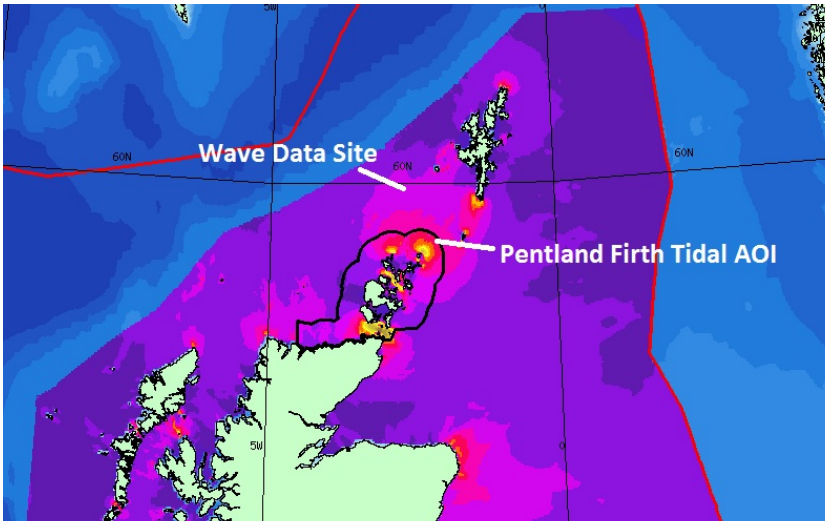

Figure 6.5: The assumed hypothetical site for the generic turbine was chosen off the north east coast of the Orkney islands, Scotland. This site provided a high maximum flow speed and a suitable average depth. The representative wave data had to be taken from the site marked on the map as there was no public data for the Pentland Firth Tidal Area of Interest (AOI). Map reproduced from `http://www.renewables-atlas.info/`.

6.2.1 Experimental wave-data

Unfortunately, no publicly available experimental wave data could be found for the exact location of the northern Orkney site in the Pentland firth tidal area of interest. Instead, the wave-rider buoy data that was used in the case study was collected between the Orkneys and Shetland as marked on the map in Figure 6.5; it was assumed that the occurrence of the sea-states would be similar between the selected tidal site and this data collection site. The wave-data is presented in histogram form for both the significant wave height and the average wave period in Figure 6.6 along with the statistics of the distributions shown as red lines.

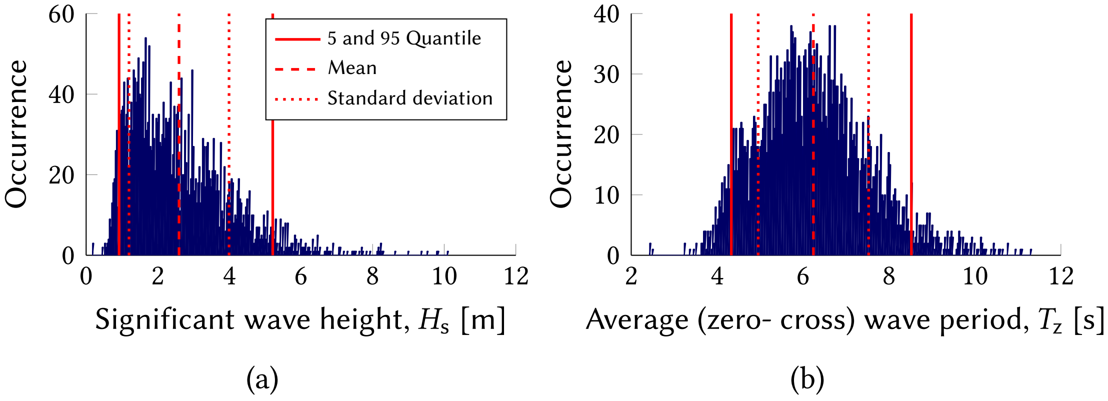

(a)

(b)

Figure 6.6: Histograms of the wave data used showing the statistical distributions of the significant wave height (a) and average wave period (b) along with additional statistics plotted in red. The data was collected over three years and each data-point was created by averaging 12 minute recordings every 3 hours.

6.2.2 Creation of occurrence matrix

To illustrate the derivation of the occurrence matrix from the wave data the three years of data is first presented in the density scatter plot in Figure 6.7a. Here, each measurement point is plotted with the significant wave height as a function of the average zero cross period. The red areas in Figure 6.7a indicate sea-states of higher occurrence and the blue areas indicate no occurrence.

Figure 6.7b shows the generation of the occurrence matrix by the discretisation of the wave data into 6x6 bins using MATLAB's built in 3-D histogram function. From this matrix, the 8 most occurrent sea-states were selected to be included in the case study. These 8 sea-states made up 90% of the total sea-states present in the data. The mean wave heights and wave periods for the bins $i = 1, 2, \ldots 8$ were then calculated along with the occurrence factors, μ_i, for sea-state.

Table 6.5 shows the values of the 8 most prevalent sea-states derived from the wave data that were used as inputs in Equation (3.40) and Equation (3.43) to generate the irregular wave-inflow in the fatigue analysis of the generic turbine along with the harsh winter condition case used for the ultimate load study.

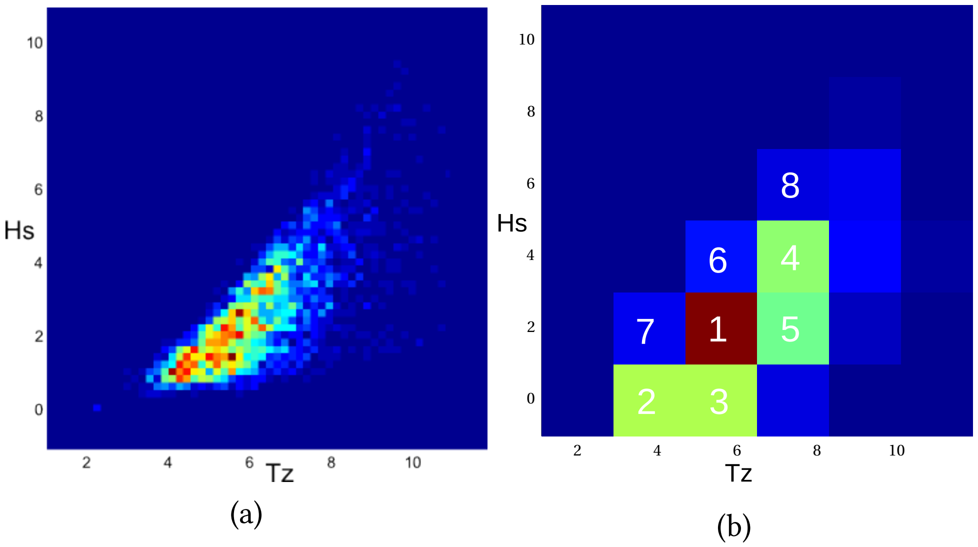

(a) (b)

Figure 6.7: The wave data was used to create a occurance matrix (a) where the significant wave height, H_s, of each data-point is plotted against its wave period, T_z. The density is shown by red areas having more occurances and dark blue areas having none. The occurance matrix was then discretised into 6x6 bins in a 2-D histogram (b) where the rank of the 8 most occuring sea-states are plotted in white.

Table 6.5: The 8 most occurent irregular sea-states and the harsh winter sea-state derived from the wave data along with the average significant wave height and wave period for each bin. Also shown are the occurance factors, μ, used in the extrapolation of the bearing fatigue damage.

Sea-state rank	1	2	3	4	5	6	7	8	Harsh winter case
H_s [m]	2.665	1.008	1.008	4.322	2.665	4.322	2.665	5.979	10.12
H_{max} [m]	4.956	1.874	1.874	4.318	2.665	4.318	4.956	11.120	10.12
T_z [s]	6.135	4.653	6.135	7.616	7.616	6.135	4.653	7.616	10.06
μ [-]	0.2574	0.2047	0.1278	0.0940	0.0855	0.0630	0.0566	0.025 91	-

6.2.3 Case-study modelling summary

As previously mentioned, the modelling campaign presented in this chapter consisted of two main cases; one ultimate load evaluation using the three-step wave current interaction model as the inflow synthesis, and one bearing fatigue evaluation using the irregular sea-state model for the inflow, both with a time-step size of 0.1s. The time-step size was selected since it was small enough to resolve the interactions between the blade rotation and the passing wave velocities while still being large enough to allow one load-case to converge in roughly 10 minutes. The harsh winter inflow case used the fifth order Stokes regular wave theory to derive the sub-surface velocities of the waves for the extreme values of the wave data, shown in Table 6.5, in conjunction with a 1/7th power law profile as described in Section 3.1.6. Wheeler stretching was also employed for the evaluation of the current function. The modelling technique used in the harsh winter inflow case allowed the velocity distribution across the rotor plane to be resolved in high spatial detail.

The modelling case investigating the bearing fatigue life was performed using the irregular sea-state model described in Section 3.1.7. Here, the sea-states derived from the occurrence matrix presented above are given in Table 6.5 along with the occurrence factors which were used in the fatigue damage extrapolation (Section 5.3.3). A uniform current was assumed in the fatigue evaluations as any other current profile was not permitted by the irregular wave model. The techniques used in this case did however give an accurate temporal distribution of the inflow over a large time-scale. A selection of the the sea-states used in the ultimate load and fatigue load cases are shown in Figure 6.8 for visual comparison.

The turbine geometry was kept constant throughout all simulation cases and a cut-through sketch of the turbine is shown in Figure 6.9 to illustrate the size of the shaft in relation to the hull and rotor hub.

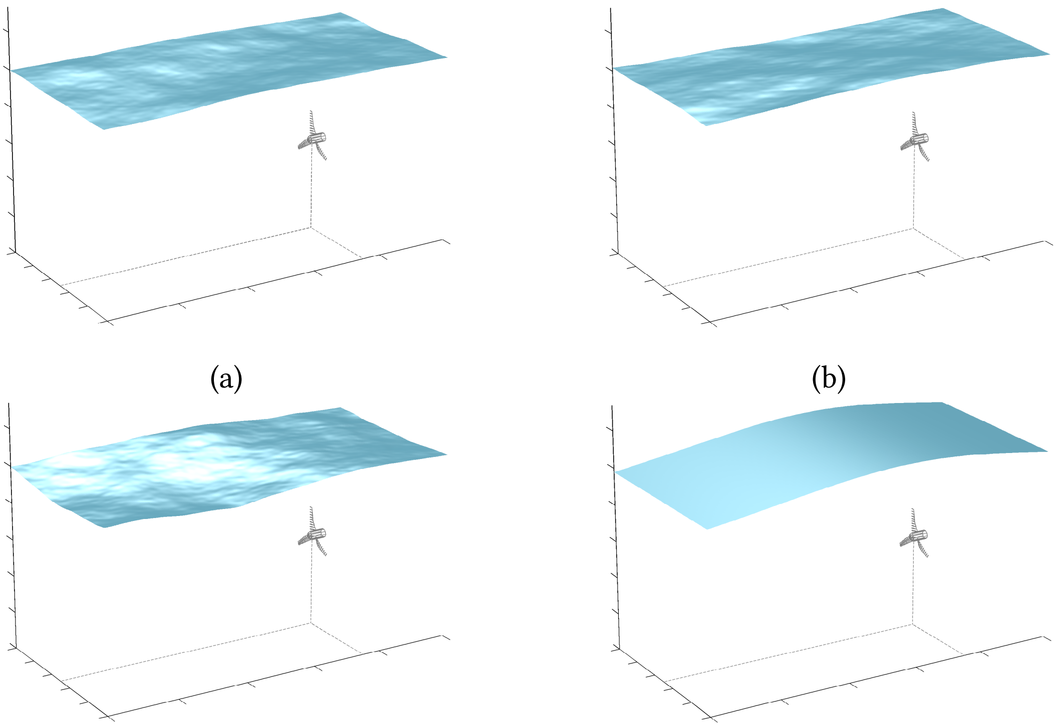

(a) (b) (c) (d)

Figure 6.8: Visualisations of a selection of the flow domains modelled in the case study including the irregular sea-states 1 (a), 4 (b) and 8 (c) and the harsh winter sea-state (d). The figure shows the turbines position in the water column in relation to the size of the waves passing over it.

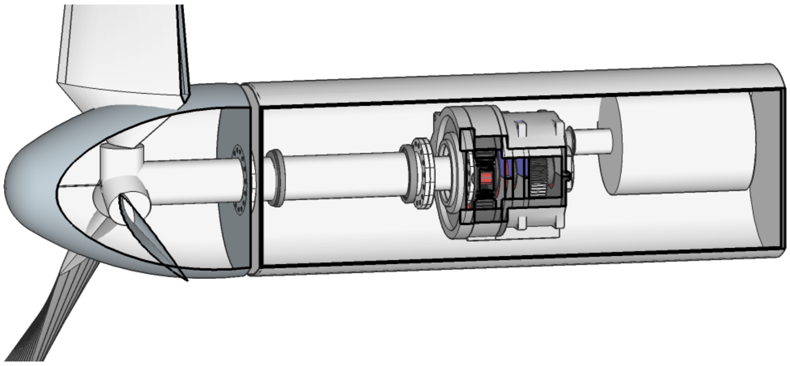

Figure 6.9: 3-D sketch of the internal layout of the generic turbine, showing the main shaft in comparrison to the rotor, a planetary gearbox and a generator. It is noted that the relative thickness of the 540mm shaft, which was the only component included in the drivetrain model, is small compared to the swept area of the rotor. The gearbox model is reproduced under licence from `https://3dwarehouse.sketchup.com/`.

6.3 Case study results and discussion

The results of the case study are presented in two separate sections, one for the ultimate load investigation and one for the bearing fatigue investigation.

6.3.1 Ultimate load evaluation results

The results from the ultimate load study are presented as comparisons between the simulation which included the rotor out-of-plane bending moments in the drivetrain model and the simulation that only included the rotor thrust and torque.

First, the hydrodynamic loads on the TST rotor are shown as the rotor thrust, rotor torque and rotor out-of-plane bending moment which were given as input loads to the drivetrain model. Secondly, the bearing reaction forces derived via the drivetrain FE model are presented, which were used in the post-processing exercise to derive the maximum internal contact stresses in the main bearing, which are presented in the last section.

Rotor loading in regular harsh winter waves

The full range of the hydrodynamic loads on the rotor operating in the harsh winter conditions are shown over four wave periods in Figure 6.10. Here, it can be seen that the rotor thrust and torque have a variation that is synchronised with the passing wave train. In Figure 6.10a it can be seen that the thrust forces on the individual turbine blades are different during most of the time-steps, with higher discrepancies occurring during the passing of a wave peak. These variations are caused by the interaction of the rotating blades and the vertical component of the wave velocity which ultimately give rise to the out-of-plane bending moment on the rotor, shown in Figure 6.10b, as was explained in Section 4.5. The magnitude of the rotor out-of-plane bending moment was seen to vary significantly with several smaller fluctuations with a period of 1.3s due to the vertical wave velocity and blade velocity interactions.

Main Bearing External Loads

The reaction loads from the three shaft bearings derived from the full DoF drivetrain model are presented as the axial reaction loads in Figure 6.11a and the radial reaction loads in Figure 6.11b. It can be seen that only the main bearing (Bearing 1) induced an axial reaction load since it was the only bearing in the shaft that was *axially locating* while the others were purely radial bearings as defined in the previous section. The radial load pattern on the bearings can be seen to have the same shape as the rotor

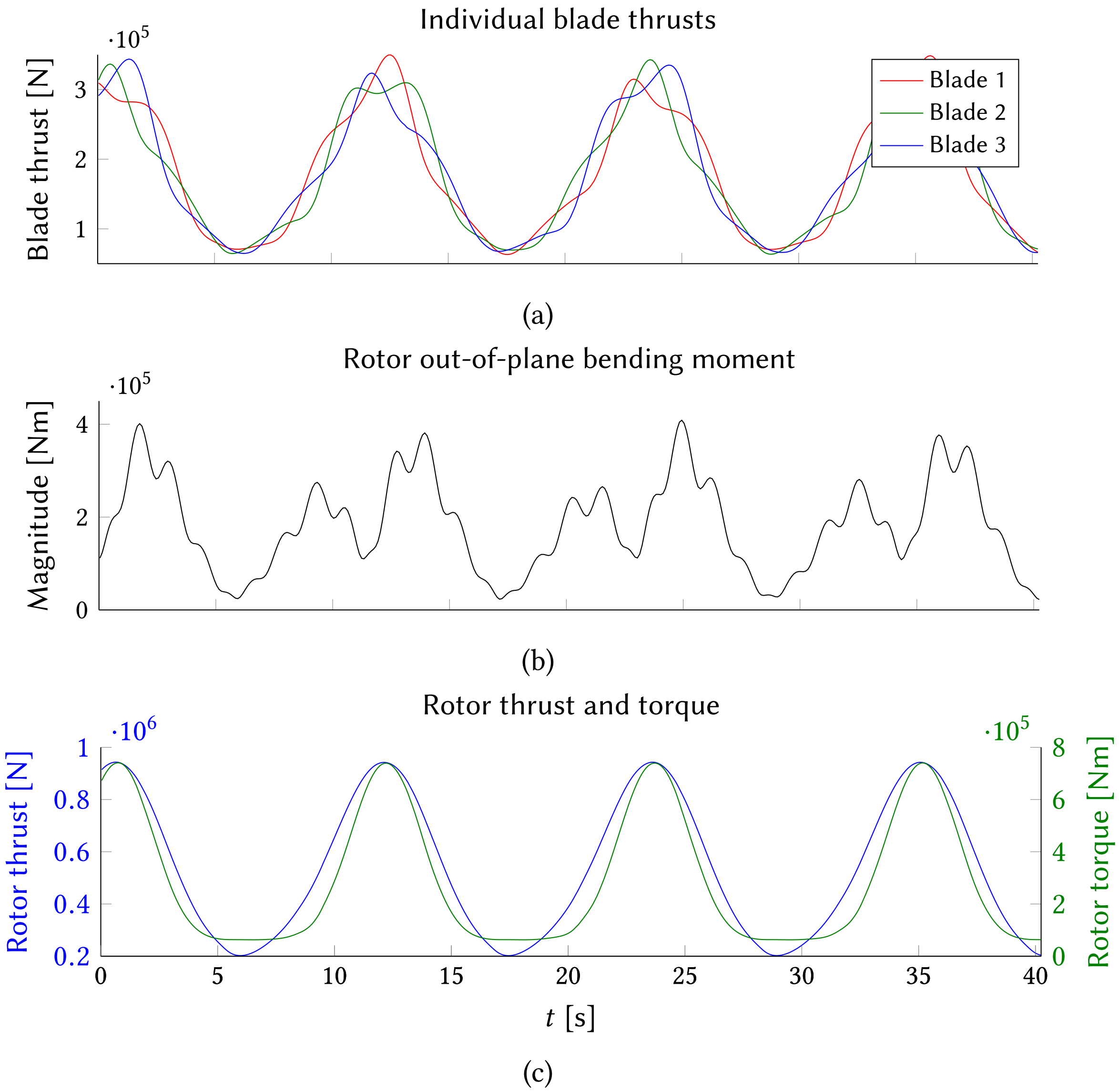

(a)

(b)

(c)

Figure 6.10: Hydrodynamic loads generated on the generic TST rotor operating in harsh winter sea-conditions over four wave periods. The differing individual blade thrust forces (a) gave rise to a thrust gradiant across the rotor blade which induced the rotor out-of-plane bending moment (b). The rotor thrust and torque is shown in (c) which were the only degrees of freedom used in the 'torsional' drivetrain model, while the full DoF model also included the rotor out-of-plane bending moment.

out-of-plane bending moment signal in Figure 6.10b.

In the interest of showing the large angular variations of the off-axis loading caused by the rotor out-of-plane bending moments, Figure 6.12a firstly shows the radial load vectors plotted spatially for each time-step in the simulation *without* the rotor out-of-plane bending moments. The radial load seen in this figure is the reaction load to the shaft weight. In contrast, Figure 6.12b shows the increase of the radial bearing reaction magnitudes when *including* the rotor bending moments in the drivetrain modelling along with the increased directional load spread. The effect that this variation in load directionality may have on the bearings covers almost all failure modes outlined in Section 2.4.3, where a seal breakage caused by the undulating loads can have knock-on effects ranging from lubricant contamination, corrosion and misalignment effects.

Main bearing ultimate internal stress results

Figure 6.13 shows the maximum internal contact stress for the most loaded element in the main bearing, as defined by Equation (B.8), which reached a maximum value of 805.75MPa.

When comparing the simulation results which included the rotor out-of-plane bending moment to the case where it was neglected in Figure 6.13, the underestimation of the internal stresses can clearly be seen in the latter case. The shape of the stress signal in the figure also shows that the inclusion of the rotor bending moments created a more complex loading pattern on the bearings, evident by the additional smaller fluctuations of the signal of the full DoF results.

The mean error between the stress results from the full DoF drivetrain model and the model including only the thrust and torque in Figure 6.13 was 106.87MPa averaged over all time-steps. This error equated to an average underestimation of 19% when neglecting the rotor out-of-plane bending moments in the drivetrain analysis compared to the full DoF model.

6.3.2 Bearing fatigue life results

The results of the bearing fatigue life as a function of the dominant input parameters of rotor radius, inflow speed, blade pitch angle, and significant wave height are presented in the following section. The first section shows the hydrodynamic load envelopes on the rotor, induced by the irregular sea-states, which were used as inputs in the full DoF drivetrain model. The bearing reaction loads from the drivetrain model were finally used to derive the main bearing L_{10} life in post-processing.

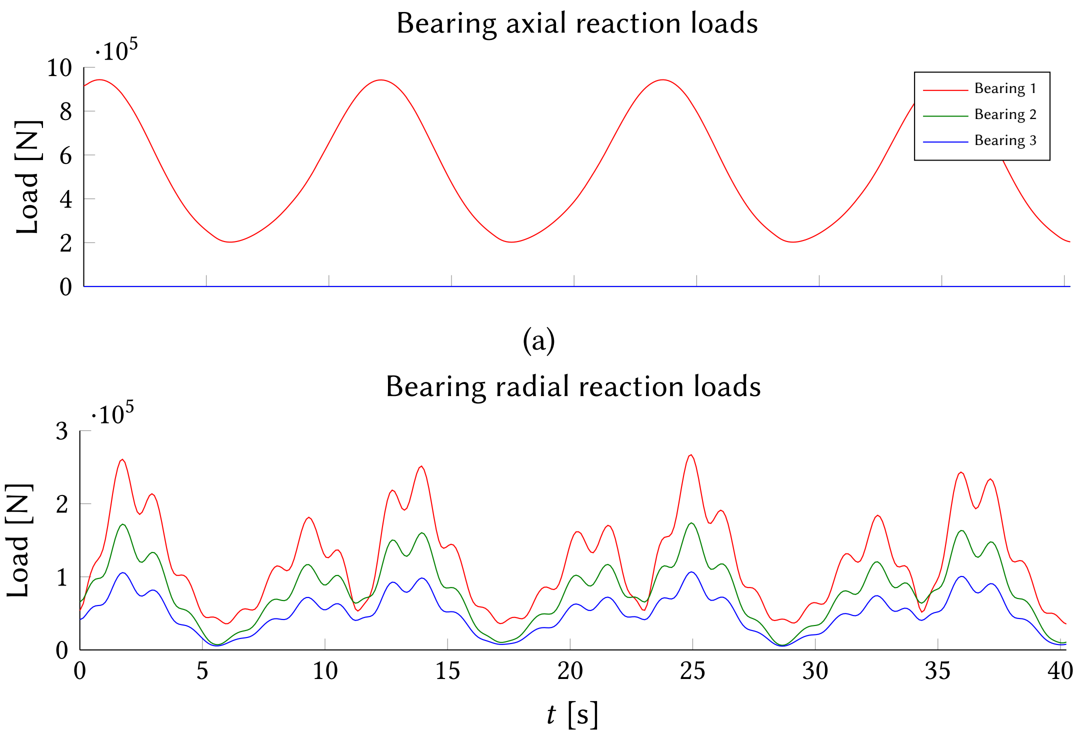

(a)

(b)

Figure 6.11: The reaction loads on the three shaft bearings of the generic TST as given by the full DoF drivetrain model incorporating the rotor out-of-plane bending moment. Only the main bearing (Bearing 1) resisted the axial loads in (a) as it was the only thrust bearing in the shaft system, resulting in the other bearings to have zero thrust loading. The radial load magnitude on all three bearings (b) was shown to vary in a similar pattern to the rotor out-of-plane bending moment in Figure 6.10b.

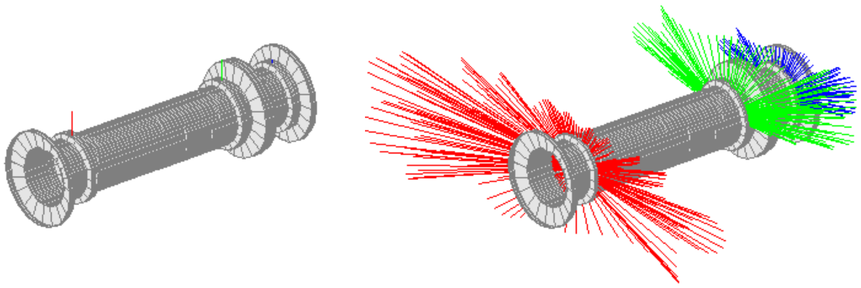

(a) (b)

Figure 6.12: The results of the radial main shaft bearing reaction loads shown in Figure 6.11b were plotted as vectors with magnitude and angle of action. The only radial loading on the bearings when excluding the rotor out-of-plane bending moments in the drivetrain analysis was the self-weight of the shaft, where the radial load vectors are shown in (a). When including the full the rotor bending moments, the radial load vectors increased significantly in magnitude and directionality (b).

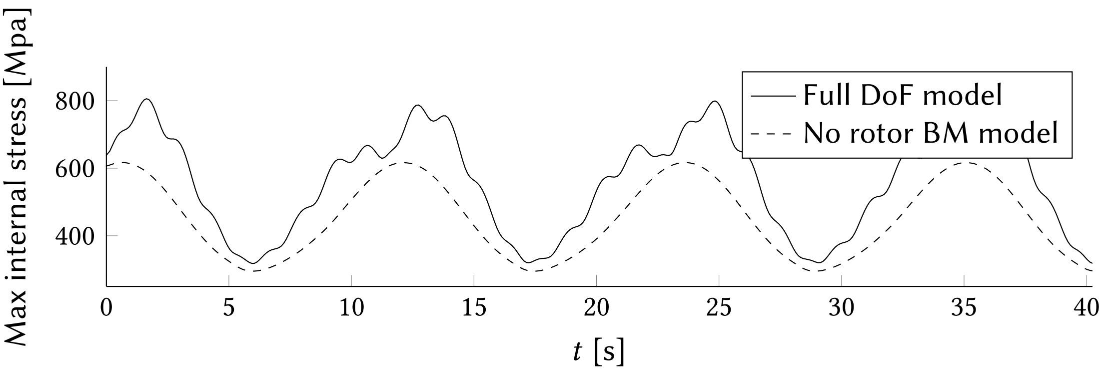

Figure 6.13: The maximum Hertzian contact stresses for the highest loaded rolling element in the main bearing over time during harsh winter sea-conditions. The effect of including the rotor out-of-plane bending moment in the full DoF simulation showed a larger, and more varying, stress in the bearing. The stress signal from the case without the rotor bending moments (BM) follows the same pattern as the bearing axial load in Figure 6.11a.

Rotor loads in irregular waves

The hydrodynamic loads generated on the TST rotor for all 8 irregular sea-states are shown superimposed in Figure 6.14, where the plotted areas represent the load envelopes created by all sea-states defined in Table 6.5. The load simulations for each sea-state were performed over 120s as to capture a representative distribution of surface elevations for each sea-state.

It can be seen that a large wave pass was captured in the time-series of one of the harsher sea-states in Figure 6.14 between 40 - 60s, causing the larger load fluctuation shown. This is a result of several waves interacting constructively at that time in the irregular wave model and it is this phenomenon that simulating over large time-scales aims to capture.

The sea-states and corresponding rotor loads presented in Figure 6.14 were defined as the *baseline* load state for which the later simulations, that included the parameter variations, were compared.

Main bearing fatigue life results

The baseline load conditions that a TST was expected to encounter during its operation, shown as the rotor loads in Figure 6.14, were input to the full DoF drivetrain FE model and the reaction loads on the bearings were calculated. The main bearing's axial and radial reaction loads were then used to calculate its L_{10} fatigue life through Palmgren-Miner's rule shown in Section 5.3.1, with a duty cycle bin-width of 2s.

For the baseline irregular sea-state of Figure 6.14, the main bearing fatigue life of the generic TST was found to be 13.82 years when the rotor out-of-plane bending

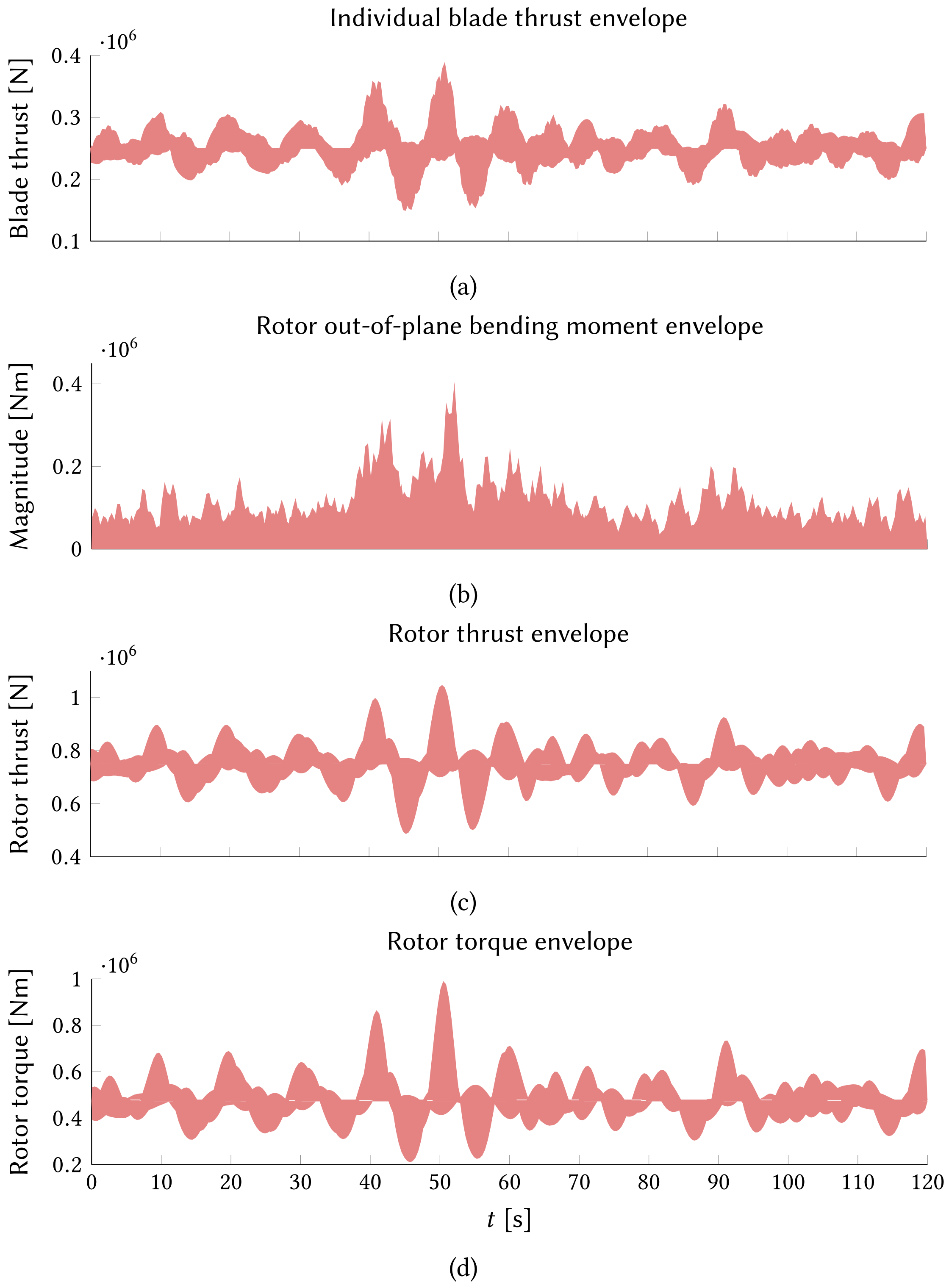

Figure 6.14: Load envelopes for the generic TST operating in irregular seas generated by superimposing the hydrodynamic loads from each load case defined in Table 6.5. The loads represented by these figures were fed as inputs to the full DoF drivetrain model. The figures show a large load peak present around 50s caused by the constructive interfreence large waves passing in sea-state 8.

moment was included in the drivetrain input. When neglecting the rotor bending moments, the main bearing's L_{10} life was calculated as 14.85 years, which equated to an 6.9% over-prediction in fatigue life.

The functional relationships of the fatigue life of generic turbine's main bearing against the variations of the primary parameters are shown in Figure 6.15. Here, the baseline load case from the 8 irregular sea-states in Table 6.5 was used as a starting point for which the other permutations were based on. Each entry in the plots in Figure 6.15 was derived by simulating the baseline case with one of the primary variables given an incremental percentile change.

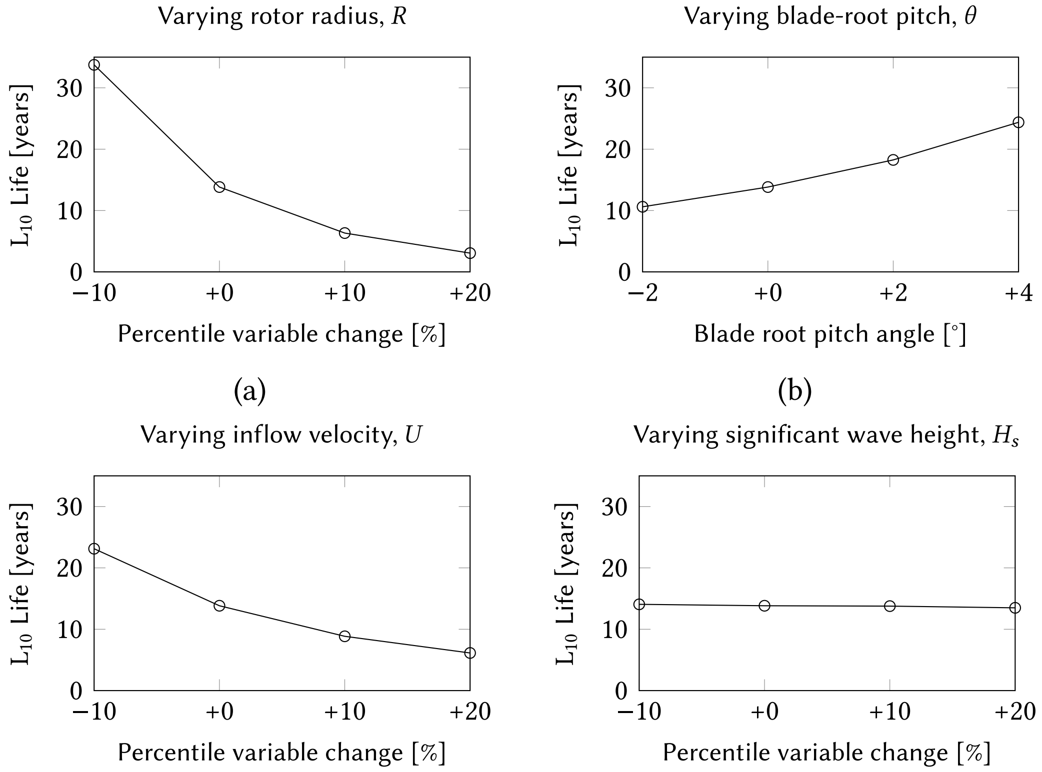

(a) (b) (c) (d)

Figure 6.15: The functional relationships of the main bearing's L_{10} fatigue life towards the variation of the dominant parameters identified from the sensitivity analysis. The figures show the change in bearing life by varying the rotor radius (a), inflow velocity (c) and significant wave height (d) for the baseline case by −10, 10 and 20%. The baseline fatigue life is shown as the 0 entry. The blade pitch (b) was however varied by incremental degree steps in stead of percentiles.

The results show that the rotor radius, R, had the largest influence on the bearing's L_{10} life which decreased in a logarithmic manner for increasing rotor radii, shown in Figure 6.15a. It is noted that this curve had a similar shape as the L-N-curve shown in Figure 5.5, which the L_{10} method is based upon. The relationship between the rotor radius and the bearing life should however be seen as a investigation into the *code's* behaviour during varying inputs, as a real turbine would see an increase in bearing capacity as the rotor increased, thus keeping the fatigue life at a more constant level.

The dependence of the bearing fatigue life on the turbine's blade root pitch setting, θ, is shown in Figure 6.15b, where the life increased with increasing pitch angle. This is consistent with the results from the study on the primary parameter variations in Section 4.4, Figure 4.13b, where the individual blade loads were shown to decrease for increasing blade pitch angles. It is however noted that the magnitude of the rotor out-of-plane bending moment also increased for that instance.

The variation of the inflow velocity, U in Figure 6.15c, showed a similar impact on the bearing life as the rotor radius, albeit less severe. It is worth pointing out that since all the load cases in the case study were assumed to have a constant maximum inflow velocity during the turbine's whole operating life, the true bearing fatigue life is likely to be longer as is illustrated by the strong dependence of the L_{10} life on the inflow velocity.

Finally, the functional dependency of the bearing fatigue life is shown to be largely unaffected by the significant wave height in Figure 6.15d, which is counter-intuitive since it is clear that the wave height causes large load fluctuations as shown by the load envelopes in Figure 6.14. The inability of the L_{10} method and Palmgren-Miner's rule to resolve the impact of the significant wave height on the bearing fatigue life is considered to be the largest shortcoming of the method and will be a source of major inaccuracies. The full implication of this finding is discussed in detail in the conclusions in Chapter 7.

6.4 Conclusions

This chapter has presented the main original findings of this thesis and addressed the research questions posed in Section 1.1.1 regarding the influence of the marine hydrodynamic environment on the durability of tidal stream turbine main bearings. The results presented have also shown the significant impact that the rotor out-of-plane bending moment has on the internal stress variations of the main bearing when included in the modelling and that a significant under-estimation arises when neglecting it, shown in Figure 6.13.

The investigations on the bearing ultimate loads and bearing fatigue life caused by the dynamic inflow were performed by means of a case study on a generic TST design in a representative sea-climate derived from experimental wave data. This allowed insight to the general trends of how the load patterns changed as functions of the varying input parameters, as well as keeping the absolute values of the results close to what might be found in contemporary devices.

The design of the investigated TST was derived through the mean values and common features from several devices that have undergone large-scale prototype testing. The internal layout of the turbine drivetrain was chosen on the basis of common ship design practice and visual inspection of commercial turbine solutions. The shaft-bearing layout was intended to be as representative as possible of common TST designs, granted that the main bearing may have been over-sized for the load conditions applied.

The results from the ultimate load evaluations showed that the maximum internal bearing Hertzian contact stress reached a highest value of 805.75MPa, which is less than the Hertzian stress for infinite fatigue life for roller bearings which has been estimated as about 1034MPa [119]. Thus the bearing selected appears to have an adequate safety margin for the harsh winter sea-state case.

It was shown that when the rotor out-of-plane bending moment was included in the drivetrain analysis model, the magnitude and directionality of the radial bearing loads increased significantly for the harsh winter sea-state case. This in turn caused the main bearing's maximum internal Hertzian contact stress to be 19% greater on average, and 28% greater at most, compared to the results where the rotor out-of-plane bending moments were neglected as shown in Figure 6.13. This contribution of increased internal bearing stresses is thought to be of major implications when deriving the fatigue life of a TST's bearing, since any potential under-predictions, which are likely to occur in the standard purely torsional models, may lead to premature failures. Additionally, the increased off-axis directionality of the load pattern may give rise to a number of secondary bearing failure modes as described in Section 2.4.3.

The investigation into the turbine's main bearing L_{10} fatigue life showed that it had an expected life of 13.82 years, assuming constant inflow and constant rotational speed. This value was seen to increase by 6.9% to 14.85 years when the rotor out-of-plane bending moments were neglected in the drivetrain analysis. It is reasonable to assume that the results of the bearing life are pessimistic since a real turbine would be subjected to less than the maximum tidal flow speed most of the time. However, the bearing fatigue analysis did not include a shear current profile which may have reduced the fatigue life by an unknown amount, as it would bring on higher off-axis loads and higher load directionality on the bearings. The limitations of the methods used in the fatigue calculations are discussed in detail in the next chapter.

The main bearing fatigue life was shown to have a strong functional dependence on the rotor radius, the blade-root pitch and the inflow velocity where the rotor radius showed the largest impact. This information can be of great value when considering the uncertainties of a turbine's operating site-conditions or operational conditions, such as blade-root pitch misalignment. For instance, Figure 6.15b shows that a turbine operating with a -2° lower pitch setting than designed for can have a significant reduction in the turbine's durability.

Finally, this chapter has presented a major insight into the applicability of the highly simplified L_{10} method and Palmgren-Miner's rule, highlighted in the methods inability to capture the effect of the significant wave height on the bearing fatigue life. It is the belief of the author that the assumption made by the Palmgren-Miner's rule of a constant bearing load in every duty cycle during variable load conditions neglects the *rate of change* of the material stresses brought on by the wave motion, which may consume additional life of the material. This hypothesis is discussed in the next chapter.

With all the research questions, theories, methodologies and results having now been presented, the final chapter will give an in-depth discussion of the methods used, the findings of the TST drivetrain loading and bearing durability and the suspected inability of the fatigue methods used to capture the full extent of the loading regime of a TST. A critical analysis of the methods, assumptions and limitations presented in this thesis will also be given, which paves the way for future research needs and questions that still need answering to assure that TST technologies reach their maximum potential in terms of durability and reliability.

Chapter 7

General discussion and conclusions

> "Science is a way of thinking much more than it is a body of knowledge."
>
> — Carl Sagan

In the vast majority of the coastal regions around Scotland, where most of the first generation TST developments have been commissioned, there persists an unforgiving and highly energetic marine environment with frequent storms during the winter months. As has been stated previously in this thesis, and by many other authors before [15, 16, 65, 99], any successful power conversion system built for extraction of tidal energy must be able to maintain high reliability during the most punishing sea conditions, since regular maintenance and service is unlikely due to the low accessibility for most devices. In essence, marine energy systems such as horizontal axis tidal turbines must demonstrate a higher level of durability than any other type of renewable energy extraction device to date, due to the high costs of access and retrieval of individual units.

As such, the thorough understanding of the hydrodynamic interactions between the instationary sea climate and the structural forces on TSTs becomes a vital piece of knowledge to ensure that the technology becomes a durable, reliable and economic renewable energy option. Knowing the path of causality from the unsteady hydrodynamics of the turbines' inflow, to the load gradients generated across the rotor plane which ultimately induce stresses on the internal critical components, gives developers a strong theoretical basis to reach optimum design solutions for a given load condition. In this context, this thesis has tried to inform the question "how does the instationary flow in the marine climate affect the loads and life of a tidal stream turbine?" through numerical modelling and statistical analysis of said models.

Although there exists an increasingly large body of literature on the topic of TST hydrodynamic loading, there is little information available on the relative importance of a turbine's various operational, inflow and geometrical parameters in regards to the loading in a general sense. As such, it can be hard to relate the different findings from different sources as the investigations of the parameters' influence on the loads tend to be highly case-specific. It was therefore the aim of this thesis to conduct the studies and present the results in a manner as general as possible, where the parameter's influences were evaluated over the whole input domain, making the interpretation of the results valid for a large range of cases.

Relating to the importance of understanding the relationships between a turbine's operating conditions and the experienced peak loads and fatigue life, the accuracy and applicability of the numerical models used to simulate these phenomena becomes key to insuring that the devices are suitably designed to withstand the expected load conditions. With that said, it has been identified that many commercially available methods regard the load-path through a TST operating in unsteady seas as a one-dimensional system, neglecting all degrees of freedom of the loads except in the axial direction. These simplifications in modelling have in this thesis been suggested to have major implications relating to the under-prediction of the actual operating loads of a TST, which may lead to premature fatigue failure in the worst case. Conversely, high fidelity models such as CFD packages tend to be too computationally intense, making them unsuitable for long term fatigue calculations. A secondary objective of this thesis was thus stated as investigating if these types of one-dimensional simplifications are applicable for marine usage, as no such studies have been found in the public domain, or if there is a need for model refinements in order to capture the full extent of the load phenomena present. In order to achieve this, and to investigate the other research questions posed, a numerical model needed to be created that struck a balance between the high fidelity 6 degree of freedom models and the fast-running simplified 1-D models. The fast convergence time of the developed model allowed a multitude of studies, such as the sensitivity analysis and the detailed parameter investigation, to be performed in a reasonable time-frame suitable for early-stage prototype testing.

This chapter presents a synthesis of the various results presented in the individual chapter conclusion sections and shows how they converge to answer the research questions presented in Chapter 1. The first section provides an overview of the findings from the numerical modelling campaigns and how they advance the knowledge needed to answer the research questions. The second section puts these findings into the greater field of the understanding TST loading and the implications they may have in terms of how modelling of TST loads is conducted and its implications on the TST sector as a whole. Presented in this section is also the original contributions of the research stated explicitly. This is followed by a discussion of the limitations of the methods used and the possible inaccuracies that arose from the choice of models. Based on these findings, the recommendations for future research are then presented where the suggested studies are aimed to further close the research gaps left by this thesis and the experimental data that would need to be obtained to verify the structural models fully. Finally, some closing remarks of the results and the greater impact they may have on the tidal stream sector are given.

7.1 Research findings and original contributions

Presented in this section is an explanation on how the various findings found throughout the chapters in this thesis converge to answer the stated research questions.

Firstly, the original contributions of this research are again for clarity summarised as:

- The delivery of a numerical model that related the varying inflow conditions of a TST to the internal loading and fatigue life of the drivetrain in six degrees of freedom.
- The inclusion of the rotor out-of-plane bending moment in the drivetrain model which resulted in an increase in bearing loads and load variability, and a subsequent reduction in bearing fatigue life when compared to the results from a traditional one-dimensional approach.
- The magnitude and variation of the rotor out-of-plane bending moment was shown to have a strong correlation to the interactions between the vertical velocity component of the wave motion and the blade rotation.
- The presentation of a sensitivity analysis on the load model which showed that the loads generated on a TST were most influenced by the current shear-steepness, rotor angular velocity, blade root-pitch, rotor radius, inflow velocity and wave height.
- The L_{10} method in combination with Palmgren-Miner's rule was found to predict a negligible change in bearing life caused by varying the significant wave height. This was believed to be a theoretical shortcoming of the method, as opposed to being representative of actual TST bearing behaviour as is discussed in Section 7.3.

Considering the research findings, the first research question that was raised was what effect the non-uniform inflow across a TSTs rotor, caused by surface waves and shear currents, had on the load magnitudes and load variability of a turbine. Firstly answering this question from a modelling perspective, it was shown in Chapter 3 that it was necessary to include the effects that the time-varying inflow had on the rotor loading by the inclusions of the dynamic wake model. The verification results showed that ignoring the dynamic wake formulation caused an error in the replication of the experimental load data in the form of incorrect prediction of the amplitude and load increases associated with operational changes such as blade pitch manoeuvres.

Secondly, for the sake of answering the first research question in a more general manner, the detailed study of the primary parameters in Section 4.4 showed that the presence of a linear shear current profile and a regular wave train did indeed induce large variations in the blade bending moments as well as a out-of-plane bending moment component of the whole rotor. Here, the current shear, blade pitch angle and rotor radius had a notable influence on the variance and magnitude on the individual blade bending moments, which consequently also had a large impact on the rotor out-of-plane bending moment. The directionality of the rotor out-of-plane bending moment can be seen to have a large range in all cases investigated in the primary variable study, showing that the TST hydrodynamic loading phenomenon cannot be considered a one-dimensional problem.

Related to the first research question, the investigation into the hydrodynamic mechanisms that caused the fluctuations in the rotor out-of-plane bending moment load pattern, observed in Figures 4.13 - 4.14, further showed that the marine flow condition poses a multi-dimensional load problem. The results of this investigation showed that the vertical velocity component of the wave kinematics causes fluctuation in the rotor's out-of-plane bending moment which will ultimately be transmitted into the drivetrain. Therefore, it is concluded that the vertical component of the wave induced flow cannot be neglected when modelling the hydrodynamic loads on TSTs, as has been suggested by researchers in the past [4, 23].

As an answer to the first research question, the studies mentioned above showed that the marine inflow conditions caused force fluctuations on the blades and rotor over time, as is in agreement with previous research and would be expected. However, the studies also showed that the loads were highly spatially varying; this makes the hydrodynamic loading of TSTs a strictly multi-dimensional phenomenon which this thesis later showed caused knock-on effects through off-axis forces on the drivetrain.

The second research question, concerning which parameters were most influential in regards to the generation of loads and load variance on a TST, was primarily addressed via the sensitivity analysis. This study found that the loads on a turbine were most sensitive to variations in the current shear-steepness, rotor angular velocity, blade root-pitch, rotor radius, inflow velocity and wave height. Insight was also given from the detailed parameter analysis on the trade-off between individual blade loading and increased rotor out-of-plane bending moment that occurs in certain operating conditions, such as during steep sheared inflow.

It should be mentioned that the identified primary parameters having the largest impact on the generated rotor loads all have different intrinsic uncertainties related to them, which must be taken into account before a 'most important' parameter can be identified. For example, the turbine's radius showed high influence on both the magnitude and variance of the rotor loading, making it a driving factor on the ultimate and fatigue loads on the device. However, since geometrical features such as the turbine radius are likely to be known with great precision prior to deployment, the over-all importance of this parameter towards unexpected load generation on the turbine can be considered low. Hence, the values of a parameter's sensitivity indices alone do not constitute as proof of a general 'importance' measure. Conversely, other parameters identified as to be influential such as the blade root-pitch setting have a larger uncertainty throughout the turbine's service life which can be attributed to system failures or degradation; pitch control mechanism bearing failure being a possible candidate. On the other side of the uncertainty spectrum lie the environmental parameters, such as wave height and shear current-steepness, which are likely to see large deviations from the expected values. These parameters should be considered as higher threats towards the durability and life of a TST since they are both uncertain and have a strong impact on the generated load levels and variations.

Although much effort has been put into making the results presented in this thesis as general as possible for contemporary TST designs, it must be remembered that the sensitivity analysis shows the response of the unsteady BEMT *code* as opposed to a real turbine. The results are meant to be interpreted as the likely general trends of the load response of a real turbine, although the numerical values will be specific for the turbine geometries investigated.

Focusing on a more specific modelling aspect of TST loading, the third research question was directed toward how the rotor out-of-plane bending moment influenced the load distribution in a TST's internal drivetrain components. It was found that expanding the drivetrain model to a full 6 degrees of freedom and including the off-axis loads from the rotor in the analysis showed an appreciable increase in the internal maximum contact stresses in the main bearing compared to the one-dimensional (torsional) model. In the case study presented, the mentioned contact stresses increased significantly by an average of 19% when including the rotor out-of-plane bending moment components; this percentage increase, although specific for the particular case investigated, is assumed to be representative of the order of magnitude in the stress-error throughout the drivetrain caused by treating the TST load problem as a one-dimensional entity. Along with an increase in the average bearing stresses, it was observed that the fluctuations in the load signal increased in the form of the smaller amplitude load variations brought on by the vertical wave velocity component, which was identified in Section 4.5; implying that the loading regime of TSTs is more dynamic than is commonly indicated by simplified design models. Furthermore, as well as increasing variations in the magnitude of the internal bearing stresses, the inclusion of the rotor bending moments caused a significantly larger spread in the directionality of the radial, off-axis, loads on the three shaft bearings in the case study; this increases the likelihood that a bearing will suffer one of the many secondary failure modes, mentioned in Section 2.4.3, which are hard to predict using analytical methods. This furthers the point that the dynamics of a TSTs drivetrain operating in a real sea climate is a complex three-dimensional problem, which will need higher fidelity methods for the calculation of the internal stress distributions and fatigue life.

Even though, as mentioned, the complex dynamics present in the three-dimensional operational loading of a TST drivetrain would preferably require higher fidelity stress and fatigue models to resolve the most accurate stress distributions and multiaxial fatigue damage, only a preliminary empirical fatigue evaluation was performed on the main bearing of the generic TST in this thesis. The results of this simple bearing fatigue analysis still showed a 6.9% reduction of fatigue life when the off-axis loads generated by the rotor bending moments were included, as compared to the axial modelling best-practice technique. Even though the methods used to derive the bearing fatigue life were originally conceived for one-dimensional bearing loading, the results serve as an indicator that the fatigue life of the internal components of a TST will be reduced as a consequence of the eccentric loading brought on by the rotor. It is also likely that more sophisticated fatigue methods, accounting for load directionality and variability and bending moments, will accentuate the effect of the highly variable forces present.

Relating to this thesis' attempt to focus on the relationships between the input parameters and the generated loads and subsequent durability of TSTs, the answer to the fourth research question showed how the fatigue life of the main bearing varied as a function of the identified primary parameters. It was shown that the main bearing's L_{10} life was strongly affected by the turbine's radius and the uniform inflow velocity. These results were expected since the bearing used was sized for a specific turbine radius and inflow velocity. Conversely, the bearing life's dependency on the blade root pitch setting was unexpected as a greater pitch setting was seen to give a longer fatigue life. However, the change in power capture was not recorded for this study, which may have seen a decrease for this case.

Finally, the most surprising results shown in the case study were the bearings life's absent relationship to the significant wave height. This is speculated to be caused by the inability of the Palmgren-Miner rule to correctly resolve the effect that the varying loads have on the internal bearing structure. This finding is discussed in more detail in the limitations section of this chapter, and it is repeated that it is the belief of the author that the significant wave height will be a prominent driver in the fatigue life of a TST, despite the results of the case study suggesting otherwise. This interpretation is supported by the synthesis of results from the various studies presented in this thesis; the sensitivity analysis identifying the wave height as influential towards the variance of the loading and the detailed study of the primary parameters where the wave height had a large impact on the rotor bending moments.

7.2 Theoretical implications of the research findings

Presented in this section is how the research findings outlined previously inform the theoretical understanding of TST loading and durability and what implications the interpretations may have in the field in a greater sense. Also presented is a reiteration the original contributions found throughout this thesis.

This thesis has found that, perhaps unsurprisingly, that the dynamic marine climate causes large load fluctuations on TST's and that a large portion of the forces are directed off-axis to the turbine's main shaft – results which are in-line with previous investigations on the topic [44]. The investigation was however expanded to show that these load variations and off-axis directionalities directly manifest themselves as increased stresses on the turbine's internal components with a high level of directional spread. It is reiterated that the implication of these findings show that the hydrodynamic loading of a TST is a 3-dimensional problem which can only be simplified to a 1-D case in the most basic of calculations, as is done by popular commercial packages [24, 80]. The results also imply that higher fidelity structural models are needed to calculate the fatigue damage caused on components subjected to multiaxial loading, as was shown by the inability of the L_{10} method to resolve the main bearing's change in life for varying wave heights. Even though the results of the L_{10} and Palmgren-Miner rule showed the basic relations of the bearing life to the input parameters, it is believed that higher order methods capable of including the off-axis bending moments on the bearings are needed to produce accurate bearing life predictions for TSTs. Again, any fatigue method used for life calculations in the highly variable marine climate should be able to resolve the damage caused by the observed smaller stress amplitudes below the fatigue limit, as these can still contribute to life consumption.

Even though the results of the absolute value of the bearing fatigue life of a TST, as modelled in this thesis, must be considered inconclusive as there is simply too much uncertainty regarding the L_{10} and Palmgren-Miner methods the *relationship* between the marine inflow parameters and the bearing life were shown to be strong, which provides enough of a basis to warrant more in-depth study on the fatigue life of TST bearings where the rate-of-change of the stresses are accounted for.

The use of off-the-shelf rolling element bearings in TST applications can also be called into question when viewing the resulting load spectra that they are subjected to. As mentioned in Section 2.4.3, the mechanical loading of a bearing can not only cause it to sustain fatigue or damage of plastic deformation, but it can also cause failure in the seals allowing for sea-water contamination of the lubrication which can degrade the bearing significantly. The fact that the bearings are unlikely to be considered as sacrificial components of the turbine drivetrain – due to the complexity of changing them – in combination with the many failure modes present, plain bearings would seem an attractive alternative. A study of the mechanical response of these bearing types was however out of the scope of this thesis.

In relating the results of this thesis to the work of previous researchers, the findings of the sensitivity analysis were in-line with previous investigations [23] and can be considered as complementary to the existing body of knowledge; relating the results from various loading studies to each other by providing the relative global importance of the various parameters. For example, in a study investigating the loads on a TST by varying only the wave height, the effect of increasing the rotor radius could be alluded from the sensitivity analysis presented here. Also, from a development perspective, performing a sensitivity analysis on a proposed design could allow engineers to make design decisions that are not case-specific, making sure that the designs are suitable over a wider operating range. It is acknowledged that most developers are likely to use more advanced methods for fatigue evaluations than have been used in the studies presented here, but this thesis has taken a step in the direction of having a standardised, unified methodology in the public domain where results can be compared over many varying cases, as was requested by Wood et al. [65].

The finding that the vertical velocity component of the wave motion had a large influence on the rotor out-of-plane bending moment of a turbine suggests that the modelling simplifications done in previous investigations [23, 99] can lead to under-prediction of the internal loading of a TST. Great care must be taken to assure that studies undertaken where the vertical wave velocity is ignored does not inform the design of a TST's drivetrain or internal components.

7.3 Limitations of the study

As is with all numerical models, there are several limitations of the methods used throughout this thesis. These can be categorised as theoretical limitations of the methods used, which may result in restrictions of the load cases that can be investigated with confidence, and limitations of scope of the project which limits how many different aspects of turbine loading could be included within the time-frame of the project.

Since the modelling approach throughout the work presented has been based on the principle of using the simplest methods possible to gain the most insight to the underlying phenomena, there will be a number of limitations of the study. Many of these limitations are related to the simplifications done in the derivations of the BEMT equations even though much work has been done in expanding the validity of the method to marine applications.

The major uncertainty that was identified in the BEMT model was supplying it with the blade section lift and drag characteristics from an external source, such as XFOIL or from experimental data. Most of the issues were encountered when very low Reynolds number flows were involved ($\mathrm{Re} \leq 5 \times 10^4$ for the small scale experimental turbines), where the panel method of XFOIL struggles with stability and to produce reliable results. Experimental data in this Reynolds number region is also hard to come across and suffers from issues of reproducibility, effectively making the BEMT results for lower Reynolds number cases more uncertain. This problem is however mitigated as the scale of the investigated devices increases, bringing the Reynolds number into a higher, more predictable ranges of 1.5×10^7 for the case study presented.

Another limitation of the BEMT method, as it was implemented in this project, was that the blades were considered as perfectly rigid bodies allowing no deflection caused by the varying flow fields. As the blades of a real TST are likely to be deformable, the loads on the blades and rotor would decrease by some amount as the projected area to the flow reduces, effectively allowing the blades to absorb some of the fatigue damage that is in this thesis only present in the drivetrain and bearings. The end effect of this load mitigation in the drivetrain through blade deflections is unknown and has been included as a suggested future research topic. Furthermore, since the whole structure of the turbine was indeed considered rigid and did not affect the flow field in this study, the relative impact of structure flexibility on the fatigue of the drivetrain has not been factored in.

Since the inflow models used to synthesize the operational flow conditions in this project were simplified potential flow models, there were mathematical constraints placed upon them in terms of only managing irrotational flows. The major implication of this was that the irregular model used in the fatigue study could only be used in conjunction with a uniform inflow profile, meaning that the fatigue lives of the bearings are likely to be less when a shear current profile is present due to the induced rotor eccentricity. Furthermore, the ambient turbulence of the flow was not considered in the flow synthesis which may increase the fatigue degradation of a device further. The effect of turbulence also covers the possibility of structural vortex-induced vibrations in idling turbines, which may cause false brinelling in the non-rotating bearings.

As was mentioned in the conclusions of Chapter 6, the use of the Palmgren-Miner linear damage accumulation rule for the highly varying load spectrum present in TST operation is considered highly over-simplified and may result in optimistic fatigue lives of components. This is backed up by the observation that the bearing fatigue life using this method did not respond to changes in the significant wave height and that stress cycles below the fatigue limit are assumed to not contribute to life consumption. A limitation of the study of the bearing fatigue life in this thesis is thus that the absolute values of the predicted lifespans are not presented with great certainty. However, the reader is reminded that it is the relationships of the fatigue life towards the input parameters that is the main focus of this thesis, and the use of the L_{10} and Palmgren-Miner rule gives a first indication towards this.

Another limitation of the bearing life investigation was that the L_{10} and Palmgren-Miner methods did not account for the varying directionality of the forces and the presence of external bending moments on the bearings. The exact impact of this phenomenon on the wear and mechanical response of the bearings is at this point unknown to the author and it would require significantly more complex modelling techniques to investigate, such as the proprietary evaluation tools used by many bearing manufacturers. This topic is therefore also given as a suggestion for future research.

Besides the theoretical limitations, there were also limitations of scope in the research presented. The most significant of these limitations is that the fatigue analysis was performed using a constant, maximum, inflow velocity. This is likely to have a conservative effect on the bearing life, as opposed to the theoretical limitations of said methods, and could be corrected for in the future by employing a joint probability between the sea-states and the tidal phases. Another limitation of this sort was keeping constant rotational speed of the turbine, as other load patterns may be present if other power control strategies are employed.

The very nature of modelling complex phenomena with simplified methods will ultimately lead to several limitations and inaccuracies as has been discussed in this section. Even so, the methods and results presented throughout this thesis do provide valuable insight into turbine load behaviour and provide a sound basis for further refinement and future research on the topic, as will be discussed in the next section.

7.4 Recommendations for future research

The recommendations that can be made based on the results in this thesis are in the form of both suggestions for recommended modelling practice of TSTs in unsteady flows and suggestions for future research topics which were left unanswered.

It has been shown that considering the hydrodynamic loading of a TST to be a purely axial phenomenon can lead to under-predictions of the internal stresses in the drivetrain-bearing system during dynamic operation of up to 6.9% compared to the six degree of freedom results. This figure is likely to increase when more complex bearing models are used which include the effects of the external bending moments acting on them and use non-linear bearing stiffnesses. Therefore, it is suggested that modellers ensure that all degrees of freedom of the rotor loads are included in the structural response analysis of the turbine to assure that the forces are represented in a realistic manner. Furthermore, the vertical velocity component of the wave motion should not be neglected in hydrodynamic load investigations.

As for the future research suggested to investigate the questions uncovered by this research, a list is presented to cover the major topics:

- Conduct a load analysis on a TST in the marine environment using a similar approach as presented, but using a more sophisticated fatigue post-processing method capable of resolving the effects of multiaxial loading and sub-fatigue limit load cycle damage. This could include using a more advanced commercial bearing model on the derived loads.

- Fundamental experimental data on how bearings respond to truly varying load spectra, as opposed to 'bulk loads' which the L_{10} method is based on, is needed to confirm or deny the applicability of the Palmgren-Miner and L_{10} method to highly varying load cases.

- The magnitude and variability of the rotor out-of-plane bending moment could be confirmed by experimental campaigns where the individual blade-thrust signals and angular position of a turbine were recorded and analysed.

- The creation of a more in-depth fatigue evaluation by expanding the current TST load model to include blade and structure flexibility along with varying current and rotational speeds. This could also include the effects of turbulence in the fatigue investigations along with the incorporation of other components such as the shaft and taking the life consumption of high-stress operating modes into account such as start-up, shut down and emergency breaks.

7.5 Final conclusions

The path towards the successful and economically viable extraction tidal stream energy will without a doubt be challenging and full of obstacles, both technical and practical. The climate in which TSTs are to be expected to survive for a considerable amount of years is, perhaps, the most hostile that any renewable energy device has encountered to date. The findings of this study do indeed confirm that the hydrodynamic loads on TSTs are large, varying and eccentric, making the efficient design of the devices without resorting to over-engineering a difficult task.

At this crucial point of the development of the TST industry, it is therefore paramount that the design methodologies used are as representative of the operational load conditions as possible while retaining high computational efficiency, allowing for the creation of turbines having highest durability and maximum load resistances.

This thesis has made a contribution in the understanding of the mechanics of the load patterns on a TST generated by the marine inflow as well as identifying the manners of how to model the device's internal structural response in a representative manner. It was shown that since the hydrodynamic phenomenon of TSTs operating in unsteady marine conditions is a multidimensional problem, the modelling techniques used must reflect this by including all degrees of freedom of the input loads, as opposed to using purely torsional models. Also, the results presented in terms of the sensitivity analysis and parameter studies have shed light on the general relationships between hydrodynamic loads generated on TSTs and the parameters of the inflow sea-state, operation and turbine geometry.

With an increased understanding of how the unsteady sea conditions affect the loads and durability of tidal stream turbines and equipped with efficient, accurate and representative modelling tools, researchers and developers will be in a stronger position to deliver tidal stream energy as a clean, reliable and economical source of renewable energy for the future.

Appendix A

Validations of FEM model and Morris algorithm

This appendix shows the validation of the FEM drivetrain method and the Morris method sensitivity algorithm. The FEM model was validated against the analytical solution to a point-loaded Timoshenko cantilever beam of the same order of dimensions as the TST shaft and the Morris algorithm was compared to the results of a similar code found in literature.

A.1 Drivetrain FEM model validation

The analytical solution for the transverse deflection of a cantilever Timoshenko beam point-loaded at the far end is given as

$$w = -\frac{P(L-x)}{\kappa AG} + \frac{Px}{2EI}\left(L^2 - \frac{x^2}{3}\right) - \frac{PL^3}{3EI} \tag{A.1}$$

where P is the point-load, L is the beam length, A is the cross sectional area ($A = \pi R^2$), G is the shear modulus as defined by Equation (5.25), E is Young's modulus and $I = (\pi/4)R^4$ is the second moment of area. The following values were used in the validation study as shown in Table A.1 and the validation results using a FEM model with 21 elements are shown in Figure A.1.

Table A.1: Parameter values for the FEM drivetrain model validation against the analytical solution of a point-loaded cantilever Timoshenko beam.

Parameter	L [m]	P [N]	R [m]	ν [-]	E [Pa]	κ [-]
Value	2	1×10^3	0.25	0.33	200×10^9	0.4477

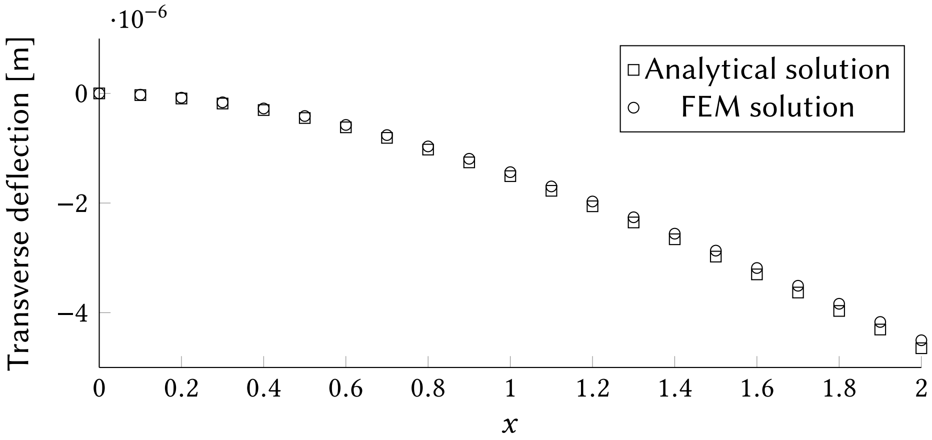

Figure A.1: Validation of the Timoshenko FE beam shaft model using 21 cylindrical elements against the analytical solution in Equation (A.1). The results shows a good match between the two transverse deflection shapes.

A.2 Code-to-code validation of Morris sensitivity analysis model

As to establish confidence that the Morris method sensitivity analysis algorithm presented had been implemented correctly, it was benchmarked against another Morris sensitivity analysis model found in literature by Iooss (2015) [132]. The model presented in this reference was tested against a simplified function for the water height of a river with 8 input parameters and two output values.

The results of the benchmark study is shown in Figure A.2 where the upper plots are the sensitivity analysis results for the river model's S and CP outputs generated using the Morris algorithm presented here and lower plots are the same results but as presented by Iooss.

It can be seen that the presented Morris method replicates the results of Iooss fairly well in the sense that the most of the parameters have the same relative ranking although the absolute values of the sensitivity indices are different. This discrepancy is put down to the fact that the original river function had its input parameters distributed according to various probability density functions, which was not implemented in the current implementation of the function.

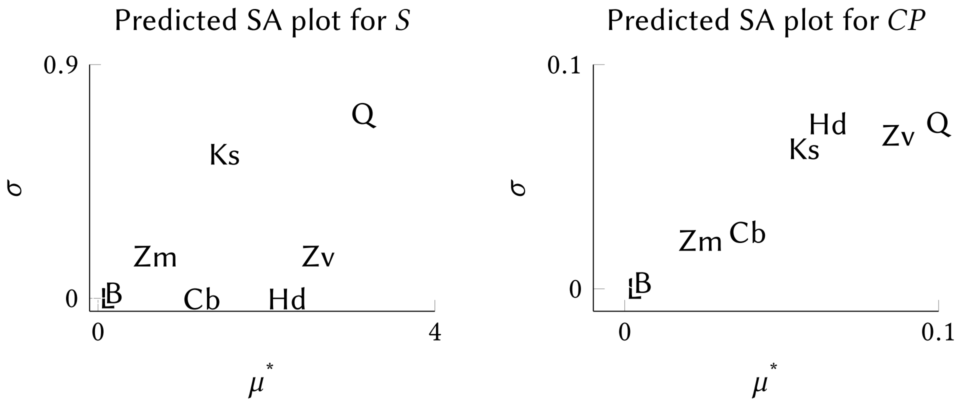

(a) (b)

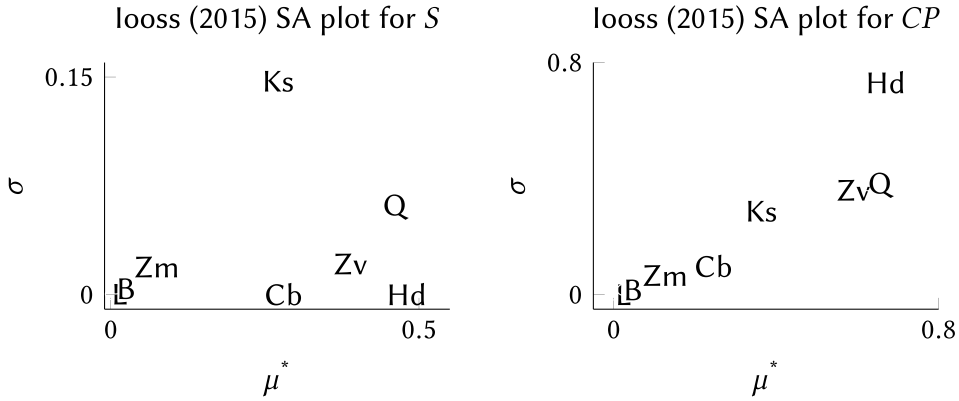

(c) (d)

Figure A.2: Bench marking of the Morris method sensitivity analysis algorithm compared to the implementation presented by Iooss on a function for river water-level height using 8 inputs denoted by letters in the plotts. The left plots are for the outputs S and the right are for the CP output.

Appendix B

Approximative bearing contact stress post-processing method

The internal bearing contract stresses were calculated using the method outlined in the design requirement standard for wind turbine gearboxes [66]. The method was implemented in post-processing by using the axial and radial reaction loads on the main bearing to calculate the Hertzian contact stress between the inner raceway and the rolling element where the highest stress concentration occurs. The method describes the bearing stress distribution using three influence factors that determine the load sharing between the rollers, the bearing misalignment and the truncation of the contact ellipse for highly loaded rolling elements. In this thesis the misalignment is assumed to be negligible, so the corresponding factor is set to unity.

In order to calculate the maximum internal stresses in the bearing, the bearing's axial and radial external loads, $F_{\mathrm{B,a}}$ and $F_{\mathrm{B,r}}$, must first be combined into a damage equivalent *static* load, P_0, as

$$P_0 = X_0 F_{\mathrm{B,a}} + Y_0 F_{\mathrm{B,r}} \tag{B.1}$$

where X_0 and Y_0 were the bearing's static load factors specific for the bearing design. The subscripts '0' denotes that static equations were used as they describe the relationship between the applied bearing load and maximum stress without adding dynamic effects.

The load sharing factor, k, was set to 4.4 when the bearing operated at a thrust-to-radial ratio ($F_{\mathrm{B,a}}/F_{\mathrm{B,r}}$) greater than the bearing's published thrust factor, e. When the bearing operated at a thrust-to-radial ratio less than the thrust factor the load sharing factor was defied as

$$k = 4.05 + 0.3209 \left[\frac{P_0}{C_{\delta L} \left(\frac{G_r}{2}\right)^{1.08} Z \cos \alpha_0} \right]^{-0.7911} \tag{B.2}$$

where $C_{\delta L} = 26200(L_{we})^{0.92}$ was the elastic constant and L_{we} was the effective roller length in millimetres, Z was the number of rolling elements, α_0 was the rolling element contact angle and G_r was the internal radial clearance set to 0.0005 mm. The single roller maximum load, Q, could then be defined as

$$Q_\mathrm{B} = \frac{P_0}{Z \cos \alpha_0} k. \tag{B.3}$$

To calculate the stress induced by the load Q_B in the contact area of the maximumly loaded rolling element, the shape of the elliptic Hertzian contact area was defined using several curvature factors, which for the spherical roller bearings used in this study were

$$\begin{aligned} \rho_{11} &= \frac{2}{D_\mathrm{w}} & \rho_{21} &= \frac{2}{\frac{D_\mathrm{pw}}{\cos \alpha_0} - D_\mathrm{w}} & \rho_{22} &= \frac{-2}{\frac{D_\mathrm{pw}}{\cos \alpha_0} + D_\mathrm{w}} \\ \rho_{12} &= -\rho_{22} S \end{aligned}$$

where D_w and D_pw were the rolling element's diameter and pitch diameter and the osculation factor, S, was the ratio between the radius of curvature of the inner ring and the rolling element which was set to 1.02. The curvature sums for the point and line contacts in the bearing become

$$\begin{aligned} \Sigma \rho_\mathrm{point} &= \rho_{11} + \rho_{12} + \rho_{21} + \rho_{22} \\ \Sigma \rho_\mathrm{line} &= \rho_{11} + \rho_{21}. \end{aligned}$$

A Hertzian auxiliary parameter, τ, was defined using the curvature factors as

$$\cos \tau = \frac{\rho_{11} - \rho_{12} + \rho_{21} - \rho_{22}}{\Sigma \rho_\mathrm{point}}$$

which the Hertzian coefficients, μ and ν that were used to compute the internal bearing stresses had a functional dependence on. These coefficients were defined as

$$\mu = 1.396748 \cos\tau^{0.665242} \cdot (1 - \cos\tau)^{-0.37399}$$

$$\nu = 0.683241 \cos\tau^{0.4} \cdot (1 - \cos\tau)^{-0.189343}$$

if $\cos\tau > 0.87$ and else as

$$\begin{aligned} \mu &= 5.6864 \cos\tau^4 - 6.0607 \cos\tau^3 + 2.7985 \cos\tau^2 \\ &\quad 0.35289 \cos\tau + 1.005 \\ \nu &= 0.0683241 \cos\tau^3 + 0.373719 \cos\tau^2 - 0.67694 \cos\tau \\ &\quad + 1.0014 \end{aligned}$$

if $\cos\tau \leq 0.87$.

With μ and ν determined, the major and semi-major axes of the Hertzian contact ellipse, a and b, between the maximumly loaded rolling element and raceway could be calculated by

$$2a = 0.0472\mu\sqrt[3]{\frac{Q_\mathrm{B}}{\Sigma\rho_\mathrm{point}}} \tag{B.4a}$$

$$2b = 0.0472\nu\sqrt[3]{\frac{Q_\mathrm{B}}{\Sigma\rho_\mathrm{point}}}. \tag{B.4b}$$

The maximum contact pressure, p_0, assuming elliptical contact on the rolling element of a spherical roller bearing and the line pressure, p_line were calculated as

$$p_0 = 270\sqrt{\frac{Q_\mathrm{B}}{2L_{we}}\Sigma\rho_\mathrm{line}} \tag{B.5a}$$

$$p_\mathrm{line} = \frac{858}{\mu\nu}\sqrt{Q_\mathrm{B}(\Sigma\rho_\mathrm{point})^2} \tag{B.5b}$$

A Truncation factor, C_T, is now defined to account for the cases where the length of the contact ellipse, $2a$, exceeds the effective roller length, L_{we}, for highly loaded bearings as

$$C_\mathrm{T} = 1 + \frac{4\left(\frac{b}{a^3}\right)\sqrt{a^2 - \left(\frac{L_{we}}{2}\right)^2}\left[\frac{64}{105}a\left(a - \frac{L_{we}}{2}\right)^2 - \frac{40}{189}\left(a - \frac{L_{we}}{2}\right)^3\right]}{\pi ab - \frac{8}{3}(a - L_{we})\frac{b}{a}\sqrt{a^2 - \left(\frac{L_{we}}{2}\right)^2}} \tag{B.6}$$

which assumes the value of unity if $2a$ is less than the effective roller length.

The last factor that was included in the calculation of the internal bearing contact stress was the ratio of maximum to nominal line contact pressure, which for spherical bearings was defined by the equation for elliptic contacts as

$$K_{lc} = \frac{p_{\mathrm{T}}}{p_{\mathrm{line}}} = \frac{c_{\mathrm{T}} \cdot p_0}{p_{\mathrm{line}}}. \tag{B.7}$$

The maximum contact pressure in the most loaded rolling element in a spherical roller bearing was finally defined as the line contact pressure adjusted with the factor described above as

$$p_{\mathrm{max}} = K_{lc} \cdot p_{\mathrm{line}}. \tag{B.8}$$

Equation (B.8) was used in this thesis to plot the variation of the magnitude of the maximumly loaded rolling element in a TST main bearing during extreme operation over time. It should be noted that the as load direction on the bearings varied for each time-step along with the rolling elements changing location, p_{max} should not be considered a continuous load signal for a single component.

Appendix C

Finite element representation of Timoshenko beam elements

With the equations for the membrane deformations of the Euler-Bernoulli and Timoshenko beam theories defined as in Chapter ??, it is possible to describe the first four steps in the finite element method. Since the detailed formulations in the ANSYS 15 APDL package are proprietary information, the methods presented in this section will again serve as a representative example of the actual methods used as shown in Paz [133]. For simplicity, the derivation of the methods are kept to two dimensions and are only performed for the Euler-Bernoulli beam theory.

Figure C.1 shows the first step of the FE method where a one-dimensional domain is discretised into four elements connected by five nodes. The second step is to define the functions describing the deformation of each element which are known as *shape functions*. With the shape functions known, it is possible to construct a matrix describing the relationships between the nodal forces and displacements of an element, called an element matrix.

In order to derive the element stiffness matrix for a Euler-Bernoulli beam element, the axial and transverse deformations $u_x(x)$ and $u_y(x)$ of an element of length L are defined as functions of the four nodal displacements $(\overline{u}_1, \overline{u}_2, \overline{u}_4, \overline{u}_5)$ and rotations $(\overline{u}_3, \overline{u}_6)$ shown in Figure C.1 as

$$u_x(x) = \sum_{n=1}^{6} \psi_{xn}(x)\overline{u}_n \tag{C.1}$$

$$u_y(x) = \sum_{n=1}^{6} \psi_{yn}(x)\overline{u}_n. \tag{C.2}$$

Here, $\psi_{xn}(x)$ and $\psi_{yn}(x)$ are shape functions that satisfy the given boundary conditions

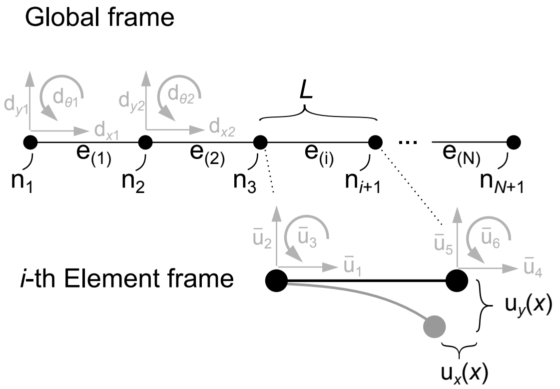

Figure C.1: 1-D array of beam elements in a global reference frame (upper) where each node is assumed to have three global degrees of freedom ($d_{xi}, d_{yi}, d_{\theta i}$). The lower figure shows an element in the i-th elemental reference frame having 6 elemental degrees of freedom and two nodal displacements are highlighted to be used in the derivations below.

at the nodes and are analytical solutions for the kinematic equations for the Euler-Bernoulli beam theory in Equation (5.17). For extension of the element's neutral axis the shape functions become

$$\psi_{x1}(x) = 1 - \frac{x}{L} \tag{C.3}$$

$$\psi_{x4}(x) = \frac{x}{L} \tag{C.4}$$

$$\psi_{x2}(x) = \psi_{x3}(x) = \psi_{x5}(x) = \psi_{x6}(x) = 0. \tag{C.5}$$

Similarly, the shape functions for the bending around the beam's neutral axis become

$$\psi_{y2}(x) = 1 - 3\left(\frac{x}{L}\right)^2 + 2\left(\frac{x}{L}\right)^3 \tag{C.6}$$

$$\psi_{y3}(x) = \left(\frac{x}{L} - 2\left(\frac{x}{L}\right)^2 + \left(\frac{x}{L}\right)^3\right)L \tag{C.7}$$

$$\psi_{y5}(x) = 3\left(\frac{x}{L}\right)^2 - 2\left(\frac{x}{L}\right)^3 \tag{C.8}$$

$$\psi_{y6}(x) = \left(-\left(\frac{x}{L}\right)^2 + \left(\frac{x}{L}\right)^3\right)L \tag{C.9}$$

$$\psi_{y1}(x) = \psi_{y4}(x) = 0. \tag{C.10}$$

The definition of the stiffness matrix is done by the principle of virtual work [117] which considers the elastic potential energy stored in a element. During small deformations, the uniform extensional strain in an element is composed of the extensional term, $\partial u_x / \partial x$, plus the bending strain term, $-(\partial^2 u_y / \partial x^2) y$, which can be re-written as

$$\begin{aligned} \epsilon_{xx} &= \frac{\partial u_x}{\partial x} - \frac{\partial^2 u_y}{\partial x^2} y = \sum_{n=1}^{6} \frac{\partial}{\partial x} \psi_{xn}(x) \bar{u}_n - \sum_{n=1}^{6} \frac{\partial^2}{\partial x^2} \psi_{yn}(x) y \bar{u}_n \\ &= \sum_{n=1}^{6} \psi'_{xn}(x) \bar{u}_n - \sum_{n=1}^{6} \psi''_{yn}(x) y \bar{u}_n = \sum_{n=1}^{6} B_n(x, y) \bar{u}_n \\ &= \mathbf{B}(x, y) \mathbf{u} \end{aligned} \tag{C.11}$$

where **B** is the strain-displacement vector that transforms the nodal displacements to strains anywhere on the element and **u** is a vector containing all nodal displacements. Inserting Equations (C.3) - (C.10) into (C.11) gives

$$\mathbf{B}(x, y) = \left[-\frac{1}{L}, \frac{6y}{L^2} - \frac{12xy}{l^3}, \frac{4y}{L} - \frac{6xy}{L^3}, \frac{1}{L}, -\frac{6y}{L^2} \frac{12xy}{L^3}, \frac{2y}{L} - \frac{6xy}{L^2} \right]. \tag{C.12}$$

The elastic strain energy in the element is composed of contributions from both the beam's extension and bending. The strain energy due to the extension can be written as

$$U = \frac{1}{2} \int_{x=0}^{L} EA (\epsilon_{xx})^2 \, \mathrm{d}x = \frac{1}{2} \int_{x=0}^{L} EA \left(\sum_{n=1}^{6} \psi'_{xn}(x) \bar{u}_n \right)^2 \, \mathrm{d}x \tag{C.13}$$

which is used in combination with the expression of a point force on an elastic body, f_i, is the gradient of the potential energy

$$f_i = \frac{\partial}{\partial u_i} U \tag{C.14}$$

leading to an expression for the i, j-th term in the stiffness matrix $\mathbf{K}_e$ as

$$K_{i,j} = \frac{\partial}{\partial u_i} \frac{\partial}{\partial u_j} U. \tag{C.15}$$

Equation (C.15) is then combined with Equation (C.13) to give the elements for indices 1 and 4 for the stiffness matrix as

$$K_{i,j} = \frac{\partial}{\partial u_i} \frac{\partial}{\partial u_j} \frac{1}{2} \int_{x=0}^{L} EA \left(\sum_{n=1}^{6} \psi'_{xn}(x) \bar{u}_n \right)^2 \, \mathrm{d}x = \int_{x=0}^{L} EA \psi'_{xi}(x) \psi'_{xj}(x) \, \mathrm{d}x. \tag{C.16}$$

The elastic potential energy in the beam caused by its bending is related to the curvature of the beam, κ_z, defined as

$$\kappa_z = \frac{\partial^2 u_y}{\partial x^2} = \sum_{n=1}^{6} \frac{\partial^2}{\partial x^2} \psi_{yn}(x) \overline{u}_n = \sum_{n=1}^{6} \psi''_{yn}(x) \overline{u}_n \tag{C.17}$$

giving an elastic potential energy contribution of

$$U = \frac{1}{2} \int_{x=0}^{L} EI_{zczc} (\kappa_z)^2 \, \mathrm{d}x = \frac{1}{2} \int_{x=0}^{L} EI_{zczc} \left(\sum_{n=1}^{6} \psi''_{yn}(x) \overline{u}_n \right)^2 \mathrm{d}x \tag{C.18}$$

which gives the expression for the stiffness matrix indices 2, 3, 4 and 6 as

$$K_{i,j} = \frac{\partial}{\partial u_i} \frac{\partial}{\partial u_j} \frac{1}{2} \int_{x=0}^{L} EI_{zczc} \left(\sum_{n=1}^{6} \psi''_{yn}(x) \overline{u}_n \right)^2 \mathrm{d}x = \int_{x=0}^{L} EI_{zczc} \psi''_{yi}(x) \psi''_{yj}(x) \, \mathrm{d}x. \tag{C.19}$$

The stiffness matrix for the 2-D Euler-Bernoulli element is finally constructed by substituting the expressions of the shape functions (Equations (C.3) - (C.10)) into Equation (C.16) and Equation (C.19) giving

$$\mathbf{K}_e = \begin{bmatrix} \frac{EA}{L} & 0 & 0 & -\frac{EA}{L} & 0 & 0 \\ & \frac{12EI}{L^3} & \frac{6EI}{L^2} & 0 & \frac{-12EI}{L^3} & \frac{6EI}{L^2} \\ & & \frac{4EI}{L} & 0 & -\frac{6EI}{L^2} & \frac{2EI}{L} \\ & & & \frac{EA}{L} & 0 & 0 \\ & \text{Sym.} & & & \frac{12EI}{L^3} & -\frac{6EI}{L^2} \\ & & & & & -\frac{4EI}{L} \end{bmatrix}. \tag{C.20}$$

Following the process outlined above, the stiffness matrix for a two dimensional Timoshenko beam element can be obtained by re-defining the shape functions to accommodate both the transverse, shear and bending deformations of the element. The non-zero shape functions for the transverse displacements are

$$\psi_{y2}(x) = \frac{1}{1+\Phi}\left[1 - 3\left(\frac{x}{L}\right)^2 + 2\left(\frac{x}{L}\right)^3 + \left(1 - \frac{x}{L}\right)\Phi\right] \tag{C.21}$$

$$\psi_{y3}(x) = \frac{1}{1+\Phi}\left[\frac{x}{L} - 2\left(\frac{x}{L}\right)^2 + \left(\frac{x}{L}\right)^3 + \frac{1}{2}\left(\frac{x}{L} - \left(\frac{x}{L}\right)^2\right)\Phi\right] \tag{C.22}$$

$$\psi_{y5}(x) = \frac{1}{1+\Phi}\left[3\left(\frac{x}{L}\right)^2 - 2\left(\frac{x}{L}\right)^3 + \frac{x}{L}\Phi\right] \tag{C.23}$$

$$\psi_{y6}(x) = \frac{L}{1+\Phi}\left[-\left(\frac{x}{L}\right)^2 + \left(\frac{x}{L}\right)^3 - \frac{1}{2}\left(\frac{x}{L} - \left(\frac{x}{L}\right)^2\right)\Phi\right] \tag{C.24}$$

and the shape functions for the shear and bending deformation are

$$\psi_{(\mathrm{b})y2}(x) = \frac{1}{1+\Phi}\left[1 - 3\left(\frac{x}{L}\right)^2 + 2\left(\frac{x}{L}\right)^3\right] \tag{C.25}$$

$$\psi_{(\mathrm{s})y2}(x) = \frac{\Phi}{1+\Phi}\left[1 - \frac{x}{L}\right] \tag{C.26}$$

$$\psi_{(\mathrm{b})y3}(x) = \frac{L}{1+\Phi}\left[\frac{x}{L} - 2\left(\frac{x}{L}\right)^2 + \left(\frac{x}{L}\right)^3 + \frac{1}{2}\left(2\frac{x}{L} - \left(\frac{x}{L}\right)^2\right)\Phi\right] \tag{C.27}$$

$$\psi_{(\mathrm{s})y3}(x) = -\frac{L\Phi}{1+\Phi}\left[\frac{1}{2}\frac{x}{L}\right] \tag{C.28}$$

$$\psi_{(\mathrm{b})y5}(x) = \frac{1}{1+\Phi}\left[3\left(\frac{x}{L}\right)^2 - 2\left(\frac{x}{L}\right)^3\right] \tag{C.29}$$

$$\psi_{(\mathrm{s})y5}(x) = \frac{\Phi}{1+\Phi}\left[\frac{x}{L}\right] \tag{C.30}$$

$$\psi_{(\mathrm{b})y6}(x) = \frac{L}{1+\Phi}\left[-\left(\frac{x}{L}\right)^2 + \left(\frac{x}{L}\right)^3 + \frac{1}{2}\left(\left(\frac{x}{L}\right)^2\right)\Phi\right] \tag{C.31}$$

$$\psi_{(\mathrm{b})y6}(x) = -\frac{L}{1+\Phi}\left[\frac{1}{2}\frac{x}{L}\Phi\right] \tag{C.32}$$

where Φ is a factor that gives the importance of the shear deformation relative to the bending deformation as

$$\Phi = \frac{12EI}{G(A/\kappa)L^2}. \tag{C.33}$$

Using the same approach as for the Euler-Bernoulli case to derive the stiffness matrix elements, through the expression of the strain energy stored in the beam, the matrix components are written as

$$
\begin{aligned}
K_{i,j} = EA \int_{x=0}^{L} \psi'_{xi}\psi'_{xj}(x)\,\mathrm{d}x + EI_{zczc} \int_{x=0}^{L} \psi''_{(\mathrm{b})yi}\psi''_{(\mathrm{b})yj}(x)\,\mathrm{d}x \\
+ G(A/\alpha) \int_{x=0}^{L} \psi'_{(\mathrm{s})yi}\psi'_{(\mathrm{s})yj}(x)\,\mathrm{d}x
\end{aligned}
\tag{C.34}
$$

where the first term is related to the axial strain, the second is related to the transverse bending strain and the third is related to the transverse shear strain. The explicit solution for the two-dimensional stiffness matrix of a Timoshenko element can then be written as

$$
\mathbf{K}_e = \begin{bmatrix}
\frac{EA}{L} & 0 & 0 & -\frac{EA}{L} & 0 & 0 \\
 & \frac{12}{1+\Phi}\frac{EI}{L^3} & \frac{6}{1+\Phi}\frac{EI}{L^2} & 0 & -\frac{12}{1+\Phi}\frac{EI}{L^3} & \frac{6}{1+\Phi}\frac{EI}{L^2} \\
 & & \frac{4+\Phi}{1+\Phi}\frac{EI}{L} & 0 & -\frac{6}{1+\Phi}\frac{EI}{L^2} & \frac{2-\Phi}{1+\Phi}\frac{EI}{L} \\
 & & & \frac{EA}{L} & 0 & 0 \\
 & \text{Sym.} & & & \frac{12}{1+\Phi}\frac{EI}{L^3} & -\frac{6}{1+\Phi}\frac{EI}{L^2} \\
 & & & & & \frac{4+\Phi}{1+\Phi}\frac{EI}{L}
\end{bmatrix}.
\tag{C.35}
$$

With the expression for a single Timoshenko beam element given, it is now possible to construct a *global stiffness matrix*, **K**, which is related to the elemental forces and displacements by

$$
\mathbf{K}\overline{u} = \overline{F}
\tag{C.36}
$$

where $\overline{u}$ is a vector containing the nodal displacements in all degrees of freedom for every element and $\overline{F}$ is a vector containing the applied nodal forces. The global stiffness matrix is assembled by the selected elemental stiffness matrices used for a specific problem and the global nodal displacements and global external forces.

A conceptual description of the global matrix assembly process is shown in Figure C.2 where the global displacement vector $\overline{u}$ is comprised by the global nodal displacements in three degrees of freedom, $d_{x1}, d_{y1}, d_{\theta1}$, as shown in Figure C.1. It is in this displacement vector that any kinematic boundary conditions are applied, which were

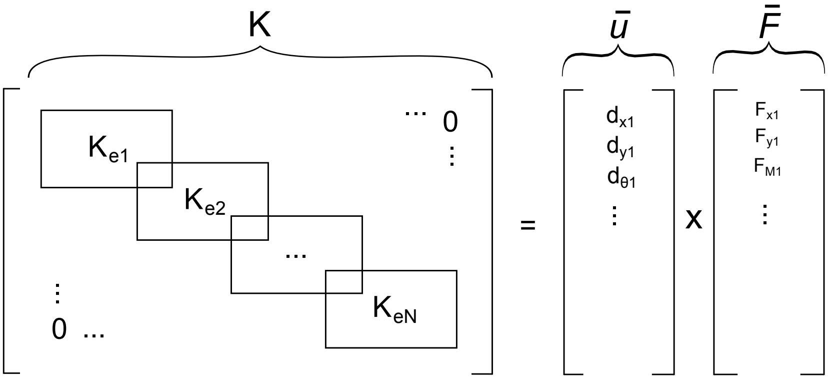

Figure C.2: Conceptual description of the numerical FEM problem to be solved through numerical methods in a FEM solver. The figure shows the global stiffness matrix **K** containing the elasticity properties of each element and their nodal relationships, the global displacement vector $\overline{u}$ containing the nodal translations and rotations and the global force vector $\overline{F}$ containing the forces and moments on the nodes.

used in Section 5.2.1 to describe the shaft bearing elasticity. The elemental stiffness matrices are then used to relate the nodal displacements and the nodal forces and moments, F_{x1}, F_{y1}, F_{M1} and the interactions between them. The solution of this system of equations is usually done using some numerical method in a commercial solver package.

Appendix D

Design standards for use in tidal energy systems

Design standards[1] provide engineers, developers and researchers with a means to achieve the minimum levels of design criteria and make possible the use of standardised methodologies for performance comparisons. Design standards can also serve as guides on how to achieve third party certification of a technology in terms of operational safety, structural integrity and risk assessment.

Although the marine current turbine sector is still in its infancy at the time of writing, several design standards are starting to emerge with regards to marine energy systems. These standards typically cover aspects of environmental load assumptions, design safety factors and recommended modelling techniques. When used in combination with standards from the wind industry, the offshore engineering sector and international standards for various sub-components, it is possible to form a clearer picture of how to address the issues facing machinery deployed in the marine environment.

In the study presented, several standards for different fields have been consulted in order to tackle the challenge of TST hydrodynamic loading and bearing fatigue life. The a brief description of the standards used are as follows:

DNV-RP-C205 [26]: This 'recommended practice' document from Det Norske Veritas (DNV) aims to provide rational design criteria for structures deployed in the marine environment. Here, the environmental conditions which may contribute to structural damage, such as from waves, currents and winds, are defined and load mod-

---

[1] In this thesis, the word 'design standards' refers to published technical documentation detailing recommended design practices including, certification standards, international standards and design requirements.

elling assumptions are presented. Of particular interest for this project is the definition of Wheeler stretching, irregular wave models, wind loading, and shear current profiles.

IEC 62600-2 [11]: This technical specification document, published by the IEC, provides the essential design requirements to ensure engineering integrity for marine energy converters (MECs) over a given design life. The purpose of the document is to provide guidance on how to manage the environmental loads brought on the primary structure of a MEC, and how to avoid premature failure. The document defines the external load conditions in terms of normal and extreme cases. This practice of a design focus on purely mechanical integrity, based on site-specific climatology, is followed in this thesis.

IEC 61400-4:2012 [66]: This is a part of the IEC 61400 series wind turbine standards that covers the design requirements for gearboxes using rolling element bearings. The document also gives guidance of the engineering of bearings which is of interest for TST bearing fatigue calculations, particularly the calculations of the maximum contact pressures and equivalent bearing loads.

ISO 76:2006 [69]: The international standard of rolling bearing static load rating, published by the International Organization for Standardization (ISO), is a often quoted document for bearing design. The document details the calculation of the static load rating for rolling element bearings and the definition of the equivalent static loads as in IEC 61400-4:2012.

ISO 281:2007 [70]: This international standard covers the method of basic dynamic rating life, based on raceway sub-surface fatigue, and is the main methodology used for bearing fatigue life predictions in this thesis. The document does not include the influence of wear, corrosion and electrical corrosion on the life of bearings.

References

[1] ANSYS Inc. *ANSYS Parametric Design Language Guide.*

[2] *European Marine Energy Centre.* `http://www.emec.org.uk/`. (Accessed on: 27-07-2016).

[3] B. Yang and C. Lawn. 'Fluid dynamic performance of a vertical axis turbine for tidal currents'. In: *Renewable Energy* 36.12 (2011), pp. 3355–3366.

[4] N. Barltrop, K. Varyani, A. Grant, D. Clelland and X. Pham. 'Wave-current interactions in marine current turbines'. In: *Proceedings of the Institution of Mechanical Engineers, Part M: Journal of Engineering for the Maritime Environment* 220.4 (2006), pp. 195–203.

[5] M. O. Hansen. *Aerodynamics of Wind Turbines.* 2:nd. Earthscan, 2008.

[6] P. Fraenkel. 'Development and testing of Marine Current Turbine's SeaGen 1.2 MW tidal stream turbine'. In: *Proc. 3rd International Conference on Ocean Energy.* 2010.

[7] I. H. Abbott and A. E. Von Doenhoff. *Theory of Wing Sections, Including a Summary of Airfoil Data.* Dover Publications, 1959.

[8] J. Andrews, N. Jelley and N. Jelley. *Energy Science: Principles, Technologies, and Impacts.* Energy Science: Principles, Technologies, and Impacts. OUP Oxford, 2013.

[9] D. R. Sutherland, B. G. Sellar, S. Harding and I. Bryden. 'Initial flow characterisation utilising turbine and seabed installed acoustic sensor arrays'. In: *Proceedings of the 10th European Wave and Tidal Energy Conference Series, Aalborg, Denmark.* 2013, pp. 2–5.

[10] A. M. Colucci, A. Bouferrouk, J. P. Hardwick and L. Johanning. 'Characterising Wave-Current Fields and their Interaction from in situ Measurements'. In: *Proceedings from the10th European Wave and Tidal Energy Conference, Aalborg, Denmark* (2011).

[11] *Design requirements for marine energy systems (IEC 62600-2).* International Electrotechnical Commission, 2013.

[12] *Energy Systems Research Unit Website.* `http://www.esru.strath.ac.uk/EandE/Web_sites/11-12/MORE/overview/tidal_currents.html`. (Accessed on: 27-07-2016).

[13] D. Magagna and A. Uihlein. *2014 JRC Ocean Energy Status Report.* Tech. rep. 2015.

[14] M. Arnold, F. Biskup and P. W. Cheng. ‘Impact of structural flexibility on loads on tidal current turbines’. In: 11th European Wave and Tidal Energy Conference. 2015.

[15] W. Batten, A. Bahaj, A. Molland and J. Chaplin. ‘Experimentally validated numerical method for the hydrodynamic design of horizontal axis tidal turbines’. In: *Ocean Engineering* 34.7 (2007-05), pp. 1013–1020.

[16] I. A. Milne, A. H. Day, R. N. Sharma and R. G. J. Flay. ‘Blade loads on tidal turbines in planar oscillatory flow’. In: *Ocean Engineering* 60 (2013), pp. 163–174.

[17] I. Milne, A. Day, R. Sharma and R. Flay. ‘Blade loading on tidal turbines for uniform unsteady flow’. In: *Renewable Energy* 77 (2015), pp. 338–350.

[18] P. W. Galloway, L. E. Myers and A. S. Bahaj. ‘Quantifying wave and yaw effects on a scale tidal stream turbine’. In: *Renewable energy* 63 (2014), pp. 297–307.

[19] I. Milne and A. Day. ‘Horizontal-axis tidal turbine blade loading for multi-frequency oscillatory motion’. In: *18th Australasian Fluid Mechanics Conference* (2012).

[20] S. Tedds, T. deHesus Henriques, I. Owen and R. Poole. ‘Near-wake characterisation of Horizontal Axis Tidal Stream Turbines in non-uniform steady flow’. In: *Proceedings of the 10th European Wave and Tidal Energy Conference Series, Aalborg, Denmark.* 2013.

[21] P. Galloway. ‘Performance quantification of tidal turbines subjected to dynamic loading’. PhD thesis. University of Southampton, 2013.

[22] B. Gaurier, P. Davies, A. Deuff and G. Germain. ‘Flume tank characterization of marine current turbine blade behaviour under current and wave loading’. In: *Renewable Energy* 59 (2013-11), pp. 1–12.

[23] I. Milne, R. Sharma, R. Flay and S. Bickerton. ‘The role of waves on tidal turbine unsteady blade loading’. In: *Proceedings of the 3rd International Conference on Ocean Energy, Bilbao, Spain.* 2010.

[24] E. Bossanyi. ‘BLADED for windows theory manual’. In: *Bristol, England: Garrad Hassan and Partners Limited* (1997).

[25] T. A. de Jesus Henriques, S. C. Tedds, A. Botsari, H. Najafian, C. J. Sutcliffe, I. Owen and R. J. Poole. ‘The Effects of Wave-Current Interactions on the Performance of a Model Horizontal Axis Tidal Turbine’. In: *Proceedings of the 10th European Wave and Tidal Energy Conference Series, Aalborg, Denmark.* 2013.

[26] *Environmental conditions and environmental loads (DNV-RP-C205).* Recommended practice. Det Norske Veritas, 2007.

[27] T. Wang and J. Li. ‘Effect of nonlinear wave-current interaction on flow fields and hydrodynamic forces’. In: *Science in China Series A: Mathematics* 40.6 (1997), pp. 622–632.

[28] D. Peregrine. ‘Interaction of water waves and currents’. In: *Advances in applied mechanics* 16 (1976), pp. 9–117.

[29] J. D. Fenton. ‘A fifth-order Stokes theory for steady waves’. In: *Journal of waterway, port, coastal, and ocean engineering* 111.2 (1985), pp. 216–234.

[30] C. Swan, J. P. Cummins and R. L. James. ‘An experimental study of two-dimentional surface water waves propagating on depth-varying currents. Part 1. Regular waves’. In: *Journal of Fluid Mechanics* 428 (2001), pp. 273–304.

[31] N. Kishida and R. J. Sobey. ‘Stokes theory for waves on a linear shear current’. In: *Journal of engineering mechanics* 114.8 (1989), pp. 1317–1334.

[32] D. Markus, R. Wüchner and K.-U. Bletzinger. ‘A numerical investigation of combined wave-current loads on tidal stream generators’. In: *Ocean Engineering* 72 (2013-11), pp. 416–428.

[33] T. Blackmore, L. E. Myers and A. S. Bahaj. ‘Effects of turbulence on tidal turbines: Implications to performance, blade loads, and condition monitoring’. In: *International Journal of Marine Energy* 14 (2016), pp. 1–26.

[34] P. Mycek, B. Gaurier, G. Germain, G. Pinon and E. Rivoalen. ‘Numerical and experimental study of the interaction between two marine current turbines’. In: *arXiv preprint arXiv:1310.4921* (2013).

[35] G. McCann. ‘Tidal current turbine fatigue loading sensitivity to waves and turbulence – a parametric study’. In: *Proceedings from 7th European wave and tidal energy conference.* 2007.

[36] J. C. Chapman. ‘Tidal Energy Device Hydrodynamics in Non-Uniform Transient Flows’. PhD thesis. Swansea University, 2008.

[37] S. Oye. *Tjaereborg Wind Turbine (Esbjerg): First dynamic inflow measurement.* AFM notat. 1991.

[38] S. Oye. *Tjaereborg Wind Turbine: 4. dynamic inflow measurement.* AFM notat. 1991.

[39] J. Schepers and H. Snel. *Final Results of the EU Joule Projects ”dynamic Inflow”.* ECN-RX. Netherlands Energy Research Foundation ECN, 1995.

[40] H. Snel and J. Schepers. ‘Engineering models for dynamic inflow phenomena’. In: *Journal of Wind Engineering and Industrial Aerodynamics* 39.1 (1992), pp. 267–281.

[41] H. Snel and J. Schepers. *Joint investigation of dynamic inflow effects and implementation of an engineering method.* Netherlands Energy Research Foundation ECN, 1995.

[42] J. Whelan, J. Graham and J. Peiro. ‘Inertia effects on horizontal axis tidal-stream turbines’. In: *the 8th European Wave and Tidal Energy Conference.* 2009.

[43] H. Buckland. ‘Combined current, wave and turbulent flows on tidal energy. Volume 1’. PhD thesis. Swansea University, 2013.

[44] S. Tatum et al. ‘Wave–current interaction effects on tidal stream turbine performance and loading characteristics’. In: *International Journal of Marine Energy* (2015),

[45] N. G. Jacobsen, D. R. Fuhrman and J. Fredsøe. 'A wave generation toolbox for the open-source CFD library: OpenFoam®'. In: *International Journal for Numerical Methods in Fluids* 70.9 (2012), pp. 1073–1088.

[46] R. A. Dalrymple. 'Water waves on a bilenear shear current'. In: *Coastal Engineering Proceedings*. 14. 1974.

[47] B. Le Méhauté. *An introduction to hydrodynamics and water waves.* Springer Verlag, New York., 1976.

[48] R. Dean and R. Dalrymple. *Water wave mechanics for engineers and scientists.* World scientific, 1991.

[49] C. Faudot and O. G. Dahlhaug. 'Prediction of wave loads on tidal turbine blades'. In: *Energy Procedia* 20 (2012), pp. 116–133.

[50] G. G. Stokes. 'On the theory of oscillatory waves'. In: *Trans Cambridge Philos Soc* 8 (1847), pp. 441–473.

[51] J. Fenton. 'Nonlinear wave theories'. In: *The Sea, Ocean Engineering Science* 9.1 (1990), pp. 3–25.

[52] A. Toumazis, R. Ahilan et al. 'Review Of Recent Analytical And Approximate Solutions Of Wave-Currnt Interaction'. In: *Environmental Forces on Offshore Structures and Their Predictions: Proceedings of an international conference.* Society of Underwater Technology. 1990.

[53] R. A. Skop. 'Approximate dispersion relation for wave-current interactions'. In: *Journal of Waterway, Port, Coastal, and Ocean Engineering* 113.2 (1987), pp. 187–195.

[54] R. A. Dalrymple. 'Nonlinear water waves on a vertically-sheared current'. In: *The Oil Industry Int. Exploration & Production Forum.* 1989.

[55] J. e. a. Wheeler. 'Method for calculating forces produced by irregular waves'. In: *Journal of Petroleum Technology* 22.03 (1970), pp. 359–367.

[56] C. Iliev and D. Val. 'Tidal current turbine reliability: power take-off train models and evaluation'. In: *Proc. 3rd International Conference on Ocean Energy, Bilbao.* 2010.

[57] I. P. Girsang, J. S. Dhupia, E. Muljadi, M. Singh and L. Y. Pao. 'Gearbox and drivetrain models to study dynamic effects of modern wind turbines'. In: *IEEE Transactions on Industry Applications* 50.6 (2014), pp. 3777–3786.

[58] Y. Hase. *Handbook of power system engineering.* John Wiley & Sons, 2007.

[59] E. V. Zaretsky, J. V. Poplawski and C. R. Miller. *Rolling Bearing Life Prediction-Past, Present, and Future.* Technical report. NASA Glenn Research Center; Cleveland, OH United States, 2000.

[60] J. Brändlein. *Ball and roller bearings: theory, design and application.* Wiley, 1999.

[61] H. Hertz. 'Ü ber die Berü hrung fester elastischer Kö rper'. In: *Gesammelte Werke (P. Lenard, ed.), Bd. 1, (J.A. Barth, Leipzig)* (1895), pp. 115–173.

[62] The barden corporation. *Bearing Failure: Causes and Cures.* 2007.

[63] P. R. Thies, L. Johanning, K. A. Karikari-Boateng, C. Ng and P. McKeever. 'Component reliability test approaches for marine renewable energy'. In: *Proceedings of the Institution of Mechanical Engineers, Part O: Journal of Risk and Reliability* (2015), p. 1748006X15580837.

[64] J. Schijve. *Fatigue of structures and materials*. Springer, 2001.

[65] R. J. Wood, A. S. Bahaj, S. R. Turnock, L. Wang and M. Evans. 'Tribological design constraints of marine renewable energy systems'. In: *Philosophical Transactions of the Royal Society of London A: Mathematical, Physical and Engineering Sciences* 368.1929 (2010), pp. 4807–4827.

[66] *Wind turbines – Part 4: Design Requirements for Wind Turbine Gearboxes (IEC 61400-4)*. International Electrotechnical Commission, 2009.

[67] D. H. Zeiner-Gundersen. 'Turbine design and field development concepts for tidal, ocean, and river applications'. In: *Energy Science & Engineering* 3.1 (2015), pp. 27–42.

[68] G. Lundberg and A. Palmgren. *Dynamic capacity of roller bearings*. 196. Generalstabens litografiska anstalts förlag, 1947.

[69] *Rolling bearings – Static load ratings (ISO 76)*. International standard. International Organization for Standardization, 2006.

[70] *Rolling bearings – Dynamic load ratings and rating life (ISO 281)*. International standard. International Organization for Standardization, 2007.

[71] P. J. Moriarty. 'AeroDyn Theory Manual'. In: January (2005).

[72] H. Glauert. 'Airplane Propellers'. English. In: *Aerodynamic Theory*. Springer Berlin Heidelberg, 1935, pp. 169–360.

[73] J. F. Manwell, J. G. McGowan and A. L. Rogers. *Wind Energy Explained: Theory, Design and Application*. 2nd ed. Wiley & Sons, 2009.

[74] T. Burton, N. Jenkins, D. Sharpe and E. Bossanyi. *Wind energy handbook*. John Wiley & Sons LTD, 2001.

[75] I. Masters and J. A. C. Orme. 'A robust blade element momentum theory model for tidal stream turbines including tip and hub loss corrections'. In: 10.1 (2011), pp. 25–36.

[76] D. M. McNae. 'Unsteady hydrodynamics of tidal stream turbines'. PhD thesis. Imperial College London, 2013.

[77] H. Dumitrescu and V. Cardos. 'Wind turbine aerodynamic performance by lifting line method'. In: *International Journal of Rotating Machinery* 4.3 (1998), pp. 141–149.

[78] M. Harrison, W. Batten, L. Myers and A. Bahaj. 'Comparison between CFD simulations and experiments for predicting the far wake of horizontal axis tidal turbines'. In: *IET Renewable Power Generation* 4.6 (2010), pp. 613–627.

[79] J. Peeters. 'Simulation of Dynamic Drive Train Loads in a Windturbine'. PhD thesis. Katholieke Universiteit Leuven, 2006.

[80] J. M. Jonkman and M. L. B. Jr. *FAST User's Guide*. National Renewable Energy Laboratory. 2005-08.

[81] E. De Vries. 'Trouble spots-Gearbox failures and design solutions'. In: *Renewable Energy World* 9.2 (2006), p. 37.

[82] S. AG. *SIMPACK Documentation*. 2013.

[83] D. King and B. Perera. 'Morris method of sensitivity analysis applied to assess the importance of input variables on urban water supply yield - A case study'. In: *Journal of Hydrology* 477 (2013), pp. 17–32.

[84] M. D. Morris. 'Factorial sampling plans for preliminary computational experiments'. In: *Technometrics* 33.2 (1991), pp. 161–174.

[85] A. Saltelli, S. Tarantola, F. Campolongo and M. Ratto. *Sensitivity analysis in practice: a guide to assessing scientific models*. John Wiley & Sons, 2004.

[86] *CBC News web page*. `http://www.cbc.ca/news/canada/nova-scotia/failed-tidal-turbine-explained-at-symposium-1.1075510`. Accessed on: 28-07-2016.

[87] *MATLAB Programming Fundamentals*. MathWorks. 2016.

[88] M. Drela. 'XFOIL: An analysis and design system for low Reynolds number airfoils'. In: *Low Reynolds number aerodynamics*. Springer, 1989, pp. 1–12.

[89] A. D. Craik. 'The origins of water wave theory'. In: *Annual review of fluid mechanics* 36.1 (2004), p. 1.

[90] O. Faltinsen. *Sea Loads on Ships and Offshore Structures*. Cambridge Ocean Technology Series. Cambridge University Press, 1993.

[91] K. Hasselmann et al. *Measurements of wind-wave growth and swell decay during the Joint North Sea Wave Project (JONSWAP)*. Tech. rep. Deutches Hydrographisches Institut, 1973.

[92] W. J. Pierson and L. Moskowitz. 'A proposed spectral form for fully developed wind seas based on the similarity theory of SA Kitaigorodskii'. In: *Journal of geophysical research* 69.24 (1964), pp. 5181–5190.

[93] Natural Environment Research Council. *British Oceanographic Data Centre web page*. `http://www.bodc.ac.uk/`. (Accessed on: 28-07-2016).

[94] R. Wilson, P. Lissaman and O. state university. *Applied Aerodynamics of Wind Power Machines. [Publ. By] Oregon State University*. 1974.

[95] W. Z. Shen, R. Mikkelsen, J. N. Sørensen and C. Bak. 'Tip loss corrections for wind turbine computations'. In: *Wind Energy* 8.4 (2005-10), pp. 457–475.

[96] H. Glauert. *The analysis of experimental results in the windmill brake and vortex ring states of an airscrew*. HM Stationery Office, 1926.

[97] M. L. Buhl. *A new empirical relationship between thrust coefficient and induction factor for the turbulent windmill state*. National Renewable Energy Laboratory, 2005.

[98] D. Spera. *Wind Turbine Technology: Fundamental Concepts of Wind Turbine Engineering*. American Society of Mechanical Engineers, 1994.

[99] N. Barltrop, K. S. Varyani, A. Grant, D. Clelland and X. P. Pham. 'Investigation into wave- current interactions in marine current turbines'. In: *Proceedings of the Institution of Mechanical Engineers, Part A: Journal of Power and Energy* 221.2 (2007-01), pp. 233–242.

[100] G. Gaonkar and D. Peters. 'Review of dynamic inflow modeling for rotorcraft flight dynamics.' In: *VERTICA.* 12.3 (1988), pp. 213–242.

[101] L. Tuckerman. *Inertia factors of ellipsoids for use in airship design.* US Government Printing Office, 1925.

[102] S. A. Ning. 'A simple solution method for the blade element momentum equations with guaranteed convergence'. In: *Wind Energy* 17.9 (2014), pp. 1327–1345.

[103] Mathworks. *Mathworks documentation center, fmincon entry.* 2013. URL: `http://www.mathworks.co.uk/help/optim/ug/fmincon.html`.

[104] N. Oreskes, K. Shrader-Frechette, K. Belitz et al. 'Verification, validation, and confirmation of numerical models in the earth sciences'. In: *Science* 263.5147 (1994), pp. 641–646.

[105] D. A. Doman, R. E. Murray, M. J. Pegg, K. Gracie, C. M. Johnstone and T. Nevalainen. 'Tow-tank testing of a 1/20th scale horizontal axis tidal turbine with uncertainty analysis'. In: *Int. J. Mar. Energy* 11 (2015), pp. 105–119.

[106] G. Pinon, P. Mycek, G. Germain and E. Rivoalen. 'Numerical simulation of the wake of marine current turbines with a particle method'. In: *Renewable Energy* 46 (2012), pp. 111–126.

[107] M. Togneri, I. Masters, R. Malki and R. A. 'Flume measurements of lift and drag for selected tidal turbine blade sections'. In: *International Journal of Marine Energy* (2015). (Submitted for publication).

[108] K. Dykes, A. Ning, R. King, P. Graf, G. Scott and P. Veers. 'Sensitivity analysis of wind plant performance to key turbine design parameters: A systems engineering approach'. In: *32nd ASME Wind Energy Symposium, National Harbor, Maryland.* 2014.

[109] L. Ziegler, S. Voormeeren, S. Schafhirt and M. Muskulus. 'Sensitivity of Wave Fatigue Loads on Offshore Wind Turbines under Varying Site Conditions'. In: *Energy Procedia* 80 (2015). 12th Deep Sea Offshore Wind R&D Conference, pp. 193–200.

[110] T. Nevalainen, C. Johnstone and G. A.D. 'An Unsteady Blade Element Momentum Theory for Tidal Stream Turbines with Morris Method Sensitivity Analysis'. In: *European Wave and Tidal Energy Conference Proceedings* (2015).

[111] T. Nevalainen, C. Johnstone and G. A.D. 'A Sensitivity Analysis on Tidal Stream Turbine Loads Caused by Operational, Geometric Design and Inflow Parameters'. In: *International Journal of Marine Energy* (2016).

[112] W. Schiffer. 'Advanced methods for static and dynamic shafting calculations'. In: *Brodogradnja* 58.2 (2007), pp. 158–164.

[113] B. Jiang. ‘Modeling of Dynamics of Driveline of Wind Stations: Implementation in LMS Imagine AMESim Software’. In: (2010).

[114] Y. W. Kwon and H. Bang. *The finite element method using MATLAB*. CRC press, 2000.

[115] J. N. Reddy. *An introduction to the finite element method*. Vol. 2. 2.2. McGraw-Hill New York, 1993.

[116] E. Carrera, G. Giunta and M. Petrolo. *Beam Structures: Classical and Advanced Theories*. EngineeringPro collection. Wiley, 2011.

[117] J. S. Przemieniecki. *Theory of matrix structural analysis*. Courier Corporation, 1985.

[118] H. Vinayak, R. Singh and C. Padmanabhan. ‘Linear dynamic analysis of multi-mesh transmissions containing external, rigid gears’. In: *Journal of Sound and Vibration* 185.1 (1995), pp. 1–32.

[119] M. M. Khonsari and E. R. Booser. *Applied tribology: bearing design and lubrication*. Vol. 12. John Wiley & Sons, 2008.

[120] E. Gargiulo. ‘A simple way to estimate bearing stiffness’. In: *Machine Design* 52.17 (1980), pp. 107–110.

[121] ANSYS Inc. *ANSYS Modeling and Meshing Guide*. Release 10.0.

[122] ANSYS Inc. *Element Reference*. (Release 12.1). 2009.

[123] E. V. Zaretsky. ‘A. Palmgren Revisited: A Basis for Bearing Life Prediction’. In: (1997).

[124] E. V. Zaretsky. *Rolling Bearing Life Prediction, Theory, and Application*. Technical paper. NASA Glenn Research Center, Cleveland, Ohio, 2013.

[125] H. O. Fuchs and I. Stephens. ‘Metal fatigue in engineering’. In: *JOHN WILEY & SONS, NY. 1980.* (1980).

[126] M. A. Miner et al. ‘Cumulative damage in fatigue’. In: *Journal of applied mechanics* 12.3 (1945), pp. 159–164.

[127] G. Hayman. ‘MLife theory manual for version 1.00’. In: *National Renewable Energy Laboratory, Golden, CO* (2012).

[128] Lloyd’s Register. *Rules and Regulations for the Classification of Special Service Craft*. Vol. 7, Part 11, Transmission Systems. 2014.

[129] Schaeffler Technologies AG and Co. KG. Accessed: June 2016. 2016-June. URL: `%7Bhttp://medias.schaeffler.de/medias/en!hp%7D`.

[130] Schaeffler (UK) Ltd. URL: `%7Bhttp://www.schaeffler.co.uk/content.schaeffler.co.uk/en/index.jsp%7D`.

[131] ABP Marine Environmental Research Ltd. *Atlas of UK Marine Renewable Energy web page*. `http://www.renewables-atlas.info/`. (Accessed on: 28-07-2016).

[132] B. Iooss and P. Lemaitre. ‘A review on global sensitivity analysis methods’. In: *Uncertainty Management in Simulation-Optimization of Complex Systems*. Springer, 2015, pp. 101–122.

[133] M. Paz. *Structural dynamics: theory and computation.* Springer Science & Business Media, 2012.